9-12-2014

# Stable Solar Cells through Controlled Block Copolymer Self-Assembly and Cooperative Hydrogen Bonding Interactions

Fei Li

Fei Li

*Candidate*

Chemistry and Chemical Biology

*Department*

This dissertation is approved, and it is acceptable in quality and form for publication:

*Approved by the Dissertation Committee:*

Prof. Yang Qin, Chairperson

Prof. John K.Grey

Prof. Charles E. (Chad) Melançon III

Prof. David H. Dunlap

# Stable Solar Cells through Controlled Block Copolymer Self-Assembly and Cooperative Hydrogen Bonding Interactions

**BY**

**Fei Li**

M.S. Organic Chemistry, Beijing University of Chemical Technology, China, 2009

B.Eng. Chemical Engineering, Hubei University, China, 2006

DISSERTATION

Submitted in Partial Fulfillment of the
Requirements for the Degree of

**Doctor of Philosophy**
**Chemistry**

**The University of New Mexico**
**Albuquerque, New Mexico**

July 2014

## ACKNOWLEDGEMENTS

First and foremost, I want to thank my advisor Dr. Yang Qin for his guidance and assistance on my project during the past four years. Dr. Qin could always use his knowledge and experience to tackle the problems in my project and push it forward. It was really my honor to work under his supervision, from whom I learned a lot, with the hands-on training and the way of scientific thinking. Without his help, it would be impossible to have this dissertation in press. More importantly, I believe the skills and knowledge that I learned from him will benefit me in the future.

Secondly, I would like to express my gratitude to my committee members, Dr. Grey, Dr. Melançon and Dr. Dunlap for their time spent in reading this dissertation and valuable suggestions on finalizing this draft. In addition, I want to thank them for their advice during my research proposal which really expedited the progress of this project.

Thirdly, all our lab collaborators are also acknowledged for their effort to facilitate this project. Specifically, Prof. Kevin Malloy and his student Noel Dawson helped us with AFM measurements; Dr. Ying-Bing Jiang trained me to be a TEM user and did all the troubleshooting during the measurements; Dr. Kevin Yager at Brookhaven National Lab spent valuable time on collecting the GISAXS and GIWAXS data for our samples. These data were very important to help us better understand the cooperative self-assembly between our block copolymers and fullerenes. Without their input, the nice

correlation work of morphologies with solar cell performances would not be possible. Besides, my thanks also go to Dr. Fu-Sen Liang for his generosity to allow me to access his lab microscope conveniently during the past years.

Fourthly, I am grateful to have Jiangzhong Yang in our lab who has done substantial amount of work on optimizing the lab conditions of the benchmark BHJ solar cells and taking the optical micrographs outside the lab at CBME during the early days of this project. Without his work, the process to publish my first paper would not be that pleasant. Moreover, other group members including Robert Sparks, Fei Chang, Wenhan He, Keda Hu and Guoshun Yang are also appreciated for the joyful time spent together in the lab.

Moreover, I want to thank my family for their understanding and support for me to pursue the Ph.D. degree in the United States. Their expectations always motivate me to overcome the difficulties in my life. My parents taught me the merits to be strong, optimistic and understanding on all sides. In the meantime, my thanks also go to local friends Jim and Priscilla Duncan and other fellows, for their generous assistance in helping me adjust the life here in Albuquerque. Jim helped me so selfishlessly with his all-around life experience so that I could spend more time and focus more on my own research.

In the end, there is one more VIP I want to address. I have known her since the year of 2009 and she will be my future wife soon. Thank you, Yafen! Without your listening, encouragements and suggestions, I could not image that I could have gone that far to the finish line to earn this Ph.D. degree. Your wisdom and integrity often flourished

me with ideas and confidence during the hard times of my project. I always feel blessed to have you in the journey of my pursuit of excellence and will strive to live up to the promises of happiness.

# Stable Solar Cells through Controlled Block Copolymer Self-Assembly and Cooperative Hydrogen Bonding Interactions

BY

FEI LI

B.Eng. Chemical Engineering, Hubei University, China, 2006

M.S. Organic Chemistry, Beijing University of Chemical Technology, China, 2009

Ph.D. Chemistry, University of New Mexico, USA, 2014

**Abstract**

Current state-of-the-art polymer solar cells adopt the bulk-heterojunction (BHJ) morphologies where the electron donors (i.e. conjugated polymer) and electron acceptors (i.e. fullerenes) as active layers are mixed in an intimate way. The phase separation that modulates the exciton diffusion and charge transport in the current BHJ morphology is an uncontrolled process and thus results in random domain sizes of the polymer/fullerene blend. In addition, the polymer and fullerenes in the blend are intrinsically two immiscible materials and they tend to undergo macrophase separation eventually, which leads to deteriorated device performance. One way to address the abovementioned issues is to attach fullerenes onto the polymers covalently or non-covalently, aiming at controlling the phase separations and suppressing the macrophase separation between the polymer and fullerenes. However, either the device performance or the morphology of the active layer is not satisfactory to meet our needs.

In my dissertation, I combine block copolymer self-assembly and hydrogen bonding interactions to construct morphologies that are not only thermally stable, but also controllable on the nanoscale. The controllability of the blend morphologies is simply achieved by tuning the fullerene contents in the polymer/fullerene blend. Moreover, solar cells fabricated from such polymer/fullerene blends perform in a comparable way with the benchmark BHJ solar cell however with much enhanced device thermal stabilities. I believe this methodology will shed light on the polymer design and morphology control for the chemists and engineers in this field to obtain high-performing solar cells with better thermal stabilities.

Specifically, I started this project by synthesizing the poly(3-hexylthiophene) (P3HT) based all-conjugated block copolymer (BCP) (**P4**) selectively functionalized with diaminopyrimidine moieties and a thymine tethered fullerene derivative (**F1**). Strong interactions between **P4** and **F1** through the "three-point" complementary hydrogen bonding are studied by $^{1}$H NMR spectroscopy, fluorescent spectroscopy, differential scanning calorimetry (DSC) and atomic force microscopy (AFM). Solar cells employing **P4** and **F1** at different weight ratios as active layers are fabricated and tested. Although the photovoltaic performances of **P4**/**F1** solar cells were not good, the morphology of the blend exhibited tunable nature simply by adjusting the **F1** ratios in the blend.

Secondly, I modified the synthesis of the BCP and obtained a polythiophene diblock copolymer selectively functionalized with 1-N-hexyl isoorotic acid (IOA) moieties (**P8**) with a longer P3HT block and a 2, 6-diaminopyridine tethered fullerene derivative (**F2**). Solar cells employing **P8** blended with different weight ratios of **F2** and phenyl-C61-butyric acid methyl ester (PCBM) were fabricated and tested. The best power conversion efficiencies (PCEs) were observed in devices made from **P8**/**F2** blends (10/8 by wt.) and ternary blends of **P8**/**F2**/PCBM (10/4/4 by wt.) as active layers, which is much better than those from **P4**/**F2** blends. Thermal stabilities of these solar cells were studied in detail by aging tests and corresponding morphological changes were closely monitored by absorption spectroscopy, optical microscopy, AFM and X-ray analyses. The "three-point" complementary hydrogen bonding interactions between **P8** and **F2**, in cooperation with block polymer self-assembly, were found to not only improve the thermal stability of solar cells significantly but also lead to tunable active layer

morphologies. Nanostructures with long-range order were identified in blend films employing **P8**, which has never been observed before in conventional polymer/fullerene bulk heterojunction (BHJ) films.

Thirdly, by employing the **P8**/PCBM blend, I further developed a novel methodology of constructing stable and controllable conjugated polymer (CP)/fullerene nanostructures. By building in non-covalent interactions between CP nanofibers (NFs) and fullerene derivatives, supramolecular polymer/fullerene composite NFs are obtained in solution for the first time. Specifically, self-assembly of **P8** in mixed solvents leads to well-defined NFs decorated with IOA groups on the periphery, onto which PCBM molecules are subsequently attached non-covalently. Formation of such complex structures are studied in detail and confirmed by UV-Vis absorption spectroscopy, transmission electron microscopy (TEM), atomic force microscopy (AFM), and X-ray scattering measurements. Application of these composite NFs (**P8**/PCBM 10/4, wt/wt) in organic photovoltaic (OPV) devices not only leads to superior performance but also much improved thermal stability and rarely observed long-range ordered morphology, when compared with conventional bulk heterojunction (BHJ) devices.

Last but not least, I also investigated the **P8**/**F2** composite nanofibers formation and found out that the width of the composite nanofibers not only depends on the type of the fullerenes added, but also the amount of fullerenes mixed in the blends. Besides, solar cells fabricated from the composite nanofibers blends outperformed their conventional BHJ devices under the same fabricating conditions. Through $^{1}$H NMR

observations, I also proposed a formation mechanism of the **P8** nanofibers that agrees well with our experimental results.

# TABLE OF CONTENTS

# LIST OF FIGURES

# LIST OF SCHEMES

# LIST OF TABLES

# LIST OF ABBREVIATIONS

| | |
|---|---|
| Ac | acetyl, acetate |
| AFM | Atomic force microscopy |
| AM | Air mass |
| ATRP | Atom transfer radical polymerization |
| BCP | Block copolymer |
| BHJ | Bulk heterojunction |
| bis-PCBA | Bis-[6, 6]-phenyl C61-butyric acid |
| C | Hexagonally packed cylinders |
| CB | Chlorobenzene |
| CCD | Charged-coupled device |
| CL | Chloroform |
| CP | Conjugated polymer |
| CV | Cyclic voltammetry |
| DCM | Dichloromethane |
| DMSO | Dimethyl sulfoxide |

| | |
|---|---|
| DSC | Differential scanning calorimetry |
| DSSC | Dye-sensitized solar cells |
| equiv. | Equivalent |
| ESI | Electrospray ionization |
| $f$ | Volume fraction |
| Fc | Ferrocene |
| FF | Fill factor |
| G | Gyroid |
| GISAXS | Grazing-incidence small angle x-ray scattering |
| GIWAXS | Grazing-incidence wide angle x-ray scattering |
| GRIM | Grignard metathesis |
| HOMO | Highest occupied molecular orbital |
| HRMS | High resolution mass spectrometry |
| ITO | Indium tin oxide |
| J | Current density |
| $J_{max}$ | Maximum current density |

| | |
|---|---|
| $J_{SC}$ | Short circuit current density |
| KCTP | Kumada catalyst-transfer polycondensation |
| L | Lamellae |
| LUMO | Lowest unoccupied molecular orbital |
| MDMO-PPV | Poly[2-methoxy-5-(3',7'-dimethyloctyloxy)-1,4-phenylenevinylene |
| MEH-PPV | Poly(2-methoxy-5-(2'-ethyl-hexyloxy)-1,4-phenylenevinylene |
| $M_n$ | The number average molecular weight |
| $M_w$ | The weight average molecular weight |
| NF | Nanofiber |
| NMP | Nitroxide mediated radical polymerization |
| NMR | Nuclear magnetic resonance |
| NSLS | National synchrotron light source |
| OPV | Organic photovoltaic |
| P3HT | Poly(3-hexylthiophene) |
| P3HT-b-P3PyT | Poly(3-hexylthiophene)-block-poly(3-(4'-(3'',7''-dimethyloctyloxy)-3'-pyridinyl)-thiophene) |
| P3HT-b-P3TODT | Poly(3-hexylthiophene)-block-poly[3-(2,5,8,11-tetraoxadodecane)thiophene] |

| | |
|---|---|
| P3HT-b-P4VP | Poly(3-hexylthiophene)-block-poly(4-vinylpyridine) |
| PCBA | [6, 6]-Phenyl-C61-butyric acid |
| PCBM | [6, 6]-Phenyl-C61-butyric acid methyl ester |
| PCDTBT | Poly[N-9''-hepta-decanyl-2,7-carbazole-alt-5,5-(4',7'-di-2-thienyl-2',1',3'-benzothiadiazole |
| PCE | Power conversion efficiency |
| PDI | Polydipersity index |
| PEDOT: PSS | Poly(3,4-ethylenedioxythiophene) polystyrene sulfonate |
| $P_{in}$ | Power input |
| $P_{max}$ | Maximum power output |
| PPV | Phenylene vinylene |
| PS | Polystyrene |
| PS-b-PLA | Polysyrene-block-polylactide |
| PS-b-PMMA | Polystyrene-block-poly(methyl methacrylate) |
| PSC | Polymer solar cell |
| PTFE | Polytetrafluoroethylene |
| PV | Photovoltaic |

| | |
|---|---|
| PvTPA-b-PPerAcr | Poly(bisphenyl-4-vinylphenylamine)-block-poly(perylene diimide acrylate) |
| RAFT | Reversible addition-fragmentation chain transfer polymerization |
| RMS | Root mean square |
| $R_p$ | Parallel resistance |
| $R_s$ | Series resistance |
| r.t | Room temperature |
| S | Body-centered cubic sphere |
| SEC | Size exclusion chromatography |
| TBAF | Tetrabutylammonium fluoride |
| TBDMS | *Tert*-butyldimethylsilyl |
| TEA | Triethylamine |
| TEM | Transmission electron microscopy |
| TW | Terawatt |
| UV-vis | Ultraviolet-visible |
| V | Volt |
| $V_{max}$ | Maximum output voltage |

| | |
|---|---|
| $V_{OC}$ | Open circuit voltage |
| vol | Volume |
| wt | Weight |
| XRD | X-ray diffraction |
| $\delta$ | Chemical shift |
| $\lambda$ | Wavelength |
| $\chi$ | Flory–Huggins interaction parameter |

# Chapter 1

# Introduction

## 1.1 Overview

Energy crisis is a constantly-debated issue that we have to tackle nowadays. Surging energy demands from our social activities drive the quest for new energy sources. Currently, the main energy sources come from burning fossil fuels which causes pollution and other environmental concerns including global warming.[1] The prime problem with the fossil-based fuels is that they are non-renewable energy which will be depleted in the foreseeable future. To complement the energy supplies and reduce the side effects from fossil fuels combustions, harvesting the solar energy from the Sun has been a desired way to generate electricity due to its clean and renewable nature. According to the 2012 annual energy report compiled by US Energy Information Administration, all the renewable energy sources only contributed 8% of the total US energy consumption in the year of 2011.[2] Among all the renewable alternatives, the solar energy is relatively less exploited than the other sources, only accountable for 2% of the overall renewable energy supplies. As a matter of fact, the sun shines on the earth with a total energy of approximately 120 000 TW (1 TW = $1\times 10^{12}$ W), far more than the overall energy that our human beings consumed.[3,4] To harness the solar energy, solar cells are the devices that convert sunlight directly into electricity. Currently, the commercialized solar cells are mostly the silicon-based inorganic ones in the marketplace, and they have reached over 20% power conversion efficiencies (PCEs) down to the lab scale.[5] However, the costs to fabricate and install the solar cells are expensive, which stimulates

the search for cheaper solar cells. Organic photovoltaics (OPVs) including dye-sensitized solar cells (DSSCs),[6,7] small molecules[8,9] and polymer solar cells (PSCs)[10,11] have attracted a great deal of attention due to their potentials to reduce the price of the electricity generated.[12] In particular, polymer solar cells are especially attractive not only due to their light-weight nature, but more because of their flexibility and amenability to printing electronic techniques for massive production. These techniques including roll-to-roll processing and ink-jet printing are estimated to further reduce the fabrication costs. In addition, their tailored chemical structures allow different functionalities, which is especially intriguing to synthetic chemists to modify the structures in order to obtain desired properties.

**1.2 Basics of polymer solar cells**

The first heterojunction organic solar cell was reported by Tang in 1985 who adopted a sequential vacuum deposition strategy to put on the electron donor (p-type), electron acceptor (n-type) materials and silver electrode onto the ITO (Indium Tin Oxide) glass substrate to fabricate a bilayer structure as shown in Figure 1.1a. He used copper phthalocyanine as the electron donor materials and a perylenetetracarboxylic derivative as the electron acceptor materials and achieved about 1% efficiency.[13] Although the efficiency of the solar cell was low, it was a great milestone at that time compared with previous reported work. Indeed, it created an era for the heterojunction solar cells. The problem with the bilayer structure lies in its limited charge separation which only occurs at the interfaces of the electron donors and electron acceptors. In 1995, Yu et al. reported a poly(2-methoxy-5-(2'-ethyl-hexyloxy)-1,4-phenylenevinylene) (MEH-PPV) and fullerenes solar cells with enhanced performances by spin coating the solutions of MEH-

PPV and fullerenes blend together as active layer materials.[14] The efficiencies were significantly improved when the MEH-PPV and fullerenes were mixed together in solution. Furthermore, thanks to Wudl's contribution in preparation of soluble fullerene derivatives,[15] it was the first time that phenyl-C61-butyric acid methyl ester (PCBM) was employed to fabricate solar cells with high fullerenes loadings due to its good solubility in common organic solvents. The interpenetrating donor/acceptor network in the film was credited for the improved photovoltaic properties. Since then, the concept of bulk-heterojunction (BHJ) (as illustrated in Figure 1.1 b) and fullerene derivatives such as PCBM were widely used as a standard consideration for the state-of-art polymer solar cells.

During the early years of BHJ polymer solar cells research, the PPV/PCBM system has been the star combination for solar cells for over two decades. The best 2.5% efficiency was made from poly[2-methoxy-5-(3',7'-dimethyloctyloxy)-1,4-phenylene vinylene (MDMO-PPV)/PCBM by Shaheen et al. at a weight ratio of 1:4.[16] The low efficiency and other inferior attributes including large bandgap and amorphous nature of PPV polymers hindered their practical application in massive production. However, it helped researchers understand the photoinduced electron transfer process in the BHJ films.[17] Since 2005, poly(3-hexylthiophene) (P3HT)/PCBM system then succeeded the PPV/PCBM combination due to its higher efficiencies (3%-5%)[18-20] and stayed as the standard benchmark devices for various investigations. As a matter of fact, the discovery of transition metal catalyzed cross coupling reactions really expedited the search of low bandgap polymers with extended photon absorption band and thus improve the efficiencies of the solar cells.[21-24] Over a decade's development, the efficiencies of

organic solar cells have reached over 10%.[25,26] Virtually, this field grows very fast when we look back at the history of other type of solar cells.[27] However, the current low efficiency is still the bottleneck that limits its commercialization. Therefore, more efforts are still needed to push the PCE limit up to 15%.[28]

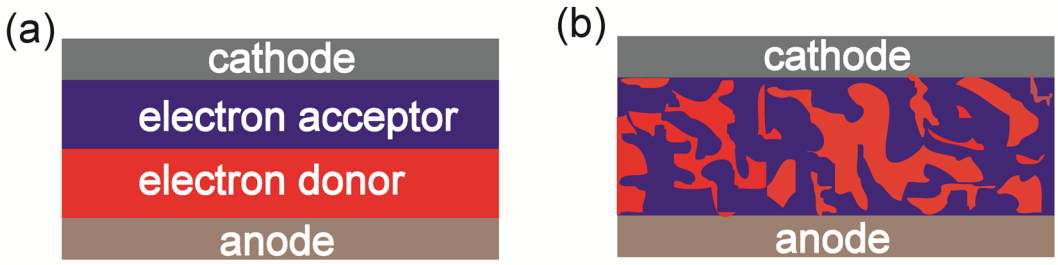


**Figure 1.1** Simplified illustrations (a) bilayer structure where electron acceptors are atop the electron donors; (b) bulk-heterojunction (BHJ) morphology in which the electron donors and electron acceptors are mixed intimately as the active layer.

Efficiencies of PSCs are evaluated by the figure-of-merit called power conversion efficiency (PCE) that is generally obtained from I-V measurements under simulated sunlight illumination.[10-12] A typical I-V curve is shown in Fig. 1.2a. The PCE is determined by the following equation: $\mathrm{PCE} = FF \times \frac{V_{oc} \bullet J_{sc}}{P_{in}}$, where $FF$ stands for fill factor, calculated as $FF = \frac{V_{max} \bullet J_{max}}{V_{oc} \bullet J_{sc}}$, which is the ratio of actual maximum power output to the theoretical power output limit of a solar cell. $V_{OC}$ is the open-circuit voltage which is the maximum voltage a cell can get. Its value is close to the energy difference between the highest occupied molecular orbital (HOMO) of the donor and the lowest unoccupied molecular orbital (LUMO) of the acceptor as illustrated in Figure 1.2b.[29-31] $J_{SC}$ is the short-circuit current, which is the maximum current through the solar cell when the two

electrodes are shorted. $P_{in}$ is the power input of the incident light, calculated from the power density and active device area.

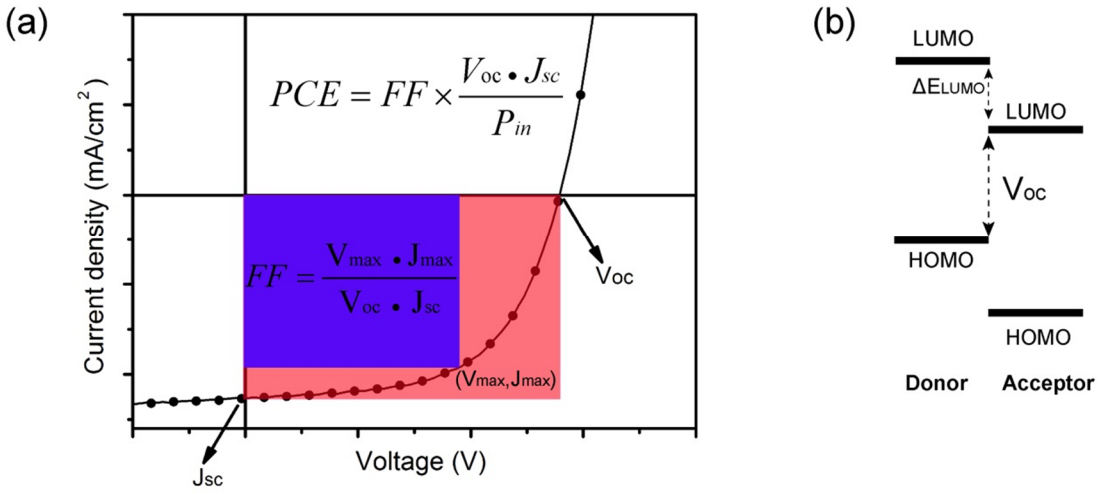


**Figure 1.2** (a) Typical I-V curve of a polymer solar cell under the simulated solar illumination; (b) energy level alignments of electron donors and acceptors for polymer solar cells.

Wang and his coworker summarized in a recent review paper that $V_{OC}$ could be influenced by several factors including temperature, light intensity, work function of the electrode and materials microstructures besides the energy gap between the HOMO of the electron donor and LUMO of the electron acceptor.[32] It is found that increasing the temperature leads to decreased $V_{OC}$. Within the temperature range from 200 K to 300 K, a linear dependence of $V_{OC}$ against temperature is observed. Higher incident light intensity promotes $V_{OC}$ in a logarithmic dependence. An Ohmic contact between the electrode and the active layer could improve the $V_{OC}$ and vice versa. The influence of materials microstructures on $V_{OC}$ is a little more complicated where regioregularity and

crystallinity of the polymers and processing conditions of the BHJ films pose an impact on the $V_{OC}$ of the solar devices.[33]

The value of $J_{SC}$ is related to the amount of absorbed photons, the efficiency of exciton dissociation and recombination, and the charge carrier mobilities of materials within the device.[34] It could be described in the generalized Shockley equation[35] (eq. 1.1) which defines the current density (J) against voltage characteristics of organic solar cells:

$$J = \frac{R_p}{R_s + R_p}\left\{ J_s\left[ \exp\left( \frac{q(V - JR_s)}{nkT} \right) - 1 \right] + \frac{V}{R_p} \right\} - J_{ph}(V) \qquad \text{eq. 1.1}$$

Herein, $R_P$ and $R_S$ represent the parallel (shunt) resistance and series resistance of the equivalent circuit, respectively. $J_S$ is the reverse saturation current density of the diode in the dark, q is the fundamental charge, n is the diode ideality factor, V is the voltage applied at the equivalent circuit, and $J_{ph}(V)$ is the voltage-dependent photocurrent density. If the solar cells have minimal leakage current ($R_P >> R_S$), eq. 1.1 could be rewritten as eq. 1.2:

$$J = J_s\left[ \exp\left( \frac{q(V - JR_s)}{nkT} \right) - 1 \right] - J_{ph}(V) \qquad \text{eq. 1.2}$$

In eq. 1.2, the first term describes the thermally generated current dominated by the charge recombination at the D/A interfaces, and the second term $J_{ph}(V)$ decides the photogenerated carriers. [35]

FF is more difficult to quantify due to the fact that the value of FF is a cooperative interplay of several parameters. In general, it is represented by the series resistance $R_s$

and parallel resistance $R_p$ of the solar cells. Wang also reviewed the possible methods to improve FF.[36] For instance, choosing proper buffer layers aimed at reducing the charge recombination, decreasing the series resistance or increasing the parallel resistance etc.

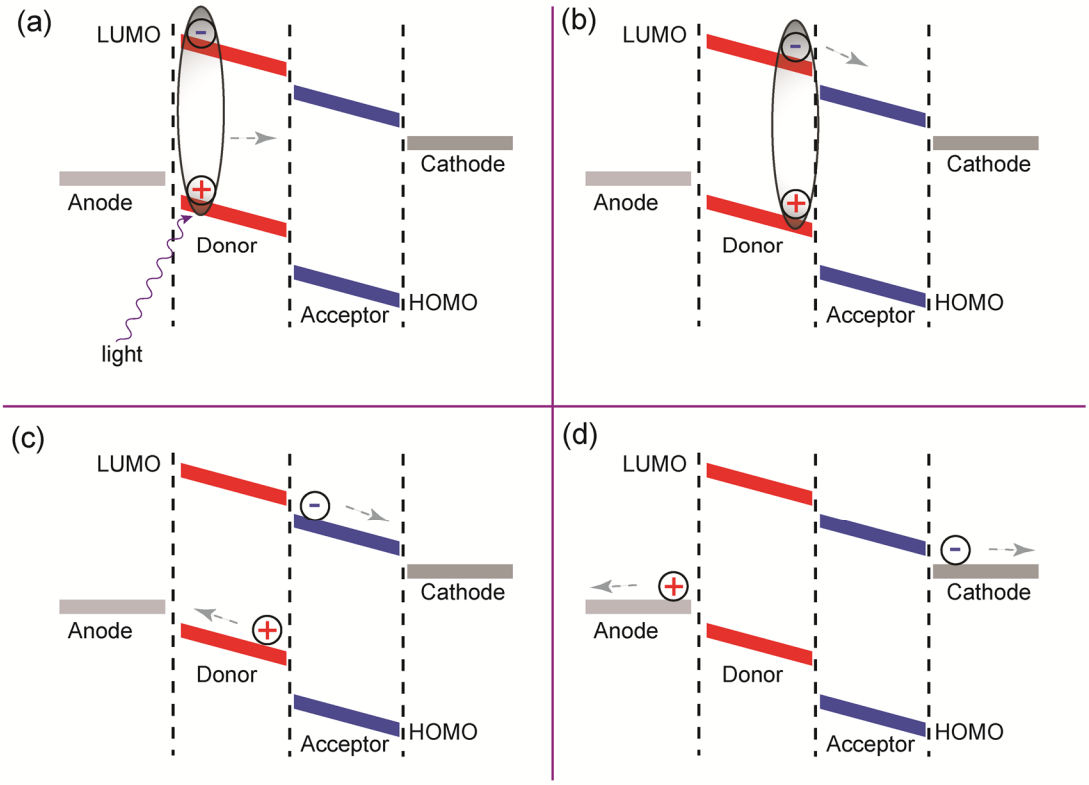


**Figure 1.3** Schematic illustration of the working mechanism of polymer solar cells.

As for the working principle of polymer solar cells, it comprises four major steps as shown in Figure 1.3. Firstly, a photon is absorbed by the donor material (i.e. conjugated polymer) and then excites an electron from the HOMO level to the LUMO level of the donor material, creating an exciton which is an electron-hole bound pair (Figure 1.3a). The generated exciton swiftly diffuses to the interface of the donor/acceptor materials to get separated (Figure 1.3b), and then the electron is transferred to the acceptor (e.g. fullerene) to form spatially separated charges (free

electron and hole) (Figure 1.3c). Finally, the separated charges then migrate to their corresponding electrodes to create a photocurrent (Figure 1.3d).[34,37-39]

### 1.3 Morphology control in polymer solar cells

One of the key factors that determine solar cell performances is the efficiency of photoexcition induced exciton diffusion to the donor/acceptor interface. The lifetime of excitons in typical conjugated polymers is very short, only allowing a maximum travel distance of about 5-10 nm before the excitons recombine and lose energy as heat and/or luminescence.[40-42] Therefore, a good morphology of the polymer/fullerene blends providing suitable domain sizes, interconnected charge transport pathways and good contacts with the electrodes and the interfacial layers, will help improve the excitons separation and the overall efficiencies of polymer solar cells.

It is difficult to predict or define what kind of morphology is beneficial to solar cells due to the random nature of the phase separation in BHJ morphology, which makes it challenging to manipulate the phase separation process in a controllable manner. However, various methods have been reported to control the morphology and eventually improve the efficiencies of the solar devices.[43-46] These strategies include solvents used to dissolve the polymer/fullerene mixtures, thermal annealing of the blend films, solvent annealing, additives incorporation and block copolymers.

A good solvent not only could solubilize both the polymer and fullerenes at the same time, but also could control the phase separation of the film during the spincoating process where the rate of solvent evaporation plays a role. The choice of solvent is proposed to modulate the crystallizations speed of the polymers and fullerenes. Shaheen

et al.[16] observed a dramatic PCE increase when they changed the solvent to chlorobenzene from toluene in which the MDMO-PPV: PCBM (1: 4 by weight) blend solution was dissolved and spincoated. Heeger and his coworkers[47] reported an efficiency of 6.1% for poly[N-9''-hepta-decanyl-2,7-carbazole-alt-5,5-(4',7'-di-2-thienyl-2',1',3'-benzothiadiazole (PCDTBT) : PC71BM cells optimized by employing different solvents. They found out that higher photovoltaic performance in devices prepared from 1, 2-dichlorobenzene outperformed those made from chloroform or chlorobenzene. Therefore, the choice of a proper solvent to dissolve the polymer/fullerene blend is critical in obtaining high performing solar cells.

Thermal annealing has been demonstrated to improve the efficiencies of polymer solar cells and it is been widely used in the lab to optimize the efficiencies of polymer solar cells.[48-50] The key operation in this method is to heat the solar devices at a given temperature for various amount of time and then cool them down in order to obtain the optimized performances. Usually, thermal annealing after the deposition of electrode showed better performance than that before the electrode deposition.[51-54] The role of thermal annealing was proposed to remove the solvent residue in the blend film, to promote the crystallizations of polymers and fullerenes through enhanced phase separation, to increase the contact between the blends and the metal electrodes, and to create percolated pathways for the charge transport.[55,56]

Solvent annealing is another way to create amenable morphologies of the active layers of polymer solar cells by keeping the as-cast films in long contact with the solvent or their solvent vapors such as dichlorobenzene in a partially closed container.[57-61] The slow evaporation of the solvent allows a controlled crystallization and phase separation of

the polymers and fullerenes in a slower manner and thus creates an ordered polymer/fullerene network with enhanced charge mobilities and balanced charge transport.

Adding additives including solvent additives and non-solvent additives into blend solutions are both effective ways to improve the PCEs of polymer solar cells. Bazan and his coworkers[62] observed a PCE increase of P3HT/PCBM solar devices by adding 5% (by volume) alkanethiol into the P3HT/PCBM system. They also found that such method also could be applied to improving the performances of other low bandgap polymer/ fullerene solar cells.[63] In view that the alkanethiols have higher boiling points than that of the solvent used to dissolve the polymer/fullerene mixture, slower evaporation of such additive could slow down the crystallization of the polymers and fullerenes. Moreover, the alkanethiols have preferably better solubility for fullerenes than that for polymers, which also alter the phase separation behavior of the blends and thus probably modulate the morphology of the active layer. Besides alkanethiols, other solvent additive[64,65] and non-solvent additives including metal nanoparticles[66,67] and carbon nanotubes[68] etc. were employed to improve the efficiencies of the polymer solar cells.

**1.4 Block copolymers for solar cells applications**

Despite the established methods to control the BHJ morphology for improved solar devices performances, this type of BHJ morphology intrinsically suffers from several drawbacks.[69,70] First and foremost, it is not thermally stable due to the intrinsically immiscible nature of the polymer and the fullerenes.[71,72] The polymer and fullerenes in the blend tend to undergo macrophase separation with time and deteriorate device performances, leading to reduced cells lifetimes. Secondly, the domain size is

difficult to control because the phase separation of the polymer/fullerene blends is a random process. Lack of certain interactions between the polymer and fullerenes is likely the cause of such phenomenon.

### 1.4.1 "Double-cable" random copolymers for solar cells applications

To modulate the phase separation of the polymer/fullerene blend, fullerenes or other electron acceptors were covalently attached onto the conjugated polymer or electron donors to form the so-called "double-cable" polymers.[11,73-75] In such case, severe macrophase separation between the electron donors and acceptors could be suppressed due to the covalent linkage between the polymer and fullerenes, and thus charge separations could be promoted due to the nano-sized domain nature. Charge separation was envisioned to be fast in view of the close proximity between the polymers and fullerenes. Two examples are listed in Figure 1.4.

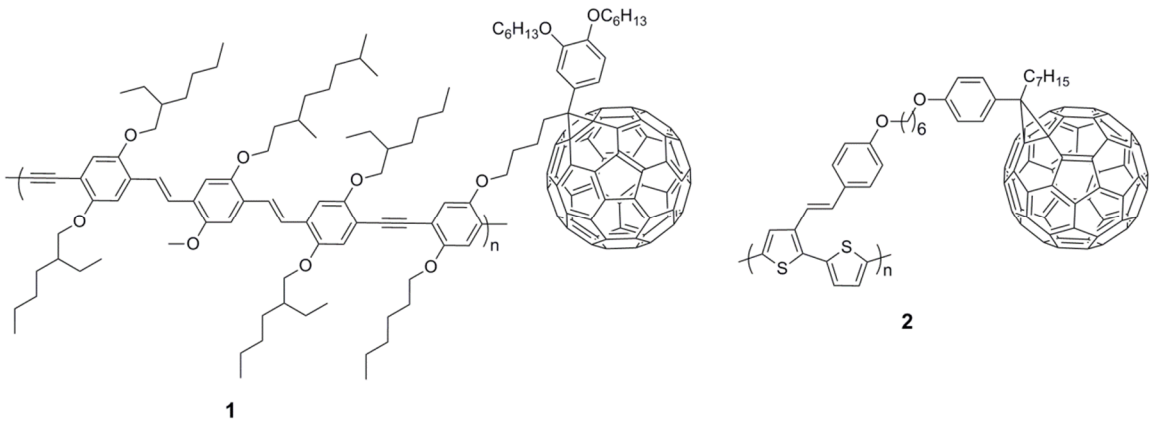


**Figure 1.4** Examples of "double-cable" random copolymers with pendant fullerenes.

Janssen and his co-workers[76] synthesized a "double-cable" PPV-type polymer with a pendent fullerene (**1**) through Sonogashira Coupling reaction. They found out that the polymerization reaction to synthesize polymer **1** reduced the degree of polymerization

of polymer **1** (Mw = 16.2 kg/mol, PDI = 2.82) when compared with that of the PPV without grafted fullerenes (Mw = 35.8 kg/mol, PDI = 2.32). Such molecular weight difference could be due to the limited solubility of fullerenes that impeded the polymerization. Nonetheless, they fabricated solar cells employing **1** as the active layer and obtained a $J_{SC}$ of 0.42 mA·cm$^{-2}$, a $V_{OC}$ of 0.83 V, and an FF of 0.29. Regardless of its ill device performance, the authors claimed that this was the first example of conjugated polymers grafted with pendant fullerenes that had shown photoinduced electron transfer.

Inspired by Janssen's work, Li and his group[77] reported a polythiophene type "double-cable" polymer **2** through Stille Coupling reaction with pendant fullerenes bridged through a phenylene vinylene linker. To avoid the influence of grafting fullerenes on decreasing the molecular weight of the resulting polymers, they chose a postpolymerization modification method to install the fullerenes. To examine the efficacy of polymer **2**, they also made the resulting solar cell and found that it did present improved photovoltaic properties, with a PCE of 0.52% and a $V_{OC}$ of 0.75 V.

Generally, solar cells fabricated from such "double-cable" polymers do not show promising photovoltaic performances mainly due to the fast charge recombination within the polymer/fullerene "double-cable" complex and lack of percolated pathways for charge transport. Besides, limited fullerene contents on the "double-cable" polymers are also accountable for their low photovoltaic performances. However, the success of regulated phase separations of the "double-cable" polymers shed light on the design of fullerene-grafted conjugated polymers, namely, functionalized block copolymers.

### 1.4.2 Block copolymers with covalently tethered pendant fullerenes

Block copolymers (BCPs) are polymers that consist of covalently linked chemically distinct polymer segments. Based on their backbone rigidity, they can be described as coil-coil BCPs, rod-coil BCPs and rod-rod BCPs. A coil polymer describes a flexible polymer that prefers to adopt an amorphous random walk conformation. A rod polymer describes a polymer chain that has a rigid, crystalline and unidirectional backbone, which is characteristic of conjugated polymers (CPs) due to delocalized $\pi$ orbitals. In this part, I will confine the discussion within the diblock copolymers which only contains block A and block B due to the focus of my project. Over the past few decades, BCPs have been utilized in organic polymer solar cells for various purposes.[78-80]

It is well-known that block copolymers (BCPs) have the capability to self-assemble into ordered microstructures due to the intrinsic immiscible nature of the two dissimilar blocks.[81-83] Such microstructures from self-assembly of BCPs are on the order of 5-200 nm, which offers a great opportunity for solar cell applications To incorporate BCPs as active layers for solar cells, one block should possess p-type electron donors (.i.e. conjugated polymers) and the other block is supposed to include n-type electron acceptors (i.e. fullerenes). Self-assembly modulated microphase separation of such materials could, in principle, produces a highly regular nanoscale structure with optimal morphology, [74,84] which offers opportunities to create stable solar cells with controlled phase separations. As a result, higher efficiencies are expected for this type of solar devices.

### 1.4.2.1 Coil-coil BCPs for polymer solar cells

Self-assembly behaviors of coil-coil BCPs have been investigated in detail over the past decades.[85-87] The formation of ordered nanostructures is induced by the effect of free energy minimization at the segment-segment interface and the covalent linkages that prevent macro-phase separation.[88] If we take a diblock copolymer for example, one block is represented in red color, the other block is depicted in blue color as shown in Figure 1.5. Various thermodynamically stable morphologies of coil–coil BCPs can be achieved by tuning the volume fraction of each block f, the Flory–Huggins interaction parameter $\chi$ which reflects the degree of incompatibility between the two blocks, and the degree of polymerization N.[81,89-92]

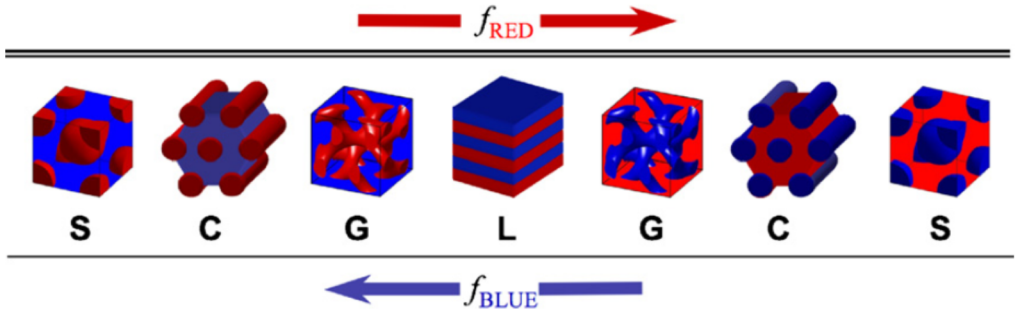


**Figure 1.5** Various nanosturctures of coil-coil diblock copolymer driven by self-assembly (f stands for volume fraction of each block): (S) Body-centered cubic spheres, (C) Hexagonally packed cylinders, (G) Gyroid, (L) Lamellae). Picture reprinted with permission from ref.91. Copyright 2008 Elsevier.

These microstructures include spherical, cylindrical, gyroidal and lamellar morphologies as shown in Figure 1.5. Usually cylindrical and lamellar morphologies account for two third of the self-assembled morphologies in coil-coil BCPs.[85] Examples

of commonly studied coil-coil BCPs are polystyrene-block-poly(methyl methacrylate) (PS-b-PMMA) and polysyrene-b-polylactide (PS-b-PLA). These polymers are extensively studied for their order-disorder transitions by thermal annealing[93] or solvent annealing[94].

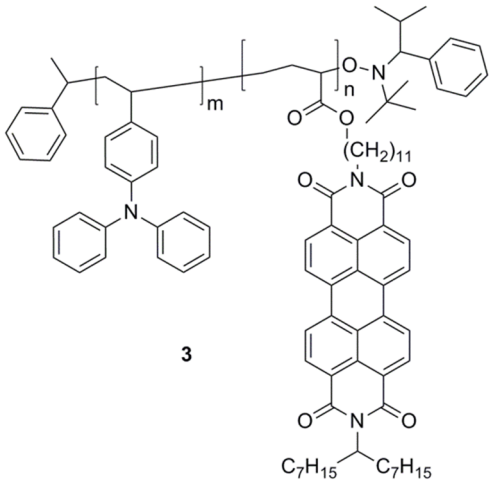


3

**Figure 1.6** Example of coil-coil BCP **3** as the active layer of polymer solar cells.

Commonly encountered coil-coil BCPs have saturated hydrocarbon backbones and are typically insulating. In order to incorporate coil-coil BCPs in polymer solar cells, a widely used strategy is to attach electron donors and electron acceptors to the polymer backbone as side groups so that a photon harvesting and converting system is established but not many reported examples. Thelakkat and his coworkers[95] reported the synthesis of a block copolymer, poly(bisphenyl-4-vinylphenylamine)-block-poly(perylene diimide acrylate) (PvTPA-b-PPerAcr) **3** via nitroxide mediated free radical polymerization as shown in Figure 1.6. The perylene diimide moieties are electron acceptors and the triphenyl amine groups act as electron donors to absorb photons. This polymer was able to self-assemble into nanofibril-like morphologies, the order of which increased with the

perylene diimide content in the BCPs. The dimension of the nanofibrils is ca. 1 μm long and 40 nm to 60 nm thick as measured by TEM with a perylene diimides block content of 78.9 wt%. BHJ solar cell devices fabricated using this polymer gave a PCE of only 0.32%.[96] The low efficiency may be due to the low charge mobility of the polymer backbone and low efficiencies of exciton dissociation due to the large phase segregation.

### 1.4.2.2 Rod-coil BCPs for polymer solar cells

Replacing one block with the semiconducting rod polymer increases the charge mobilities and light absorption abilities, mainly due to the conjugated nature of the rod polymer. Typical rod polymers include polyphenylenevinylenes, polythiophenes, polycarbazoles and so on. Self-assembly process of rod-containing block copolymers is more complex than that of coil-coil block copolymers.

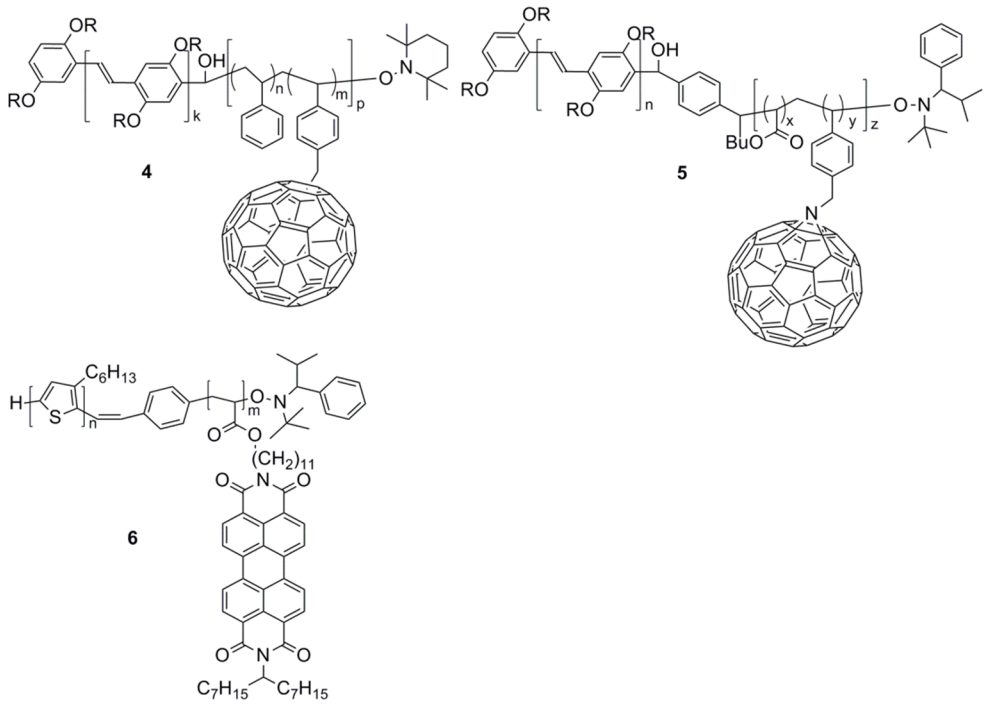


**Figure 1.7** Examples of rod-coil block copolymers as active layers used for solar cells.

Because there is an additional driving force to the microphase separation arising from the crystallization of the rod blocks.[97,98] Rod polymers have a high propensity to form planar liquid crystalline domains rather than spherical morphologies. Consequently, the phase separation is dominated by lamellae or liquid-crystalline like structures.[34]

PPV[99-101] and P3HT[102] based rod-coil BCPs incorporating fullerenes or other electron acceptors could be synthesized through controlled living radical polymerizations techniques including atom transfer radical polymerization (ATRP),[103] nitroxide mediated radical polymerization (NMP),[104,105] and reversible addition-fragmentation chain transfer polymerization(RAFT).[106] Such controlled polymerization method offers precise structural control of the polymers and thus could access different morphologies. Examples of such polymers with grafted fullerenes (**4**-**6**) are shown in Figure 1.7.

Solar cells fabricated from these rod-coil polymers as active layers are not very high-performing, with reported PCE usually less than 1%.[84,107] Possible reasons are the low charge carrier mobilities of the coil block and the small loading of the fullerenes grafted onto the polymer backbone. Such limited fullerene loading is presumably due to the low reactivity with fullerenes. Moreover, attaching fullerene onto the polymer backbone reduces the solubility of the related polymer-fullerene "double-cable" complex, and removal of unreacted fullerenes is difficult from the "double-cable" polymer.

#### 1.4.2.3 Rod-rod BCPs for polymer solar cells

Rod-rod BCPs are all-conjugated block copolymers. Since the independent discovery of Grignard metathesis (GRIM) polymerization and nickel catalyzed Kumada catalyst-transfer polycondensation (KCTP) by McCullough[66,67] and Yokozawa,[108,109]

respectively, synthesis of well-ordered all-conjugated block copolymers has become possible.[110] GRIM or KCTP was proposed to follow a chain growth mechanism in a quasi-living manner. As a result, various rod-rod block copolymers have been synthesized starting from polythiophenes and their self-assembled morphologies were also investigated.[111-118] One intriguing strategy includes the "double-cable" structures of rod-rod block copolymers by attaching fullerene derivatives to the backbone as pendant side chains.[74,119,120] Such structures applied to PSCs can be regarded as a single component BHJ OPV and some examples are shown in Figure 1.8.[121,122]

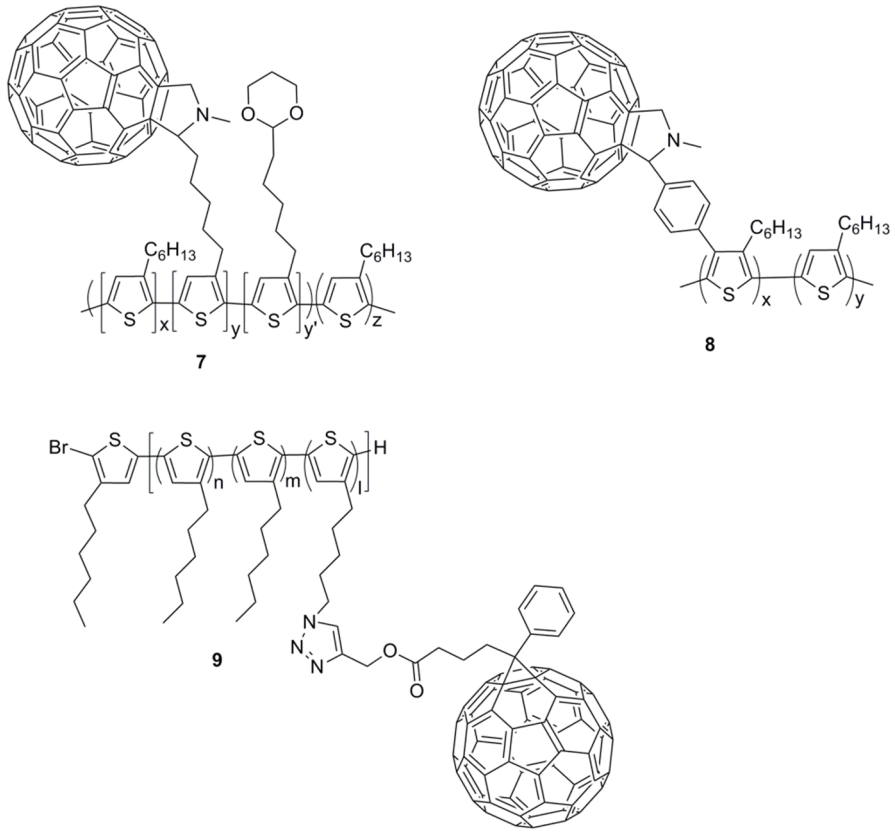


**Figure 1.8** Examples of rod-rod block copolymers carrying pendant fullerenes

Hashimoto and coworkers[121,123] reported an all-conjugated fullerene-containing BCP **9** prepared through GRIM polymerization to synthesize the polymer backbone and Click chemistry to install the fullerene moieties onto the polymer **9** with tethered fullerenes. The rational design of **9** could ensure 11 mol% fullerenes attachment without sacrificing its solubility. Similar to previous work, the authors employed **9** to make solar cells and obtained a PCE of 1.7% upon thermal annealing at 130 °C. They claimed their value as the highest PCE for the single component polymer-fullerene solar cells so far. Furthermore, they tested the thermal stabilities of the optimized solar cells and found out that their solar devices are thermally robust upon annealing at 130 °C for 80 h, with 94% PCE retention. Whereas the P3HT/PCBM (10/6, wt/wt) solar devices exhibited over 70% power loss under identical conditions. They further revealed the thermal stability of solar cells fabricated from **9** via optical microscopy and AFM investigations, indicative of the crystallization suppression of the covalently tethered fullerenes for the diblock copolymer **9**. However, the cell performances were still low in contrast to the widely studied benchmark P3HT/PCBM BHJ solar cells.

The problems with installing fullerenes covalently onto the rod-rod BCPs encountered similar problems with the rod-coil "double cables". Firstly, due to low reactivity of fullerenes, the degree of fullerenes functionalization onto the polymer is low; Secondly, the fullerene loading onto the polymers has to be taken into account to guarantee the solubility of the "double cable" polymers after grafting the fullerenes onto the polymer; thirdly, separation of the resulting polymer-fullerene "double cables" from the unreacted fullerenes is laborious, which is similar to other covalent linking methods

discussed in the previous part. In most cases, the unreacted fullerene molecules coexist with the "double cables", which interferes with the self-assembly process of BCPs, and thus the resulting morphology remains hard to control.

### 1.4.3 Block copolymers with tethered fullerenes via non-covalent interactions

To address the issues of covalent attachment of fullerenes, non-covalent interactions between the BCPs and fullerenes were employed to bypass the solubility and purification issues while still maintain the interactions between polymer and fullerenes. In such case, fullerene loading is not limited by the reactions to install the fullerenes that are commonly encountered in the covalently attaching fullerenes strategy. Besides, less harsh reaction conditions are required to modify the fullerenes and polymers in contrast to that used in the covalently linking method. More importantly, solar cells employing such non-covalent linked polymer/fullerenes exhibited better photovoltaic performances than the counterparts of their covalent "double-cable" polymers, probably due to better morphology to split the excitons and more fullerenes to transport the charges.[124,125] This area is less explored and representative examples are shown in Figure 1.9.[126-128]

Sary et al.[126] reported the synthesis of a rod–coil BCP poly(3-hexylthiophene)-block-poly(4-vinylpyridine) (P3HT-b-P4VP) (**10**) via GRIM polymerization and investigated the photovoltaic performances of BHJ solar cells fabricated from blended with PCBM. The pyridine moieties on P4VP block was able to form supramolecular interactions with fullerenes and thus confined fullerenes only to the P4VP side. Solar devices fabricated from P3HT-b-P4VP and PCBM exhibited a better thermal stability in contrast to P3HT/PCBM system upon thermal annealing. The solar cell device they fabricated showed poor efficiencies with a FF below 30%, $V_{OC}$ of 0.33 V and PCE below

0.03%. The authors explained the poor performance may be attributed to the presence of the P4VP-rich layer on top of the anode interfacial layer PEDOT : PSS, leading to PCBM accumulation near the device anode which introduced a hole collection barrier and/or interfacial dipoles. Improved PCE up to 1.2% was obtained for inverted cell structures of this BCP/PCBM blend. The intrinsic isolating nature of P4VP segment of P3HT-b-P4VP probably accounted for the low PV performance.

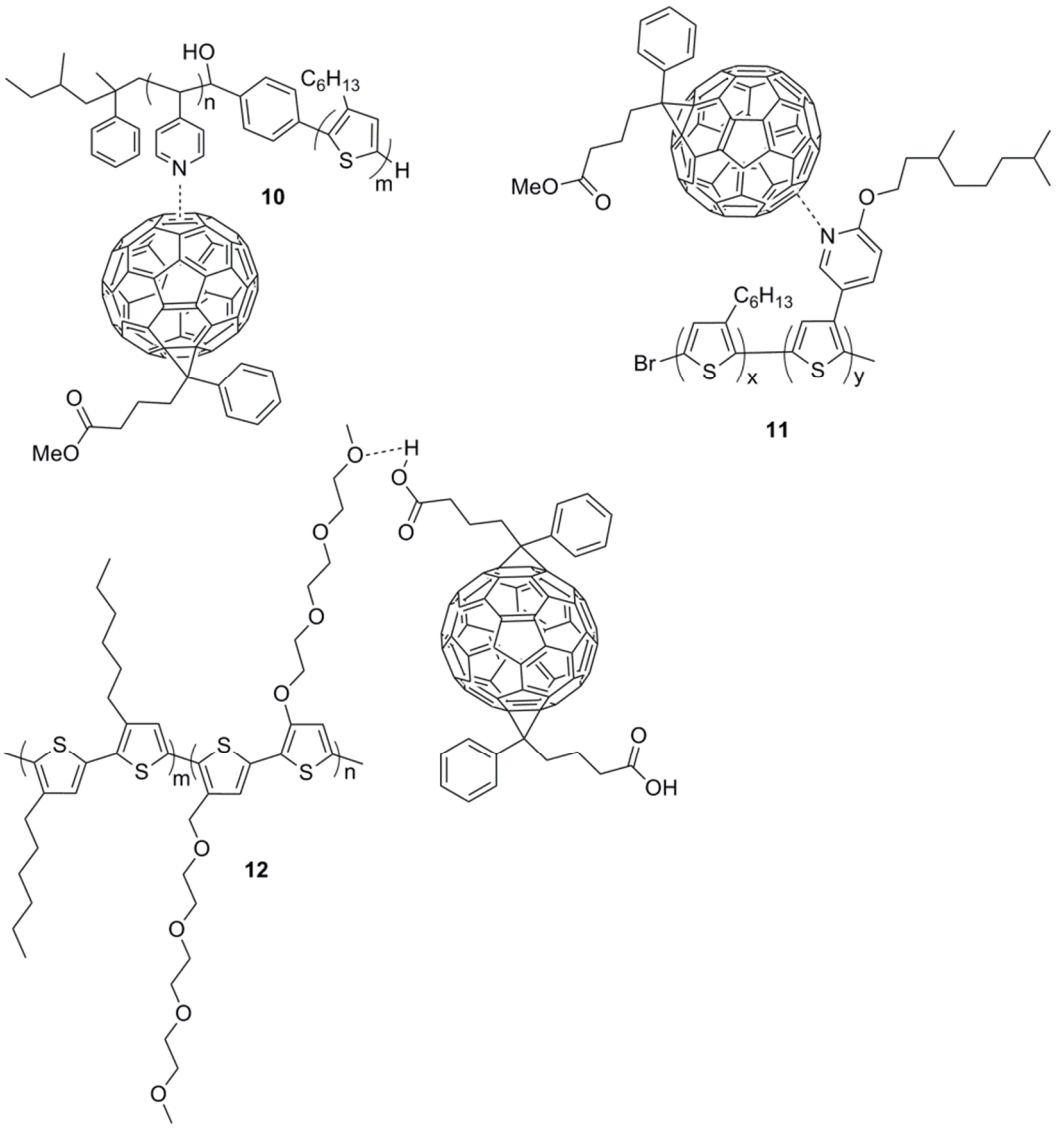


**Figure 1.9** Examples of BCP/fullerenes complexes through non-covalent interactions.

Chen and his coworkers[127] reported the synthesis of an all-conjugated BCP, poly(3-hexylthiophene)-block-poly(3-(4'-(3'',7''-dimethyloctyloxy)-3'-pyridinyl)-thiophene) (P3HT-b-P3PyT) (**11**). The number of repeating units of P3HT to P3PyT is 62:29 for P3HT-b-P4VP based on gel permeation chromatography analysis. They found out that the optimized BHJ solar cell devices were obtained from the P3HT-b-P3PyT/PCBM (1:0.5 wt%) blend. To understand the photovoltaic performance differences, they carried out morphological investigation on the P3HT-b-P3PyT/PCBM blends via AFM and found amorphous-rich morphology with a root mean square (RMS) roughness of 1.19 nm and 3.17 nm for films casted from chloroform (CL) and chloroform/dichlorobenzene (CL/DCB = 1/1, v/v). Such RMS difference indicates the fast evaporation of chloroform during the spin coating limited the crystallization of the blend. Film cast from the less volatile DCB or DCB (3% diiodooctane as an additive) shows elongated fiber-like structure. TEM images of P3HT-b-P3PyT/PCBM blend film shows a weaker phase contrast as compared to P3HT/PCBM film, suggesting that the supramolecular interaction formed between pyridine unit of P3HT-b-P3PyT and PCBM prevents the large aggregation of PCBM. However, this kind of supramolecular interactions between BCPs and fullerenes is too weak.

Lin et al.[128] investigated the cooperative self-assembly between functionalized fullerenes bis-[6, 6]-phenyl C61-butyric acid (bis-PCBA) and all-conjugated BCPs poly(3-hexylthiophene)-block-poly[3-(2,5,8,11-tetraoxadodecane)thiophene] (P3HT-b-P3TODT) (**12**). Favorable hydrogen bonding interactions between the COOH- of bis-PCBA and the triethyleneglycol side chains allow for high loading of bis-PCBA (up to 40 wt% to the blend) within the P3TODT domains while preserving the lamellar

morphology networks on the 10-20 nm domain size, as confirmed by combining GISAXS analysis with AFM and TEM investigations. The hydrogen bond interactions between bis-PCBA and P3TODT segments further suppress crystallization and macrophase separation of the fullerenes, and BHJ solar cells using P3HT-b-P3TODT/bis-PCBA as active layer exhibited a top PCE of 2.04%. It showed slightly enhanced thermal stability over a benchmark P3HT/PCBM solar devices over an ageing period of 6 h. However, about 50% PCE lose was still observed. One possible is that the monotopic hydrogen bonding interactions between BCPs and fullerenes is still relatively weak and could not withstand the thermal annealing for long time.

### 1.5 Stabilities of polymer solar cells

Stabilities of polymer solar cells are equally important with regard to improving the PCEs of solar cells if the commercialization of such technology eventually goes to the market for massive production. Traditionally, the commercially available silicon PV modules are able to work outdoors for many years. In contrast, stabilities of polymer solar cells remained largely untapped and gradually gained more attention in recent years in light of its significance. Several review articles have elaborated the possible causes to the instability and degradation of PSCs and enlightened with the reported methods to improve their stabilities.[71,72,129]

The instability of PSCs mainly comes from two aspects: chemical degradation and physical degradation. Chemical degradation involves the interplay of oxygen and moisture with the active layer materials or the electrodes through diffusion and photooxidation;[130,131] whereas physical degradation originates from the way that the BHJ solar cells was fabricated. Because polymers and fullerenes are two immiscible materials,

and the nano-sized morphologies of the active layers made from such materials are thermodynamically instable. Direct illumination on the cells for extended hours would induce the macrophase separation of the materials, leading to increased domain sizes exceeding the exciton diffusion length. The commonly used fullerenes acceptors tend to evolve into micro-sized large crystalline domains with time and are reported to be associated with deteriorations of cell performances.[132,133]

Encapsulation of the solar devices[134-136] and rational design of the cell structures i.e. inverted structures where more stable metal electrodes[137,138] and metal oxides as buffer layers[139,140] could also be more resistant with the contact of oxygen and moisture and thus improve their devices stability. Inverted solar cell structures involving the exploitation of more air-stable noble metals as anode and metal oxides for interfacial layers are totally different topics and will not be elaborated herein in this thesis; the readers could refer to other literatures if interested.[141-145] To improve solar stabilities, various inorganic and organic materials could be used to encapsulate the organic solar devices by sandwiching the organic solar devices between the protecting materials and thus improve the lifetimes of the solar cells.[146]

Another way to improve the stabilities of organic solar cells is to ameliorate the intrinsic stabilities of the active layers of the polymer solar cells. Crosslinking of active components in the active layers via thermal or photochemical treatment is one such way by locking in the optimized morphology of the active layer and thus slow down the macrophase separation of the active layers.[147-150] However, the thermally induced crosslinking requires external heat to initiate the crosslinkable units which could interfere

with the optimized morphology that was obtained through thermal annealing. On the other hand, photo-crosslinkable units have the merit of heat-free operations to lock in the optimized morphology; however, UV irradiation upon the polymer/fullerene blend films induces the aggravated photooxidation of the polymer. In addition, the crosslinking efficiency is hard to determine. As a result, the stability of the solar devices is also difficult to characterize and guarantee.

Apart from crosslinking the active units in the active layers to achieve the stabilized morphologies, adding compatibilizers into the polymer/fullerene blend solution during the solution preparation process have shown enhanced devices thermal stabilities during the ageing tests. Compatibilizers in BHJ morphologies were proposed to reduce the interfacial tension and domain size and thus suppress the macrophase separation.[129,151] Traditional compatibilizers have been successfully repurposed to control the domain size of the BHJ polymer solar cells.[152] Specifically, block copolymers containing polythiophenes in one block and fullerenes in the other block have also been synthesized as compatibilizers to improve the stabilities of BHJ solar cells (Figure 1.10). Fréchet and his coworkers[153] first reported a graft–block type copolymer based on hanging P3HT repeat units in one block and pendent fullerene derivatives in the other (**13**). Adding a few weight percent of such polymer **13** could improve the stability of the benchmark P3HT/PCBM BHJ solar cells. Other block copolymers carrying pendant fullerenes (**14-16**) were also synthesized and studied as compatibilizers to improve stabilities of the BHJ solar cells.[80,154,155]

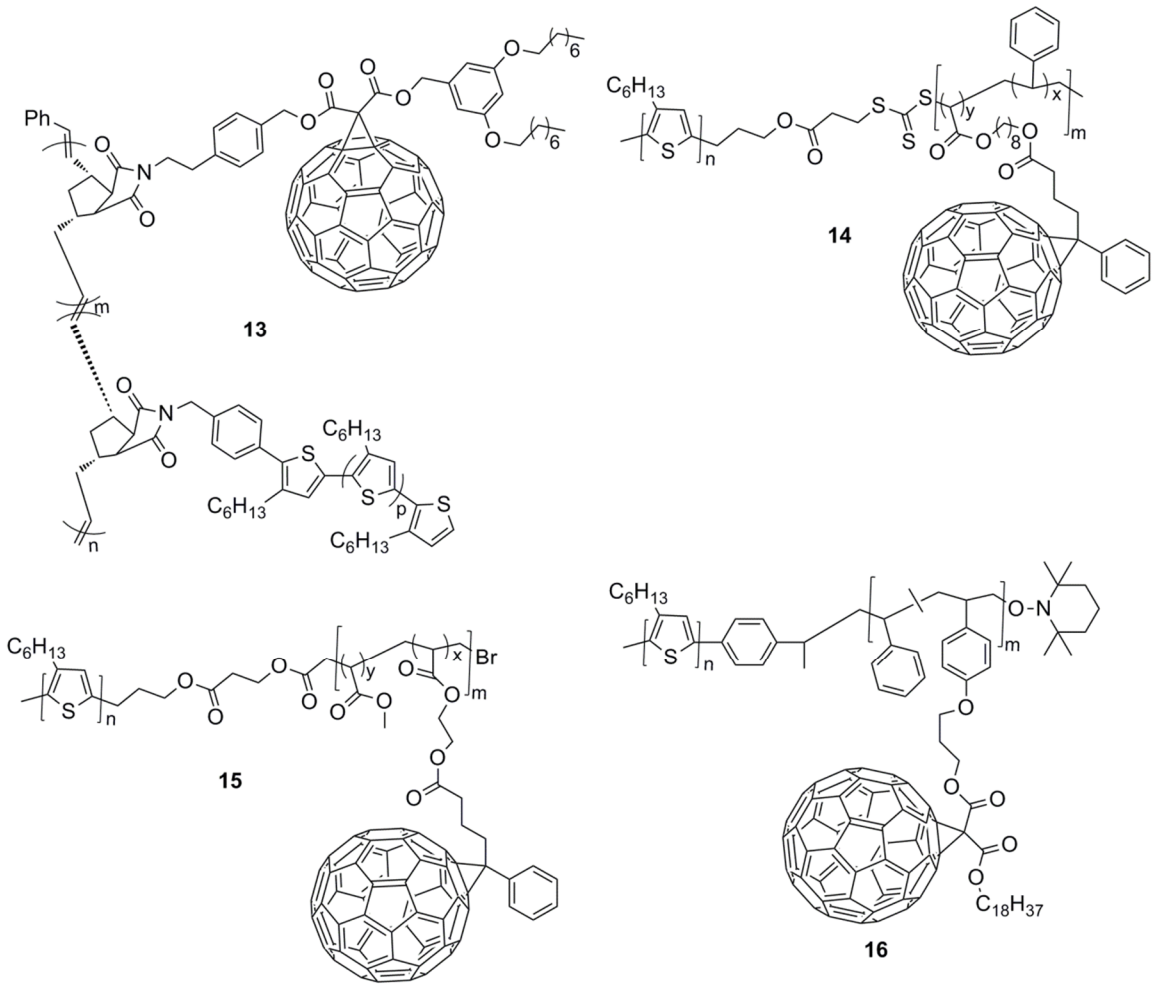


**Figure 1.10** Examples of block copolymers carrying pendant fullerenes as compatibilizers

Despite the efficacy of such block copolymers in improving the stabilities of BHJ solar cells, the synthesis of such polymers functionalized with fullerenes is tedious, often requiring multi-step synthesis and the separation is also painstaking. Moreover, functionalization of fullerenes onto the polymers is challenging as previously stated similar to the "double-cable" polymers covalently grafted with fullerene. It backfires on the goal of reducing the fabrication cost of polymer solar cells. Therefore, tethering the

fullerenes non-covalently has been proposed in my project to utilize such polymer/fullerene complex as compatibilizers to enhance the solar device stabilities.

### 1.6 Motivations of my project

Block copolymer self-assembly for solar cells applications have been studied for years, however, controlled morphologies resulting from the block copolymers and fullerenes with high efficiencies from their devices were rarely reported. One possible reason is the strong tendency of fullerene aggregations. Morphology of the active layers plays a vital role in determining the cell performances.

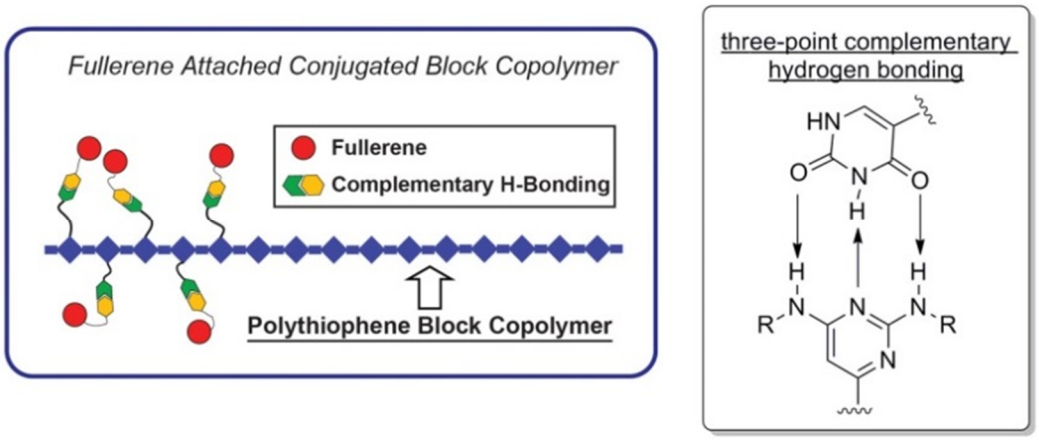


**Figure 1.11** Schematic illustration of designed fullerene attached block polymer through a complementary "three-point" hydrogen bonding.

My methodology is inspired by nature and designed to specifically target abovementioned issues (random phase separation and low thermal stability of the active layers) with existing polymer scaffold, through self-assembly of tailor-made all-conjugated block copolymers (block polythiophenes) and electron acceptors (fullerenes) employing stronger non-covalent supramolecular interactions, i.e. complementary triple

hydrogen bonding interactions (Figure 1.11). Such strong non-covalent interactions have been demonstrated as a powerful tool to modulate the self-assembly properties.[156-159] Given the fact that currently reported monotopic hydrogen bonding motif is still relatively weak, I hope by installing the "three-point" hydrogen bonding moieties onto the block copolymer and fullerenes in a complementary way, I could modulate the self-assembly of such BCP and fullerenes simply by controlling the fullerenes content on the block copolymer. By doing so, I hope to achieve several things: (i) better optical density and conductivity by using all-conjugated polymer backbone; (ii) increased solubility and thus higher and tunable degree of functionalization from non-covalent fullerene attachment; and (iii) optimizing self-assembly of the resulting block polymer through facile fine-tuning of relative block lengths, fullerene loading percentages and nature/strength of the non-covalent interactions. Self-assembly of such rod-rod BCPs can potentially lead to controlled nanomorphologies that contribute to high-performing solar cells. In addition, the strong triple complementary hydrogen bonding interactions between the conjugated polymer and fullerene are expected to slow down the macrophase separation by suppressing fullerenes crystallizations and therefore improve the thermal stability of BHJ solar cell devices.

## 1.7 References


(1) Armaroli, N.; Balzani, V. *Angew. Chem., Int. Ed.* **2007**, 46, 52.

(2) US Department of Energy, *Annual Energy Review 2011*, Washington, DC; www. eia. doe. gov/emeu/aer.

(3) Krebs, F. C. In *Polymer photovoltaics: a practical approach*; SPIE press Bellingham: **2008**, p 175.

(4) Delgado, J. L.; Bouit, P.-A.; Filippone, S.; Herranz, M. a. A.; Martin, N. *Chem. Commun.* **2010**, 46, 4853.

(5) Zhao, J.; Wang, A.; Green, M. A.; Ferrazza, F. *Appl. Phys. Lett.* **1998**, 73, 1991.

(6) Grätzel, M. *J. Photochem. Photobiol. C: Photochem. Rev.* **2003**, 4, 145.

(7) Hagfeldt, A.; Boschloo, G.; Sun, L.; Kloo, L.; Pettersson, H. *Chem. Rev.* **2010**, 110, 6595.

(8) Lin, Y.; Li, Y.; Zhan, X. *Chem. Soc. Rev.* **2012**, 41, 4245.

(9) Mishra, A.; Bäuerle, P. *Angew. Chem., Int. Ed.* **2012**, 51, 2020.

(10) Günes, S.; Neugebauer, H.; Sariciftci, N. S. *Chem. Rev.* **2007**, 107, 1324.

(11) Zhan, X.; Zhu, D. *Polym. Chem.* **2010**, 1, 409.

(12) Kalowekamo, J.; Baker, E. *Sol. Energy* **2009**, 83, 1224.

(13) Tang, C. W. *Appl. Phys. Lett.* **1986**, 48, 183.

(14) Yu, G.; Gao, J.; Hummelen, J. C.; Wudl, F.; Heeger, A. J. *Science* **1995**, 270, 1789.

(15) Hummelen, J. C.; Knight, B. W.; LePeq, F.; Wudl, F.; Yao, J.; Wilkins, C. L. *J. Org. Chem.* **1995**, 60, 532.

(16) Shaheen, S. E.; Radspinner, R.; Peyghambarian, N.; Jabbour, G. E. *Appl. Phys. Lett.* **2001**, 79, 2996.

(17) Sariciftci, N. S.; Smilowitz, L.; Heeger, A. J.; Wudl, F. *Science* **1992**, 258, 1474.

(18) Reyes-Reyes, M.; Kim, K.; Carroll, D. L. *Appl. Phys. Lett.* **2005**, 87, 083506.

(19) Kim, J. Y.; Kim, S. H.; Lee, H. H.; Lee, K.; Ma, W.; Gong, X.; Heeger, A. J. *Adv. Mater.* **2006**, 18, 572.

(20) Dang, M. T.; Hirsch, L.; Wantz, G. *Adv. Mater.* **2011**, 23, 3597.

(21) Cheng, Y.-J.; Yang, S.-H.; Hsu, C.-S. *Chem. Rev.* **2009**, 109, 5868.

(22) Chen, J.; Cao, Y. *Acc. Chem. Res.* **2009**, 42, 1709.

(23) Beaujuge, P. M.; Fréchet, J. M. J. *J. Am. Chem. Soc.* **2011**, 133, 20009.

(24) Zhou, H.; Yang, L.; You, W. *Macromolecules* **2012**, 45, 607.

(25) He, Z.; Zhong, C.; Su, S.; Xu, M.; Wu, H.; Cao, Y. *Nat Photon* **2012**, 6, 591.

(26) You, J.; Chen, C.-C.; Hong, Z.; Yoshimura, K.; Ohya, K.; Xu, R.; Ye, S.; Gao, J.; Li, G.; Yang, Y. *Adv. Mater.* **2013**, 25, 3973.

(27) Service, R. F. *Science* **2011**, 332, 293.

(28) Dou, L.; You, J.; Hong, Z.; Xu, Z.; Li, G.; Street, R. A.; Yang, Y. *Adv. Mater.* **2013**, 25, 6642.

(29) Gadisa, A.; Svensson, M.; Andersson, M. R.; Inganäs, O. *Appl. Phys. Lett.* **2004**, 84, 1609.

(30) Brabec, C. J.; Cravino, A.; Meissner, D.; Sariciftci, N. S.; Fromherz, T.; Rispens, M. T.; Sanchez, L.; Hummelen, J. C. *Adv. Funct. Mater.* **2001**, 11, 374.

(31) Scharber, M. C.; Mühlbacher, D.; Koppe, M.; Denk, P.; Waldauf, C.; Heeger, A. J.; Brabec, C. J. *Adv. Mater.* **2006**, 18, 789.

(32) Qi, B.; Wang, J. *J. Mater. Chem.* **2012**, 22, 24315.

(33) Guo, J.; Ohkita, H.; Benten, H.; Ito, S. *J. Am. Chem. Soc.* **2010**, 132, 6154.

(34) Topham, P. D.; Parnell, A. J.; Hiorns, R. C. *J. Polym. Sci., Part B: Polym. Phys.* **2011**, 49, 1131.

(35) Perez, M. D.; Borek, C.; Forrest, S. R.; Thompson, M. E. *J. Am. Chem. Soc.* **2009**, 131, 9281.

(36) Qi, B.; Wang, J. *Phys. Chem. Chem. Phys.* **2013**, 15, 8972.

(37) Blom, P. W. M.; Mihailetchi, V. D.; Koster, L. J. A.; Markov, D. E. *Adv. Mater.* **2007**, 19, 1551.

(38) Kirova, N. *Polym. Int.* **2008**, 57, 678.

(39) Clarke, T. M.; Durrant, J. R. *Chem. Rev.* **2010**, 110, 6736.

(40) Brédas, J.-L.; Norton, J. E.; Cornil, J.; Coropceanu, V. *Acc. Chem. Res.* **2009**, 42, 1691.

(41) Halls, J. J. M.; Pichler, K.; Friend, R. H.; Moratti, S. C.; Holmes, A. B. *Appl. Phys. Lett.* **1996**, 68, 3120.

(42) Stübinger, T.; Brütting, W. *J. Appl. Phys.* **2001**, 90, 3632.

(43) Slota, J. E.; He, X.; Huck, W. T. S. *Nano Today* **2010**, 5, 231.

(44) Yang, X.; Loos, J. *Macromolecules* **2007**, 40, 1353.

(45) Chen, L.-M.; Hong, Z.; Li, G.; Yang, Y. *Adv. Mater.* **2009**, 21, 1434.

(46) van Bavel, S.; Veenstra, S.; Loos, J. *Macromol. Rapid Commun.* **2010**, 31, 1835.

(47) Park, S. H.; Roy, A.; Beaupre, S.; Cho, S.; Coates, N.; Moon, J. S.; Moses, D.; Leclerc, M.; Lee, K.; Heeger, A. J. *Nat Photon* **2009**, 3, 297.

(48) Kim, Y.; Choulis, S. A.; Nelson, J.; Bradley, D. D. C.; Cook, S.; Durrant, J. R. *Appl. Phys. Lett.* **2005**, 86, 063502.

(49) Ma, W.; Yang, C.; Gong, X.; Lee, K.; Heeger, A. J. *Adv. Funct. Mater.* **2005**, 15, 1617.

(50) Padinger, F.; Rittberger, R. S.; Sariciftci, N. S. *Adv. Funct. Mater.* **2003**, 13, 85.

(51) Kim, H.; So, W.-W.; Moon, S.-J. *Sol. Energy Mater. Sol. Cells* **2007**, 91, 581.

(52) Li, G.; Shrotriya, V.; Yao, Y.; Yang, Y. *J. Appl. Phys.* **2005**, 98, 0437041.

(53) Kim, C. S.; Kim, J. B.; Lee, S. S.; Kim, Y. S.; Loo, Y.-L. *Org. Electron.* **2009**, 10, 1483.

(54) Kim, H. J.; Park, J. H.; Lee, H. H.; Lee, D. R.; Kim, J.-J. *Org. Electron.* **2009**, 10, 1505.

(55) Dang, M. T.; Hirsch, L.; Wantz, G.; Wuest, J. D. *Chem. Rev.* **2013**, 113, 3734.

(56) Liu, F.; Gu, Y.; Jung, J. W.; Jo, W. H.; Russell, T. P. *J. Polym. Sci., Part B: Polym. Phys.* **2012**, 50, 1018.

(57) Li, G.; Yao, Y.; Yang, H.; Shrotriya, V.; Yang, G.; Yang, Y. *Adv. Funct. Mater.* **2007**, 17, 1636.

(58) Li, G.; Shrotriya, V.; Huang, J.; Yao, Y.; Moriarty, T.; Emery, K.; Yang, Y. *Nat. Mater.* **2005**, 4, 864.

(59) Mihailetchi, V. D.; Xie, H.; de Boer, B.; Popescu, L. M.; Hummelen, J. C.; Blom, P. W. M.; Koster, L. J. A. *Appl. Phys. Lett.* **2006**, 89, 012107.

(60) Shrotriya, V.; Yao, Y.; Li, G.; Yang, Y. *Appl. Phys. Lett.* **2006**, 89, 063505.

(61) Tang, H.; Lu, G.; Li, L.; Li, J.; Wang, Y.; Yang, X. *J. Mater. Chem.* **2010**, 20, 683.

(62) Peet, J.; Soci, C.; Coffin, R. C.; Nguyen, T. Q.; Mikhailovsky, A.; Moses, D.; Bazan, G. C. *Appl. Phys. Lett.* **2006**, 89, 252105.

(63) Peet, J.; Kim, J. Y.; Coates, N. E.; Ma, W. L.; Moses, D.; Heeger, A. J.; Bazan, G. C. *Nat. Mater.* **2007**, 6, 497.

(64) Yao, Y.; Hou, J.; Xu, Z.; Li, G.; Yang, Y. *Adv. Funct. Mater.* **2008**, 18, 1783.

(65) Chen, F.-C.; Tseng, H.-C.; Ko, C.-J. *Appl. Phys. Lett.* **2008**, 92, 103316.

(66) Kim, K.; Carroll, D. L. *Appl. Phys. Lett.* **2005**, 87, 203113.

(67) Naidu, B. V. K.; Park, J. S.; Kim, S. C.; Park, S.-M.; Lee, E.-J.; Yoon, K.-J.; Joon Lee, S.; Wook Lee, J.; Gal, Y.-S.; Jin, S.-H. *Sol. Energy Mater. Sol. Cells* **2008**, 92, 397.

(68) Berson, S.; de Bettignies, R.; Bailly, S.; Guillerez, S.; Jousselme, B. *Adv. Funct. Mater.* **2007**, 17, 3363.

(69) Patrick, G. N.; Fernando, A. C. *Nanotechnology* **2010**, 21, 492001.

(70) Wang, Y.; Wei, W.; Liu, X.; Gu, Y. *Sol. Energy Mater. Sol. Cells* **2012**, 98, 129.

(71) Jørgensen, M.; Norrman, K.; Krebs, F. C. *Sol. Energy Mater. Sol. Cells* **2008**, 92, 686.

(72) Jørgensen, M.; Norrman, K.; Gevorgyan, S. A.; Tromholt, T.; Andreasen, B.; Krebs, F. C. *Adv. Mater.* **2012**, 24, 580.

(73) Delgado, J. L.; Bouit, P.-A.; Filippone, S.; Herranz, M. Á.; Martín, N. *Chem. Commun.* **2010**, 46, 4853.

(74) Cravino, A.; Sariciftci, N. S. *J. Mater. Chem.* **2002**, 12, 1931.

(75) Roncali, J. *Chem. Soc. Rev.* **2005**, 34, 483.

(76) Ramos, A. M.; Rispens, M. T.; van Duren, J. K. J.; Hummelen, J. C.; Janssen, R. A. J. *J. Am. Chem. Soc.* **2001**, 123, 6714.

(77) Tan, Z. a.; Hou, J.; He, Y.; Zhou, E.; Yang, C.; Li, Y. *Macromolecules* **2007**, 40, 1868.

(78) Tao, Y.; McCulloch, B.; Kim, S.; Segalman, R. A. *Soft Matter* **2009**, 5, 4219.

(79) Botiz, I.; Darling, S. B. *Macromolecules* **2009**, 42, 8211.

(80) Yang, C.; Lee, J. K.; Heeger, A. J.; Wudl, F. *J. Mater. Chem.* **2009**, 19, 5416.

(81) Meuler, A. J.; Hillmyer, M. A.; Bates, F. S. *Macromolecules* **2009**, 42, 7221.

(82) Cheng, J. Y.; Ross, C. A.; Smith, H. I.; Thomas, E. L. *Adv. Mater.* **2006**, 18, 2505.

(83) Darling, S. B. *Prog. Polym. Sci.* **2007**, 32, 1152.

(84) Darling, S. B. *Energy & Environ. Sci.* **2009**, 2, 1266.

(85) Matsen, M. W.; Bates, F. S. *Macromolecules* **1996**, 29, 1091.

(86) Bates, F. S.; Fredrickson, G. H. *Annu. Rev. Phys. Chem.* **1990**, 41, 525.

(87) Fredrickson, G. H.; Bates, F. S. *Annu. Rev. Mater. Sci.* **1996**, 26, 501.

(88) He, M.; Qiu, F.; Lin, Z. *J. Mater. Chem.* **2011**, 21, 17039.

(89) Leibler, L. *Macromolecules* **1980**, 13, 1602.

(90) Fung, M. K.; Sun, Y. C.; Ng, A.; Ng, A. M. C.; Djurišić, A. B.; Chan, H. T.; Chan, W. K. *ACS Appl. Mater. Interfaces* **2011**, 3, 522.

(91) Lynd, N. A.; Meuler, A. J.; Hillmyer, M. A. *Prog. Polym. Sci.* **2008**, 33, 875.

(92) Klok, H. A.; Lecommandoux, S. *Adv. Mater.* **2001**, 13, 1217.

(93) Weissman, J. M.; Sunkara, H. B.; Albert, S. T.; Asher, S. A. *Science* **1996**, 274, 959.

(94) Zhao, B.; Haasch, R. T.; MacLaren, S. *J. Am. Chem. Soc.* **2004**, 126, 6124.

(95) Lindner, S. M.; Thelakkat, M. *Macromolecules* **2004**, 37, 8832.

(96) Lindner, S. M.; Hüttner, S.; Chiche, A.; Thelakkat, M.; Krausch, G. *Angew. Chem., Int. Ed.* **2006**, 45, 3364.

(97) Reenders, M.; ten Brinke, G. *Macromolecules* **2002**, 35, 3266.

(98) de Cuendias, A.; Hiorns, R. C.; Cloutet, E.; Vignau, L.; Cramail, H. *Polym. Int.* **2010**, 59, 1452.

(99) de Boer, B.; Stalmach, U.; van Hutten, P. F.; Melzer, C.; Krasnikov, V. V.; Hadziioannou, G. *Polymer* **2001**, 42, 9097.

(100) Stalmach, U.; de Boer, B.; Videlot, C.; van Hutten, P. F.; Hadziioannou, G. *J. Am. Chem. Soc.* **2000**, 122, 5464.

(101) Barrau, S.; Heiser, T.; Richard, F.; Brochon, C.; Ngov, C.; van de Wetering, K.; Hadziioannou, G.; Anokhin, D. V.; Ivanov, D. A. *Macromolecules* **2008**, 41, 2701.

(102) Zhang, Q.; Cirpan, A.; Russell, T. P.; Emrick, T. *Macromolecules* **2009**, 42, 1079.

(103) Braunecker, W. A.; Matyjaszewski, K. *Prog. Polym. Sci.* **2007**, 32, 93.

(104) Grubbs, R. B. *Polym. Rev.* **2011**, 51, 104.

(105) Renaud, C.; Mougnier, S.-J.; Pavlopoulou, E.; Brochon, C.; Fleury, G.; Deribew, D.; Portale, G.; Cloutet, E.; Chambon, S.; Vignau, L.; Hadziioannou, G. *Adv. Mater.* **2012**, 24, 2196.

(106) Bicciocchi, E.; Chen, M.; Rizzardo, E.; Ghiggino, K. P. *Polym. Chem.* **2013**, 4, 53.

(107) Yassar, A.; Miozzo, L.; Gironda, R.; Horowitz, G. *Prog. Polym. Sci.* **2013**, 38, 791.

(108) Miyakoshi, R.; Yokoyama, A.; Yokozawa, T. *J. Am. Chem. Soc.* **2005**, 127, 17542.

(109) Yokoyama, A.; Miyakoshi, R.; Yokozawa, T. *Macromolecules* **2004**, 37, 1169.

(110) Scherf, U.; Gutacker, A.; Koenen, N. *Acc. Chem. Res.* **2008**, 41, 1086.

(111) Ren, G.; Wu, P.-T.; Jenekhe, S. A. *Chem. Mater.* **2010**, 22, 2020.

(112) Ohshimizu, K.; Takahashi, A.; Rho, Y.; Higashihara, T.; Ree, M.; Ueda, M. *Macromolecules* **2011**, 44, 719.

(113) Izuhara, D.; Swager, T. M. *Macromolecules* **2011**, 44, 2678.

(114) Ho, C.-C.; Liu, Y.-C.; Lin, S.-H.; Su, W.-F. *Macromolecules* **2012**, 45, 813.

(115) Higashihara, T.; Ohshimizu, K.; Ryo, Y.; Sakurai, T.; Takahashi, A.; Nojima, S.; Ree, M.; Ued, M. *Polymer* **2011**, 52, 3687.

(116) He, M.; Han, W.; Ge, J.; Yang, Y.; Qiu, F.; Lin, Z. *Energy & Environ. Sci.* **2011**, 4, 2894.

(117) Zhang, Y.; Tajima, K.; Hirota, K.; Hashimoto, K. *J. Am. Chem. Soc.* **2008**, 130, 7812.

(118) Ge, J.; He, M.; Qiu, F.; Yang, Y. *Macromolecules* **2010**, 43, 6422.

(119) Chen, M.; Li, M.; Wang, H.; Qu, S.; Zhao, X.; Xie, L.; Yang, S. *Polym. Chem.* **2013**, 4, 550.

(120) Imahori, H.; Kitaura, S.; Kira, A.; Hayashi, H.; Nishi, M.; Hirao, K.; Isoda, S.; Tsujimoto, M.; Takano, M.; Zhe, Z.; Miyato, Y.; Noda, K.; Matsushige, K.; Stranius, K.; Tkachenko, N. V.; Lemmetyinen, H.; Qin, L.; Hurst, S. J.; Mirkin, C. A. *J. Phys. Chem. Lett.* **2012**, 3, 478.

(121) Miyanishi, S.; Zhang, Y.; Tajima, K.; Hashimoto, K. *Chem. Commun.* **2010**, 46, 6723.

(122) Li, M.; Xu, P.; Yang, J.; Yang, S. *J. Mater. Chem.* **2010**, 20, 3953.

(123) Miyanishi, S.; Zhang, Y.; Hashimoto, K.; Tajima, K. *Macromolecules* **2012**, 45, 6424.

(124) Cravino, A. *Polym. Int.* **2007**, 56, 943.

(125) Venkataraman, D.; Yurt, S.; Venkatraman, B. H.; Gavvalapalli, N. *J. Phys. Chem. Lett.* **2010**, 1, 947.

(126) Sary, N.; Richard, F.; Brochon, C.; Leclerc, N.; Lévêque, P.; Audinot, J.-N.; Berson, S.; Heiser, T.; Hadziioannou, G.; Mezzenga, R. *Adv. Mater.* **2010**, 22, 763.

(127) Lai, Y.-C.; Ohshimizu, K.; Takahashi, A.; Hsu, J.-C.; Higashihara, T.; Ueda, M.; Chen, W.-C. *J. Polym. Sci., Part A: Polym. Chem.* **2011**, 49, 2577.

(128) Lin, Y.; Lim, J. A.; Wei, Q.; Mannsfeld, S. C. B.; Briseno, A. L.; Watkins, J. J. *Chem. Mater.* **2012**, 24, 622.

(129) Lee, J. U.; Jung, J. W.; Jo, J. W.; Jo, W. H. *J. Mater. Chem.* **2012**, 22, 24265.

(130) Chambon, S.; Rivaton, A.; Gardette, J.-L.; Firon, M.; Lutsen, L. *J. Polym. Sci., Part A: Polym. Chem.* **2007**, 45, 317.

(131) Schafferhans, J.; Baumann, A.; Wagenpfahl, A.; Deibel, C.; Dyakonov, V. *Org. Electron.* **2010**, 11, 1693.

(132) Yang, X.; van Duren, J. K. J.; Janssen, R. A. J.; Michels, M. A. J.; Loos, J. *Macromolecules* **2004**, 37, 2151.

(133) Yang, X.; Loos, J.; Veenstra, S. C.; Verhees, W. J. H.; Wienk, M. M.; Kroon, J. M.; Michels, M. A. J.; Janssen, R. A. J. *Nano Lett.* **2005**, 5, 579.

(134) Krebs, F. C. *Sol. Energy Mater. Sol. Cells* **2006**, 90, 3633.

(135) Dennler, G.; Lungenschmied, C.; Neugebauer, H.; Sariciftci, N. S.; Latrèche, M.; Czeremuszkin, G.; Wertheimer, M. R. *Thin Solid Films* **2006**, 511–512, 349.

(136) Zhang, F.; Xu, X.; Tang, W.; Zhang, J.; Zhuo, Z.; Wang, J.; Wang, J.; Xu, Z.; Wang, Y. *Sol. Energy Mater. Sol. Cells* **2011**, 95, 1785.

(137) Litzov, I.; Brabec, C. *Materials* **2013**, 6, 5796.

(138) Zimmermann, B.; Würfel, U.; Niggemann, M. *Sol. Energy Mater. Sol. Cells* **2009**, 93, 491.

(139) Lloyd, M. T.; Peters, C. H.; Garcia, A.; Kauvar, I. V.; Berry, J. J.; Reese, M. O.; McGehee, M. D.; Ginley, D. S.; Olson, D. C. *Sol. Energy Mater. Sol. Cells* **2011**, 95, 1382.

(140) Meyer, J.; Hamwi, S.; Kröger, M.; Kowalsky, W.; Riedl, T.; Kahn, A. *Adv. Mater.* **2012**, 24, 5408.

(141) Krebs, F. C.; Gevorgyan, S. A.; Alstrup, J. *J. Mater. Chem.* **2009**, 19, 5442.

(142) Hau, S. K.; Yip, H.-L.; Baek, N. S.; Zou, J.; O'Malley, K.; Jen, A. K.-Y. *Appl. Phys. Lett.* **2008**, 92.

(143) Krebs, F. C. *Sol. Energy Mater. Sol. Cells* **2008**, 92, 715.

(144) Norrman, K.; Madsen, M. V.; Gevorgyan, S. A.; Krebs, F. C. *J. Am. Chem. Soc.* **2010**, 132, 16883.

(145) Yang, T.; Wang, M.; Duan, C.; Hu, X.; Huang, L.; Peng, J.; Huang, F.; Gong, X. *Energy Environ. Sci.* **2012**, 5, 8208.

(146) Ahmad, J.; Bazaka, K.; Anderson, L. J.; White, R. D.; Jacob, M. V. *Renew. Sust. Energy Rev.* **2013**, 27, 104.

(147) Drees, M.; Hoppe, H.; Winder, C.; Neugebauer, H.; Sariciftci, N. S.; Schwinger, W.; Schaffler, F.; Topf, C.; Scharber, M. C.; Zhu, Z.; Gaudiana, R. *J. Mater. Chem.* **2005**, 15, 5158.

(148) Kim, B. J.; Miyamoto, Y.; Ma, B.; Fréchet, J. M. J. *Adv. Funct. Mater.* **2009**, 19, 2273.

(149) Nam, C.-Y.; Qin, Y.; Park, Y. S.; Hlaing, H.; Lu, X.; Ocko, B. M.; Black, C. T.; Grubbs, R. B. *Macromolecules* **2012**, 45, 2338.

(150) Kim, H. J.; Han, A. R.; Cho, C.-H.; Kang, H.; Cho, H.-H.; Lee, M. Y.; Fréchet, J. M. J.; Oh, J. H.; Kim, B. J. *Chem. Mater.* **2011**, 24, 215.

(151) Yuan, K.; Chen, L.; Chen, Y. *Polym. Int.* **2014**, 63, 4.

(152) Brabec, C. J.; Padinger, F.; Sariciftci, N. S.; Hummelen, J. C. *J. Appl. Phys.* **1999**, 85, 6866.

(153) Sivula, K.; Ball, Z. T.; Watanabe, N.; Fréchet, J. M. J. *Adv. Mater.* **2006**, 18, 206.

(154) Lee, J. U.; Cirpan, A.; Emrick, T.; Russell, T. P.; Jo, W. H. *J. Mater. Chem.* **2009**, 19, 1483.

(155) Heuken, M.; Komber, H.; Erdmann, T.; Senkovskyy, V.; Kiriy, A.; Voit, B. *Macromolecules* **2012**, 45, 4101.

(156) Nair, K. P.; Breedveld, V.; Weck, M. *Macromolecules* **2008**, 41, 3429.

(157) Yang, S. K.; Ambade, A. V.; Weck, M. *Chem. Soc. Rev.* **2011**, 40, 129.

(158) De Greef, T. F. A.; Smulders, M. M. J.; Wolffs, M.; Schenning, A. P. H. J.; Sijbesma, R. P.; Meijer, E. W. *Chem. Rev.* **2009**, 109, 5687.

(159) Ligthart, G. B. W. L.; Ohkawa, H.; Sijbesma, R. P.; Meijer, E. W. *J. Am. Chem. Soc.* **2004**, 127, 810.

# Chapter 2

# Synthesis and Characterization of Polythiophene Block Copolymer and Fullerene Derivative Capable of "Three-Point" Complementary Hydrogen Bonding Interactions and Their Application in Bulk-Heterojunction Solar Cells

(Reproduced with permission from

*Journal of Polymer Science Part A: Polymer Chemistry* **2013**, 51, 3339-3350.



The other coauthor, Jianzhong Yang, is acknowledged.

Supporting information of the publication is incorporated into this chapter)

## 2.1. Introduction

Best performing polymer solar cell (PSC) devices[1-4] are typically fabricated by blending conjugated polymers and fullerene derivatives to form the so-called bulk heterojunction (BHJ) morphology characterized as an interpenetrating donor-acceptor binary network with domain sizes on the nanometer scale.[5-8] However, BHJ is intrinsically at a thermodynamic meta-stable state that causes environmental instability and reduced cell lifetimes.[9,10] One of the most studied methodologies toward stable BHJs in PSCs is self-assembly of conjugated block copolymers (BCPs) having electron acceptors selectively attached to one block.[11-16] Most existing examples of this type have

fullerene derivatives attached to conjugated backbones via covalent linkages.[13,17-21] Fullerene concentrations in these examples are generally low due to limited solubility and strong aggregation tendency of fullerenes. An intriguing alternative approach is to attach fullerene acceptors onto conjugated polymer backbones non-covalently, by which fullerene loading percentages can be easily adjusted and solubility of the resulting complexes can be enhanced. Several recent reports have described complexation between fullerene derivatives and polythiophene based diblock and random copolymers through "single-point" hydrogen bonding[22,23] and π-π[24] interactions. However, these interactions are relatively weak. Complementary hydrogen bonding is among the strongest and most studied non-covalent interactions and has found widespread applications in supramolecular chemistry.[25] In this chapter, the synthesis and characterization of a polythiophene diblock copolymer and a fullerene derivative bearing diaminopyrimidine and thymine moieties were described, respectively. Complexation between these two components via "three-point" complementary hydrogen bonding[26,27] was studied in detail, which showed strong interactions leading to stabilized morphologies. The solar cell device performance employing **P4**/**F1** blends at varied weight ratios were also investigated. Additionally, **P4**/**F1** complexes were applied as compatibilizers in order to improve the stability of benchmark BHJ polymer solar cells.

### 2.2 Synthesis and characterization

Chemical synthesis of the diaminopyrimidine functionalized block copolymer (**P4**) and thymine tethered fullerene derivative (**F1**) is shown in Scheme 2.1; $^{1}$H NMR spectra and size exclusion chromatography (SEC) profiles of the polymers are shown in

Figure 2.1. The key steps in Scheme 2.1 lie in the synthesis of **P2** and installation of hydrogen bonding moieties **M3** onto **P3** to get **P4** as well as the preparation of **F1**.

**Scheme 2.1** Synthesis of polymers **P1- P4** and Fullerene Derivative **F1**.

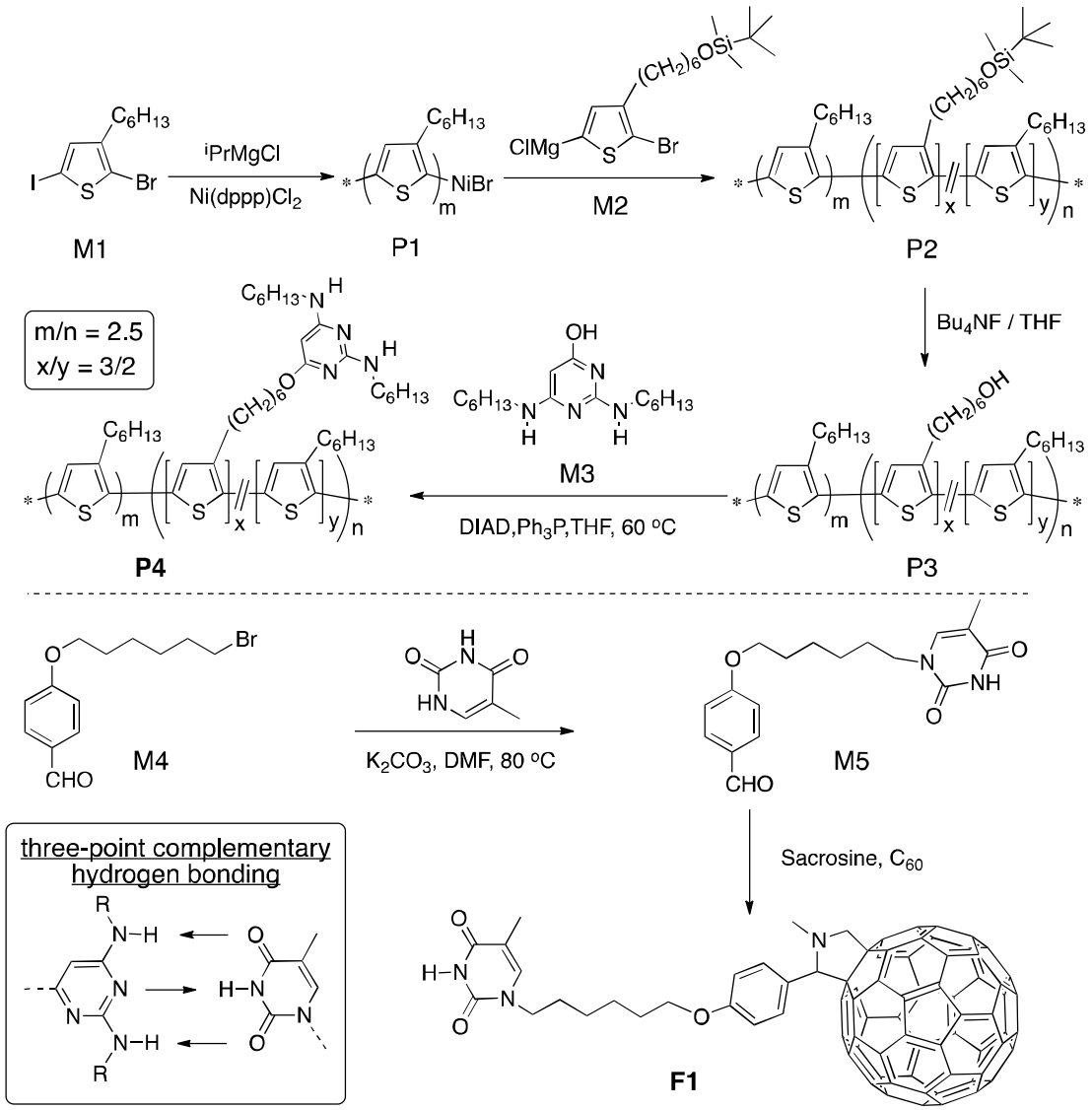


Monomers **M1** and **M2** were sequentially polymerized using a typical Grignard metathesis (GRIM) polymerization protocol.[28] Figure 2.2 summarizes the kinetic study of 2-bromo3-hexyl-5-iodothiophene monomer **M1** in solution. It followed a quasi-living process as indicated by the two linear fittings plots from the Ln([$M_0$]/[M]) against

reaction time and number average molecular weight $M_n$ against monomer conversion This quasi-living characteristic of **M1** polymerization offers excellent opportunity to prepare polythiophene based all-conjugated block copolymers **P2** from **P1**.

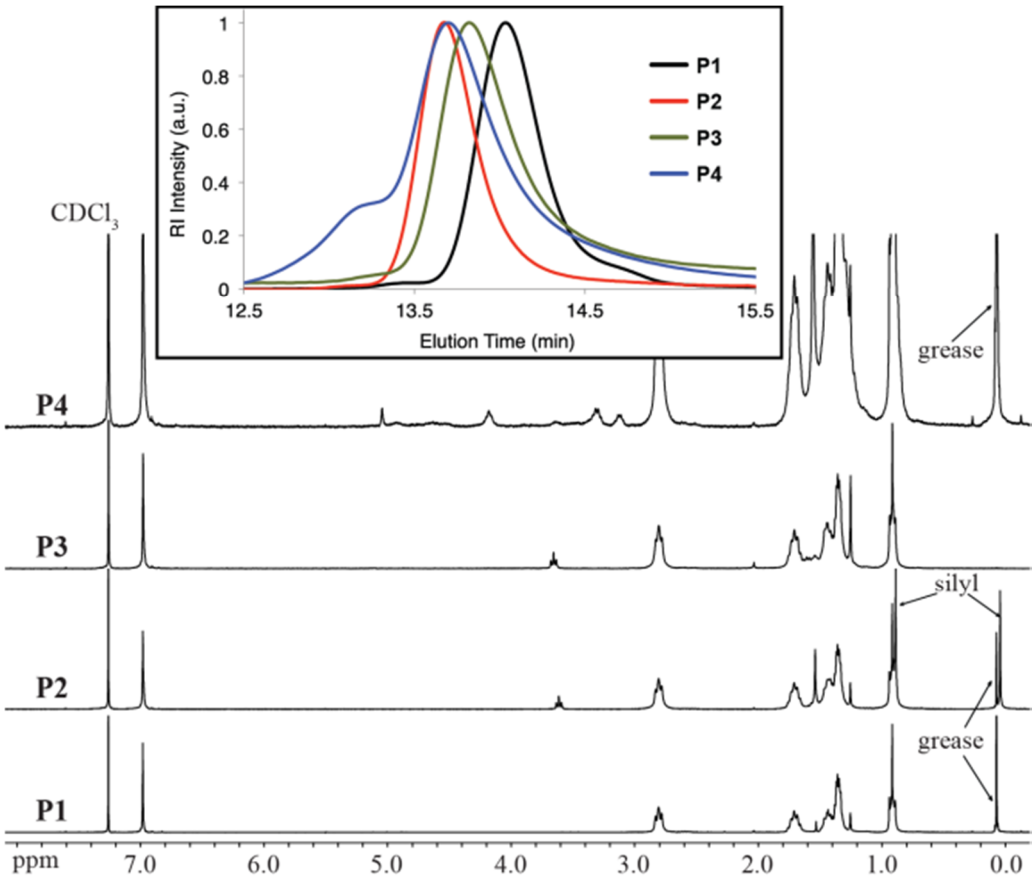


**Figure 2.1** $^1$H NMR spectra of **P1**, **P2**, **P3** and **P4** in $CDCl_3$. Insert: Size exclusion chromatography traces of **P1** (black), **P2** (red), **P3** (green) and **P4** (blue) recorded by a refractive index detector, using chloroform (0.5% TEA) as the eluent (1 mL/min).

An **M1**/**M2** ratio of 4/1 was chosen in this study and **M2** was added at ca. 70% **M1** conversion during the polymerization in order to ensure complete chain extension. As a result, the longer block in **P2** has the structure of regio-regular poly(3-hexylthiophene) (P3HT, *i.e.* **P1**) and the shorter block is expected to be a random copolymer of **M1** and **M2**. From $^1$H NMR analysis, functional group concentration of **P2**

is estimated to be ca. 16%. From SEC results (for **P1**, $M_n$ = 23,645, $M_w$ = 25,082; for **P2**, $M_n$ = 36,683, $M_w$ = 38,094) the block length ratio is calculated to be ca. 2.5 and the **M1**/**M2** ratio in the shorter random copolymer block is ca. 2/3. Controllability of the polymerization was confirmed by kinetic studies and SEC measurements (Figure 2.2). As seen in Figure 2.1 (insert), SEC traces of both **P1** and **P2** have symmetrical shapes and narrow polydispersities (PDIs). The lack of low molecular weight shoulder in the SEC profile of **P2** indicates quantitative chain extension of **P1** and the formation of block copolymers in the absence of homopolymers.

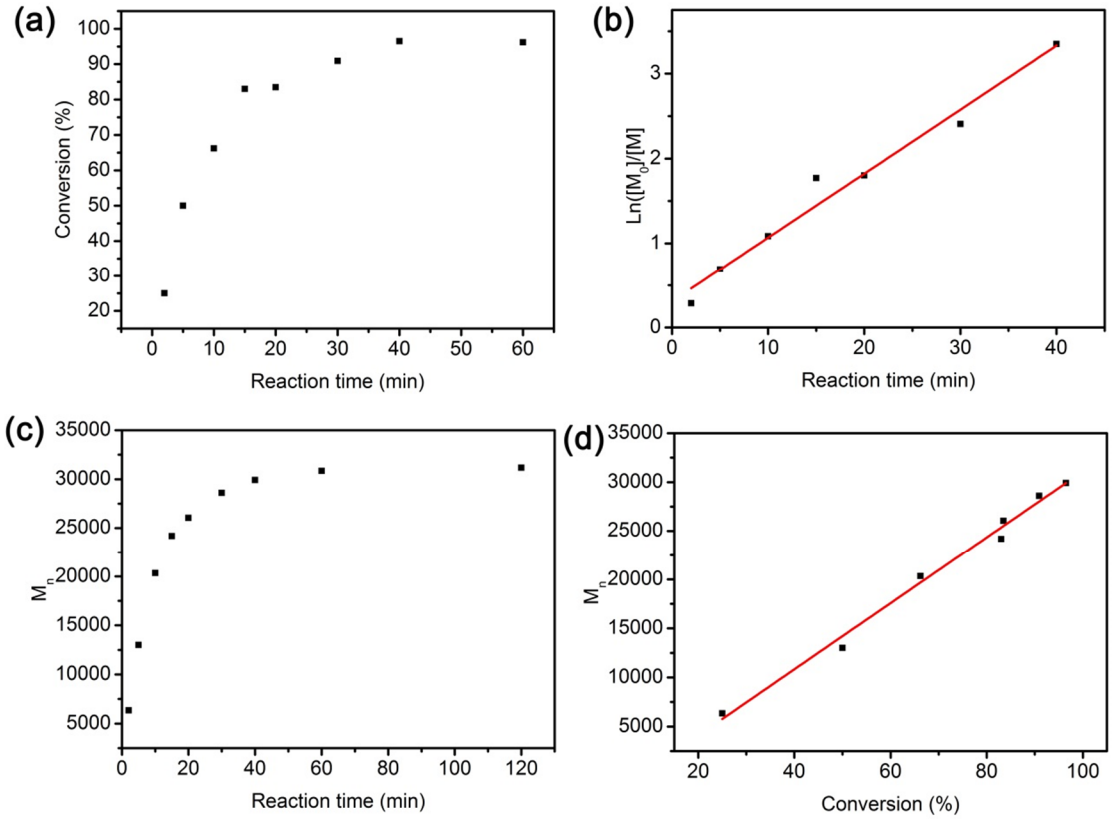


**Figure 2.2** Kinetic plots of GRIM polymerization of **M1** in THF (0.1 M) using Ni(dppp)$Cl_2$ (0.5 mol%) as the catalyst. (a) Monomer conversion vs. reaction time. (b) ln([$M_0$]/[M]) vs. reaction time; (c) $M_n$ (SEC against PS standards) vs. reaction time; (d) $M_n$ vs. conversion.

The hydroxyl functionalized block copolymer **P3** was then obtained through deprotection of silylether moieties in **P2** using tetrabutylammonium fluoride. Complete disappearance of $^1$H NMR signals of the silyl groups at 0.04 and 0.89 ppm in the spectrum of **P3** indicates quantitative chemical transformation. The SEC trace of **P3** tails toward longer elution times and gives somewhat lower molecular weight than expected, which is possibly caused by interactions between the polar hydroxyl groups and column materials. Finally, diaminopyrimidine moieties were installed through Mitsunobu reaction between **P3** and **M3**. $^1$H NMR signals for the oxygen bound methylene groups in **P4** downfield shifts to 4.19 ppm from 3.66 ppm as in **P3**, the integration of which gives ca. 15% functional group concentration, indicating nearly quantitative functionalization.

**Scheme 2.2** Synthesis of model compound **S5** and a random copolymer **P4'**.

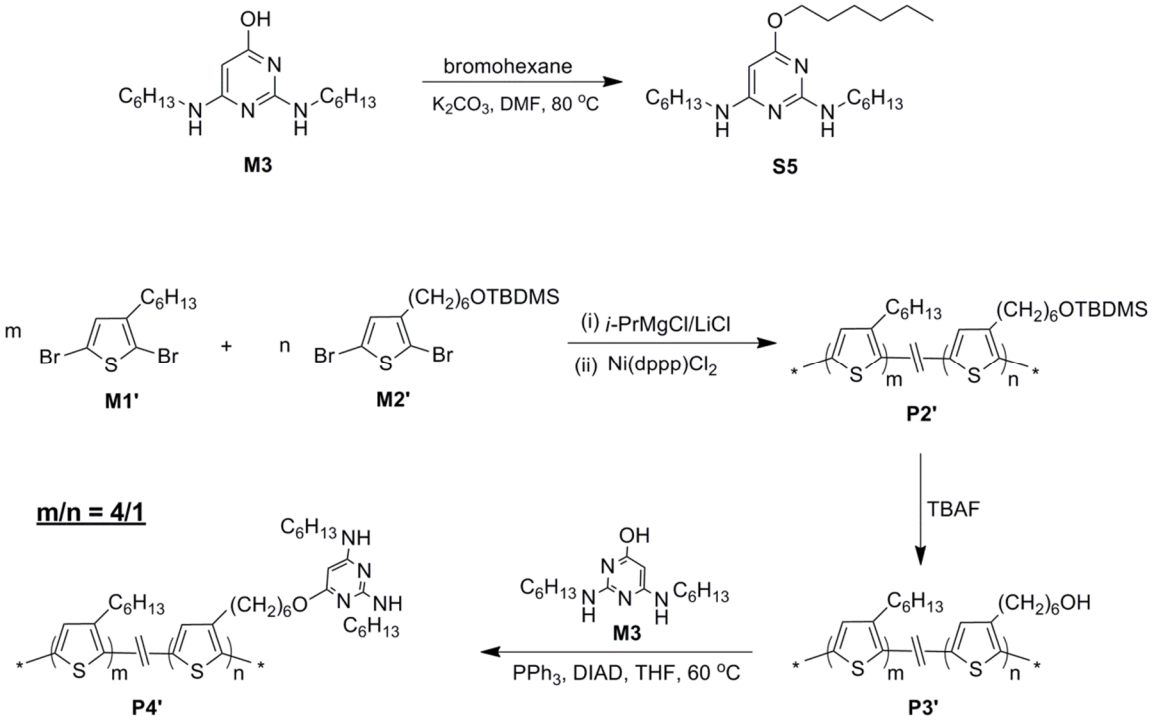

To further elucidate the structure of **P4**, a similar random copolymer **P4'** containing 20% diaminopyrimidine functionality and a small molecule model compound **S5**, the hexyloxy substituted **M3**, were synthesized (Scheme 2.2). Close match between $^1$H NMR spectra of both the polymers and model compound (Figure 2.3) unambiguously confirms the chemical structure of **P4**.

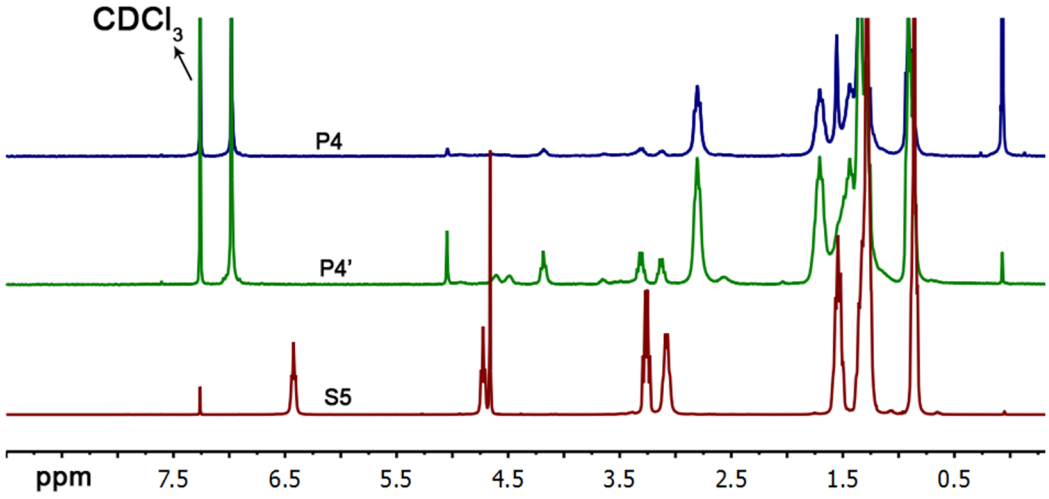


**Figure 2.3** $^1$H NMR ($CDCl_3$, 300.13 MHz) spectra of block copolymer **P4** (top), random copolymer **P4'** (middle) and model compound **S5** (bottom). The signals at ca. 0.08 ppm in all spectra are due to grease contaminants from air-free synthesis involving greased glass joints.

It was noticed that $^1$H NMR signals of the diaminopyrimidine moieties in **P4** are broader and less resolved than those of **P4'**, which is presumably caused by inter- and intra-chain hydrogen bonding between the functional groups and the much higher functional group concentration in **P4** (60% within the functionalized block). The SEC profile of **P4** also shows both a high molecular weight shoulder and low molecular

weight tail (Figure 2.1, insert), likely due to such hydrogen bonding interactions as well as interaction with column materials.

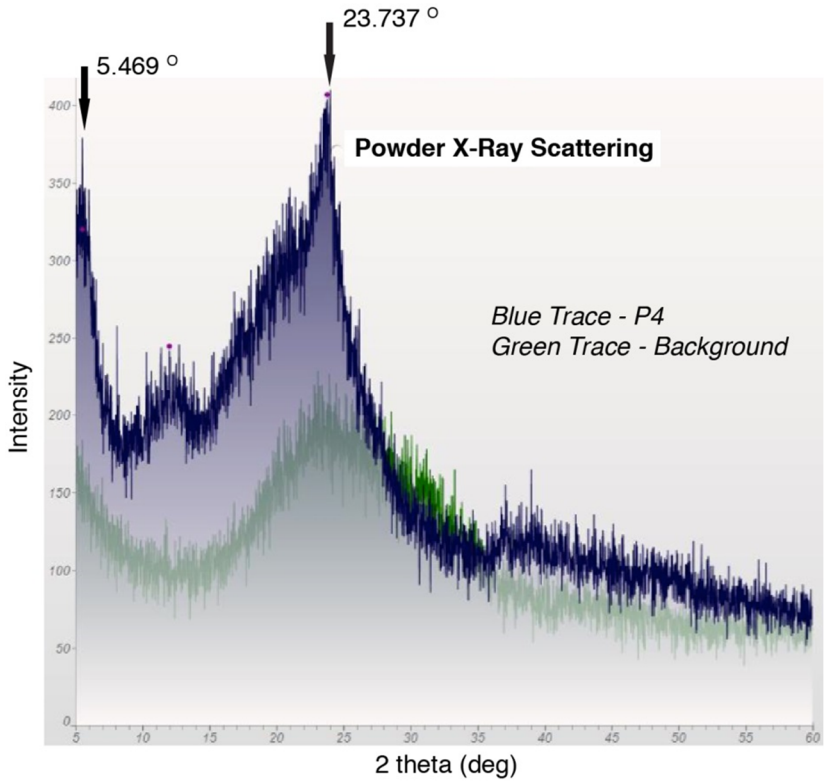


**Figure 2.4** Powder X-ray scattering pattern of **P4**: blue trace: **P4**; Green trace: background

Powder X-ray scattering measurements (Figure 2.4) were performed on **P4** in order to assess the influence of hydrogen bonding units on molecular packing of the P3HT main chain. Two major scattering peaks are clearly seen at 2θ values of 5.469 and 23.737 degrees, corresponding to d-spacings of 16.15 and 3.75 Å, respectively. These numbers are very similar to but slightly smaller than respective lamellar and π-π stacking distances observed in thin films and nanofibers of regioregular P3HT homopolymers.[29-31] This indicates that the pyrimidine moieties on **P4** do not significantly change the main

chain packing motif except slightly reducing inter-molecular distances possibly caused by self-complementary hydrogen bonding interactions.

The thymine tethered fullerene derivative, **F1**, was prepared through a Prato-type addition reaction as shown in Scheme 2.1 and fully characterized by NMR spectroscopy and high resolution mass spectrometry. Cyclic voltammetry measurement of **F1** in THF solution reveals three quasi-reversible reduction peaks having $E_{1/2}$'s at −1.04 V, −1.60 V and −2.21 V (ref. to $Fc/Fc^+$ at −4.8 V), giving a LUMO energy level at ca. −3.8 eV, consistent with literature reported values for pyrrolidine functionalized fullerene derivatives.[32,33]

## 2.3 Hydrogen bonding interactions in solution

### 2.3.1 $^1$H NMR study

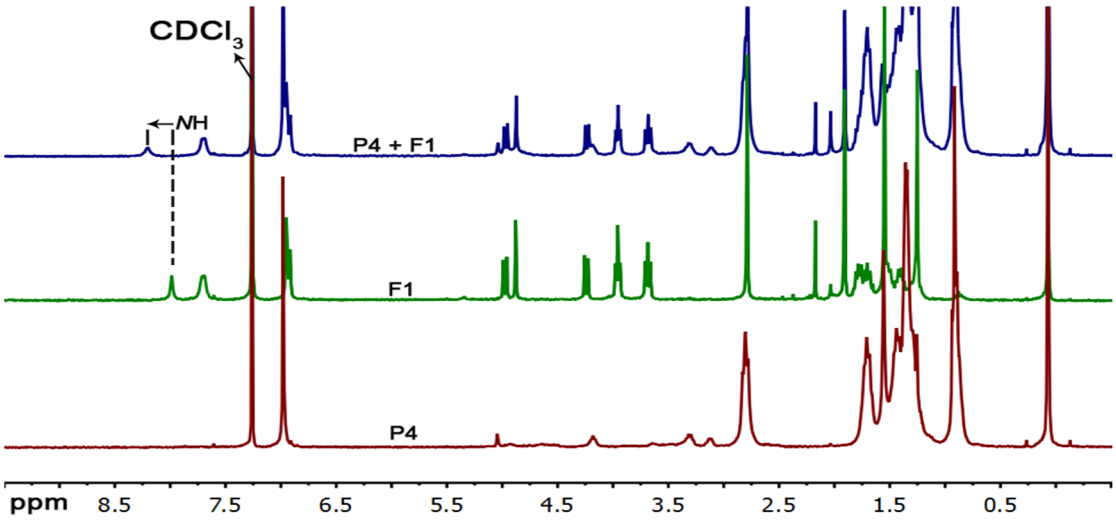


**Figure 2.5** $^1$H NMR ($CDCl_3$, 300.13 MHz) spectra of **P4** (bottom, red), **F1** (middle, green) and a 1:1 mixture of **P4** (30 mM based on diaminopyrimidine units) and **F1** (30 mM). The signals at ca. 0.08 ppm in all spectra are due to grease contaminants from air-free synthesis involving greased glass joints.

The DAD-ADA "three-point" complementary hydrogen bonding between respective diaminopyrimidine units in **P4** and thymine moieties in **F1** was first studied by $^1$H NMR spectroscopy. The **F1** imide-H signal was conveniently monitored since it experiences large downfield shift upon complexation and does not overlap with other proton signals. When **P4** was mixed in $CDCl_3$ with equimolar **F1** (based on diaminopyrimidine units, corresponding to a weight ratio of ca. 10/9), the imide-H signal experienced a downfield shift from 7.99 ppm to 8.20 ppm (Figure 2.5). On the other hand, no chemical shift changes were observed when P3HT and **F1** were mixed at the same ratio in $CDCl_3$ (Figure 2.6).

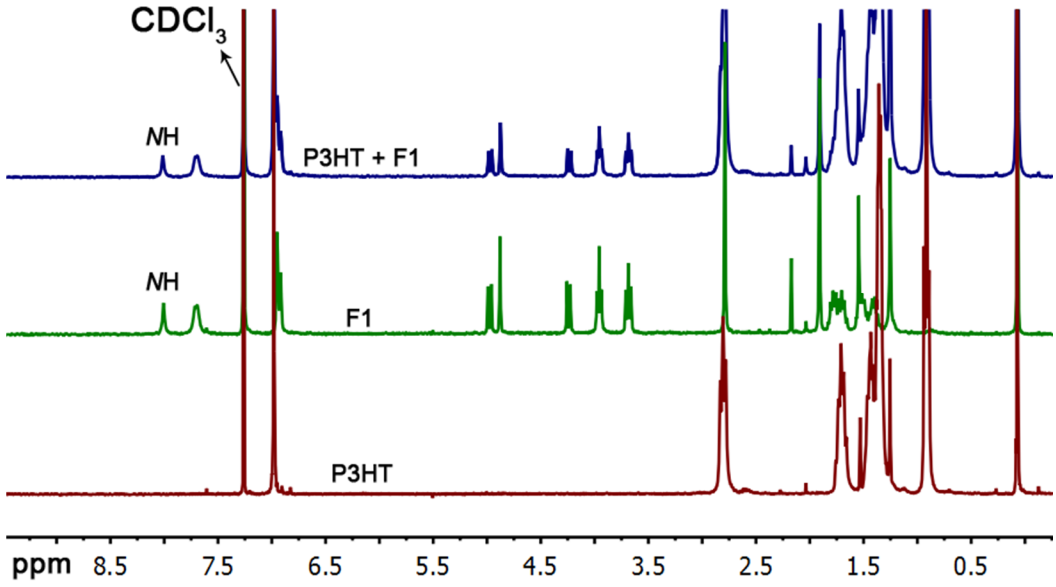


**Figure 2.6** $^1$H NMR ($CDCl_3$, 300.13 MHz) spectra of **P3HT** (bottom), **F1** (middle) and a mixture of **P3HT** and **F1** (10/9 by weight, top). The signals at ca. 0.08 ppm in all spectra are due to grease contaminants from air-free synthesis involving greased glass joints.

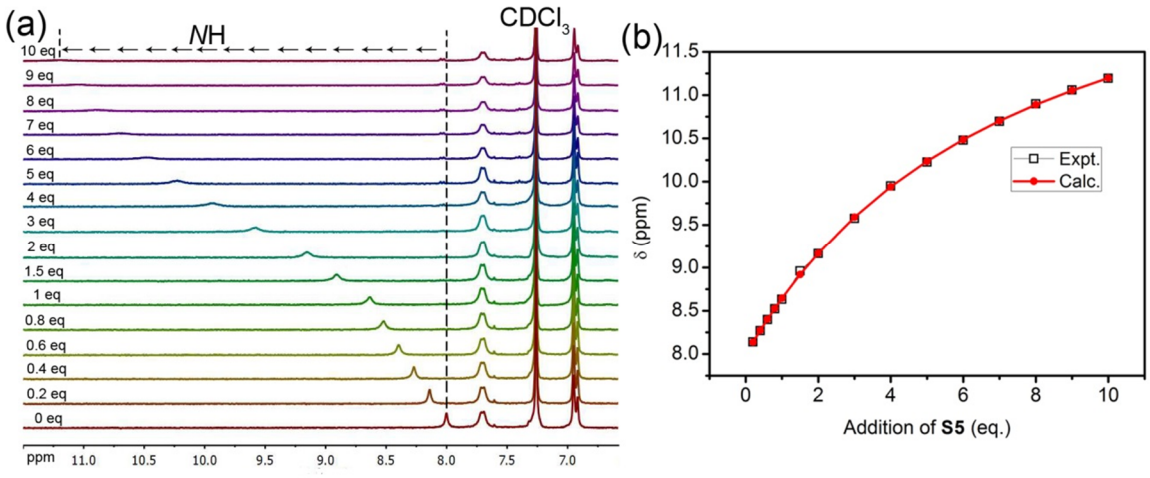


**Figure 2.7** (a) $^{1}$H NMR spectra ($CDCl_3$, 300.13 MHz) of **F1** (4 mM) titrated by model compound **S5** (0.2 M in $CDCl_3$). Solution volume was assumed constant throughout the titration range in the experiment. (b) chemical shift changes of the **F1** amide proton (δ = 8.0 ppm) vs. **S5** guest molecule equivalents (Black empty square); fitting curve by WinEQNMR (Version 1.10) (Red solid circle)

In order to quantify the strength of such three-point hydrogen bonding, the solution binding constant was estimated through NMR titration experiments between **F1** and the model compound **S5** in $CDCl_3$ (Figure S4 and S5). The small molecule model compound **S5** was used instead of **P4** in order to avoid complications commonly associated with polymers, including neighboring group effects and difficulties of preparing solutions with high polymer concentrations. As seen from the titration plot (Figure 2.7 a), only one signal is observed for the imide-H with additions of **S5** up to 10 equivalents, which gradually shifts downfield and becomes broadened. A binding constant of 32.8 ± 1.1 $M^{-1}$ was obtained by fitting the imide-H chemical shifts vs. **S5** equivalents as shown in Figure 2.7b using WinEQNMR program (Version 1.10).[34] This

value is ca. 4-5 times lower than previously reported binding constants between similar diaminopyrimidine and uracil/thymine derivatives.[35-37]

### 2.3.2 Fluorescence quenching studies

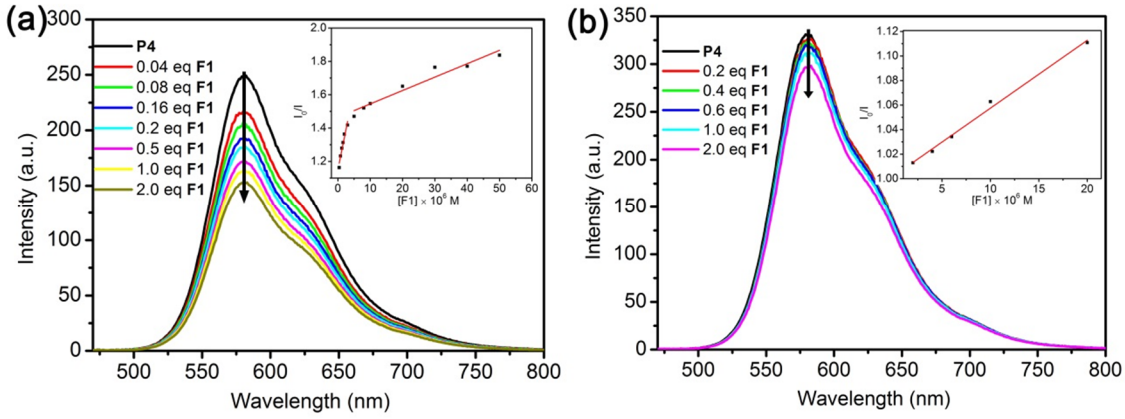


**Figure 2.8** Fluorescence quenching measurements on **P4** (a) and P3HT (b) in chlorobenzene ($10^{-5}$ M) excited at 458 nm with gradual addition of **F1** ($5 \times 10^{-4}$ M). The concentrations of polymers and equivalents of **F1** are calculated based on total number of repeating units in corresponding polymers. The inserts are Stern-Volmer plots and linear fits for calculations of quenching constants.

Figure 2.8 summarizes the fluorescence quenching experiments, in which fluorescence intensity of **P4** in chlorobenzene ($10^{-5}$ M based on total repeat units) was monitored with gradual addition of **F1** ($5 \times 10^{-4}$ M). For comparison, an in-house made P3HT ($M_n$=31,171, $M_w$=32,504, *PDI*=1.04) polymer which is not capable of complementary hydrogen bonding was studied under the same quenching conditions. Both **P4** and P3HT showed identical solution absorption and fluorescence emission spectra but distinct quenching behaviors with **F1**. In the case of P3HT, less than 10% fluorescence quenching was observed with the addition of up to 2 eq. of **F1** and a linear

fit of the Stern-Volmer plot gave a quenching constant of ca. $5.5\times10^3$ $M^{-1}$. A much more pronounced quenching was observed for **P4**, in which over 40% fluorescence was quenched with the addition of 2 eq. of **F1**. This enhanced quenching is expected since **P4** is capable of hydrogen bonding with **F1** and form closely associated complexes that facilitate short-range electron transfer. Furthermore, the Stern-Volmer plot of **P4** shows a two-step transition. The initial step has a large quenching constant of $1.2\times10^5$ $M^{-1}$ up to 0.2 eq. of **F1**, which is also the amount of **F1** needed to fully complex all the diaminopyrimidine moieties in **P4**. After this point, the quenching constant is reduced to $8.0\times10^3$ $M^{-1}$, similar to that of P3HT. Such sharp transition in quenching constant suggests strong complexation between **P4** and **F1** in chlorobenzene solution.[38] The large Stern-Volmer constant in the first step of **P4**/**F1** fluorescent quenching is also observed in silimar small molecule complementrary "multiple-point" hydrogen bonding systems.[39]

**2.4 Solid-state morphology stabilization**

Differential scanning calorimetry (DSC) measurements were performed on **P4**, P3HT, **F1** and their blends in order to probe the effects of complementary hydrogen bonding on morphology stabilization. All samples (ca. 10 mg) were subjected to identical heating and cooling sequences (−50 °C to 250 °C, 10 °C/min); blends were obtained by dissolving polymers and fullerene in a 10/9 weight ratio followed by extensive drying. The first cooling and heating curves are shown in Figure 2.9. Both P3HT and **P4** show crystallization transitions at ca. 205 °C and 165 °C, respectively. The mixture of P3HT and **F1** shows distinct crystallization peak for the polymer, indicating phase separation of these two components to form pure polymer domains. This phenomenon is normally observed in BHJs involving conjugated polymers and fullerene derivatives where no

interactions are present between the two materials. However, the melting and crystallization transitions of **P4** are mostly quenched by the addition of **F1**. This strongly suggests lack of macro-phase separation in the **P4**/**F1** blend caused by the complementary hydrogen bonding that is stable up to 250 °C.

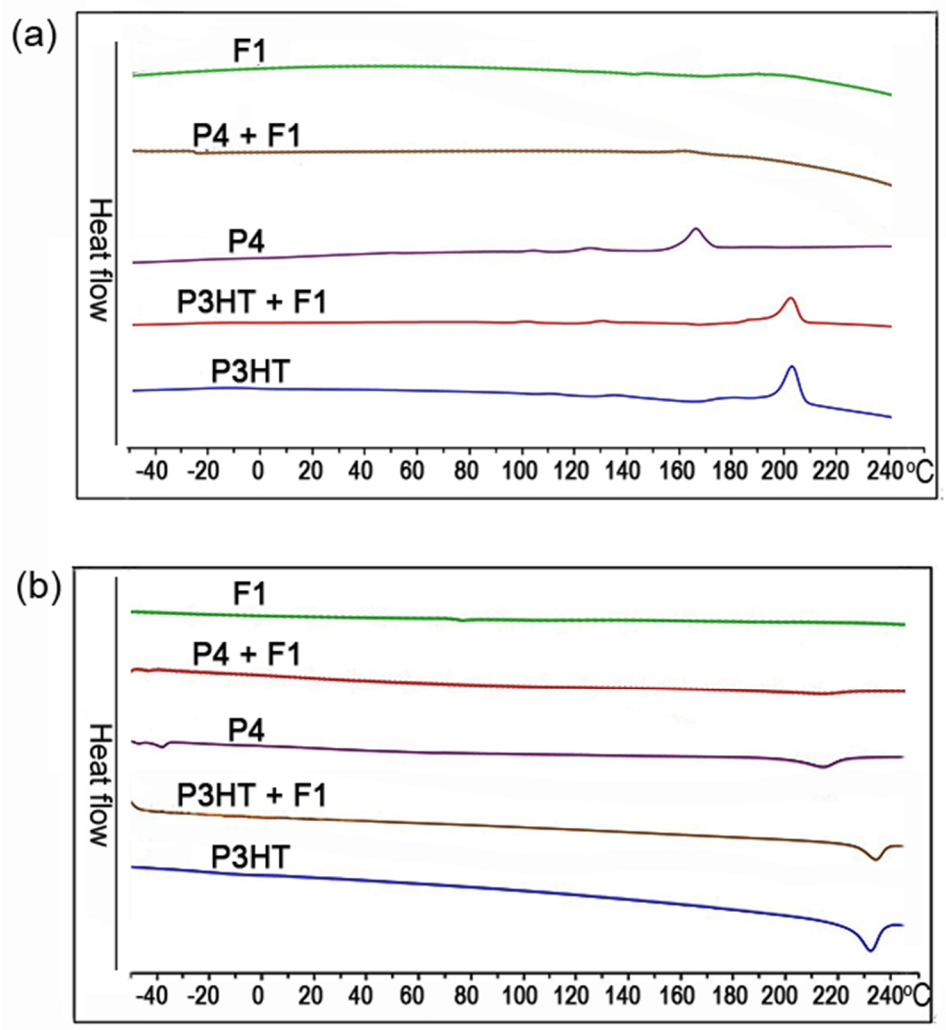


**Figure 2.9** Differential scanning calorimetry (DSC) plots of P3HT, **P4**, **F1** and their blends with ca. 10 mg sample and a scanning rate of 20 °C/min. (a) first cooling curves; (b) second heating curves; exotherm up.

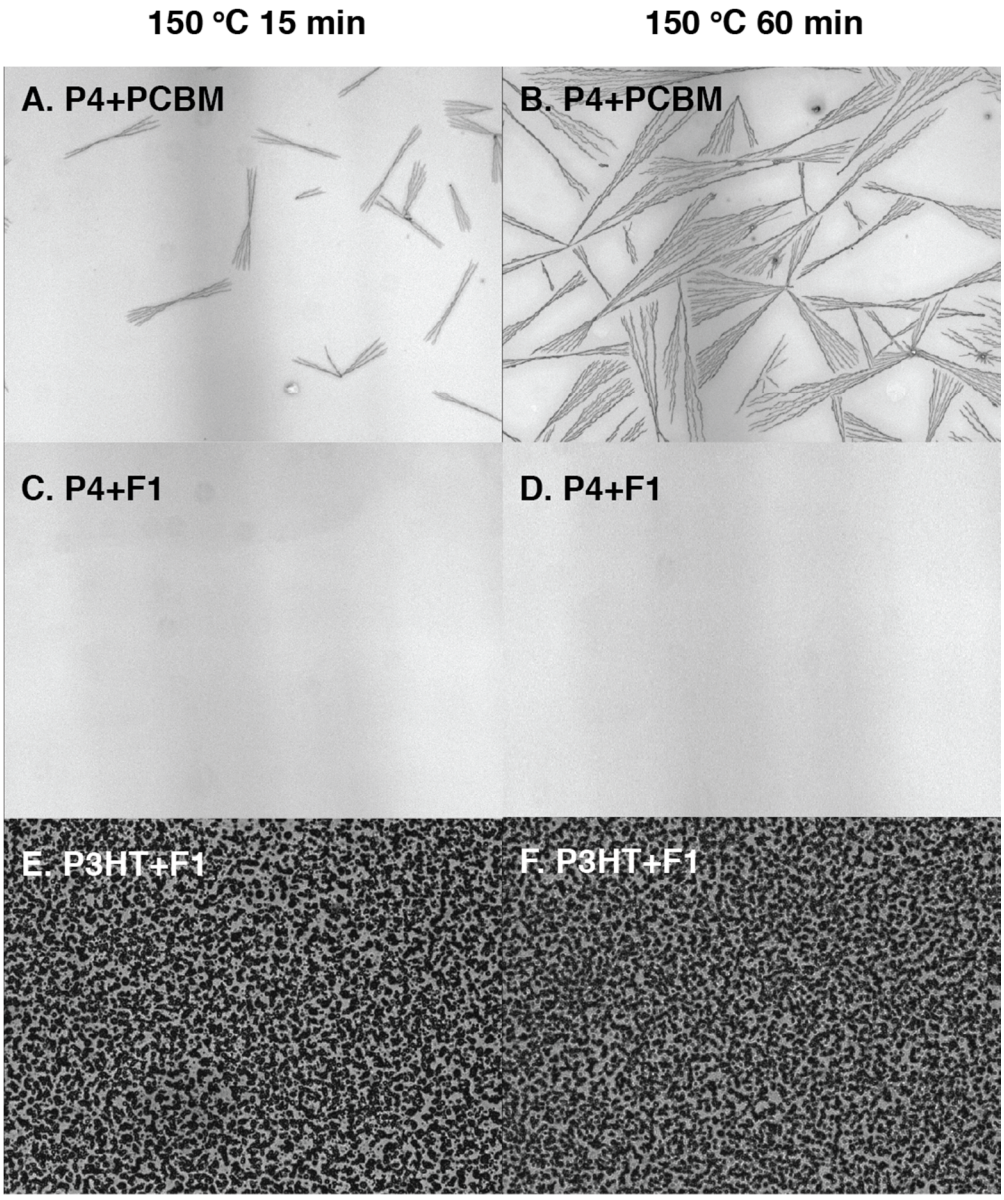


**Figure 2.10** Thin film optical micrographs (10× magnification) of **P4**/PCBM blends (10/9, wt/wt, A and B), **P4**/**F1** blends (10/9, wt/wt, C and D) and P3HT/**F1** blend (10/9 wt/wt, E and F) annealed at 150 °C for 15 minutes (A, C and E) and for 60 minutes (B, D and F).

To further confirm the phase stabilization effect, optical micrographs were taken on thin films (ca. 100 nm in thickness) of **P4**/phenyl-C61-butyric acid methyl ester

(PCBM), **P4**/**F1** and P3HT/**F1** blends spin cast from chlorobenzene solutions. Polymer to fullerene ratio was kept at 10 to 9 by weight. Thin films were annealed at 150 °C for various times and representative optical graphs are shown in Figure 2.10. In the **P4**/PCBM films, thread-like PCBM crystals in starburst arrangement are observed after annealing for 15 min and become significant after 1 h. On the other hand, no observable change can be found in the **P4**/**F1** films. Furthermore, temperature-independent macro-phase separation is found in the P3HT/**F1** film, suggesting incompatibility of these two materials presumably due to **F1** aggregation from self-complementary hydrogen bonding interactions.

**2.5 P4/F1 complexes as solar cell active layer**

Solar cells employing **P4**/**F1** complexes at different weight ratios were fabriacated using a common device geometry of ITO/$MoO_3$/polymer complexes/Al. The frequently applied PEDOT/PSS anode interfacial layer was avoided in this study due to its high acidity that can potentially disrupt the complementray hydrogen bonding interactions. Device performances under simulated AM 1.5G solar irradiation are summarized in Table 2.1.

Device performance was initially enhanced by reducing fullerene contents in the blends and reached an apparent maximum at a **P4/F1** weight ratio of 10/6. Further reduction in **F1** content led to decreased device performance. Such trend is quite different from the well-studied P3HT/PCBM systems that perform best at polymer-to-fullerene weight ratios around 10/10–10/8.[40] Furthermore, power conversion efficiency (PCE) differences in the **P4**/**F1** devices are mostly resulted from short circuit current ($J_{SC}$) changes, while little variations were observed for the other parameters. This is possibly

due to thin film morphology differences, since $J_{SC}$ is directly related to active layer morphologies that eventually determine exciton dissociation and charge collection efficiencies.

**Table 2.1** Device performance of solar cells fabricated using **P4**/**F1** at different weight ratios as active layers.[a]

| **P4**: **F1** (wt:wt) | PCE[b] % | $J_{SC}$[b] ($mA/cm^{-2}$) | $V_{OC}$[b] (V) | FF[b] |
|---|---|---|---|---|
| 10: 10 | 0.81 | 3.81 | 0.59 | 0.36 |
| 10 : 8 | 0.85 | 3.99 | 0.58 | 0.37 |
| 10 : 6 | 1.05 | 4.75 | 0.61 | 0.36 |
| 10 : 4 | 0.48 | 2.13 | 0.59 | 0.39 |

[a] Thermal annealed at 150 °C for 15 min. [b] Averaged over five cells.

Indeed, distinctly different morphologies were observed in atomic force microscopy (AFM) images for thin films of **P4**/**F1** blends at different weight ratios, as seen in Figure 2.11. Large and disconnected aggregates are observed in the 10/10 blend film, which became smaller and more connected in the 10/8 film. A relatively rough film with no aggregation was observed for the 10/6 blend film and the 10/4 blend gave a featureless and smooth morphology.

Such morphology and $J_{SC}$ differences are rationalized as follows. When **P4** is complexed with **F1**, a "bottle-brush" type conjugated block copolymer is obtained. In a 10/10 complex, the relatively high fullerene contents lead to a large fullerene volume fraction. Phase separation of such "bottle-brush" complex is likely dominated by fullerene aggregation, which leads to large islands as seen in Figure 2.11a. Domain discontinuity is detrimental for charge collection and thus leads to low $J_{SC}$. As fullerene

contents decrease, its corresponding volume fraction reduces accordingly and thus aggregation between polymer and fullerene becomes more balanced, which leads to smaller aggregates and eventually to smooth films as normal BHJs. Charge separation and collection are thus facilitated by domain size reduction and inter-connection. On the other hand, with decreasing **F1** contents, a continuous fullerene path for electron transport becomes less likely, which can lead to imbalanced charge transport and inefficient exciton splitting. A clear S-type kink around $V_{OC}$ in the I-V curve of the 10/4 device (Figure 2.12) is likely resulted from space charge build-up due to inefficient electron transport.

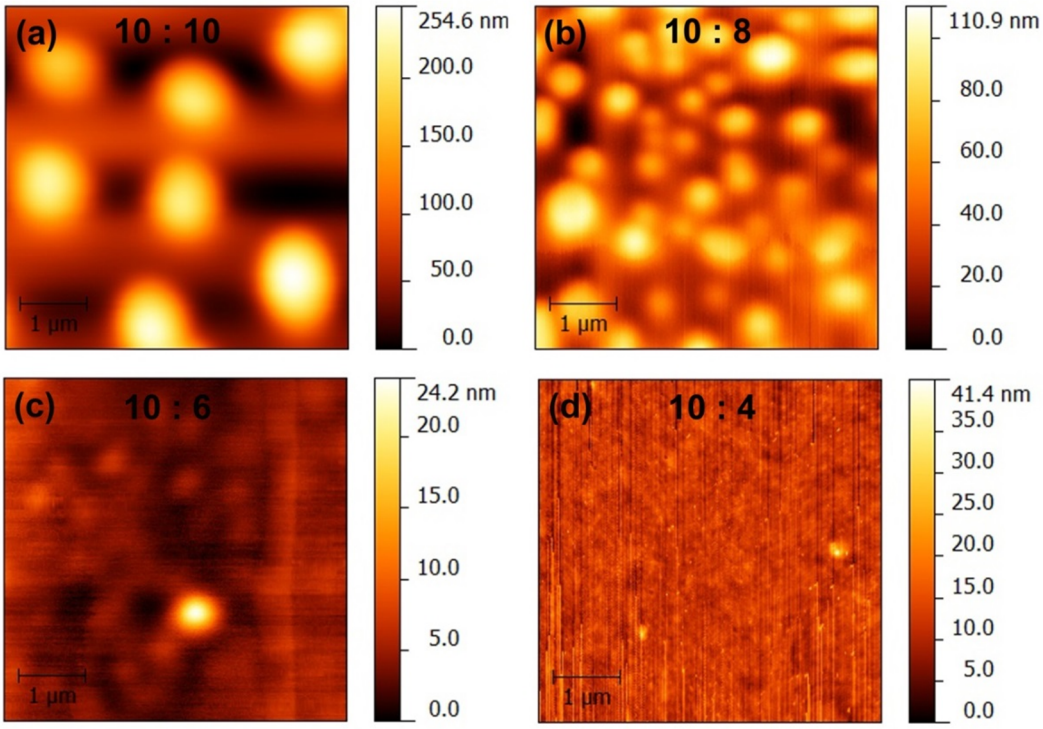


**Figure 2.11** AFM height images (5 µm × 5 µm) of **P4**/**F1** complexes films spin cast from blend solutions at varied polymer-to-fullerene weight ratios of (a) 10:10; (b) 10:8; (c) 10:6; (d) 10:4. All films were annealed at 150 °C for 15 min.

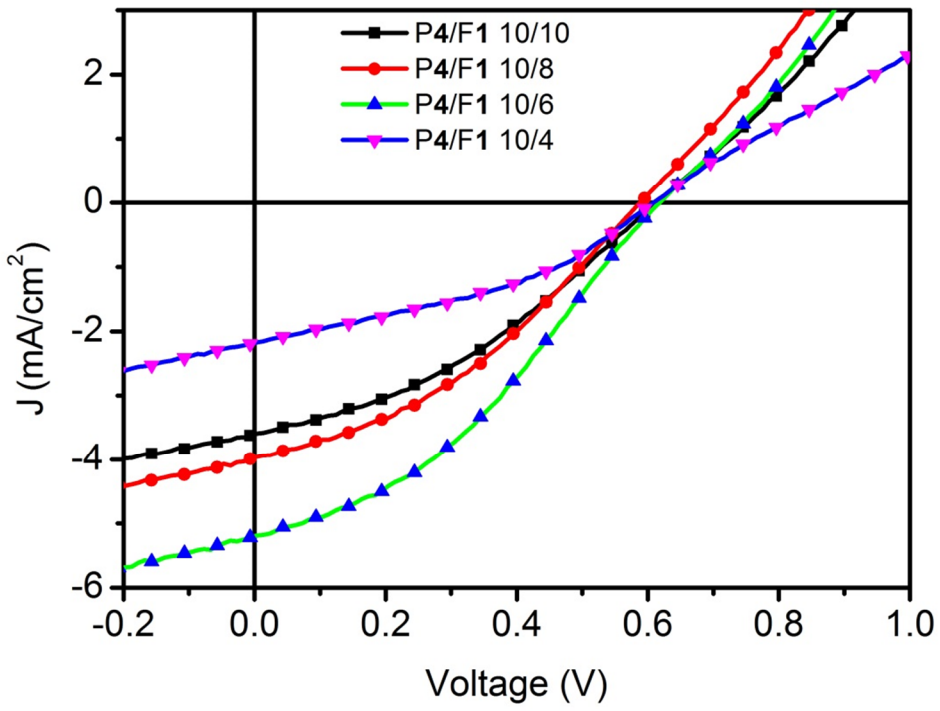


**Figure 2.12** I-V curves of **P4**/**F1** at various weight ratios (under simulated AM1.5 G illumination).

In summary, device performance for the **P4**/**F1** block copolymer complexes depends on both domain sizes and inter-connectivity, which can be tuned by varying fullerene loading percentages. However, for the present system, a blend ratio of 10/6 was found to be optimal but not necessarily ideal due to the relatively low fullerene content. The low photovoltaic properties of current system may be due to the improper block ratios of **P4** or high hydrogen bonding moieties on **P4** which reduced the crystallinity of the polymer. Changing block length ratios and functional group concentrations can

provide opportunities for balanced phase separation as well as bicontinous charge conducting pathways.

### 2.6 P4/F1 complex as compatibilizers

Block copolymers based on polythiophene backbone having fullerene moieties selectively attached to one block have shown to improve performances and, more pronouncedly, thermal stability of P3HT/PCBM BHJ devices as compatibilizers.[41,42] Such block copolymer systems can stabilize P3HT/PCBM interfaces, which effectively reduces domain sizes and slows down macrophase separation. We have preliminarily investigated the stabilization effect of **P4**/**F1** complexes as phase compatibilizers in the benckmark P3HT/PCBM BHJ solar cells.

**Table 2.2** Device performance of BHJ P3HT/PCBM solar cells containing **P4**/**F1** complex (1:1, wt:wt) as compatibilizers at different concentrations.[a]

| **P4**/**F1**[b] | PCE[c] (%) | $J_{SC}$[c] (mA/cm$^{-2}$) | $V_{OC}$[c](V) | FF[c] |
|---|---|---|---|---|
| 0 | 4.60 | 12.45 | 0.58 | 0.64 |
| 2.5% | 4.83 | 12.30 | 0.58 | 0.68 |
| 5% | 4.65 | 11.75 | 0.58 | 0.68 |
| 7.5% | 4.55 | 12.13 | 0.58 | 0.64 |
| 10% | 4.14 | 11.27 | 0.57 | 0.64 |

[a] Annealed at 150 °C for 15 min. [b] Based on the total weight of P3HT/PCBM. [c] Averaged over five cells.

Table 2.2 and Figure 2.13 summarize the device performance of P3HT/PCBM (10:10, wt:wt) BHJ solar cells containing **P4**/**F1** (1:1 wt:wt) at various concentrations. By adding a few percent (2.5% and 5%) of the polymer complexes, device performance was slightly enhanced, as reflected by a small increase in fill factors (FFs). Such increase is

likely due to polymer/fullerene interface stabilization by the compatibilizers, which leads to smaller domain sizes and better morphologies for charge generation and collection. Further increase of compatibilizer concentration up to 10% led to a decrease in device performance by reduction in all parameters, possibly due to more significant unfavorable aggregation effects as seen in the pure **P4**/**F1** blend films (Figure 2.11).

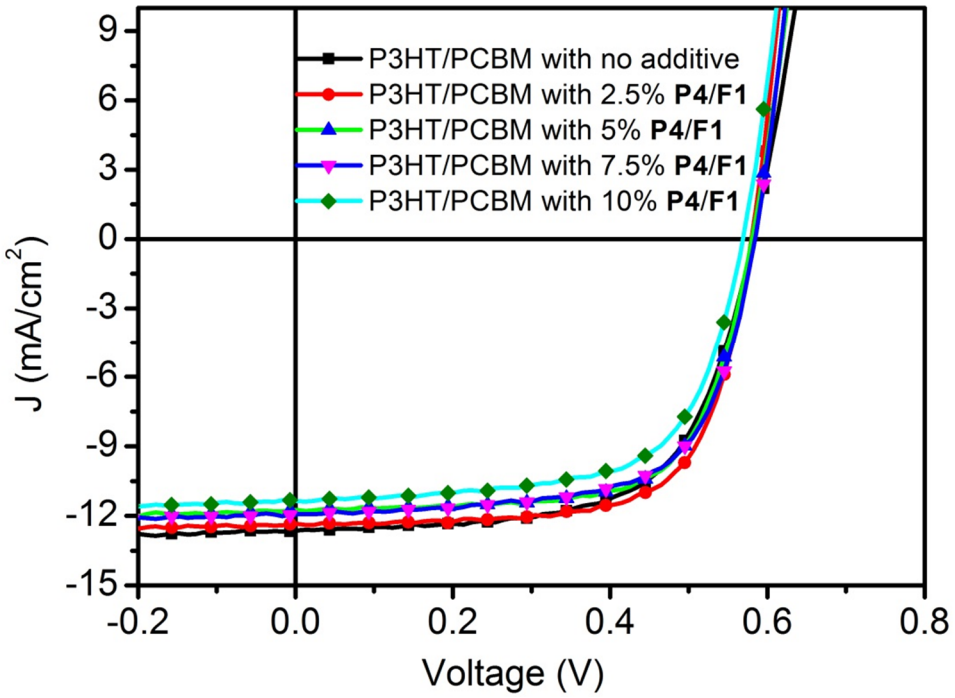


**Figure 2.13** I-V curves (under simulated AM1.5 G illumination) of P3HT/PCBM BHJ devices containing **P4**/**F1** (1:1 by wt.) complexes as compatibilizers at different concentrations.

Thermal stabilities of these compatibilized devices were evaluated at 110 °C for prolonged time intervals and the results are summarized in Figure 2.14 and Figure 2.15. Without **P4**/**F1** compatibilizers, the P3HT/PCBM BHJ device lost ca. 60% of its original performance after 150 h. The best stability was observed in the device containing 2.5%

compatibilizer, for which up to 60% efficiency was retained. Interestingly, the device containing 5% compatibilizer still exhibited slightly enhanced thermal stability over the uncompatibilized P3HT/PCBM device, but further increasing the **P4**/**F1** compatibilizer concentration to 10% led to less thermal stability of the solar device. Therefore, for the **P4**/**F1** system, only adding 2.5% and 5% would help improve the stability of the P3HT/PCBM devices.

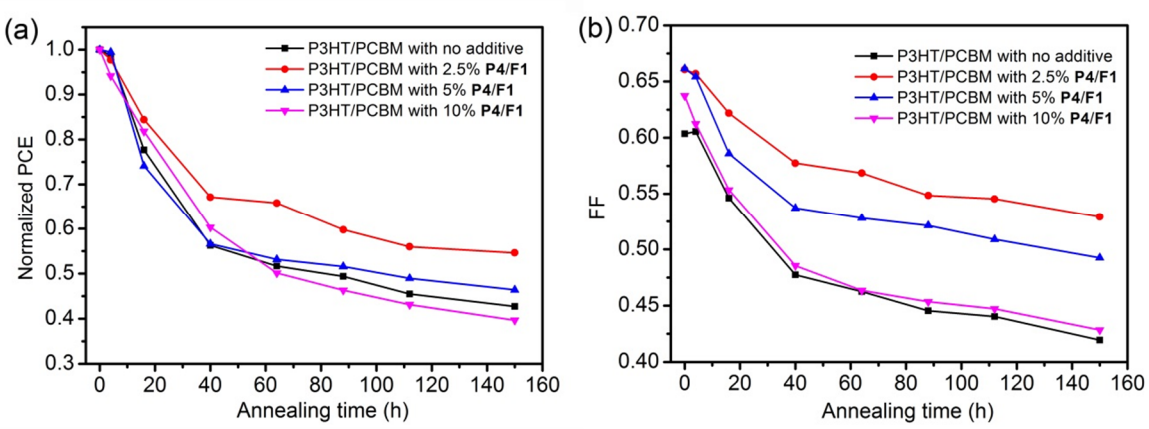


**Figure 2.14** Thermal stability test of P3HT/PCBM BHJ solar cells containing **P4**/**F1** complexes as compatibilizers at different concentrations, annealed at 110 °C up to 150 h. (a) Normalized power conversion efficiency (PCE) vs. annealing time; (b) fill factor (FF) vs. annealing time.

The stability differences were mainly caused by differences in FF changes as seen in Figure 2.14 and Figure 2.15. FFs dropped significantly for the non-compatibilized devices and a slight S-type kink was observed after annealing for 150 h. This indicates that unfavorable phase separation which leads to imbalanced charge transport. On the other hand, relatively small decreases in FFs were observed for the device containing 2.5% compatibilizer, indicating unfavorable phase separation to a lesser degree.

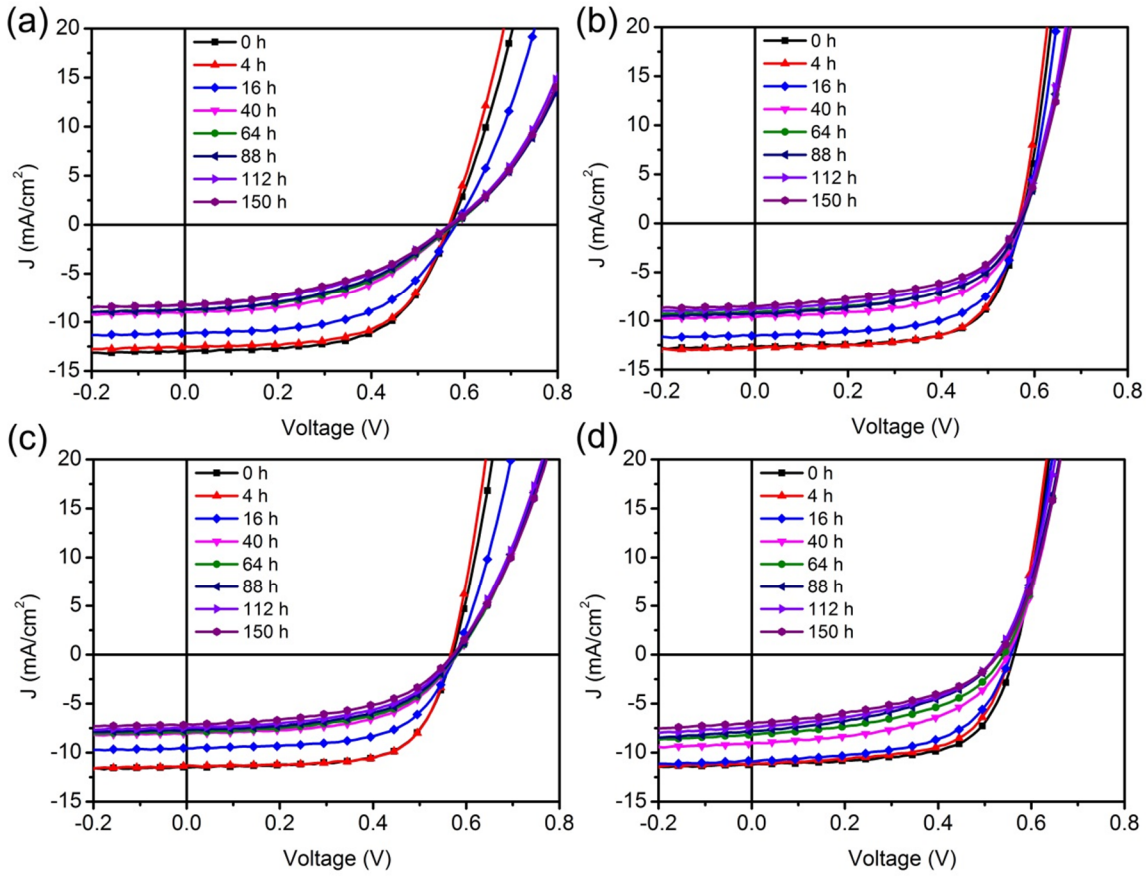


**Figure 2.15** I-V curves (under simulated AM1.5 G illumination) of P3HT/PCBM BHJ devices containing **P4**/**F1** (1:1 by wt.) complexes at different concentrations, annealed at 110°C up to 150 h. (a) P3HT/PCBM with no **P4**/**F1**, (b) P3HT/PCBM with 2.5 wt% **P4**/**F1**, (c) P3HT/PCBM with 5 wt% **P4**/**F1**, (d) P3HT/PCBM with 10 wt% **P4**/**F1**.

Moreover, the current density also drops with extended annealing time in all four devices as indicated in Figure 2.15, suggesting less efficient charge separation and transport over prolonged ageing time. It is noted that all the devices showed slower photovoltaic performance deterioration within the first 16 hours, after which such devices performance reduction aggravated with the increasing ageing time. We also observed a $V_{OC}$ decrease in the devices containing 10% **P4**/**F1**, from 0.56 V to 0.53 V (Figure 2.15

d). Such $V_{OC}$ change was not seen in other devices. We speculate that it was possibly caused by the increased crystallinity of the blend film over the ageing test.

## 2.7 Conclusion

In conclusion, we have successfully prepared a novel conjugated block copolymer and a fullerene derivative capable of "three-point" complementary hydrogen bonding interactions. Strong complexation between these compounds leads to stabilization of blend morphologies. Fullerene loading percentages can easily be adjusted by taking advantage of the non-covalent attachment, which significantly affects thin film morphologies and device performance. Preliminary results also demonstrated that these block copolymer complexes can be used as phase compatibilizers in BHJ solar cells in order to enhance device long-term stability.

## 2.8 Future work

Through the initial results, we found out that our strategy worked regarding controlling the morphology of the polymer/fullerene blends by tuning the polymer/fullerene ratios in the blends. The interactions between the polymers and fullerenes through the complementary hydrogen bonding interactions enable strong attachment of the fullerenes selectively onto one block of the block copolymer. However, the PCEs of solar devices employing such **P4**/**F1** as active layer did not present promising results. One possible reason is that fullerene domains dominate the self-assembly of **P4**/**F1** complexes when all the hydrogen bonding sites are occupied by **F1**. This is bad for charge separation and transport in solar cells.

To modulate the self-assembly of block polymer/fullerenes toward amenable charge separation and transport in solar cells, we envision that changing the block ratio

with a longer pure P3HT block as the first block and reduce the hydrogen bonding moieties on the block copolymer would probably be beneficial for solar cells employing the block copolymer/fullerenes complexes as active layers.

## 2.9 Experimental

### 2.9.1 Materials and general methods

All reagents and solvents were used as received from Sigma-Aldrich or VWR unless otherwise noted. 2-Bromo-3-hexyl-5-iodothiophene (**M1**),[43-46] ((6-(2-bromo-5-chloromagnesiothiophen-3-yl)hexyl)oxy)(*tert*-butyl)dimethylsilane (**M2**),[36,47] 4-((6-bromohexyl)oxy)benzaldehyde (**M4**)[48-50] were synthesized according to previously reported procedures. THF was distilled from Na/benzophenone prior to use. Anhydrous chloroform was obtained by distillation over $CaH_2$ and degassed through several freeze-pump-thaw cycles. 300.13 MHz $^1$H and 75.48 MHz $^{13}$C NMR spectra were recorded on a Bruker Avance III Solution 300 spectrometer. All solution $^1$H and $^{13}$C NMR spectra were referenced internally to solvent signals. Size exclusion chromatography (SEC) analyses were performed in chloroform with 0.5% (v/v) triethylamine (1 mL/min) using a Waters Breeze system equipped with a 2707 autosampler, a 1515 isocratic HPLC pump and a 2414 refractive index detector. Two styragel columns (Polymer Laboratories; 5 μm Mix-C), which were kept in a column heater at 35 °C, were used for separation. The columns were calibrated with polystyrene standards (Varian). Ultraviolet-Visible (UV-Vis) absorption spectra were recorded on a Shimadzu UV-2401 PC spectrometer over a wavelength range of 240-800 nm. Fluorescence emission spectra were obtained using a Varian Cary Eclipse Fluorimeter. Differential scanning calorimetry (DSC) measurements were performed on a Mettler Toledo DSC STAR$^e$ system with ca. 10 mg sample and at a

scan rate of 10 °C / min. The results reported are from the first cooling and second heating cycles. High resolution mass spectrometry (HRMS) was performed on a Waters/Micromass LCT Premier system operating under electrospray ionization (ESI) mode. Cyclic Voltammetry was performed at 25 °C on a CH Instrument CHI604xD electrochemical analyzer using a glassy carbon working electrode, a platinum wire counter electrode and a Ag/AgCl reference electrode calibrated using ferrocene redox couple (4.8 eV below vacuum). Optical Microscopy images were taken from an Axio Imager A2 instrument under bright field. Powder X-ray diffraction measurements were performed on a Rigaku SmartLab instrument. Atomic force microscopy (AFM) images were obtained on a Thermomicroscopes Autoprobe CP Research AFM instrument operated under tapping mode. For the solution binding constant studies, an **S5** solution in $CDCl_3$ (0.2 M) was gradually added into a **F1** solution in $CDCl_3$ (4 mM) in a NMR tube. After each addition, the solution was allowed to equilibrate for 5 min and subjected to $^1H$ NMR measurements.

### 2.9.2 Solar cell fabrication and testing

Blend solutions were prepared by dissolving **P4** and **F1** at predetermined weight ratios in chlorobenzene and the concentration of **P4** was kept at 1 wt%. P3HT (synthesized in-house; $M_n$=26,077, $M_w$=27,120, PDI: 1.04)/PCBM (American Dye Source, Inc.) blend solutions were prepared by dissolving P3HT/PCBM (1:1 in weight) in chlorobenzene at a total concentration of 2 wt%. The compatibilizer solution was prepared by dissolving **P4** and **F1** (1:1 in weight) in chlorobenzene at a total concentration of 2 wt%, and stirred at 100 °C for 3 h. The compatibilizer solutions of predetermined volumes were then added to the P3HT/PCBM solution using

microsyringes to form mixture solutions. All solutions were stirred at 100 °C for 10 h in a nitrogen glove box (Innovative Technology, model PL-He-2GB, $O_2$ < 0.1 ppm, $H_2O$ < 0.1 ppm) before device fabrication. Solar cell devices were fabricated according to the following procedure: ITO-coated glass substrates (China Shenzhen Southern Glass Display. Ltd, 8 Ω/□) were cleaned by ultrasonication sequentially in detergent, DI water, acetone and isopropyl alcohol, each for 15 min. These ITO-coated glass substrates were further treated by UV-ozone (PSD Series, Novascan) for 45 min before being transferred to a nitrogen glove box (Innovative Technology, model PL-He-4GB-1800, $O_2$ < 0.1 ppm, $H_2O$ < 0.1 ppm) for $MoO_3$ deposition. $MoO_3$ (10 nm) was deposited using an Angstrom Engineering Åmod deposition system at a base vacuum level < $7 \times 10^{-8}$ Torr. The polymer/fullerene blend solution was first filtered through a 1 μm PTFE filter and spin-coated on top of the $MoO_3$ layer at 400 rpm for 30 s. Al (100 nm) was thermally evaporated through patterned shadow masks as anodes. Current−voltage (I−V) characteristics were measured by a Keithley 2400 source-measuring unit under simulated AM1.5G irradiation (100 mW/cm$^{-2}$) generated by a Xe arc-lamp based Newport 67005 150-W solar simulator equipped with an AM1.5G filter. The light intensity was calibrated by a Newport thermopile detector (model 818P-010-12) equipped with a Newport 1916-C Optical Power Meter.

### 2.9.3 Synthetic procedure of the new compounds and characterizations

**2,6-Bis(hexylamino)pyrimidin-4-ol (M3).** To a 100 mL flask was added 3 g 2,6-diaminopyrimidin-4-ol (23.8 mmol) and 17 mL hexanoic anhydride (71.4 mmol). The solution was refluxed for 4 h with vigorous stirring. During the reflux, the solution may become solidified. The solid was washed with copious $CHCl_3$ and isolated by gravity

filtration. The product, N,N'-(6-hydroxypyrimidine-2,4-diyl)dihexanamide, was isolated by recrystallization from MeOH/$CHCl_3$ as a white powder (6.8 g, 89%). $^1$H NMR (300.13 MHz, DMSO-$d_6$, δ): 0.84-0.88 (m, 6H), 1.25-1.30 (m, 8H), 1.52-1.59 (m, 4H), 2.39 (t, 2H, J = 7.5 Hz), 2.46 (t, 2H, J = 7.5 Hz), 6.67 (s, 1H),9.93 (s, 1H), 11.23 (s, 1H), 11.68 (s, 1H). $^{13}$C NMR (75.48 MHz, DMSO-$d_6$, δ): 176.6, 173.1, 161.7, 156.6, 150.4, 92.7, 36.2, 36.0, 30.8, 30.6, 24.4, 24.0, 21.9, 21.8, 13.8. To a 250 mL Schlenk flask equipped with a septum and a stir bar was added under nitrogen 1.0 g N,N'-(6-hydroxypyrimidine-2,4-diyl)dihexanamide (6.20 mmol) and ca. 100 mL anhydrous THF and the flask was placed in an ice bath for 10 min. 0.59 g $NaBH_4$ (31.02 mmol) was added into the solution portion-wise during a period of 5 min, and the resulting solution was kept at 0 °C for 10 min before 1.92 mL (31.02 mmol) $BF_3{\cdot}Et_2O$ was added to the solution dropwise. The reaction mixture was kept at 0 °C for 1h and then warmed up to r.t. The reaction mixture was stirred for another 5 h and poured into a large excess of water. The water solution was extracted with EtOAc (50 mL × 2) and the combined organic layers were washed with saturated $NaHCO_3$ (50 mL) solution and brine (50 mL). The organic layer was dried over $Na_2SO_4$ and volatile materials were removed under reduced pressure. **M3** was obtained as a white solid (550 mg, 60%) through column chromatography with DCM/MeOH (100/3, v/v) as the eluent. $^1$H NMR (300.13 MHz, $CDCl_3$, δ): 0.83-0.89 (m, 6H), 1.25-1.36 (m, 12H), 1.38-1.57 (m, 4H), 3.08 (d, 2H, J = 6.0 Hz), 3.23-3.29 (m, 2H), 4.66 (s, 1H),4.73 (t, 1H,N*H*), 6.42 (s, 1H,N*H*), 11.06 (s, 1H, O*H*). $^{13}$C NMR (75.48 MHz, $CDCl_3$, δ): 165.8, 164.9, 154.3, 75.4, 42.1, 40.8, 31.7, 31.6, 29.5, 29.3, 26.8, 26.7, 22.7, 14.2, 14.1. HRMS (ESI): calcd. for $C_{16}H_{30}N_4O$, 295.2420 [M+H]; found, 295.2491 [M+H].

**4-((6-(5-Methyl-2,4-dioxo-3,4-dihydropyrimidin-1(2H)-yl)hexyl)oxy)-benzaldehyde (M5).** The synthesis of **M5** is similar to previously reported literature procedures.[51] $K_2CO_3$ (3.18g, 23 mmol) was added to a solution of thymine (2.92 g, 23 mmol) in 200 mL DMF and the solution was stirred at 80 $^oC$ for 1 h. 4-((6-Bromohexyl)oxy)benzaldehyde (**M4**) (6.6 g, 23 mmol) in 20 mL DMF was then added dropwise and the reaction mixture was kept at 80 °C overnight. DMF was removed under vacuum and the residue was dissolved in 100 mL $CH_2Cl_2$. The organic layer was washed twice with water and dried over $Na_2SO_4$. After removal of $CH_2Cl_2$ under reduced pressure, column chromatography with DCM/EtOAc (1/1, v/v) gave **M5** as a white solid (2.54 g, 33.4%). $^1$H NMR (300.13 MHz, $CDCl_3$, δ): 1.44-1.83 (m, 8H), 1.90 (s, 3H), 3.71 (t, 2H, J = 7.2 Hz), 4.04 (t, 2H, J = 6.0 Hz), 6.96 (d, 3H, J = 5.4 Hz), 7.83 (d, 2H, J = 5.4 Hz), 9.86 (s, 1H). $^{13}$C NMR (75.48 MHz, $CDCl_3$, δ): 190.9, 164.5, 164.2, 151.1, 140.4, 132.1, 129.9, 114.8, 110.8, 68.2, 48.5, 29.1, 29.0, 26.2, 25.8, 12.4.

**1-(1-Methylfulleropyrrolidin-2-yl)-4-((6-(5-methyl-2,4-dioxo-3,4-dihydropyrimidin-1(2H)-yl)hexyl)oxy)benzene (F1).** The synthesis of **F1** is similar to reported procedures.[52,53] A solution of C60 (436.4 mg, 0.606 mmol), N-methylglycine (81 mg, 0.909 mmol) and **M5** (200 mg, 0.808 mmol) in toluene (100 mL) was heated at reflux for 15 h under nitrogen. After removal of solvent under reduced pressure, the crude product was purified by column chromatography using DCM/EtOAc (7/3, v/v) as a brownish powder (146 mg, 23%). $^1$H NMR (300.13 MHz, $CDCl_3$, δ): 1.40-1.54 (m, 6H), 1.69-1.81 (m, 4H), 1.90 (s, 3H), 2.78 (s, 3H), 3.69 (t, 2H, J = 7.2 Hz), 3.96 (t, 2H, J = 6.3 Hz), 4.24 (d, 1H, J = 12.3 Hz), 4.88 (s, 1H), 4.98 (d, 1H, J = 9.3 Hz), 6.95 (t, 3H, J = 11.7 Hz), 7.70 (d, 2H, J = 5.7 Hz), 7.97 (s, 1H). HRMS (ESI): Calcd. for $C_{80}H_{27}N_3O_3$,

1078.2130 [M+], 1079.2163 for [M+H]; found, 1078.2111 [M+], 1079.2162 [M+H]. Cyclic voltammetry (0.1 M $TBAPF_6$ in THF, 100 mV/s, vs. $Fc/Fc^+$): $E_{1/2}(1) = -1.04$ V, $E_{1/2}(2) = -1.60$ V, $E_{1/2}(3) = -2.21$ V.

**N2, N4-dihexyl-6-(hexyloxy) pyrimidine-2, 4-diamine (S5).** In a 25 mL flask was added 200 mg **M3** (0.679 mmol), 0.08 mL bromohexane (0.543 mmol), 141 mg $K_2CO_3$ (1.102 mmol) and 5 mL anhydrous DMF. The solution was heated at 80 °C overnight and then poured into a large excess of water. The aqueous phase was extracted with 10 mL EtOAc for three times and the combined organic layer was washed with water and brine. The organic layer was then dried over $Na_2SO_4$ and the solvent was removed under reduced pressure. The residue was purified via column chromatography (DCM/EtOAc = 10/1, v/v) to yield **S5** (146 mg, 71%) as the small molecule model compound. $^1$H NMR (300.13 MHz, $CDCl_3$, δ): 0.86-0.88 (m, 9H), 1.29-1.39 (m, 18H), 1.50-1.54 (m, 4 H), 1.65-1.74 (m, 2H), 3.12 (q, 2H, J1 = 6.3 Hz, J2 = 6.9 Hz), 3.31(q, 2H, J1 = 6.3 Hz, J2 = 6.9 Hz), 4.16 (t, 2H, J = 6.6), 4.61 (d, 1H, J = 5.1 Hz), 4.71 (t, 1H, J = 5.4 Hz), 5.05 (s, 1H). $^{13}$C NMR (75.48 MHz, $CDCl_3$, δ): 171.1, 165.3, 162.2, 74.9, 65.8, 41.8, 41.5, 31.7, 31.7, 30.0, 29.5, 29.2, 26.8, 25.8, 22.7, 14.1.

**Block copolymer P2**. The precursor block copolymer **P2** was prepared through modified procedures according to literature reports.[54-57] Two three-necked round-bottomed flasks (250 mL and 50 mL) equipped with stopcock and septa were flamed dried under high vacuum and cooled to room temperature under $N_2$. Monomer **M1** (1.482 g, 3.972 mmol) was placed in the 250 mL flask under $N_2$, and then evacuated under high vacuum to remove any residual water and oxygen. After adding dry THF (40 mL) into the flask via a syringe, the solution was cooled to 0 °C. A 2M solution of *i*-PrMgCl in

THF (2 mL, 3.972 mmol) was added via syringe and the mixture was stirred at 0 °C for 30 min (solution 1). In the other 50 mL flask, 0.5 g (0.993 mmol) ((6-(2-bromo-5-iodothiophen-3-yl)hexyl)oxy)(*tert*-butyl)dimethylsilane was first reacted with 0.5 mL *i*-PrMgCl in the presence of 42 mg LiCl (0.943 mmol) in 10 mL THF (solution 2) to yield **M2**. Solution 1 was heated up to 35 °C and Ni(dppp)$Cl_2$ catalyst (21.52 mg, 0.0397 mmol), which was suspended in 5 mL dry THF, was added in one portion. The reaction mixture was stirred at 35 °C for 15 min and an aliquot was withdrawn with a syringe and injected into a methanol solution to give **P1** for SEC analysis (RI, $CHCl_3$, 1 mL/min: $M_n$ = 23,645, $M_w$ = 25,082, *PDI* = 1.07). Solution 2 containing **M2** was then transferred to solution **1** via a cannula. The resulting red solution was stirred at 35 °C for 1 h before 0.5 mL EtMgCl solution (2M in THF) was added. The polymer was isolated by precipitation into MeOH and successively washed by Soxhlet extraction using methanol, acetone, and chloroform. The polymer was recovered by precipitation of the chloroform solution into methanol and dried under high vacuum to give a black solid (0.8 g, 83%). $^1$H NMR (300.13 MHz, $CDCl_3$, δ): 0.041 (s), 0.070 (s), 0.8-0.94 (m), 1.25-1.73 (m), 2.81(t), 3.61 (t), 6.98 (s). SEC (RI, $CHCl_3$ 1 mL/min): $M_n$ = 36,683, $M_w$ = 38,094, *PDI* = 1.04.

**Block copolymer P3**. In a 100 mL Schlenk flask was added 200 mg polymer **P2** and 20 mL THF under $N_2$. The solution became clear after stirring at 60 °C for ca. 30 min. Tetrabutylammonium fluoride (TBAF) solution (0.2 mL, 2M in THF) was then added dropwise via syringe. The reaction mixture was kept stirring at 60 °C for 8 h and concentrated under reduced pressure to ca. 5 mL. **P2** was recovered as a black solid by precipitation into a mixture of methanol and acetone (1/1, v/v) and dried under vacuum overnight (168 mg 95%). $^1$H NMR (300.13 MHz, $CDCl_3$, δ): 0.915 (t), 1.25-1.73 (m),

2.04 (s), 2.81 (t), 3.66 (t), 6.98 (s). SEC (RI, $CHCl_3$ 1 mL/min): $M_n$ = 25,830, $M_w$ = 29,572, *PDI* = 1.15.

**Block copolymer P4**. In a 50 mL Schlenk flask was added 100 mg **P3** and 157 mg 2,6-bis(hexylamino)pyrimidin-4-ol **M3** (0.532 mmol), 139 mg $PPh_3$ (0.532 mmol) and 20 mL THF under $N_2$. The mixture was stirred at 60 °C for ca. 30 min and became a clear solution. Diisopropyl azodicarboxylate (DIAD) (0.11 mL, 0.532 mmol) was then added dropwise via syringe. The reaction mixture was kept stirring at 60 °C for 24 h and concentrated under reduced pressure to ca. 5 mL. The crude polymer was isolated by precipitation into a methanol water mixture (4/1, v/v) and successively Soxhlet extracted using methanol, acetone, and chloroform. The chloroform solution was concentrated and precipitated into MeOH to give **P4** as a black solid (110 mg, 84%). $^1$H NMR (300.13 MHz, $CDCl_3$, δ): 0.91 (t), 1.25-1.71 (m), 2.80 (t), 3.12 (br), 3.32 (br),3.49 (br), 3.64 (br), 4.19 (br), 4.92 (br), 5.04 (br), 6.98 (s). SEC (RI, $CHCl_3$ 1 mL/min): $M_n$ = 29,501, $M_w$ = 37,577, *PDI* = 1.27.

The synthesis of the random copolymer **P4'** bearing 20 mol% diaminopyrimidine functionality was similar to that of its analogous block copolymer **P4** (Scheme 2). Yield: 80%. $^1$HNMR (300.13 MHz, $CDCl_3$, δ): 0.85-0.91 (m), 1.25-1.71 (m), 2.57 (s), 2.81 (t), 3.12-3.14 (m), 3.28-3.34 (m), 3.66 (br), 4.18 (t), 4.49 (s), 4.61 (s), 5.05 (s), 6.98 (s). SEC (RI, $CHCl_3$ 1 mL/min): $M_n$ = 41,905, $M_w$ = 95,007, *PDI* = 2.27.

## 2.10 References


(1) Chen, H.-Y.; Hou, J.; Zhang, S.; Liang, Y.; Yang, G.; Yang, Y.; Yu, L.; Wu, Y.; Li, G. *Nat. Photon.* **2009**, 3, 649.

(2) Zhao, G.; He, Y.; Li, Y. *Adv. Mater.* **2010**, 22, 4355.

(3) Chu, T.-Y.; Lu, J.; Beaupré, S.; Zhang, Y.; Pouliot, J.-R.; Wakim, S.; Zhou, J.; Leclerc, M.; Li, Z.; Ding, J.; Tao, Y. *J. Am. Chem. Soc.* **2011**, 133, 4250.

(4) Zhou, H.; Yang, L.; Stuart, A. C.; Price, S. C.; Liu, S.; You, W. *Angew. Chem. Int. Ed.* **2011**, 50, 2995.

(5) Blom, P. W. M.; Mihailetchi, V. D.; Koster, L. J. A.; Markov, D. E. *Adv. Mater.* **2007**, 19, 1551.

(6) Günes, S.; Neugebauer, H.; Sariciftci, N. S. *Chem. Rev.* **2007**, 107, 1324.

(7) Thompson, B. C.; Fréchet, J. M. J. *Angew. Chem. Int. Ed.* **2008**, 47, 58.

(8) Dennler, G.; Scharber, M. C.; Brabec, C. J. *Adv. Mater.* **2009**, 21, 1323.

(9) Jørgensen, M.; Norrman, K.; Krebs, F. C. *Sol. Energy. Mater. Sol. Cells* **2008**, 92, 686.

(10) Jørgensen, M.; Norrman, K.; Gevorgyan, S. A.; Tromholt, T.; Andreasen, B.; Krebs, F. C. *Adv. Mater.* **2012**, 24, 580.

(11) Sommer, M.; Huettner, S.; Thelakkat, M. *J. Mater. Chem.* **2010**, 20, 10788.

(12) Topham, P. D.; Parnell, A. J.; Hiorns, R. C. *J. Polym. Sci., Part B: Polym. Phys.* **2011**, 49, 1131.

(13) Miyanishi, S.; Zhang, Y.; Tajima, K.; Hashimoto, K. *Chem. Commun.* **2010**, 46, 6723.

(14) Chan, S.-H.; Lai, C.-S.; Chen, H.-L.; Ting, C.; Chen, C.-P. *Macromolecules* **2011**, 44, 8886.

(15) Botiz, I.; Schaller, R. D.; Verduzco, R.; Darling, S. B. *J. Phys. Chem. C* **2011**, 115, 9260.

(16) Verduzco, R.; Botiz, I.; Pickel, D. L.; Michael Kilbey II, S.; Hong, K.; Dimasi, E.; Darling, S. B. *Macromolecules* **2011**, 44, 530.

(17) Ramos, A. M.; Rispens, M. T.; van Duren, J. K. J.; Hummelen, J. C.; Janssen, R. A. J. *J. Am. Chem. Soc.* **2001**, 123, 6714.

(18) Tan, Z.; Hou, J.; He, Y.; Zhou, E.; Yang, C.; Li, Y. *Macromolecules* **2007**, 40, 1868.

(19) Chan, S.-H.; Chen, C.-P.; Chao, T.-C.; Ting, C.; Lin, C.-S.; Ko, B.-T. *Macromolecules* **2008**, 41, 5519.

(20) Zhang, F.; Svensson, M.; Andersson, M. R.; Maggini, M.; Bucella, S.; Menna, E.; Inganäs, O. *Adv. Mater.* **2001**, 13, 1871.

(21) Li, M.; Xu, P.; Yang, J.; Yang, S. *J. Mater. Chem.* **2010**, 20, 3953.

(22) Yao, K.; Chen, L.; Li, F.; Wang, P.; Chen, Y. *J. Phys. Chem. C* **2012**, 116, 714.

(23) Lin, Y.; Lim, J. A.; Wei, Q.; Mannsfeld, S. C. B.; Briseno, A. L.; Watkins, J. J. *Chem. Mater.* **2012**, 24, 622.

(24) Lai, Y.-C.; Ohshimizu, K.; Takahashi, A.; Hsu, J.-C.; Higashihara, T.; Ueda, M.; Chen, W.-C. *J. Polym. Sci., Part A: Polym. Chem.* **2011**, 49, 2577.

(25) Steed, J. S.; Atwood, J. L. *Supramolecular Chemistry, 2nd Ed.*; John Wiley & Sons, Ltd.: West Sussex, United Kingdom, **2009**.

(26) Uzun, O.; Sanyal, A.; Nakade, H.; Thibault, R. J.; Rotello, V. M. *J. Am. Chem. Soc.* **2004**, 126, 14773.

(27) Uzun, O.; Frankamp, B. L.; Sanyal, A.; Rotello, V. M. *Chem. Mater.* **2006**, 18, 5404.

(28) Iovu, M. C.; Sheina, E. E.; Gil, R. R.; McCullough, R. D. *Macromolecules* **2005**, 38, 8649.

(29) Chen, S. A.; Ni, J. M. *Macromolecules* **1992**, 25, 6081.

(30) Hugger, S.; Thomann, R.; Heinzel, T.; Thurn-Albrecht, T. *Colloid Polym. Sci.* **2004**, 282, 932.

(31) Roehling, J. D.; Arslan, I.; Moule, A. J. *J. Mater. Chem.* **2012**, 22, 2498.

(32) Carano, M.; Da Ros, T.; Fanti, M.; Kordatos, K.; Marcaccio, M.; Paolucci, F.; Prato, M.; Roffia, S.; Zerbetto, F. *J. Am. Chem. Soc.* **2003**, 125, 7139.

(33) Ren, B.-Y.; Ou, C. J.; Zhang, C.; Chang, Y.-Z.; Yi, M.-D.; Liu, J.-Q.; Xie, L.-H.; Zhang, G.-W.; Deng, X.-Y.; Li, S.-B.; Wei, W.; Huang, W. *J. Phys. Chem. C* **2012**, 116, 8881.

(34) Hynes, M. J. *J. Chem. Soc. Dalton Trans.* **1993**, 311.

(35) Emge, A.; Bäuerle, P. *Synt. Met.* **1999**, 102, 1370.

(36) Tang, H.; Radosz, M.; Shen, Y. *J. Polym. Sci., Part A: Polym. Chem.* **2006**, 44, 6607.

(37) Carroll, J. B.; Cooke, G.; Garety, J. F.; Jordan, B., J.; Mabruk, S.; Rotello, V. M. *Chem. Commun.* **2005**, 3838.

(38) We have also performed variable concentration UV-Vis absorption measurements on **P4**. No significant change was found in absorption maxima and spectral line-shape,

and a linear relation between absorbance and concentration were observed. This indicates **P4** does not show aggregation behavior under these dilute conditions as applied in fluorescence quenching measurements.

(39) Neuteboom, E. E.; Beckers, E. H. A.; Meskers, S. C. J.; Meijer, E. W.; Janssen, R. A. J. *Org. Biomol. Chem.* **2003**, 1, 198.

(40) Dang, M. T.; Hirsch, L.; Wantz, G. *Adv. Mater.* **2011**, 23, 3597.

(41) Cheng, Y.-J.; Yang, S.-H.; Hsu, C.-S. *Chem. Rev.* **2009**, 109, 5868.

(42) Sivula, K.; Ball, Z. T.; Watanabe, N.; Fréchet, J. M. J. *Adv. Mater.* **2006**, 18, 206.

(43) Locke, J. R.; McNeill, A. J. *Macromolecules* **2010**, 43, 8709.

(44) Zhang, Y.; Tajima, K.; Hirota, K.; Hashimoto, K. *J. Am. Chem. Soc.* **2008**, 130, 7812.

(45) Miyakoshi, R.; Yokoyama, A.; Yokozawa, T. *J. Am. Chem. Soc.* **2005**, 127, 12542.

(46) Yokoyama, A.; Miyakoshi, R.; Yokozawa, T. *Macromolecules* **2004**, 37, 1169.

(47) Nam, C.-Y.; Qin, Y.; Park, Y. S.; Hlaing, H.; Lu, X.; Ocko, B. M.; Black, C. T.; Grubbs, R. B. *Macromolecules* **2012**, 45, 2338.

(48) Iqbal, P.; Critchley, K.; Atwood, D.; Tunnicliffe, D.; Evans, S. D.; Preece, J. A. *Langmuir* **2008**, 24, 13969.

(49) Kim, O.-K.; Je, J.; Melinger, J. S. *J. Am. Chem. Soc.* **2006**, 128, 4532.

(50) Atilgan, S.; Ozdemir, T.; Akkaya, E. U. *Org. Lett.* **2010**, 12, 4792.

(51) Wang, B.; Wang, M.; Zhang, H.; Sobal, N. S.; Tong, W.; Gao, C.; Wang, Y.; Giersig, M.; D., W.; Mohwald, H. *Phys. Chem. Chem. Phys.* **2007**, 9, 6313.

(52) Maggini, M.; Scorrano, G.; Prato, M. *J. Am. Chem. Soc.* **1993**, 115, 9798.

(53) D'Souza, F.; Maligaspe, E.; Zandler, M. E.; Subbaiyan, N. K.; Ohkubo, K.; Fukuzumi, S. *J. Am. Chem. Soc.* **2008**, 130, 16959.

(54) Lee, E.; Hammer, B.; Kim, J.-K.; Page, Z.; Emrick, T.; Hayward, R. C. *J. Am. Chem. Soc.* **2011**, 133, 10390.

(55) Wu, P.-T.; Xin, H.; Kim, F. S.; Ren, G.; Jenekhe, S. A. *Macromolecules* **2009**, 42, 8817.

(56) Ohshimizu, K.; Ueda, M. *Macromolecules* **2008**, 41, 5289.

(57) Jeffries-EL, M.; Sauve, G.; McCullough, R. D. *Adv. Mater.* **2004**, 16, 1017.

# Chapter 3

# Complementary Hydrogen Bonding and Block Copolymer Self-Assembly in Cooperation toward Stable Solar Cells with Tunable Morphologies

(Reproduced with permission from

*Macromolecules*, **2013**, 46, 9021–9031



The other coauthors, Kevin G. Yager, Noel M. Dawson, Jianzhong Yang and Kevin J. Malloy are acknowledged.

Supporting information of the publication is incorporated into this chapter)

## 3.1 Introduction

In Chapter 2, we initially reported the preparation of a polythiophene BCP selectively functionalized with diaminopyrimidine moieties (**P4**) and a thymine tethered fullerene derivative (**F1**).[1] We found that the thermal stability of benchmark P3HT/PCBM BHI solar devices employing **P4**/**F1** as compatilizers was significantly improved through the "three-point" complementary hydrogen bonding interactions between diaminopyrimidine and thymine moieties. More interestingly, BHJ morphologies can be systematically adjusted by simply varying the blend ratio of BCPs to fullerene derivatives. However, the overall device efficiencies were still quite low

compared with benchmark poly(3-hexylthiophene) (P3HT)/phenyl-C61-butyric acid methyl ester (PCBM) BHJ devices.

We suspected that the low device performance was caused by non-optimal block length ratio in the BCP. The block length ratio between functionalized and unfunctionalized blocks was ca. 1/2; and such high functionality led to either discrete micron-sized aggregates when the BCP was fully complexed with the fullerene derivative or smooth morphology but unbalanced charge transport when much less fullerenes were applied. Additionally, the functionalized pyrrolidine fullerene was not an ideal electron acceptor for PSCs since previously reported analogous pyrrolidine fullerenes have all shown inferior performance in PSCs when compared with devices employing PCBM.[2-5]

In this chapter, we describe the synthesis of a new diblock polythiophene copolymer, **P8**, having a relatively shorter functionalized block carrying isoorotic acid moieties and a diaminopyridine tethered fullerene (**F2**) derived directly from PCBM. "Three-point" complementary hydrogen bonding interactions between these functionalities are studied in detail and a large solution binding constant was revealed. Solar cells employing these materials show not only comparable *PCE*s with standard P3HT/PCBM devices but also much enhanced stability and tunable active layer morphologies by simply varying polymer/fullerene weight ratios.

### 3.2 Synthesis and characterization

#### 3.2.1 Synthesis of polymers P5-P8

Synthesis of the 1-N-hexylisoorotic acid functionalized block copolymer (**P8**) and the PCBM analogue **F2** is shown in Scheme 1. $^{1}$H NMR spectra and size exclusion chromatography (SEC) profiles of the polymers are shown in Figure 3.1. The block copolymer synthesis was accomplished by following typical Grignard metathesis (GRIM).

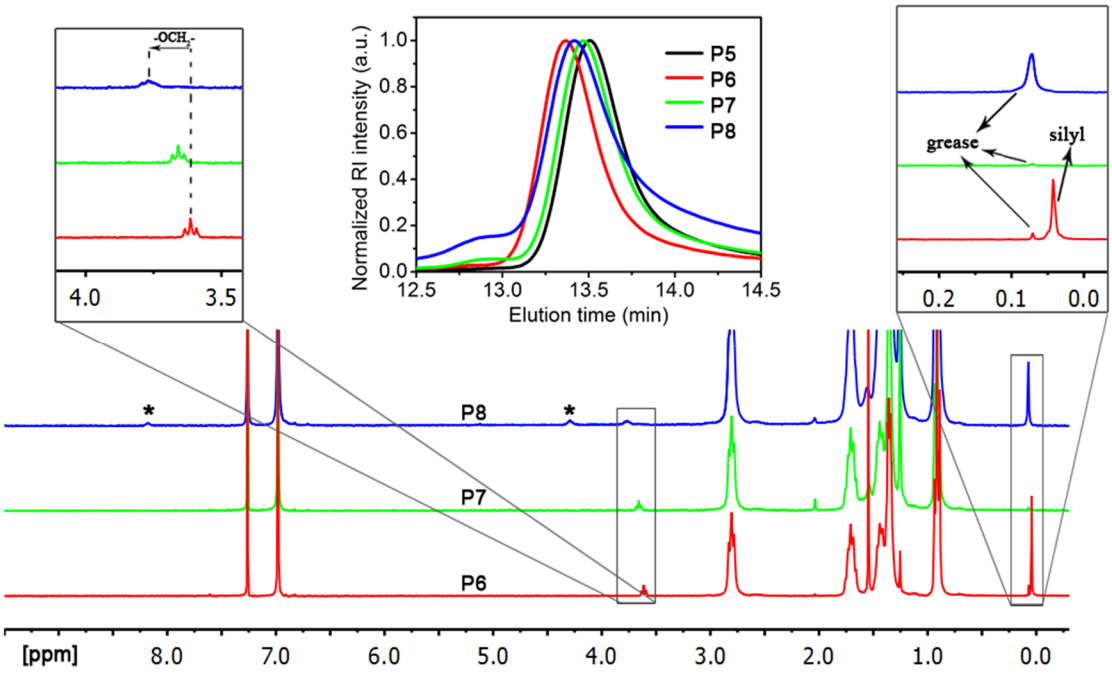


**Figure 3.1** $^{1}$H NMR spectra (300.13 MHz, $CDCl_3$) of **P6**, **P7**, and **P8**. Insert: size exclusion chromatography (SEC) traces of **P5** (black), **P6** (red), **P7** (green) and **P8** (blue). The peaks at 0.07 ppm in all spectra are due to grease involved in air-free operations.

**Scheme 3.1** Synthesis of polymers **P5-P8** and fullerene derivative **F2**

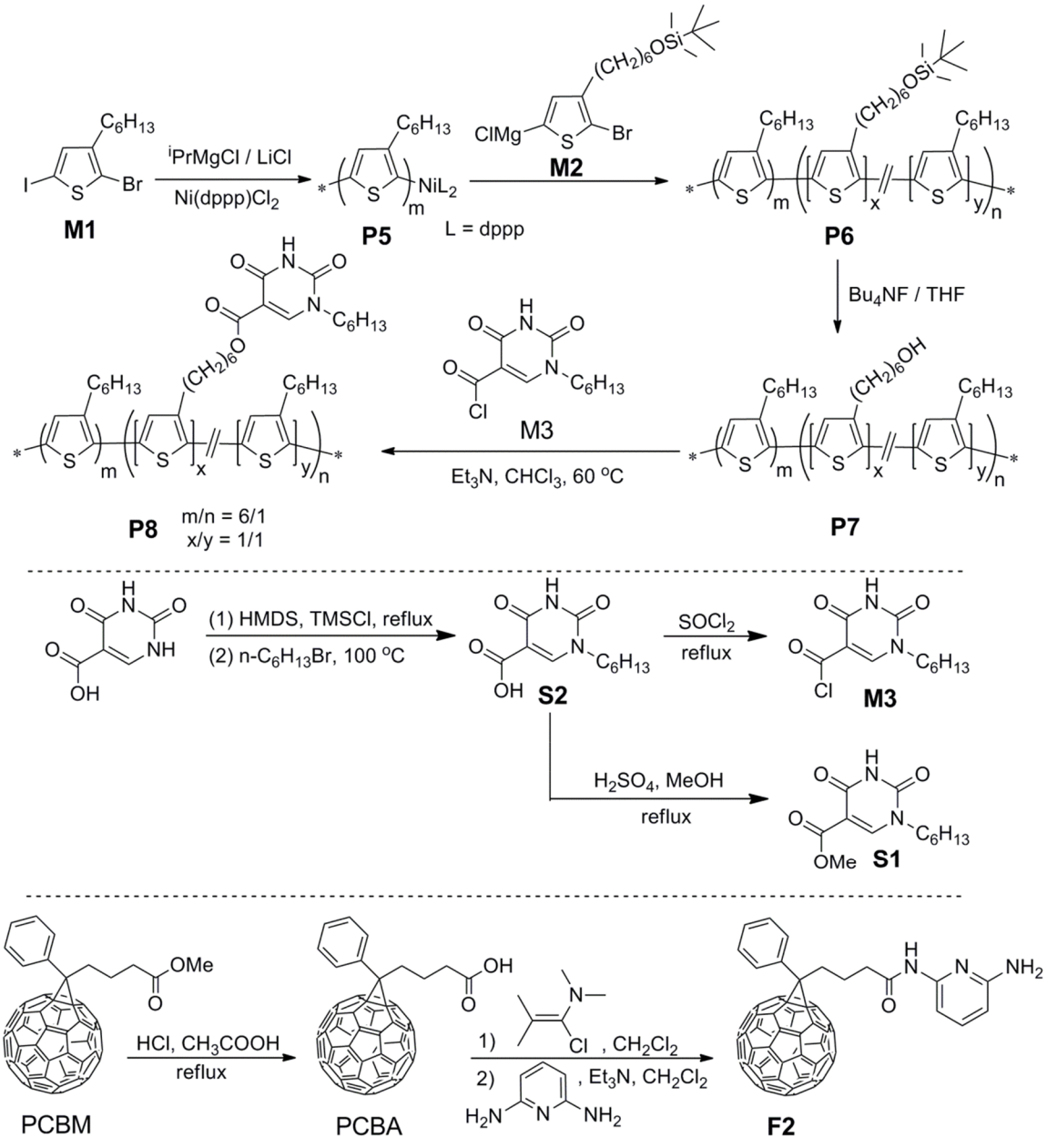

The **M1**/**M2** monomer feed ratio was set to be 10/1 during the synthesis of **P6**, and **M2** was added at a **M1** conversion of 90%. The 2nd block was thus expected to be a statistical copolymer composed of equal amount of **M1** and **M2**, and the overall block length ratio is calculated to be 4.5 to 1 assuming 100% conversion. Integration of methylene group signals at 3.61 ppm (-$OCH_2$-) and 2.80 ppm (Th-$CH_2$-) in the $^1$H NMR spectrum of **P6** gave a functionalization percentage to be ca. 7%, corresponding to ca. 75% conversion of **M2** during the chain-extension step, from which a block length ratio of ca. 6:1 was calculated. Molecular weights of **P5** ($M_n$ = 35,300, *PDI* = 1.2) and **P6** ($M_n$ = 42,700, *PDI* = 1.2) obtained from SEC analysis gave a functional group concentration of ca. 6.5% and a block length ratio of ca. 6.6 to 1, matching closely with the NMR calculation results. SEC traces of both **P5** and **P6** have symmetrical shapes and narrow polydispersities (PDIs) as shown in Figure 3.1. The lack of low molecular weight shoulder in the SEC profile of **P6** indicates quantitative chain extension of **P5** and the formation of block copolymers in the absence of homopolymers.

Removal of the *tert*-butyldimethylsilyl (TBDMS) protecting groups on **P6** with tetrabutylammonium fluoride (TBAF) afforded the hydroxyl functionalized BCP **P7**. Complete shift of the methylene group $^1$H NMR signal from 3.61 ppm in **P6** to 3.66 ppm in **P7**, together with the disappearance of silyl methyl signals at 0.89 ppm and 0.04 ppm, confirmed quantitative chemical transformation. Molecular weight of **P7** was decreased a little more than expected accompanied by slight broadening ($M_n$ = 35,900, *PDI* = 1.3, Figure 3.1), presumably due to column interactions with the polar hydroxyl groups in **P7**. Finally, **P8** was obtained smoothly through esterification of **P7** with **M3** that was

conveniently prepared from commercial isoorotic acid as shown in Scheme 3.1. Quantitative transformation was confirmed by the downfield shift of the methylene $^1$H NMR signal to 3.77 ppm from 3.66 ppm in **P7** and the appearance of new peaks at 8.20 ppm (-NH) and 4.29 ppm (-$NCH_2$-), as well as by integration giving a consistent 7% functionality.

### 3.2.2 Influence of hydrogen bonding interactions on molecular weight of P8

The SEC profile of **P8** was significantly broadened and gave a lower than expected molecular weight ($M_n$ = 27,200, *PDI* = 1.6). We suspected that this could be caused by interactions between **P8** and the column materials. To test this hypothesis, **P8** was subjected to SEC analysis at 50 ºC (Figure 3.2) and it indeed showed increased molecular weight and narrower distribution ($M_n$ = 32,100, *PDI* = 1.5).

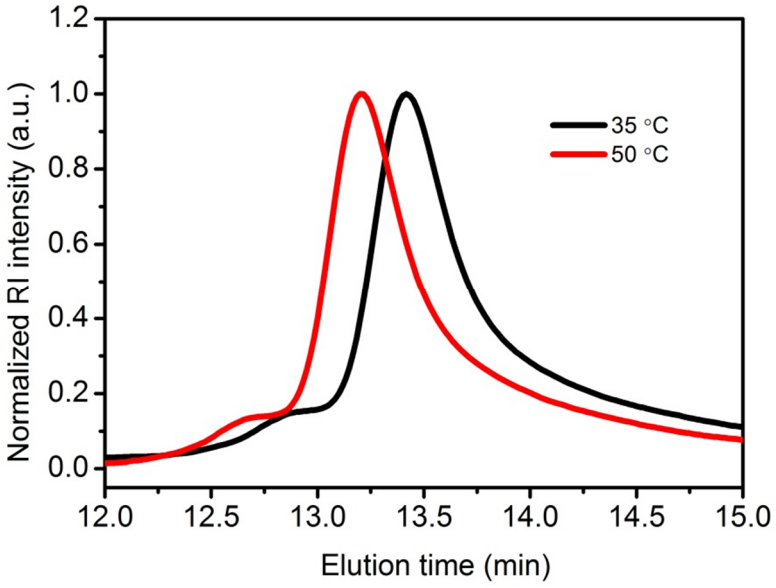


**Figure 3.2** Size exclusion chromatography (SEC) traces of block copolymer **P8** at different temperatures ($CHCl_3$, 1 mL/min, RI).

### 3.2.3 UV-vis spectroscopy and XRD measurements

In order to investigate the influence of post polymerization modification on the electronic and solid-state properties of polythiophenes, as-cast thin films of **P8** and P3HT (synthesized in-house, $M_n$ = 31,200, *PDI* = 1.04, SEC) were first subjected to UV-Vis absorption and X-ray diffraction (XRD) measurements. As shown in Figure 3.3a, absorption profile of **P8** resembles that of regio-regular P3HT but showed less pronounced vibronic structures, indicating relatively lower degree of crystallinity, which is also reflected from the XRD measurements as the (200) reflection peak is less resolved in the film of **P8** (Figure3.3b). From the absorption edge, a bandgap of 1.9 eV was estimated for both **P8** and P3HT, in good agreement with reported values.[6]

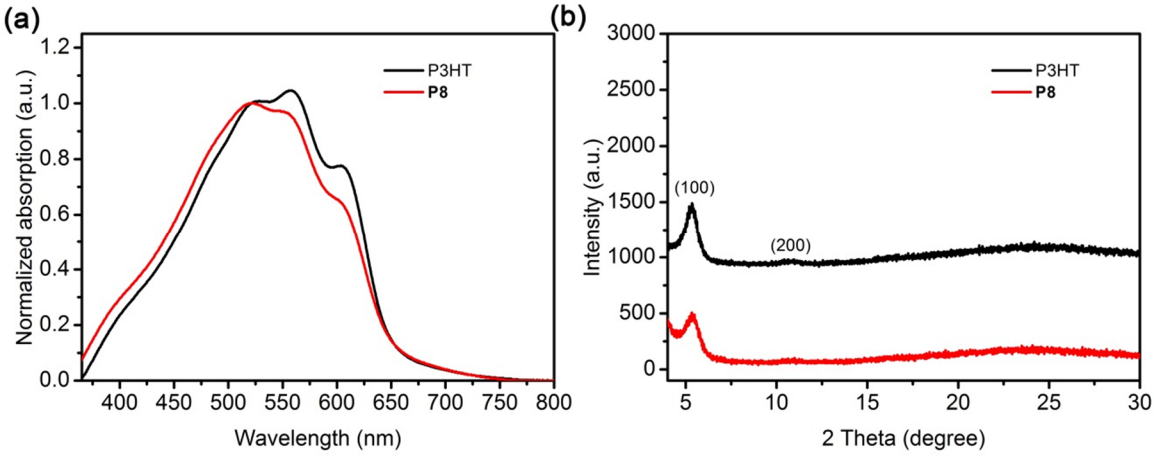


**Figure 3.3** UV-Vis absorption spectra (a) and out-of-plane X-ray diffraction profiles (b) of **P8** and P3HT thin films spin-cast from 10 mg/mL chlorobenzene solutions onto ITO glass slides at 400 rpm for 30 s.

### 3.2.4 HOMO level measurement of P8 via cyclic voltammetry

Cyclic voltammetry (CV) measurements on **P8** films revealed a quasi-reversible oxidation having an onset at +0.1 V (vs. $Fc/Fc^+$ redox couple) as shown in Figure 3.4. A HOMO level of −4.9 eV was calculated, consistent with previously reported values of P3HT.[7] These observations suggest that attachment of 1-N-hexylisoorotic acid moieties onto the side-chains of **P8** has minimum impact on electronic properties of the main-chain of the conjugated polymer. Moreover, the HOMO level value of **P8** is identicial with what we measured for polymer **P4** in Chapter 2, suggesting the postpolymerization reaction to install the pendant functional groups does not alter the HOMO level of the polymer.

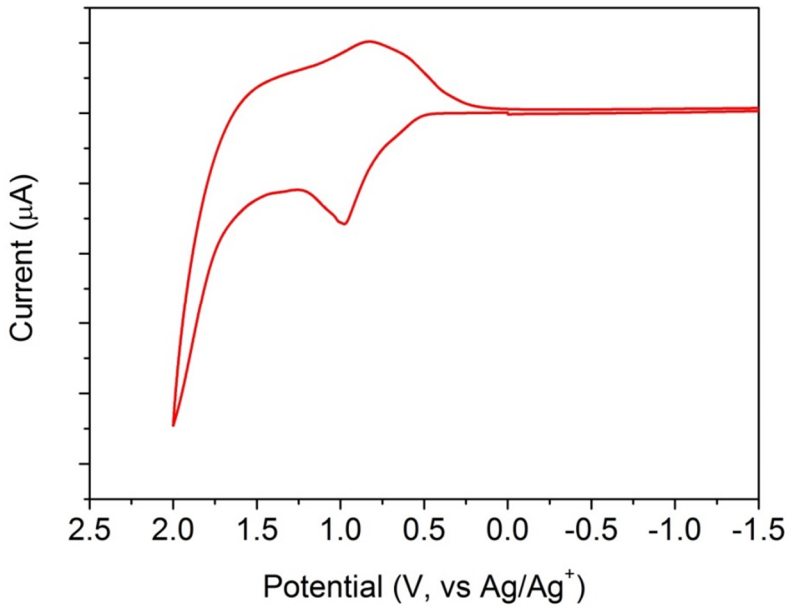


**Figure 3.4** Cyclic voltammogram of **P8** thin film drop-coated on the glassy carbon working electrode (0.1 M $Bu_4NPF_6$ in $CH_3CN$, 100 mV/s, referenced externally to $Fc/Fc^+$ redox couple).

### 3.2.5 Synthesis and characterization of fullerene derivative F2

As shown in Scheme 3.1, the synthesis of [6, 6]-Phenyl-C61-butyric acid N-(6-aminopyridin-2-yl) amide (**F2**) was straightforward. Hydrolysis of PCBM under acidic condition in dichlorobenzene yielded quantitatively the intermediate PCBA, which was then converted to its corresponding acid chloride using a mild chlorination reagent,[8] 1-chloro-N,N-2-trimethylprop-1-en-1-amine. Coupling of the fullerene acid chloride in-situ with 2,6-diaminopyridine gave rise to the final product **F2** in high yields. $^{1}$H NMR and high resolution mass spectrometry (HRMS) unambiguously confirmed its structure. Electronic properties of **F2** are very similar to those of PCBM.

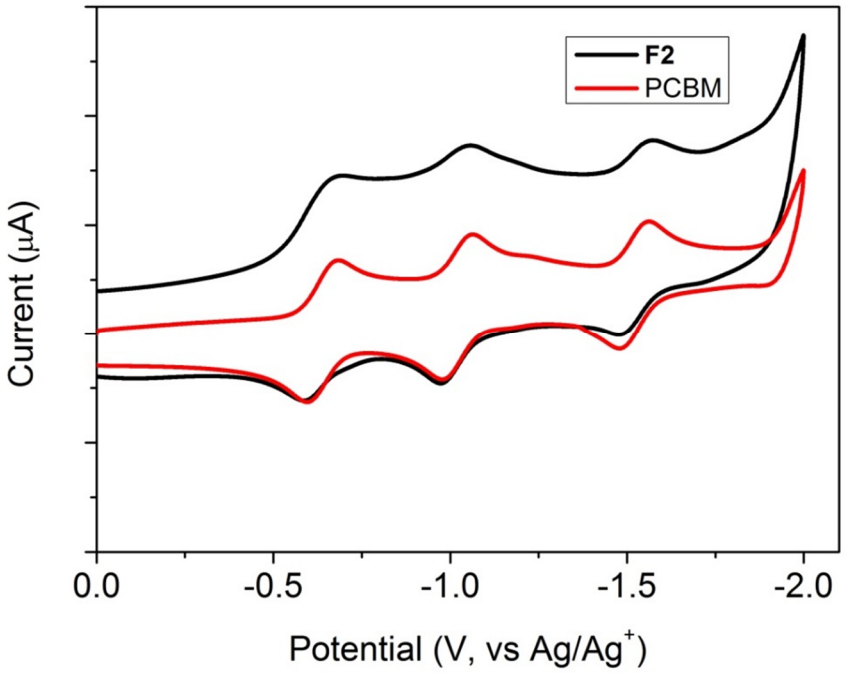


**Figure 3.5** Cyclic voltammograms of PCBM and **F2** in mixed solutions of ortho-dichlorobenzene/acetonitrile (5:1, v/v) containing 0.1 M $Bu_4NPF_6$ as supporting electrolytes (100 mV/s, referenced externally to $Fc/Fc^+$ redox couple).

Three quasi-reversible reduction peaks at identical voltages were observed for both compounds in solution CV measurements (Figure 3.5). From onsets of the first reduction waves, a LUMO energy level of −3.7 eV was calculated for both **F2** and PCBM, which is consistent with the literature reported value.[9,10]

### 3.3 Hydrogen bonding studies

#### 3.3.1 Fluorescent quenching titrations

The "three-point" complementary hydrogen bonding interactions between **P8** and **F2** were studied by fluorescence titration experiments as shown in Figure 3.6a. For comparison, titration experiments with P3HT, which is not capable of hydrogen bonding with **F2**, were carried out under identical conditions (Figure 3.6b).

With gradual addition of **F2** up to 2 equivalents (relative to total number of repeating units of polymers), about 26% fluorescence intensity of **P8** ($10^{-5}$ M in chlorobenzene) was quenched, while the decrease of fluorescence intensity in P3HT ($10^{-5}$ M in chlorobenzene) was less than 7%. Interestingly, the quenching behavior of **P8** showed a two-step transition as seen in the Stern-Volmer plot (insert, Figure 3.6a). A sharp rise with a large Stern-Volmer constant ($K_{SV}$) of $1.6\times10^{5}$ $M^{-1}$ was initially observed for **P8** with the addition of up to 0.07 eq. **F2**, the amount needed to fully complex all the hydrogen bonding sites in **P8**. Further addition of **F2** up to 2 eq. showed a very similar quenching behavior as that of P3HT, both of which gave straight Stern-Volmer plots with similar quenching constants of $7\times10^{3}$ $M^{-1}$ and $3.8\times10^{3}$ $M^{-1}$, respectively. These

observations suggest strong binding between **P8** and **F2** in chlorobenzene at room temperature.

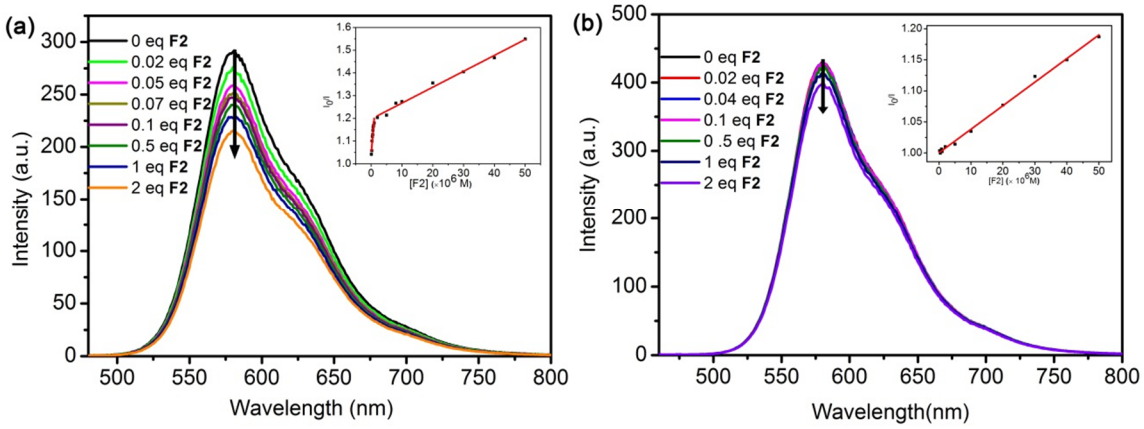


**Figure 3.6** Fluorescence quenching measurements on **P8** (a) and P3HT (b) in chlorobenzene ($10^{-5}$ M) excited at 458 nm with gradual addition of **F2** ($1 \times 10^{-4}$ M for the first 0.07 eq, and $5 \times 10^{-4}$ M thereafter). The concentrations of polymers and equivalents of **F2** are calculated based on total number of repeating units in corresponding polymers. The inserts are Stern-Volmer plots and linear fits for calculations of quenching constants. A few inside and later points in the fluorescence quenching graphs for **P8** are omitted for clarity.

### 3.3.2 $^1$H NMR titrations

In order to quantify the strength of such "three-point" hydrogen bonding, we carried out $^1$H NMR titration experiments between **F2** and a small molecule model compound **S1** (Scheme 3.1) in $CDCl_3$ (Figure 3.7). The small molecule model compound **S1** was used instead of **P8** in order to avoid complications commonly associated with polymers, including neighboring group effects and difficulties of preparing solutions of

high polymer concentrations. As seen in the $^{1}$H NMR spectra (Figure 3.8), signals of the amide proton (7.92 ppm) and amine protons (4.26 ppm) of **F2** gradually shift downfield with additions of **S1** up to 10 equivalents. A binding constant of 273 ± 3.78 $M^{-1}$ was obtained by fitting the amide-H chemical shifts vs. **S1** equivalents using WinEQNMR program (Version 1.10)[11]. This value is consistent with previous reports on binding constants between similar diaminopyrimidine and uracil/thymine derivatives.[12-14]

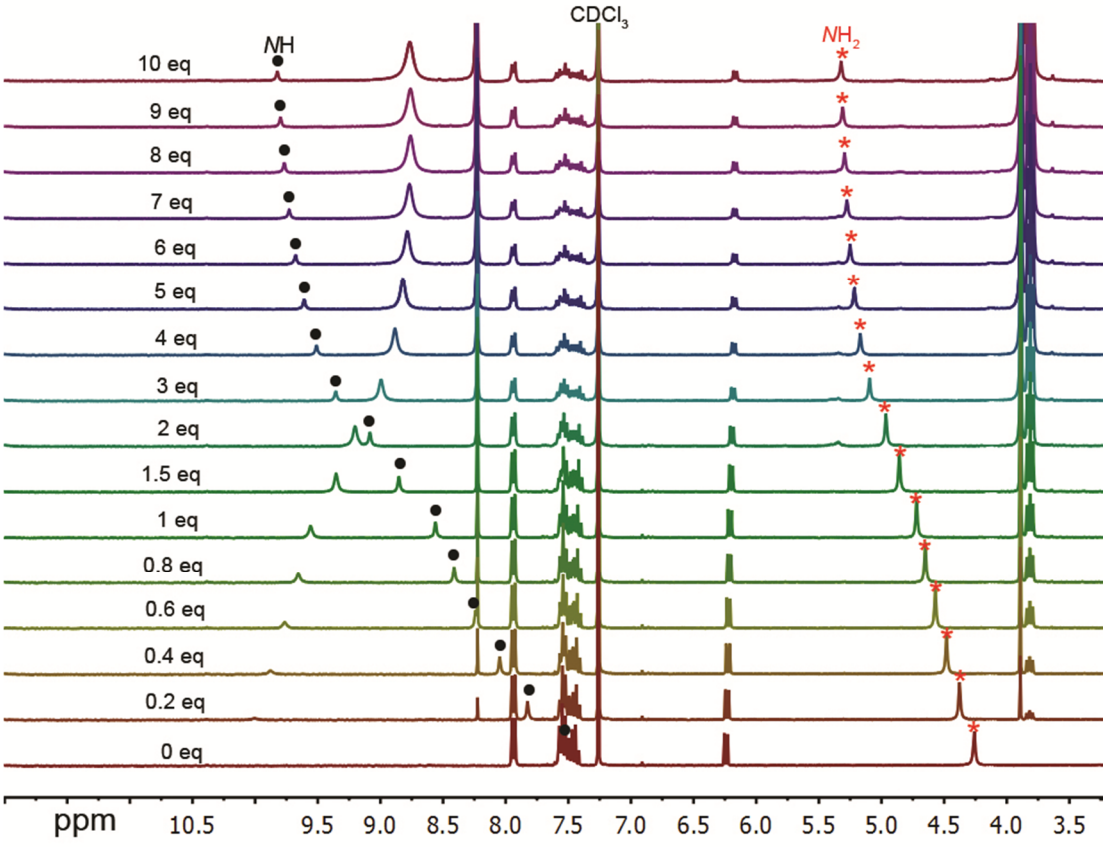


**Figure 3.7** $^{1}$H NMR spectra ($CDCl_3$, 300.13 MHz) of **F2** (4 mM) titrated by model compound **S1** (0.2 M in $CDCl_3$). Solution volume was assumed constant throughout the titration range in the experiment. Black dot: shift of amide proton; red star: shift of amine proton of **F2**.

### 3.4 DSC measurements

DSC measurements were performed on **P8**, **F2** and their blends in order to probe the effects of complementary hydrogen bonding on their thermal properties in solid state as shown in Figure 3.8.

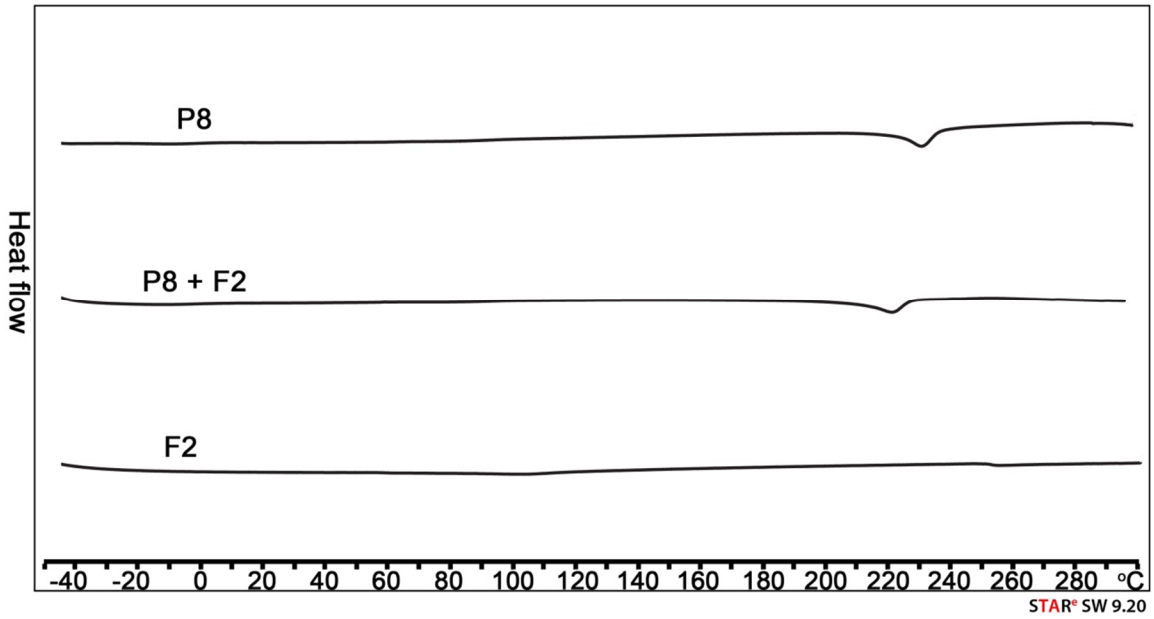


**Figure 3.8** Differential scanning calorimetry (DSC) plots of **P8**, **F2** and their blends with ca. 10 mg sample and a scanning rate of 10 °C/min (second heating curve; exotherm up).

All samples (ca. 10 mg) were subjected to identical heating and cooling sequences (−50 °C to 300 °C, 10 °C/min); blends were obtained by dissolving polymers and fullerene in a 1:1 molar ratio followed by extensive drying. The second heating curves are shown in Figure 3.8. No melting point could be observed for **F2**, presumably due to "two-point" self-complementary hydrogen bonding between the diaminopyridine moieties. **P8** showed a melting point at 222 ºC, slightly smaller than that of P3HT at ca.

230 °C, which was decreased to 212 ºC when the polymer was mixed with **F2**. Disruption of self-complementary hydrogen bonding interactions in **P8**, crystalline domain size reduction upon **F2** complexation and lack of macro-phase separation are likely causes of the observed melting point suppression.

### 3.5 Device performance and active layer morphologies correlations

#### 3.5.1 Solar devices performances and thermal stability evaluation

Our methodologies are specifically designed in aim at tuning active layer morphologies, by simply varying polymer to fullerene weight ratios, to be optimal for device performance and at the same time more thermally robust. To testify our concepts, we have fabricated organic solar cells employing **P8** with **F2** and PCBM at different weight ratios. A reference P3HT/PCBM (10/8, wt./wt.) cell was also fabricated (*PCE* = 3.56%, $J_{SC}$ = 11.25 mA/cm$^{-2}$, $V_{OC}$ = 0.56 V and *FF* = 0.57).

All devices adopt conventional structures, *i.e.* ITO/$MoO_3$ (10 nm)/active layer (ca. 100 nm)/Al (100 nm), which were constructed under identical conditions. Devices were optimized by thermal annealing at different temperatures for various times, among which annealing at 150 °C for 15 min was found to maximize *PCE*s of all cells tested.[15] Aging tests were conducted by thermal annealing devices at 110 °C for pre-determined time intervals and after each interval, current-voltage (I-V) curves were measured and active layer morphologies were closely monitored by absorption spectroscopy, optical microscopy (OM), atomic force microscopy (AFM) and X-ray analyses.

Device performance data are summarized in Table 3.1, Figure 3.9 and 3.10, aging test results are shown in Figure 3.11 and 3.12, and morphology studies are depicted in Figure 3.13, 3.14, 3.15 and 3.16.

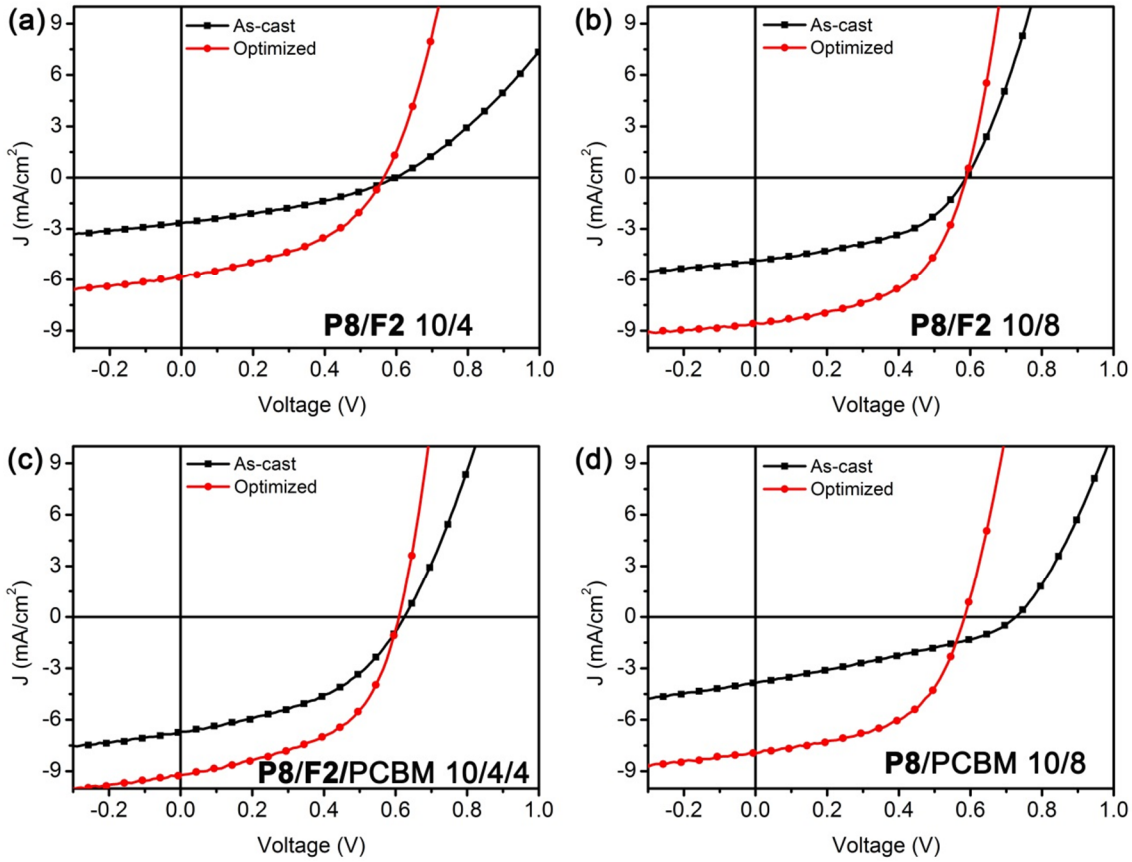


**Figure 3.9** I-V curves (under simulated AM1.5 G irradiation) of **P8** blended with PCBM and **F2** at various weight ratios. All devices were optimized by annealing at 150 ºC for 15 min.

We started out with devices using **P8** and **F2** at a weight ratio of 10/4, corresponding approximately to a 1/1 molar ratio between the complementary hydrogen bonding units on each component. Unannealed devices showed low *PCE*s mostly limited

by small short circuit current ($J_{SC}$) and fill factor (*FF*), which were significantly improved through thermal annealing.

**Table 3.1** PV performance of **P8** blended with **F2** and PCBM at different weight ratios.[a]

| Condition | **P8**/**F2**/PCBM[b] | *PCE* (%)[c] | $J_{SC}$ (mA/cm$^{-2}$)[c] | $V_{OC}$ (V)[c] | *FF*[c] |
|---|---|---|---|---|---|
| As-cast | 10 : 4 : 0 | 0.53 ± 0.06 | 2.71 ± 0.28 | 0.58 ± 0.01 | 0.34 ± 0.01 |
| | 10 : 8 : 0 | 1.34 ± 0.12 | 5.20 ± 0.34 | 0.58 ± 0.02 | 0.44 ± 0.05 |
| | 10 : 4 : 4 | 1.86 ± 0.08 | 6.93 ± 0.15 | 0.63 ± 0.01 | 0.43 ± 0.02 |
| | 10 : 0 : 8[d] | 0.87 ± 0.12 | 3.75 ± 0.32 | 0.70 ± 0.01 | 0.33 ± 0.03 |
| Optimized[e] | 10 : 4 : 0 | 1.46 ± 0.01 | 6.02 ± 0.15 | 0.56 ± 0.01 | 0.44 ± 0.00 |
| | 10 : 8 : 0 | 2.65 ± 0.14 | 8.59 ± 0.26 | 0.59 ± 0.00 | 0.52 ± 0.01 |
| | 10 : 4 : 4 | 2.87 ± 0.01 | 9.25 ± 0.01 | 0.61 ± 0.00 | 0.51 ± 0.00 |
| | 10 : 0 : 8[d] | 2.36 ± 0.08 | 7.76 ± 0.26 | 0.59 ± 0.01 | 0.52 ± 0.01 |

[a] Spin-cast at 400 rpm for 30s from chlorobenzene solution, with 2 vol% MeOH added. [b]All ratios by weight. [c] Average of five cells. [d] No MeOH added. [e] Thermal annealing at 150 °C for 15 min.

Both **P8**/**F2** (10/4) and the reference P3HT/PCBM cells showed the worst thermal stability among tested devices with ca. 50% and 60% *PCE* reductions after annealing at 110 °C for 112 h, respectively (Figure 3.10). Performance degradation in the P3HT/PCBM device was mainly caused by decrease of the *FF* (Figure 3.10, green traces)

and S-shaped kinks around $V_{OC}$ in the I-V curves were clearly developed during the course of aging tests (Figure 3.11). Such phenomena indicate macro-phase separation and unbalanced charge transport as also evidenced by dense micron-sized PCBM crystallites from optical microscopy (Figure 3.12).

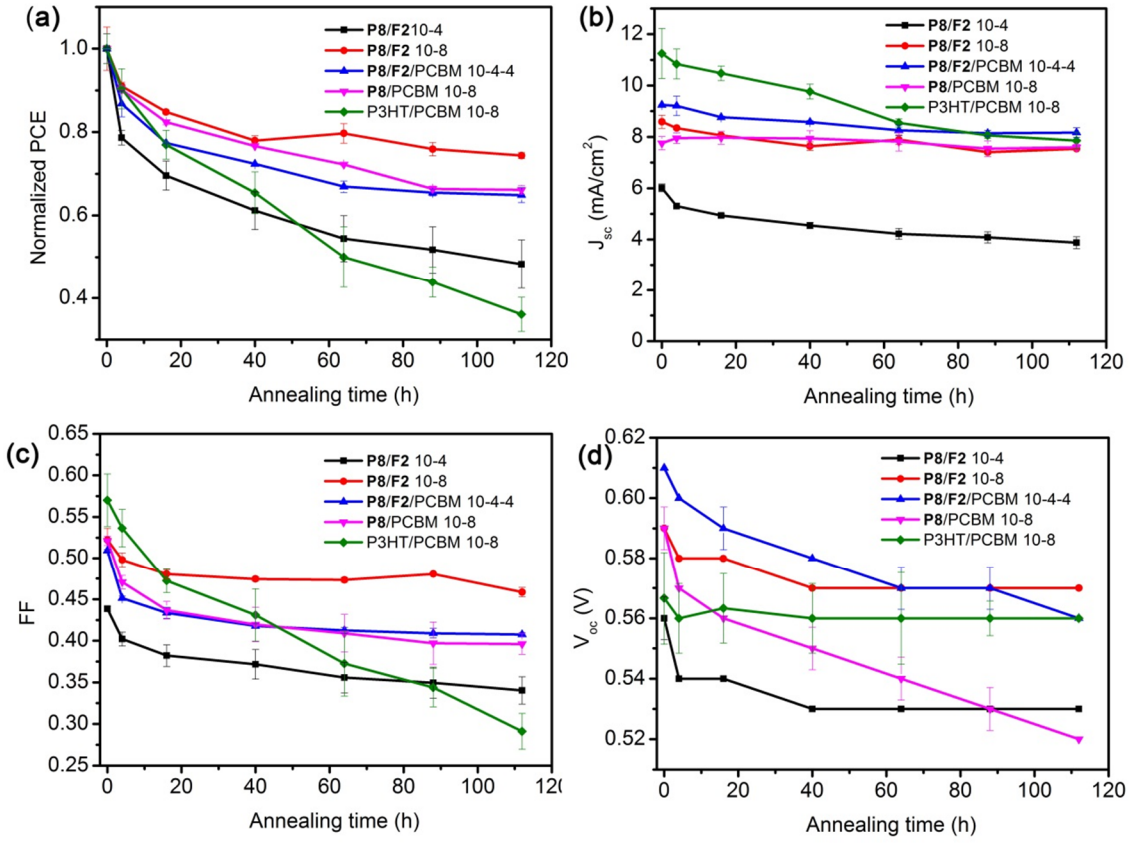


Thermal stability tests of devices employing **P8** with **F2** and PCBM at different weight ratios and a standard P3HT/PCBM BHJ device. Devices were annealed at 110 ºC under nitrogen for various times: (a) normalized *PCE* against annealing time; (b) $J_{SC}$ against annealing time; (c) *FF* against annealing time; (d) $V_{OC}$ against annealing time.

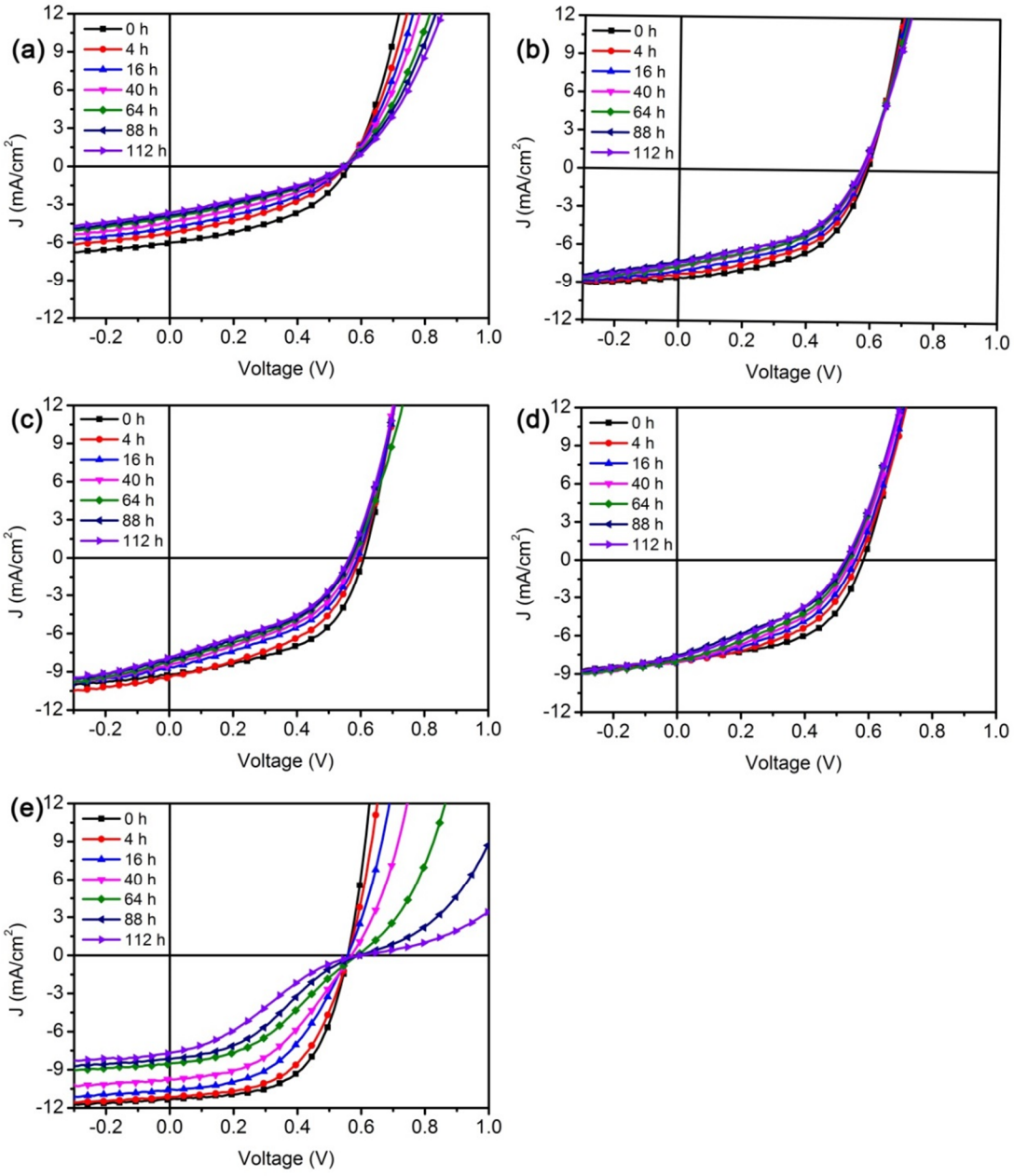


**Figure 3.10** I-V curves (under simulated AM1.5 G irradiation) of different devices measured after annealing at 110 °C for various times: (a) **P8**/**F2** (10:4); (b) **P8**/**F2** (10:8); (c) **P8**/**F2**/PCBM (10:4:4); (d) **P8**/PCBM (10:4); (e) P3HT/PCBM (10:8). All ratios by weight.

### 3.5.2 Morphological correlation with PV performance

#### 3.5.2.1 UV-vis, optical microscopy and AFM analyses

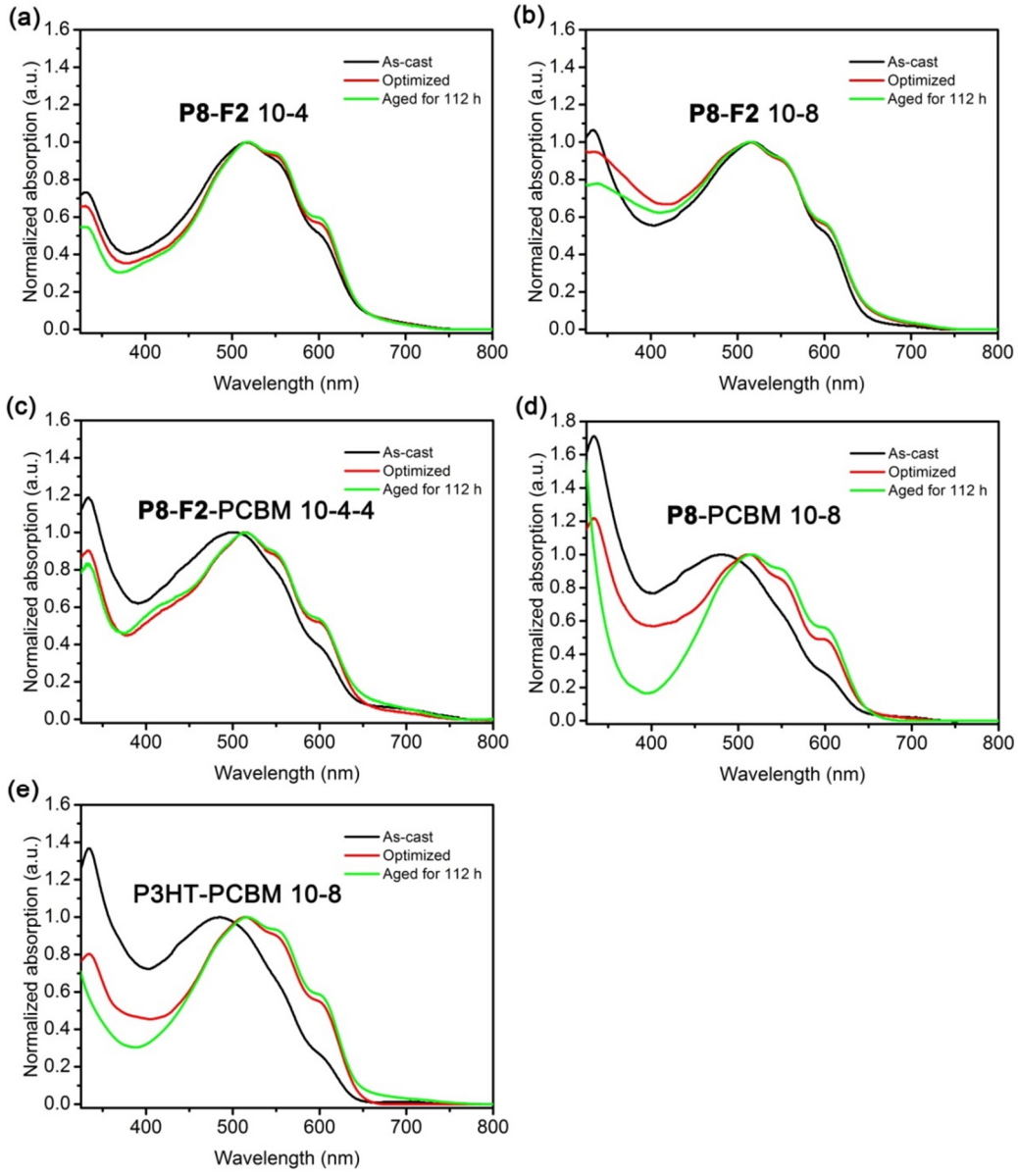


**Figure 3.11** UV-Vis absorption spectra of devices employing **P8** with **F2** and PCBM at different weight ratios (a to d), and a standard BHJ device of P3HT/PCBM (e) (black: as-cast; red: annealed at 150 °C for 15 min; green: aged at 110 °C for 112 h).

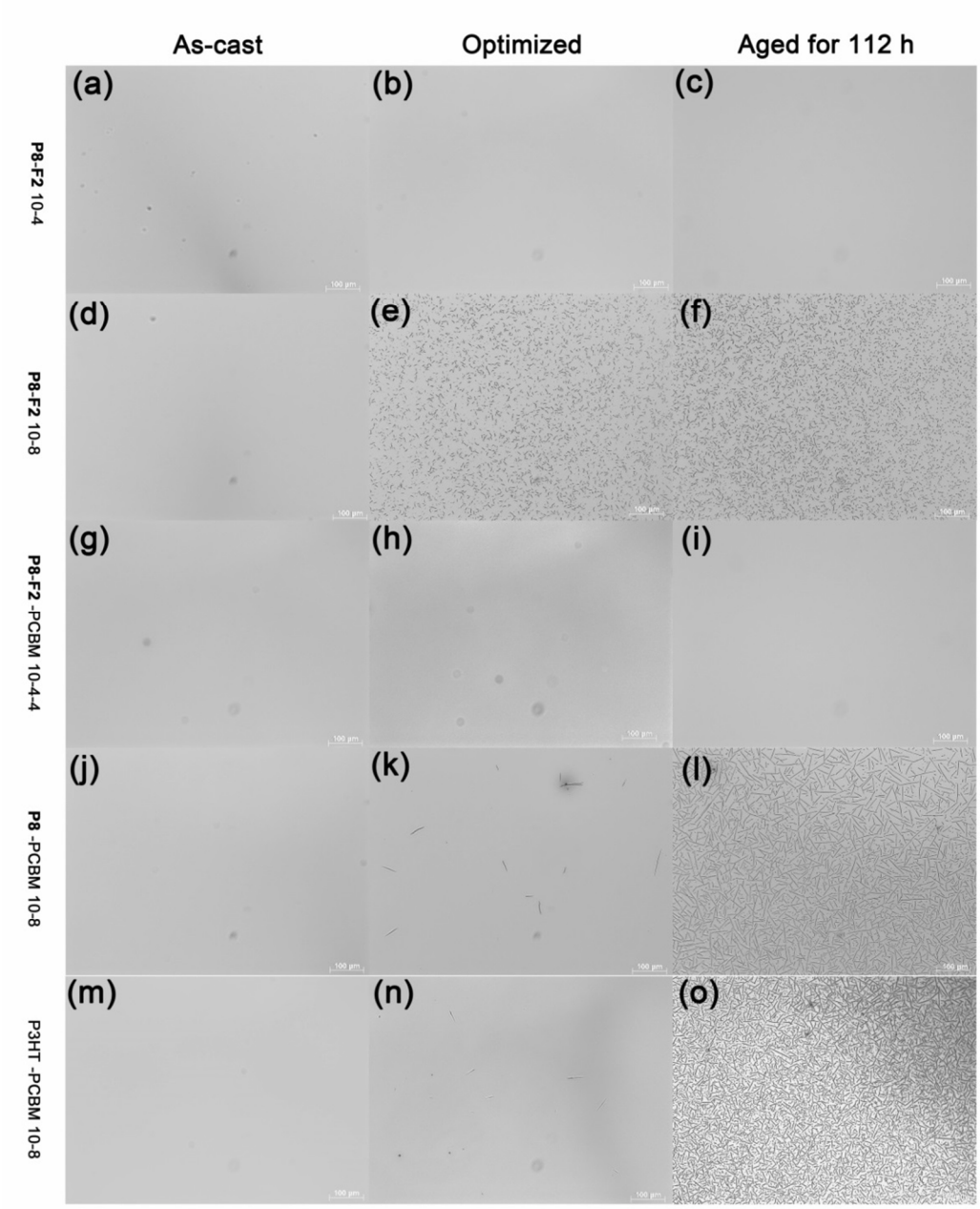


**Figure 3.12** Optical micrographs of devices empolying **P8** with **F2** and PCBM at different weight ratios (a to l), and a standard BHJ device of P3HT/PCBM (m to o) (left column: as-cast; middle column: annealed at 150 °C for 15 min; right column aged at 110 °C for 112 h). The scale bar is 100 μm.

UV-Vis absorption spectra (Figure 3.12e) revealed mostly amorphous P3HT chains in as-cast devices, which became more crystalline after optimization as vibronic peaks at ca. 550 nm and 600 nm were clearly discernable. Such structured absorption profiles became even more pronounced after aging tests, indicating more P3HT chains self-organized into domains of higher crystallinity.

AFM images (Figure 3.14) showed similar trend. Rough surface with isolated PCBM aggregates were observed in the as-cast device, which became smoother and bi-continuous after optimization. The film became even more flat after aging tests and only P3HT fibrils, absent of any PCBM aggregates could be observed in the phase image (micron-sized PCBM crystallites as seen in optical micrographs were intentionally avoided in all AFM measurements). The lack of specific interaction between P3HT and PCBM, as well as self-aggregation tendency of both materials, is responsible for the macro-phase separation and device instability. On the other hand, the **P8**/PCBM (10/4) device showed a *PCE* reduction resulted from decreases in all parameters (Figure 3.10). However, macro-phase separation is not likely the cause since very similar absorption profiles and AFM images, identical optical micrographs without any large aggregates and no S-shaped I-V curves were observed before and after aging tests. We suspect that the low performance and stability is caused by the relatively low fullerene contents in the device.

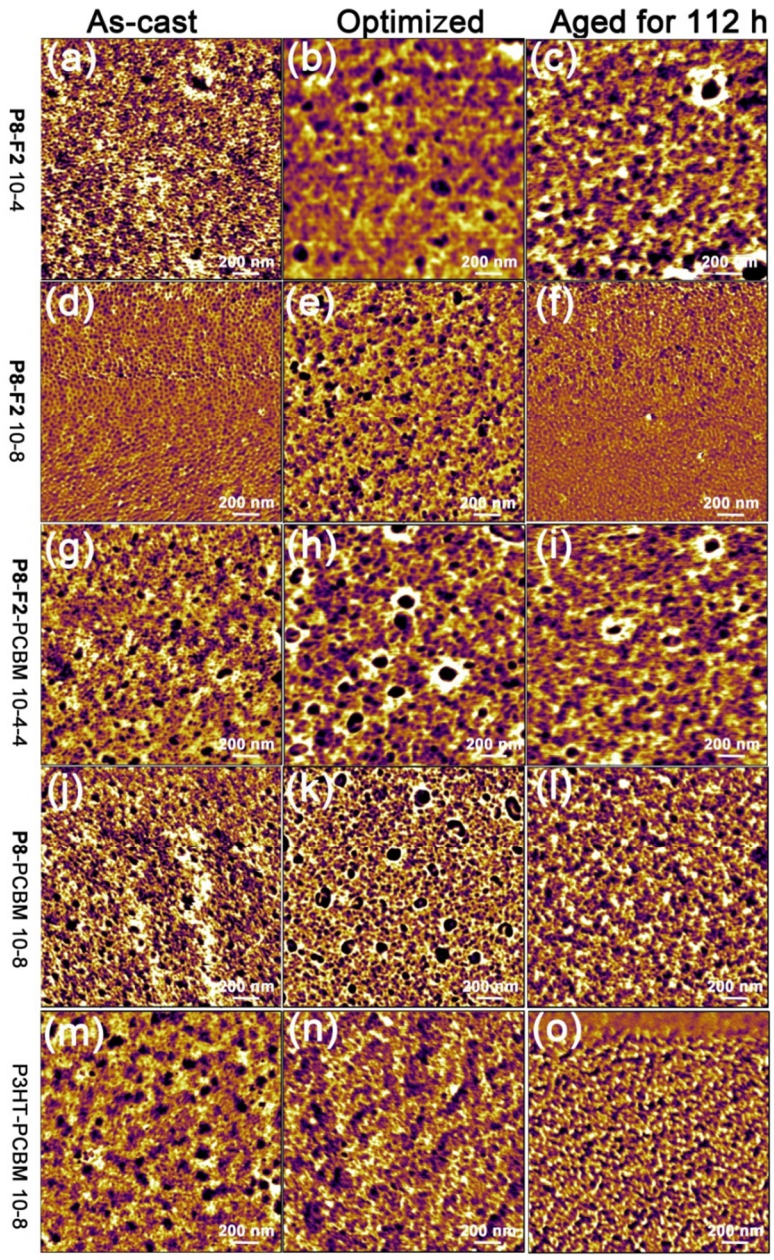


**Figure 3.13** Atomic force microscopy (AFM) phase images (2 μm × 2 μm) of devices employing **P8** with **F2** and PCBM at different weight ratios (a to l), and a standard BHJ device of P3HT/PCBM (m to o) (left column: as-cast; middle column: annealed at 150 °C for 15 min; right column aged at 110 °C for 112 h).

As seen in Figure 3.14, the as-cast film showed fibril like polymer chains lacking of any appreciable fullerene domains, which could potentially promote unwanted charge recombination and inefficient electron extraction. After optimization, coarser phase separation and larger **F2** aggregates could be observed, thus leading to enhanced device performance. This micro-phase separation could have continued during aging tests, and due to the low fullerene contents, connectivity between **F2** domains was partially lost by surrounding polymers. However, the strong "three-point" complementary hydrogen bonding interactions held **P8** and **F2** together and thus no macro-phase separation could be observed. In order to connect these isolated fullerene domains, a simple solution would be adding more fullerenes to bridge the gaps. We have thus fabricated devices with double the fullerene contents by adding either **F2** or PCBM.

Indeed, both **P8**/**F2** (10/8) and **P8**/**F2**/PCBM (10/4/4) devices showed significantly improved *PCE*s before and after optimization, the later of which performed slightly better mainly due to a larger $J_{SC}$. Interestingly, as-cast thin films of the **P8**/**F2** (10/8) devices showed somewhat ordered morphology (Figure 3.14d), in which fullerene-rich phase packed into arrays of dots or cylinders, ca. 20 nm in diameter, imbedded in fibril-like polymer matrices. After optimization, the order was lost and a coarser morphology was obtained as shown in the AFM images. Micron-sized **F2** crystallites were already obvious after optimization as shown in the optical micrograph.

Since only 40% **F2** (relative to **P8** by weight) was needed to fully complex isoorotic acid moieties on **P8**, the excess **F2** are capable of self-complementary hydrogen bonding interactions that presumably led to these large aggregates. Both optimized and

as-cast devices showed very similar structured absorption spectra, which was also seen in the **P8**/**F2** (10/4) devices but not in any other device containing PCBM (Figure 3.12). Less tendency of **F2** to be incorporated into P3HT crystalline domains due to the larger size and self-complementary hydrogen bonding is likely the cause for such observations.

The **P8**/**F2** (10/8) device showed the highest thermal stability among all tested systems with only 20% *PCE* reduction after aging tests. Denser **F2** crystallites were observed in the optical micrograph and the more pronounced vibronic peaks in the absorption spectrum indicate higher order in polymer chain packing. This is possibly due to aggregation of the excess **F2** into micron-sized crystallites leaving more free room for the polymer to self-organize, as confirmed by the AFM image after aging test, revealing a smooth film morphology without apparent **F2** nanocrystals (Figure 3.14f). Although large crystallites were formed, connectivity among **F2** domains must still be maintained since thermal aging did not seem to impact device performance significantly.

The **P8**/**F2**/PCBM (10/4/4) devices showed similar but slightly better *PCE*s than those of **P8**/**F2** (10/8) cells, before and after optimization, and slightly reduced thermal stability with ca. 70% performance retention after aging tests. Compared with as-cast films, the optimized films showed coarser morphologies and nano-aggregates of fullerenes (Figure 3.14h), accompanied by formation of more crystalline polymer domains (Figure 3.14c), which explains the efficiency enhancement upon optimization. Surprisingly, no apparent morphology changes could be observed after aging tests. Similar absorption spectrum and AFM images were obtained and no micron-sized fullerene crystallites could be discovered before and after aging tests. We ascribe this

lack of macro-phase separation behavior to strong fullerene aggregation tendency. PCBM and **F2** are structurally similar analogs and thus have strong interactions to co-crystalize or co-aggregate. Since half of these fullerene molecules, *i.e.* **F2**, are attached to one block of **P8** through strong complementary hydrogen bonding, as well as strong interaction between PCBM and **F2**, a non-covalent "bottle-brush" type BCP is formed that modulates phase separation and suppresses large-scale segregation. For a proof of such concepts, we have fabricated **P8**/PCBM (10/8) devices, in which no "three-point" complementary hydrogen bonding interactions exist and phase separation is no longer strongly modulated by the BCP.

Low *PCE*s were obtained in as-cast devices likely due to lack of certain phase separation and amorphous nature of the polymer, as seen in the AFM images and absorption spectra, respectively. Coarser morphologies and much improved device performance were obtained after optimization, as well as micron-sized crystallites started to appear in the optical micrograph. After aging tests, dense needle-like PCBM crystallites were observed (Figure 3.13i), which was very similar to the phase behavior of reference P3HT/PCBM (10/8) devices. The **P8**/PCBM (10/8) devices demonstrated higher thermal stability than the reference cell with ca. 70% *PCE* retention after aging tests, indicating morphology stabilization was still achieved to certain extent. Hydrogen bonding between the ester group on PCBM and isoorotic acid moieties on **P8**, although weaker than the "three-point" complementary interactions, likely contributes to the stabilization effect observed.

### 3.5.2.2 X-ray analyses

In order to probe in detail influence of the hydrogen bonding mediated conjugated BCP self-assembly on device morphologies, we have performed both out-of-plane wide-angle and grazing incidence small-angle X-ray scattering measurements on all the device thin films. The wide-angle experiments are summarized in Figure 3.15. As-cast thin films containing **P8** all show very low crystallinity that becomes significantly enhanced after optimization and aging tests. This is presumably due to strong attachment of fullerene derivatives through hydrogen bonding interactions, which makes P3HT packing more difficult during thin film forming solution processes. On the other hand, only slight crystallinity enhancement can be observed in the P3HT/PCBM blend films. The d-spacings observed in all thin films were calculated to be ca. 1.6 nm, corresponding to the lamellar stacking distance in regio-regular P3HT.

The AFM images (Figure 3.14) suggest that the phase-separation of **P8**/**F2** has a preferred size-scale: *i.e.* it is nanostructured, in contrast to the conventional P3HT/PCBM BHJ which exhibits a broad distribution of domain sizes and no well-defined nanostructure. To probe this in more detail, we conducted grazing-incidence small-angle X-ray scattering (GISAXS) experiments using a high-flux synchrotron beamline and the results are summarized in Figure 3.16 and Figure 3.17.

Appearance of a peak in the GISAXS data is an unambiguous signature of periodic variation of electron density at the nanoscale. Whereas conventional P3HT/PCBM blends do not exhibit any peak in GISAXS, our **P8**/**F2** materials exhibit a distinct scattering peak indicative of nanostructuring of the phase-separated materials.

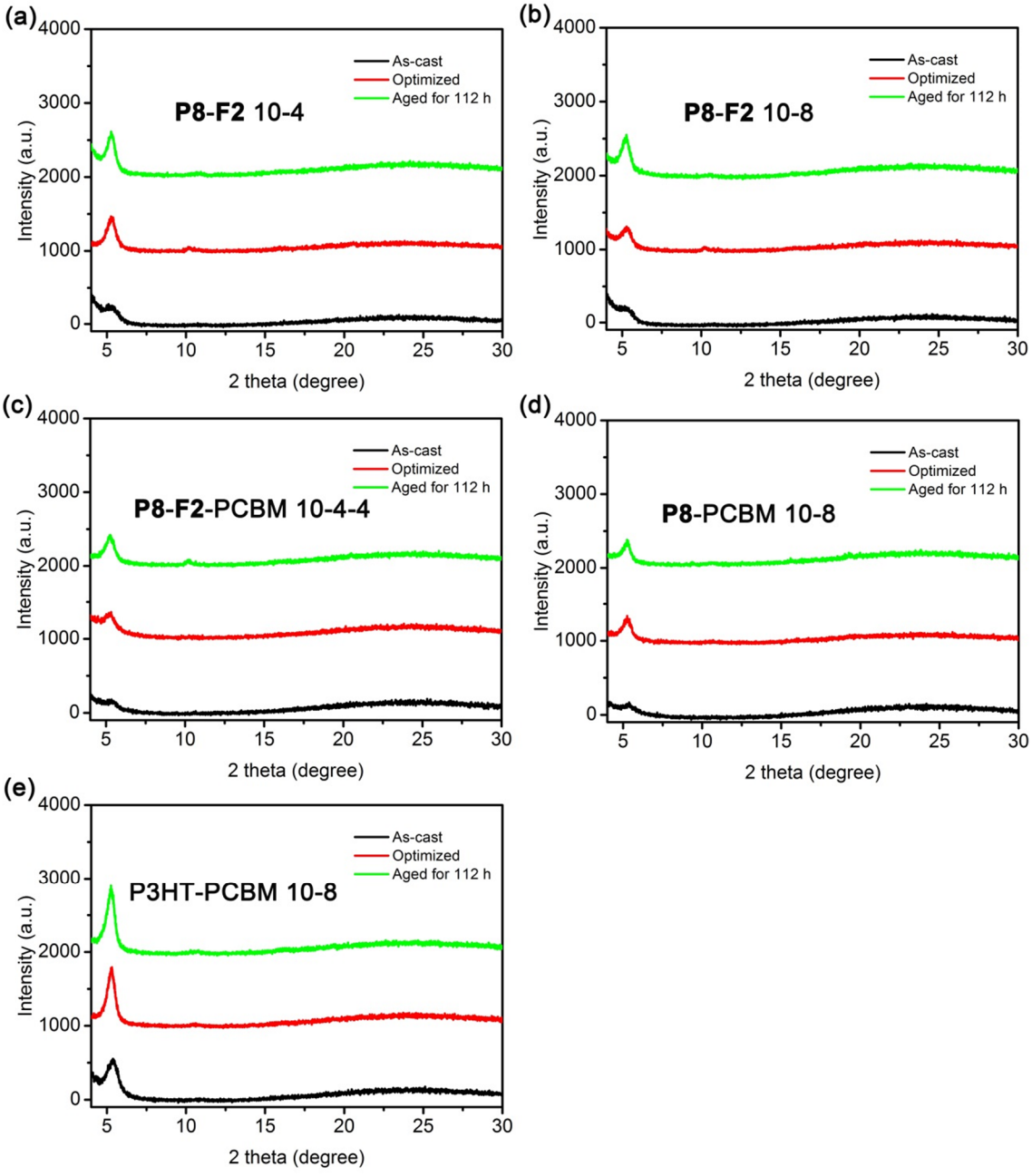


**Figure 3.14** Out-of-plane wide-angle X-ray Diffraction (XRD) profiles of solar cell thin films of **P4**/fullerene derivatives at different weight ratios (a to d) and P3HT/PCBM (e) under as-cast (black), optimized (red) and aged (green) conditions.

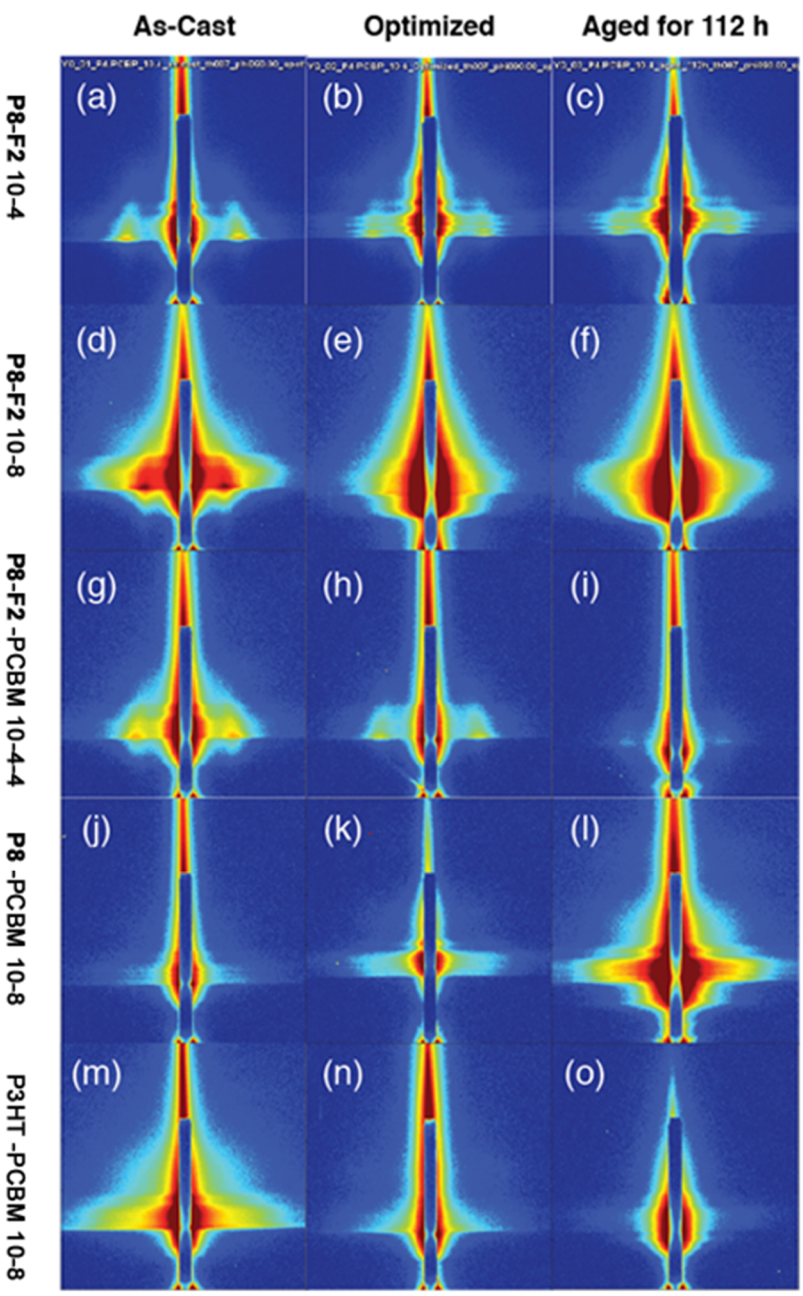


**Figure 3.15** Grazing-incidence small-angle X-ray scattering (GISAXS) profiles of devices employing **P8** with **F2** and PCBM at different weight ratios (a to l), and a standard BHJ device of P3HT/PCBM (m to o) (left column: as-cast; middle column: annealed at 150 °C for 15 min; right column aged at 110 °C for 112 h).

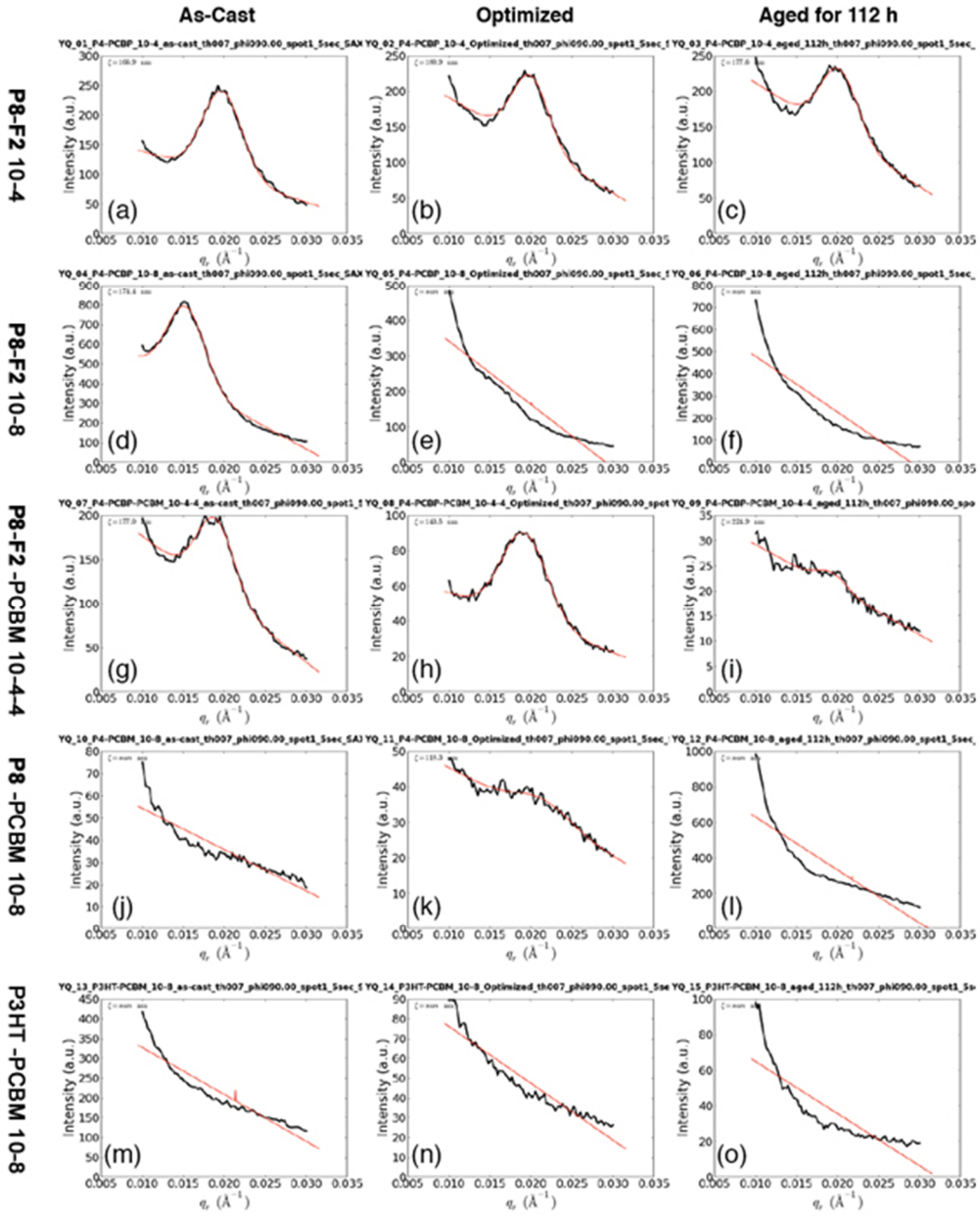


**Figure 3.16** Grazing incidence small angle X-ray scattering (GISAXS) line-cut profiles of devices employing **P8** with **F2** and PCBM at different weight ratios (a to l), and a standard BHJ device of P3HT/PCBM (m to o) (left column: as-cast; middle column: annealed at 150 °C for 15 min; right column aged at 110 °C for 112 h).

As shown in Figure 3.16 and 3.17, the size-scale of this ordering scales with the blending ratio: 32 nm for 10/4 blends and increasing to 41 nm for the 10/8 blends; while the ternary 10/4/4 blend of **P8**/**F2**/PCBM is ordered at 33 nm. This indicates that in our materials, blending can tune the size-scale of the heterojunction morphology.

More importantly, the materials exhibit a much better-defined size-scale of phase separation than is seen for any other heterojunction materials. By applying a Debye-Scherrer analysis to the peak widths, we estimate a correlation length for the nano-morphology of ca. 170 nm (ca. 5 repeats of the nanostructure). Thus the ordering is relatively weak and local (consistent with AFM), yet likely plays a role in solar cell performance. By varying the incident angle of the GISAXS measurement, we are able to distinguish between the ordering at the film surface (by measuring below the film-vacuum critical angle), and the ordering in the film interior (by measuring above the critical angle). These measurements indicated that the well-defined ordering was concentrated at the film surface, pointing to the possible role of interfacial energies in driving this ordering. Processing of the thin films led to the elimination of the nanoscale ordering for the 10/8 blend and the ternary blend. However, the 10/4 blend films exhibited well-defined and essentially unmodified morphology even after prolonged aging tests.

### 3.6 Conclusion

In summary, a polythiophene BCP selectively functionalized with isoorotic acid moieties (**P8**) and a diaminopyridine tethered fullerene derivative (**F2**) have been prepared and fully characterized. Strong complexation between these two components

through “three-point” complementary hydrogen bonding interactions is demonstrated by fluorescence quenching and NMR titration experiments. BHJ solar cells employing **P8** with varying amount of **F2** and PCBM were fabricated and tested. Thermal stability of devices were evaluated by aging tests and closely monitored by spectroscopy and microscopy. Cooperative effects from orthogonal non-covalent interactions, *i.e.* complementary hydrogen bonding and BCP self-assembly, not only led to much improved device stability but also tunable and long-range ordered morphologies by simply adjusting the amount and nature of fullerene derivatives. Our methodology provides new opportunities to achieve stable and ordered morphologies and potentially higher performing PSCs when applied on conjugated BCPs possessing lower bandgaps.

### 3.7 Future work

Through the redesign on the block ratio of BCPs and fullerenes, we found out that our BCP **P8**/**F2** system could improve the efficiencies and thermal stabilities of the solar cells employing **P8**/**F2** as the active layers. More importantly, the PCEs of **P8**/**F2** solar cells are better than the **P4**/**F1** ones. Therefore, the strategy we adopted was successful. In addition, the morphologies of **P8**/**F2** blend films are tunable and nanostructured. However, we don’t know the specific types. We postulate that such nanostructures are beneficial to the device performances. With an aim to further improve the device performances employing BCP and **F2** as active layers, we could design BCP to form certain nanostructures and then study their photovoltaic behaviors.

## 3.8 Experimental

### 3.8.1 Materials and general methods

All reagents and solvents were used as received from Sigma-Aldrich or Alfa Aesar unless otherwise noted. 2-Bromo-3-hexyl-5-iodothiophene (**M1**), ((6-(2-bromo-5-chloromagnesiothiophen-3-yl)hexyl)oxy)(tert-butyl)dimethylsilane (**M2**) were synthesized according to previously reported procedure.[1] THF was distilled from Na/benzophenone prior to use. Anhydrous chloroform and dichloromethane were obtained by distillation over $CaH_2$ and degassed through several freeze-pump-thaw cycles. 300.13 MHz $^{1}H$ and 75.48 MHz $^{13}C$ NMR spectra were recorded on a Bruker Avance III Solution 300 spectrometer. All solution $^{1}H$ and $^{13}C$ NMR spectra were referenced internally to solvent signals. Size exclusion chromatography (SEC) analyses were performed in chloroform with 0.5% (v/v) triethylamine (1 mL/min) using a Waters Breeze system equipped with a 2707 autosampler, a 1515 isocratic HPLC pump and a 2414 refractive index detector. Two styragel columns (Polymer Laboratories; 5 μm Mix-C), which were kept in a column heater at 35 °C, were used for separation. The columns were calibrated with polystyrene standards (Varian). Ultraviolet-Visible (UV-Vis) absorption spectra were recorded on a Shimadzu UV-2401 PC spectrometer over a wavelength range of 240-800 nm. Fluorescence emission spectra were obtained using a Varian Cary Eclipse Fluorimeter. Differential scanning calorimetry (DSC) measurements were performed on a Mettler Toledo DSC STAR$^{e}$ system with ca. 10 mg sample and at a scan rate of 10 °C/min. The results reported are from the second heating cycle. High resolution mass spectrometry (HRMS) was performed on a Waters/Micromass LCT

Premier system operating under electrospray ionization (ESI) mode. Cyclic Voltammetry was performed at 25 °C on a CH Instrument CHI604xD electrochemical analyzer using a glassy carbon working electrode, a platinum wire counter electrode and a Ag/AgCl reference electrode calibrated using ferrocene redox couple (4.8 eV below vacuum). Optical Micrographs were taken on a Carl Zesis Axio Imager 2 microscope. Atomic force microscopy (AFM) images were obtained on an Asylum MFP3D AFM instrument operated under tapping mode. For the solution binding constant studies, an **S1** solution in $CDCl_3$ (0.2 M) was gradually added into a F2 solution in $CDCl_3$ (4 mM) in a NMR tube. After each addition, the solution was allowed to equilibrate for 5 min and subjected to $^1H$ NMR measurements. Wide-angle X-ray diffraction measurements were performed on a Rigaku SmartLab instrument. Small-angle X-ray scattering experiments were performed at the X9 undulator-based beamline at the National Synchrotron Light Source (NSLS). An incident X-ray beam of energy 13.5 keV (wavelength = 0.0918 nm) was collimated using a two-slit system, and focused to a beam 50 um tall by 100 um wide at the sample position using a KB mirror system. Grazing-incidence experiments were performed over a range of incidence angles, both below and above the film-vacuum critical angle. Two-dimensional scattering images were measured in the small-angle (GISAXS) using a charged-coupled device (CCD) detectors positioned at 5.122 m from the sample. Data conversion to q-space was accomplished using Silver Behenate powder as a standard.

### 3.8.2 Solar cell fabrication and testing

The solar cell devices adopt a structure of ITO/$MoO_3$/active layer/Al. Thin films of active layers were spun-cast from blend solutions prepared by dissolving **P8** and

fullerenes at predetermined weight ratios in chlorobenzene and the concentration of **P8** was kept at 1 wt%. P3HT (synthesized in-house; $M_n$ = 31,200, *PDI* = 1.04)/PCBM (American Dye Source, Inc.) blend solutions were prepared by dissolving P3HT/PCBM (10 mg : 8 mg) in 1 mL chlorobenzene. All solutions were stirred at 100 °C for 10 h in a nitrogen glove box (Innovative Technology, model PL-He-2GB, $O_2$ < 0.1 ppm, $H_2O$ < 0.1 ppm) before device fabrication. Solar cell devices were fabricated according to the following procedure: ITO-coated glass substrates (China Shenzhen Southern Glass Display. Ltd, 8 Ω/□) were cleaned by ultrasonication sequentially in detergent, DI water, acetone and isopropyl alcohol, each for 15 min. These ITO-coated glass substrates were further treated by UV-ozone (PSD Series, Novascan) for 45 min before being transferred to a nitrogen glove box (Innovative Technology, model PL-He-4GB-1800, $O_2$ < 0.1 ppm, $H_2O$ < 0.1 ppm) for $MoO_3$ deposition. $MoO_3$ (10 nm) was deposited using an Angstrom Engineering Åmod deposition system at a base vacuum level < $7 \times 10^{-8}$ Torr. The polymer/fullerene blend solution was first filtered through a 1 μm PTFE filter and spin-coated on top of the $MoO_3$ layer at 400 rpm for 30s. Al (100 nm) was thermally evaporated through patterned shadow masks as anodes. Current−voltage (I−V) characteristics were measured by a Keithley 2400 source-measuring unit under simulated AM1.5G irradiation (100 mW/cm$^{-2}$) generated by a Xe arc-lamp based Newport 67005 150-W solar simulator equipped with an AM1.5G filter. The light intensity was calibrated by a Newport thermopile detector (model 818P-010-12) equipped with a Newport 1916-C Optical Power Meter.

### 3.8.3 Synthesis of BCPs P6-P8 and fullerene derivative F2

**[6, 6]-Phenyl-C61-butyric acid (PCBA)**. The synthesis of PCBA was similar to reported literature.[9,16] Acetic acid (50 ml) and HCl (30 ml) were added to a solution of [6,6]-Phenyl-C61-butyric acid methyl ester (PCBM) (510 mg, 0.560 mmol) in 100 ml of *o*-dichlorobenzene, and the solution was refluxed for 18 h. After the solvent was removed under reduced pressure, the residue was treated with methanol and then filtered to give 490 mg PCBA as a black powder (yield 97.6%). $^1$H NMR (300.13 MHz, $CDCl_3/d_6$-DMSO/$CS_2$): δ (ppm) = 2.05-1.98 (-*CH*$_2$-, m, 2H). 2.30 (-*CH*$_2$-, t, *J* = 7.5 Hz, 2H), 2.78-2.73 (-*CH*$_2$-, m, 2H), 7.39-7.29 (*Ph-H*, m, 3H), 7.76 (*Ph-H*, d, *J* = 7.2 Hz, 2H),

**[6, 6]-Phenyl-C61-butyric acid N-(6-aminopyridin-2-yl) amide (F2)**. **F2** was prepared according to a modified literature procedure.[17] In a dry Schlenk flask was added PCBA (200 mg, 0.223 mmol) and $CH_2Cl_2$ (40 mL) under nitrogen. To this solution was added 1-chloro-N, N, 2-trimethylpropenylamine (0.04 mL, 0.268 mmol). The reaction mixture was stirred at r.t. for 4 h resulting in a homogeneous solution, and then evaporated to provide the corresponding acid chloride that was dissolved in 40 mL $CHCl_2$ and used directly in the next step. To a solution of 2, 6-diaminopyridine (674 mg, 4.460 mmol) in $CH_2Cl_2$ (40 mL) was added the solution of acid chloride in $CH_2Cl_2$ dropwise over 30 min. The reaction mixture was stirred at r.t. overnight, and then quenched with MeOH. The solvent was evaporated under reduced pressure and the residue was washed with excess MeOH to remove the unreacted 2, 6-diaminopyridine. **F2** was purified by flash chromatography on silica gel ($CH_2Cl_2$/EtOAc, 20:1) as a dark brown powder (160 mg, 73% yield). $^1$H NMR (300.13 MHz, $CDCl_3$): δ (ppm) = 2.26-

2.31 (-*CH*$_2$-, m, 2H), 2.55 (-*CH*$_2$-, t, *J* = 7.5 Hz, 2H), 2.93-2.98 (-*CH*$_2$-, m, 2H), 4.26 (-*NH*$_2$, s, 2H), 6.24 (*Pyr-H*, d, *J* = 6.9 Hz, 1 H), 7.41-7.57 (m, 6H), 7.92-7.95 (*Ph-H*, m, 2H). HRMS (ESI): Calcd. for $C_{76}H_{18}N_3O$, 988.1450 [M+], 989.1483 for [M+H]; found, 988.1471 [M+], 989.1490 [M+H].

**1-N-hexylisoorotic acid (S2)**. Synthesis of **S2** is similar to a reported procedure.[18] Isoorotic acid (6.41 mmol, 1 g) was suspended in hexamethydisilazane (HMDS) (40.2 mmol, 8.4 mL), and trimethylchlorosilane (TMSCl) (13.46 mmol, 2.0 mL) was added. The mixture was refluxed in a pressure vessel at 120 °C for 4 h until the mixture appeared clear. The reaction vessel was cooled to room temperature, and then1-bromohexane (64.1 mmol, 9 mL) was added. The mixture was then heated to 100 °C for 48 h. The solvent was then removed under reduced pressure, and the residue was stirred with 10 mL of ice water and 10 mL of glacial acetic acid for 20 min. The precipitate formed was collected by filtration and washed with copious cold water and hexanes to afford 1.4 g product as pale-grey solids (yield 91%). $^1$H NMR (300.13 MHz, $CDCl_3$): δ (ppm) = 0.89 (-*CH*$_3$, t, 3H), 1.32 (br, 6 H), 1.75 (-*CH*$_2$CH$_3$, t, 2H), 3.89 (*NCH*$_2$-, t, 2H), 8.50 (*C=CH*, s, 1H), 9.84 (-CO*NH*CO-, s, 1H), 12.21 (-*COOH*, s, 1H). $^{13}$C NMR (75.48 MHz, $CDCl_3$): δ (ppm) = 165.4, 163.3, 153.1, 149.5, 102.2, 50.7, 31.29, 29.1, 26.1, 22.5, 14.1.

**1-N-hexylisoorotic acid methyl ester (S1)**. In a 100 mL flask was added 1-hexyl-2,4-dioxo-1,2,3,4-tetrahydropyrimidine-5-carboxylic acid **S2** (200 mg, 0.832 mmol), 50 mL MeOH and 10 drops of conc. $H_2SO_4$. The solution was refluxed overnight before solvents were removed under vacuum. Recrystallization from $CHCl_3$/hexanes gave **S1** as a white

powder (200 mg, 94%). $^{1}$H NMR (300.13 MHz, $CDCl_3$): δ (ppm) = 0.90 (-*CH*$_3$, t, 3H), 1.32 (br, 6 H), 1.73 (-*CH*$_2$CH$_3$, t, 2H), 3.81 (*NCH*$_2$-, t, 2H), 3.89 (-OCH$_3$, s, 3H), 8.14 (-CO*NH*CO-, s, 1H), 8.23 (*C*=*CH*-, s, 1H). $^{13}$C NMR (75.48 MHz, $CDCl_3$): δ (ppm) = 163.8, 159.4, 152.2, 150.0, 104.9, 52.6, 50.0, 31.3, 29.2, 26.1, 22.5, 14.0.

**Poly(3-hexylthiophene)-b-Poly(3-(6'-dimethyl-*tert*-butylsilyloxyl) hexylthiophene) (P6)**. Two three-necked round-bottomed flasks (250 mL and 50 mL) equipped with stopcocks and septa were flamed dried under high vacuum and cooled to room temperature under $N_2$. Monomer **M1** (1.48 g, 3.972 mmol) and LiCl (168 mg, 3.972 mmol) was placed in the 250 mL flask under $N_2$, and then evacuated under high vacuum to remove any residual water and oxygen. After adding dry THF (40 mL) into the flask via a syringe, the solution was cooled to 0 °C. A 2 M solution of *i*-PrMgCl in THF (2 mL, 3.972 mmol) was added via syringe and the mixture was stirred at 0 °C for 30 min (solution 1). In the other 50 mL flask, 0.2 g (0.397 mmol) 2,5-dibromo-3-(6'-dimethyl-*tert*-butylsilyloxyl)hexylthiophene was first reacted with 0.2 mL *i*-PrMgCl in the presence of 20 mg LiCl (0.397 mmol) in 10 mL THF (solution 2) to yield **M2**. Solution 1 was heated up to 35 °C and Ni(dppp)$Cl_2$ catalyst (10.76 mg, 0.0397 mmol), which was suspended in 5 mL dry THF, was added in one portion. The reaction mixture was stirred at 35 °C for 15 min, an aliquot was withdrawn with a syringe and injected into a methanol solution to give **P5** for SEC analysis (RI, $CHCl_3$, 1 mL/min: $M_n$ = 35,300, $M_w$ = 42,400, *PDI* = 1.2). Solution 2 containing **M2** was then transferred to solution **1** via a cannula. The resulting red solution was stirred at 35 °C for 40 min before 0.5 mL EtMgCl solution (2M in THF) was added. The polymer was isolated by precipitation into MeOH

and successively washed by Soxhlet extraction using methanol, acetone, and chloroform. The polymer was recovered by precipitation of the chloroform solution into methanol and dried under high vacuum to give a black solid (0.86 g, 89%). $^1$H NMR (300.13 MHz, $CDCl_3$): δ (ppm) = 0.041 (-O-($^t$Bu)Si*(C$H_3$)$_2$*), 0.90-0.94, 1.25-1.71, 2.81(hexyl-*H*'s, methylene-*H*'s and $^t$Bu-*H*'s), 3.61(-O*C*$H_2$C$H_2$-), 6.98 (*Th-H*). SEC (RI, $CHCl_3$ 1 mL/min): $M_n$ = 42,700, $M_w$ = 50,800, *PDI* = 1.2.

**Poly(3-hexylthiophene)-b-Poly(3-(6'-hydroxyl)hexylthiophene) (P7)**. In a 100 mL Schlenk flask was added 750 mg polymer **P6** and 100 mL THF under $N_2$. The solution became clear after stirring at 60 °C for ca. 30 min. Tetrabutylammonium fluoride (TBAF) solution (2 mL, 2M in THF) was then added dropwise via syringe. The reaction mixture was kept stirring at 60 °C for 8 h and concentrated under reduced pressure to ca. 5 mL. **P7** was recovered as a black solid by precipitation into a mixture of methanol and acetone (1/1, vol/vvol) and dried under vacuum overnight (650 mg, 88%). $^1$H NMR (300.13 MHz, $CDCl_3$): δ (ppm) = 0.92, 1.25-1.73, 2.04, 2.81 (hexyl-*H*'s and methylene-*H*'s), 3.66 (-O*C*$H_2$C$H_2$-), 6.98(*Th-H*). SEC (RI, $CHCl_3$ 1 mL/min): $M_n$ = 35,900, $M_w$ = 48,300, *PDI* = 1.3.

**Poly(3-hexylthiophene)-b-Poly(3-(6'-(1-hexylisoorotic acid amido))hexylthiophene) (P8)**. In a 25 mL three-neck flask equipped with a condenser and septa was added 246 mg (1.02 mmol) 1-N-hexylisoorotic acid and 2 mL thionyl chloride under nitrogen, and the solution was refluxed for 8 h to give the corresponding acid chloride. The excess $SOCl_2$ was removed under vacuum and the residue was dissolve in 10 mL of dry $CHCl_3$ and the solvent was removed under reduced pressure remove residual $SOCl_2$. In the other

250 mL Schlenk flask was added 200 mg **P7** and 30 mL $CHCl_3$ under nitrogen. The reaction mixture was kept stirring at 60 °C for 20 min until all polymer dissolved and then triethylamine (0.3 mL) was added into the polymer solution. The acid chloride was dissolved in 15 mL $CHCl_3$ and transferred into the polymer solution via cannula. The reaction was kept at 60 °C for another 8 h and concentrated under reduced pressure to ca. 5 mL. The crude polymer was isolated by precipitation into methanol and successively Soxhlet extracted using methanol, acetone, and chloroform. The chloroform solution was concentrated and precipitated into MeOH to give **P8** as a black solid (200 mg, 78%). $^1$H NMR (300.13 MHz, $CDCl_3$): δ (ppm) = 0.92, 1.25-1.71, 2.80 (hexyl-*H*'s and methylene-*H*'s), 3.77 (-COO*CH*$_2$-), 4.29 (N*CH*$_2$-), 6.98 (*Th-H*), 8.19 (C=*CH*-). SEC (RI, $CHCl_3$ 1 mL/min) at 35 °C: $M_n$ = 27,200, $M_w$ = 43,500, *PDI* = 1.6; at 55 °C: $M_n$ = 32,100, $M_w$ = 47,900, *PDI* = 1.5.

## 3.9 References


(1) Li, F.; Yang, J.; Qin, Y. *J. Polym. Sci., Part A: Polym. Chem.* **2013**, 51, 3339.

(2) Ren, B.-Y.; Ou, C.-J.; Zhang, C.; Chang, Y.-Z.; Yi, M.-D.; Liu, J.-Q.; Xie, L.-H.; Zhang, G.-W.; Deng, X.-Y.; Li, S.-B.; Wei, W.; Huang, W. *J. Phys. Chem. C* **2012**, 116, 8881.

(3) Wang, N.; Bao, X.; Yang, C.; Wang, J.; Woo, H. Y.; Lan, Z.; Chen, W.; Yang, R. *Org. Electron.* **2013**, 14, 682.

(4) Matsumoto, K.; Hashimoto, K.; Kamo, M.; Uetani, Y.; Hayase, S.; Kawatsura, M.; Itoh, T. *J. Mater. Chem.* **2010**, 20, 9226.

(5) Camaioni, N.; Ridolfi, G.; Casalbore-Miceli, G.; Possamai, G.; Maggini, M. *Adv. Mater.* **2002**, 14, 1735.

(6) Wu, P.-T.; Xin, H.; Kim, F. S.; Ren, G.; Jenekhe, S. A. *Macromolecules* **2009**, 42, 8817.

(7) Hou, J.; Chen, T. L.; Zhang, S.; Huo, L.; Sista, S.; Yang, Y. *Macromolecules* **2009**, 42, 9217.

(8) We first tried thionyl chloride to prepare the corresponding acid chloride of PCBA, but we found out that there was some adduct product between PCBA and thionyl chloride somehow even at room temperature.

(9) Hummelen, J. C.; Knight, B. W.; LePeq, F.; Wudl, F.; Yao, J.; Wilkins, C. L. *J. Org. Chem.* **1995**, 60, 532.

(10) Liu, C.; Li, Y.; Li, C.; Li, W.; Zhou, C.; Liu, H.; Bo, Z.; Li, Y. *J. Phys. Chem. C* **2009**, 113, 21970.

(11) Hynes, M. J. *J. Chem. Soc. Dalton Trans.* **1993**, 311.

(12) Emge, A.; Bäuerle, P. *Synt. Met.* **1999**, 102, 1370.

(13) Tang, H.; Radosz, M.; Shen, Y. *J. Polym. Sci., Part A: Polym. Chem.* **2006**, 44, 6607.

(14) Carroll, J. B.; Cooke, G.; Garety, J. F.; Jordan, B., J.; Mabruk, S.; Rotello, V. M. *Chem. Commun.* **2005**, 3838.

(15) Ma, W.; Yang, C.; Gong, X.; Lee, K.; Heeger, A. J. *Adv. Funct. Mater.* **2005**, 15, 1617.

(16) Reiriz, C. s.; Brea, R. J.; Arranz, R. o.; Carrascosa, J. L.; Garibotti, A.; Manning, B.; Valpuesta, J. M.; Eritja, R. n.; Castedo, L.; Granja, J. R. *J. Am. Chem. Soc.* **2009**, 131, 11335.

(17) Gan, Q.; Li, F.; Li, G.; Kauffmann, B.; Xiang, J.; Huc, I.; Jiang, H. *Chem. Commun.* **2010**, 46, 297.

(18) Accetta, A.; Corradini, R.; Sforza, S.; Tedeschi, T.; Brognara, E.; Borgatti, M.; Gambari, R.; Marchelli, R. *J. Med. Chem.* **2009**, 52, 87.

# Chapter 4

# Complementary Hydrogen Bonding Mediated Self-Assembly of Block Polythiophenes towards Tunable Nanomorphologies and Their Applications in Solar Cells

(This chapter is based on a manuscript in preparation)

## 4.1 Introduction

In Chapter 2, I described the synthesis of a polythiophene block copolymer selectively modified with 2,6-bis(hexylamino)pyrimidine moieties **P4** and a fullerene derivative **F1** capable of complementary "three-point" hydrogen bonding interactions as illustrated in Figure 4.1a. The hydrogen bonding interactions between **P4** and **F1** could form a non-covalent "bottle-brush" type polythiophene/fullerene block copolymer complex. Furthermore, the self-assembly of such **P4**/**F1** complex could successfully suppress the **F1** crystallizations in spite of the bad photovoltaic performances of solar cells fabricated from **P4**/**F1** as the active layers.[1] To pursue higher efficiencies while still maintaining the complementary hydrogen bonding motif, I then modified the block ratios and synthesized a polythiophene block copolymer functionalized with 7% isoorotic acid moieties with a longer pure P3HT block (**P8**) and a diaminopyridine tethered fullerene (**F2**) derived directly from phenyl-C61-butyric acid methyl ester (PCBM) as shown in Figure 4.1b. Such "three point" hydrogen bonding between the polymer and **F2** enabled higher thermal stability of the resulting polymer solar cells with tunable ordered morphologies.[2]

In the **P8**/**F2** case, I changed the block ratio of the BCP and the type of fullerene at the same time. I then proposed the change of block ratio of **P8** with a longer pure P3HT block accounted more for the enhanced photovoltaic properties. To seek the evidence for the hypothesis and further explore the utility of such "three-point" hydrogen bonding in tuning the morphologies, by keeping **F2** unchanged, I intentionally increased the isoorotic acid moieties to 22% on the polyhtiophene block copolymer and synthesized **P11** (Figure 4.1c), a "cousin polymer" of the **P8** reported in chapter 3.

Herein, the block ratio of **P11** is roughly similar to that of **P4**. I envisioned that higher concentration of the hydrogen bonding functionalities on **P11** would have different self-assembly behaviors and allow more flexibility for morphology tuning. By employing the same **F2** as electron acceptor, I could confirm the influence of block ratio change on eventual photovoltaic performances. Furthermore, different morphologies were revealed in the thin film via AFM, UV-vis and X-ray diffraction analyses by adjusting **F2** content in the **P11**/**F2** blends. Moreover, the tunable nanomorphologies were also observed in solution via TEM when hexanes were added into **P11**/**F2** solutions at different weight ratios in chlorobenzene, which is distinct from the **P4**/**F1** or **P8**/**F2** cases and is rarely studied. I also investigated the resulting solar cells properties fabricated from **P11**/**F2** as active layers and corresponding morphologies were correlated with the polymer solar device performances.

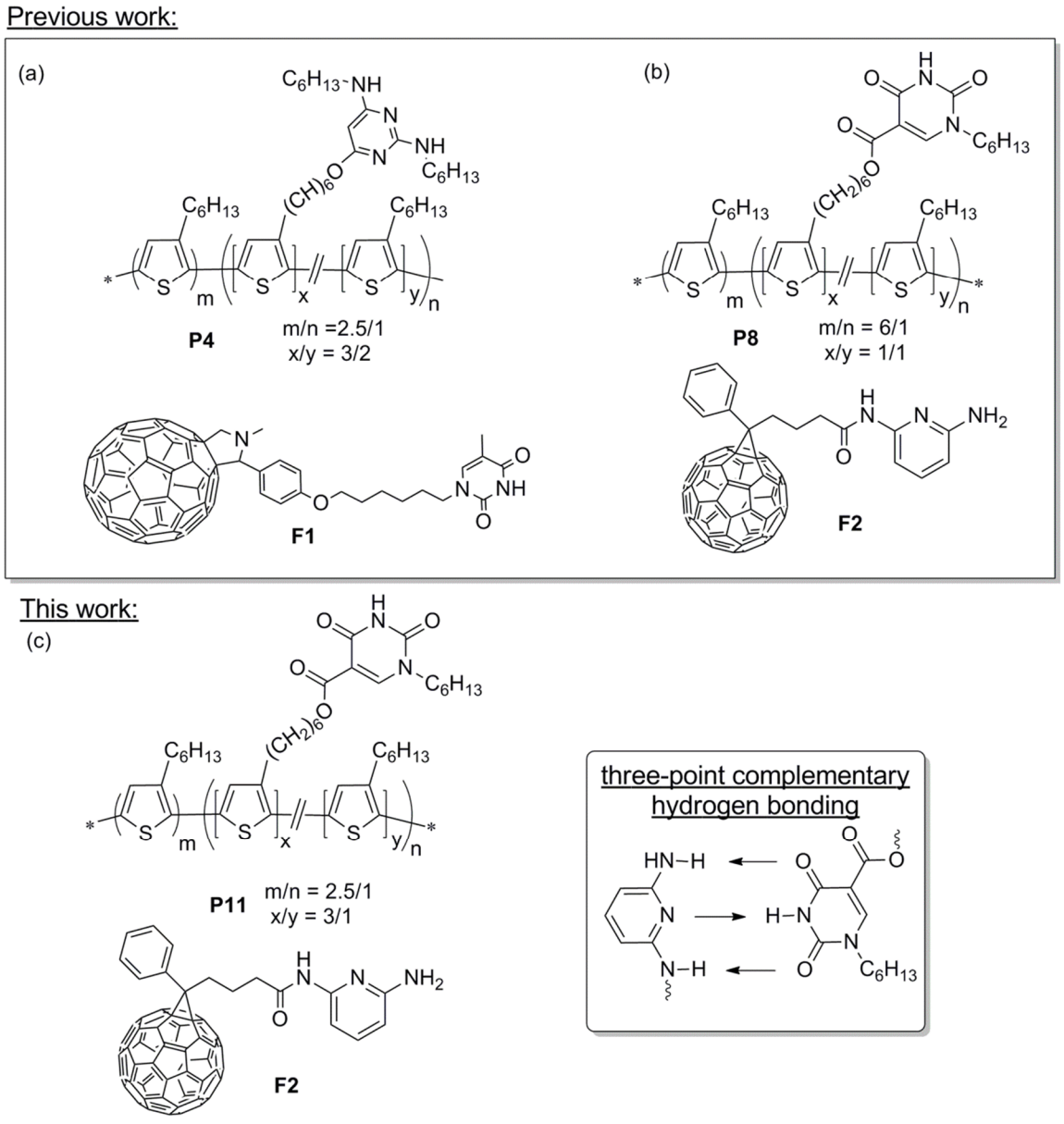


**Figure 4.1** Molecular structures of functionalized block polythiophenes and fullerenes capable of "three-point" complementary hydrogen bonding interactions reported in Chapter 2 (a) and Chapter 3 (b) and studied herein (c)

## 4.2 Synthesis and characterization

### 4.2.1 Synthesis of BCPs P9-P11

Synthesis of the 1-N-hexylisoorotic acid functionalized block copolymer (**P11**) was described in Scheme 4.1, which was based on a similar methodology reported in chapter 3.[2] $^1$H NMR spectra and size exclusion chromatography (SEC) profiles of the polymers **P1**-**P11** were presented in Figure 4.2.

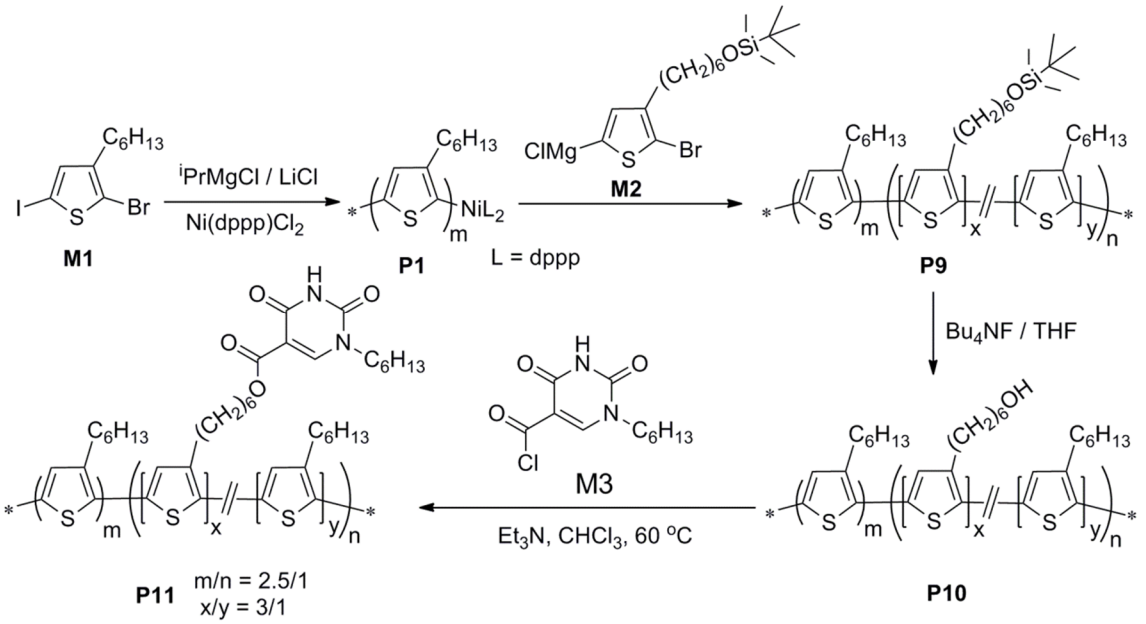


**Scheme 4.1** Synthesis of isoorotic acid-tethered block polythiophene **P11**

**M1**/**M2** monomer feed ratio was set to be 3/1 during the synthesis of **P2**, and **M2** was added when the conversion of **M1** reached 80% in order to have a second block with higher **M2** content while still maintaining a statistical nature.[3-8] Integration of methylene group signals at 3.61 ppm (-$OCH_2$-) and 2.80 ppm (Th-$CH_2$-) in the $^1$H NMR spectrum of **P9** gave the percentage of post-polymerization modification to be ca. 22%, corresponding

to ca. 88% conversion of **M2** during the chain-extension step and a block ratio of 2.4 to 1. Molecular weights of **P1** ($M_n$ = 17396, *PDI* = 1.10) and **P9** ($M_n$ = 28,741, *PDI* = 1.20) obtained from SEC analysis gave a functional group concentration of ca. 22% and a block length ratio of ca. 2.4 to 1, matching closely with the $^1$H NMR calculations.

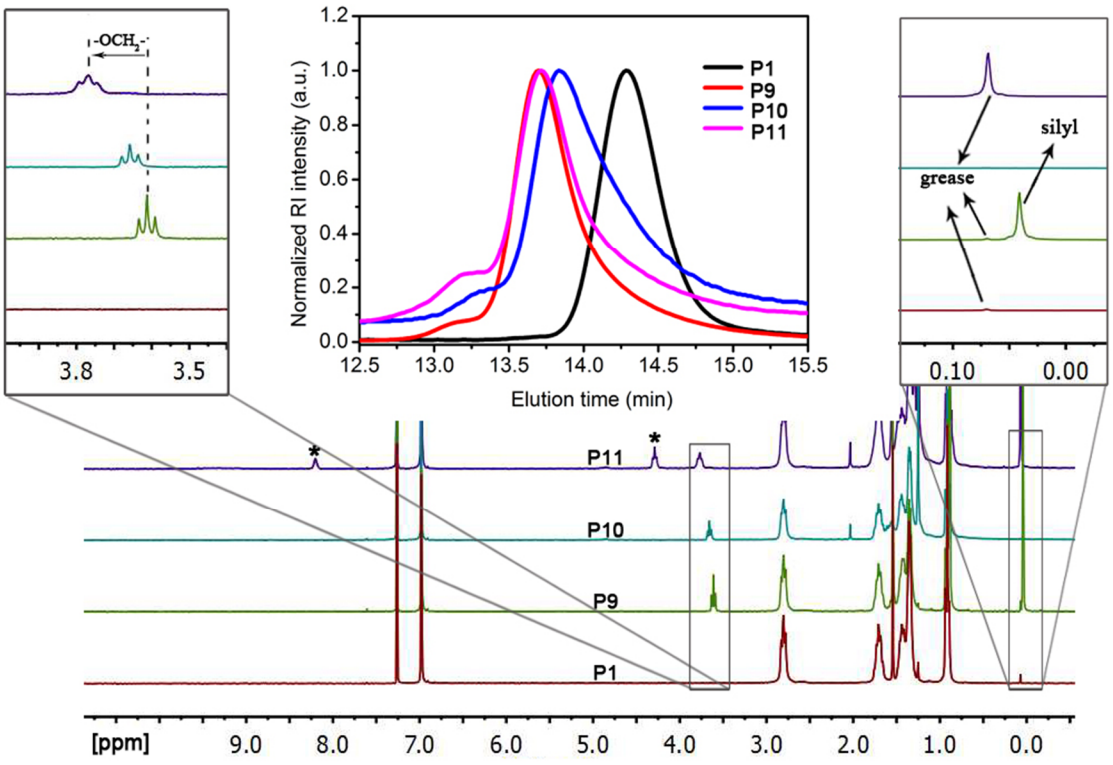


**Figure 4.2** $^1$H NMR spectra (300.13 MHz, $CDCl_3$) of **P1**, **P9**, **P10**, and **P11**. Inset (middle): size exclusion chromatography (SEC) traces of **P1** (black), **P9** (red), **P10** (blue) and **P11** (pink). The zoom-in regions indicate the changes during the chemical transformations. The peaks with asterisks on **P11** are from the isoorotic acid moieties after the reaction. The peaks at 0.07 ppm indicated by the arrows in all spectra are due to grease involved in air-free operations.

### 4.2.2 Optical, electrochemical and thermal properties

In order to investigate the influence of degree of post-polymerization modification on the electronic properties of polythiophenes, UV-Vis absorption measurements were carried out on **P11** solution and thin films (as-cast and thermal annealed) as shown in Figure 4.3. Absorption profile of **P11** showed a unimodal peak at 458 nm which shifted to 516 nm for its as-cast film, accompanied by the appearance of vibronic peaks at 551 nm and 600 nm).

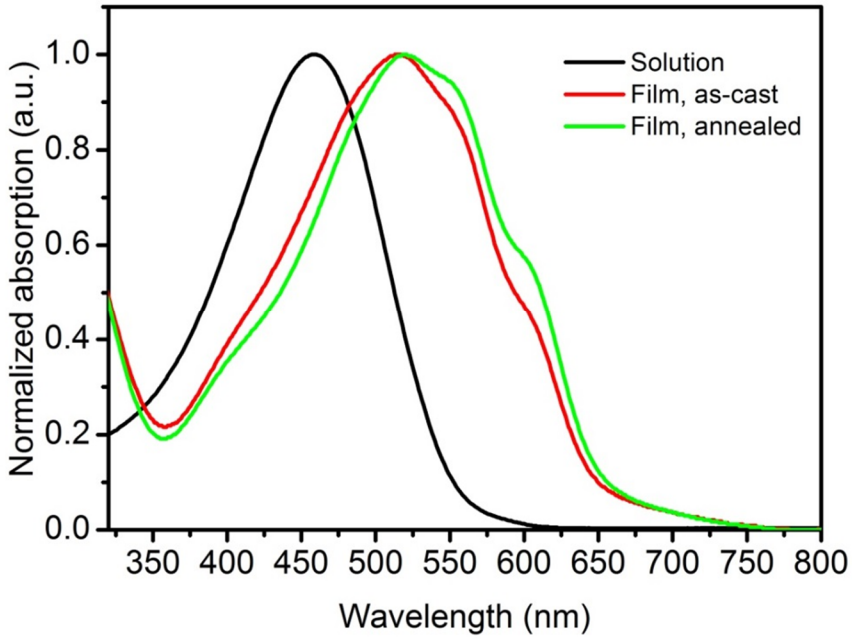


**Figure 4.3** UV-Vis absorption spectra of **P11** in solution ($10^{-5}$ M) and films, spin-cast from chlorobenzene solution (10 mg/mL) at 400 rpm for 30 s, anneal at 110 ºC for 15 min

Thermal annealing slightly promoted the reorganization of the polymer as indicated by increased intensities of the vibronic peaks. It is noted that such vibronic

pattern indicates lower degree of crystallinity of the polymer compared with that of its analogue with 7% functionalities (**P8**) in our previous report,[9] possibly due to increased self-complementary hydrogen bonding interactions from isoorotic acid moieties on **P11**. From the absorption edge of the spectra of as-cast film, a bandgap of 1.9 eV was estimated for **P11**, in good agreement with the optical bandgaps of **P8** as well as with reported value for P3HT.[10-12]

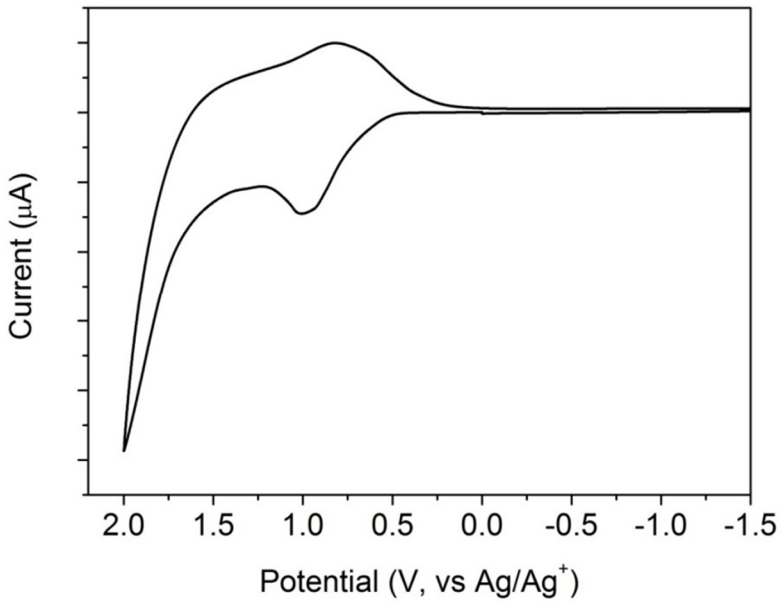


**Figure 4.4** Cyclic voltammogram of **P11** thin film drop-coated on the glassy carbon working electrode (0.1 M $Bu_4NPF_6$ in $CH_3CN$, 100 mV/s, referenced externally to $Fc/Fc^+$ redox couple).

Cyclic voltammetry (CV) measurements on **P11** films revealed a quasi-reversible oxidation with an onset at +0.1 V (vs. $Fc/Fc^+$ redox couple) as shown in Figure 4.4. It gave a HOMO level of 4.9 eV below vacuum, which is identical with our measured value

of **P8**. These observations imply that higher percentage of 1-N-hexylisoorotic acid moieties as attachments onto **P11** does not change the electronic properties of the conjugated main-chain compared with its lower percentage analogue **P8**.

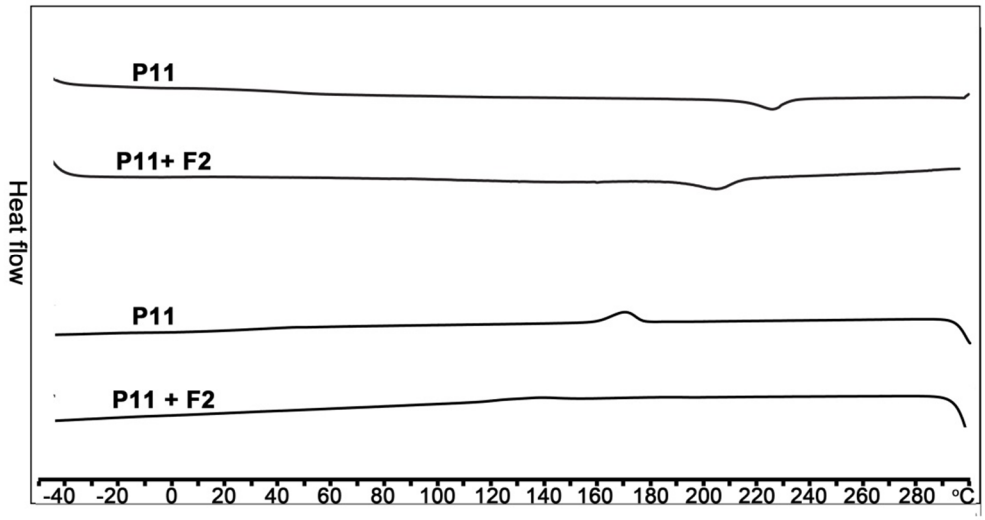


**Figure 4.5** DSC plots of **P11** and its **F2** blend with ca.10 mg sample and a scanning rate of 10°C/min (top two: 2nd heating curves; bottom two: 1st cooling curve, exotherm up).

In order to probe the effects of higher density of the functional groups on the thermal properties of the polymer in solid state, DSC measurements were performed on **P11** and its blend with **F2**, respectively. All samples (ca. 10 mg) were tested using the same heating and cooling sequences (−50 °C to 300 °C, 10 °C/min). Blend was obtained by dissolving **P11** and fullerene at a 1:1 molar ratio in chloroform followed by extensive drying under vacuum. The second heating and first cooling curves were used for analysis and shown in Figure 4.5. **P11** showed a melting point at 213 ºC, about 9 ºC lower than that of **P8** (222 °C), which decreased to 189 ºC when the polymer was mixed with **F2**. Such phenomenon suggested a less crystalline nature of **P11**, probably due to a shorter

block length ratio of monomers **M1**/**M2** and higher functionality concentration tethered with the main chain of the polymer. It agreed well with the film UV-vis absorption analysis. Interestingly, it is noted that the blend of **P11** and **F2** took slightly longer time to melt completely than that of **P11** alone, which was probably due to increased percentage of hydrogen bonding moieties in the blend. Such trend was more obvious in their 1st cooling curve, as indicated by a longer phase transition in **P11**/**F2** blend.

### 4.3 Tunable morphologies of the blends in thin films

#### 4.3.1 UV-vis and XRD measurements

To investigate the morphology tunability of **P11**/ **F2** at different ratios, I first subjected all thin films to UV-Vis spectroscopy measurements as shown in Figure 4.6.

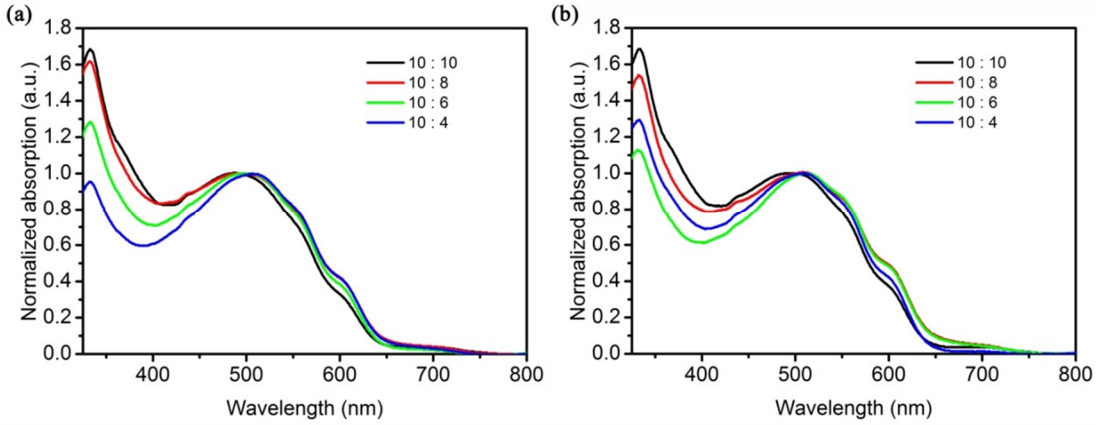


**Figure 4.6** Film UV-Vis spectra of **P11**/**F2** blends at different weight ratios; (a) as-cast; (b) thermally annealed at 110 ºC 15 min.

The intensity of fullerenes absorption at ca. 334 nm decreased with reduced **F2** contents in the **P11**/**F2** as-cast films as shown in Figure 4.6a, whereas thermal annealing

promoted the reorganization of **P11** and **F2** that rendered higher fullerenes absorption intensities in the 10/4 blend than that of 10/6 blend (Figure 4.6b). The order of the polymer **P11** packing in the blends was indicated by the intensities of those vibronic peaks at ca. 554 nm and 600 nm. Surprisingly, the 10/4 and 10/8 blends exhibited the most pronounced vibronic peaks among all the as-cast films while 10/6 and 10/8 blends turned out to be have higher order of interchain packing after thermal annealing. It is worth noting that a gradual peak shift was observed when less **F2** was present in the film blends, from 487 nm (10/10) to 503 nm (10/4), indicating that self-assembly between **P11** and **F2** could tune the packing between **P11** and **F2** for lower energy conformations.

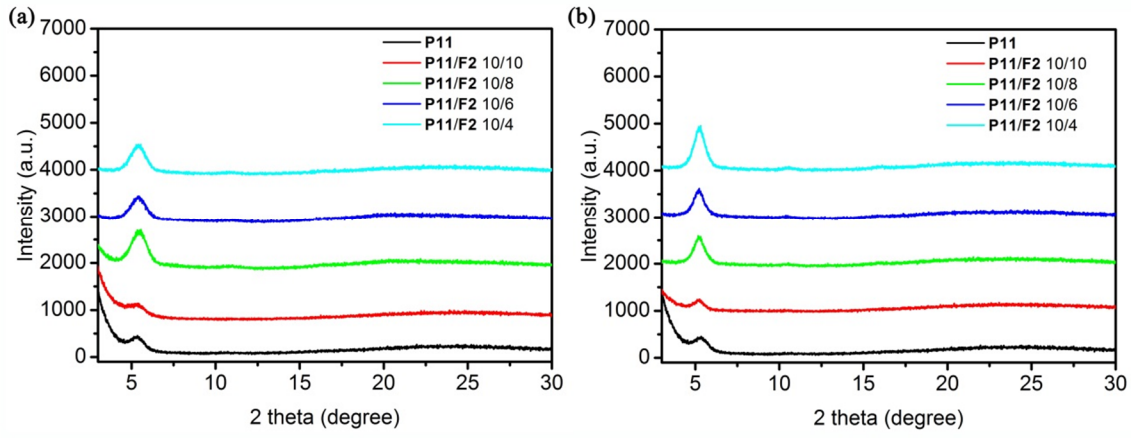


**Figure 4.7** Drop-cast thin-film XRD profiles of **P11** blended with **F2** at different weight ratios on glass substrate (a) as-cast; (b) thermal annealed at 110 C for 15 min

### 4.3.2 AFM investigations on the P11/F2 blend films

To further investigate the morphology control over the **P11**/**F2** blends simply by adjusting the ratios of **P11**/**F2**, XRD measurements were carried out on the thin films of **P11**/**F2** blends at different weight ratios as shown in Figure 4.7. Each diffraction

micrograph shows a distinct (100) peak near 2θ of 5º with varied intensities. Such (100) peak corresponds to the d-spacing between each polymer chain at the vertical direction for the edge-on configuration.[13-15] All films show a d-spacing around 1.60 to 1.7 nm. As shown in Figure 4.7, before mixing with **F2**, **P11** has a d-spacing of 1.65 nm, and the d-spacing was increased to 1.71 nm for the 10/10 blend. Such d-spacing increase could be explained by the fact that thermal annealing helps the reorganization of the **F2** with **P11** due to the "three-point" hydrogen bonding interactions. A slight smaller d-spacing of 1.68 nm is observed for the 10/8 blend, indicating less **F2** intercalation between the polymer chains after thermal annealing than that in the fully complexed 10/10 case. All the films exhibited similar packing patterns which indicated that the attachments of **F2** did not change the way of **P11** to pack in the thin-film blends.

To further visualize the morphologies difference of such **P11**/**F2** blends at different weight ratios, atomic force microscopy (AFM) was employed to probe the morphologies for the thin films fabricated from **P11**/**F2** as shown in Figure 4.8. Upon thermal annealing, hydrogen bonding interactions and self-assembly between **P11** and **F2** played in cooperation to achieve favorable morphologies of the blends. The blend exhibits uniformly distributed nanofiber morphology at a **P11**/**F2** weight ratio of 10/10, where all the active hydrogen bonding sites on **P11** are filled with **F2** due to the "three-point" hydrogen bonding interactions (Figure 4.8a).

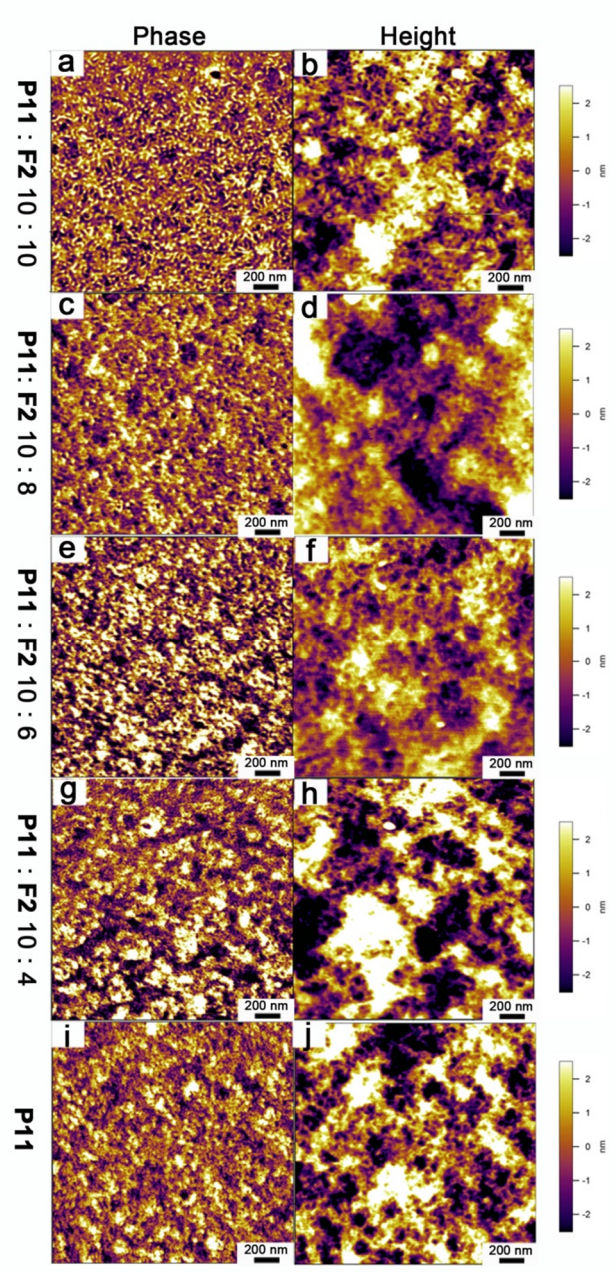


**Figure 4.8** AFM images (2 μm × 2 μm) of films employing **P11** with **F2** at different weight ratios, thermal annealed at 110 ºC for 15 min. Left column: phase images, right column: height images. Top to bottom: 10/10 (a and b); 10/8 (c and d); 10/6 (e and e); 10/4 (g and h); **P11** only (i and j)

The domain size of such nanofibers is ca. 20 nm and **P11** and **F2** are mixed in a homogenous way. Slight reduction of **P11**/**F2** weight ratio to 10/8 gives a coarser film and such nanofiber morphologies become less pronounced (Figure 4.8c). I speculate that less **F2** attachment on **P11** reduces the volume fraction of the block functionalized with hydrogen bonding moieties and results in slight different self-assembly patterns. Further decreasing the **P11**/**F2** ratio to 10/6 and 10/4 sees even less nanofiber features, in which the 10/4 blend resembles that of **P11** itself as shown in Figure 4.8 e to i. Again, the morphology controllability could be simply realized by adjusting the fullerene ratios in the **P11**/**F2** blend.

### 4.4 Tunable morphologies of P11/F2 blends in solution

Polythiophenes were reported to form nanofibers in solution by adding a "bad" solvent to a "good" solvent, known as the mixed-solvent method, which could improve the solar cell performances employing such nanofibers as active layers due to their enhanced charge separation and transport efficiencies.[16-19] Yang and his coworkers reported that P3HT could form nanofibers by slow addition of a "bad" solvent - hexanes into well-dissolved P3HT solution in *o*-dichlorobenzene.[20] Cho and his coworkers also disclosed another way of preparing P3HT nanofibers in the presence of PCBM in situ by adding cyclohexanone into their chlorobenzene solutions.[21] The formation of P3HT nanofibers was indicated by the vibronic peaks (ca. 560 nm and 600 nm) in their UV-vis spectra solution. In order to explore the influence of hydrogen bonding moieties on the nanofibers formation of **P11**, **P11** was first dissolved in chlorobenzene(CB) and then in which hexanes were slowly added to induce the nanofibers formation. In addition, the

self-assembled morphologies of **P11**/**F2** in solution were also explored when **F2** was added in situ at different weight ratios.

### 4.4.1 UV-vis measurements

With gradual addition of hexanes, the UV-vis spectra of **P11** solution showed a red-shift from 455 nm to 462 nm as shown in Figure 4.9 and Figure 4.10a, indicative of aggregates formation. Interestingly, no observable peak shift was spotted when the ratio of hexanes in CB was increased from 1/6 (vol/vol) to 1/3 (vol/vol). Besides, no vibronic peaks were observed for the 1/2 (vol/vol) solution, suggesting strong interactions from self-complementary hydrogen bonding preventing the packing of P3HT block in **P11** in a packed way.

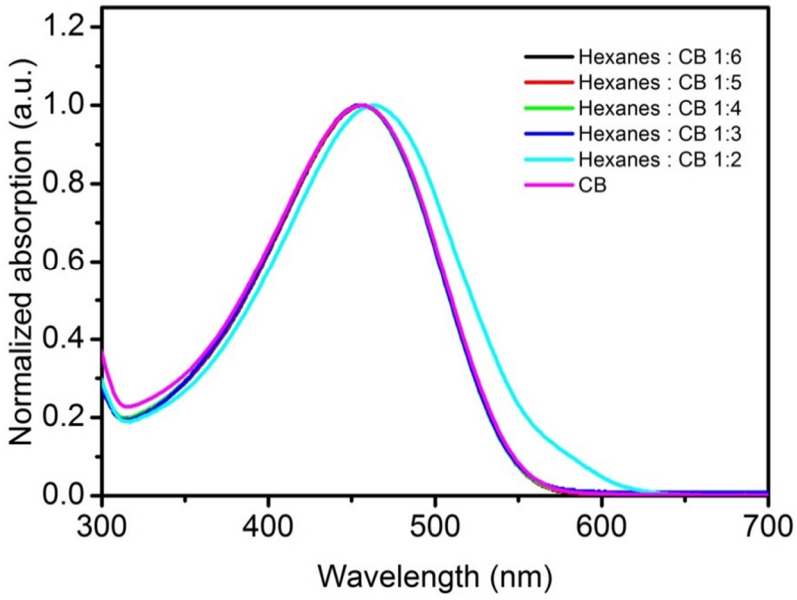


**Figure 4.9** UV-vis spectra of solution of **P11** in hexanes/CB system at different ratios (0.2 g/mL)

Further TEM investigations confirmed the micelles formation in the 1/2 (vol/vol) solution and the result was shown in Figure 4.10b. The micelles of **P11** have a width of 7.27 ± 0.73 nm, the length of which ranges from ca. 50 nm to over several hundred nanometers. Surprisingly, the width of **P11** micelles is shorter than that of reported P3HT of similar molecular weight, which is usually around 15 nm.[22,23] This is probably caused by the hydrogen bonding block of **P11** segregation in the presence of hexanes due to self-complementary hydrogen bonding interactions (intrachain and interchain), which forced the block segment less stretched than that of P3HT case.

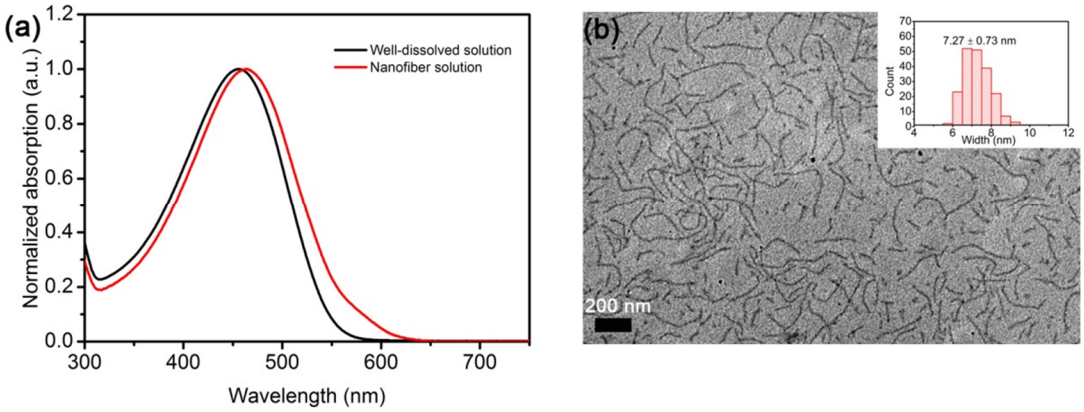


**Figure 4.10** (a) UV-vis spectra of well-dissolved solution and micelles solution of **P11** (0.2 mg/mL); (b) TEM image of **P11** grown from hexanes/ CB (1/2, vol/vol) solution (1 $mg \cdot mL^{-1}$).

Surprisingly, all the **P11**/**F2** solutions exhibited two vibronic patterns at ca. 560 nm and 610 nm when **F2** was mixed with **P11** before the hexanes addition as shown in Figure 4.11a. Such vibronic patterns are more pronounced in their films as shown in

Figure 4.11b in contrast to their bulk films spun casted from pure chlorobenzene under similar conditions.

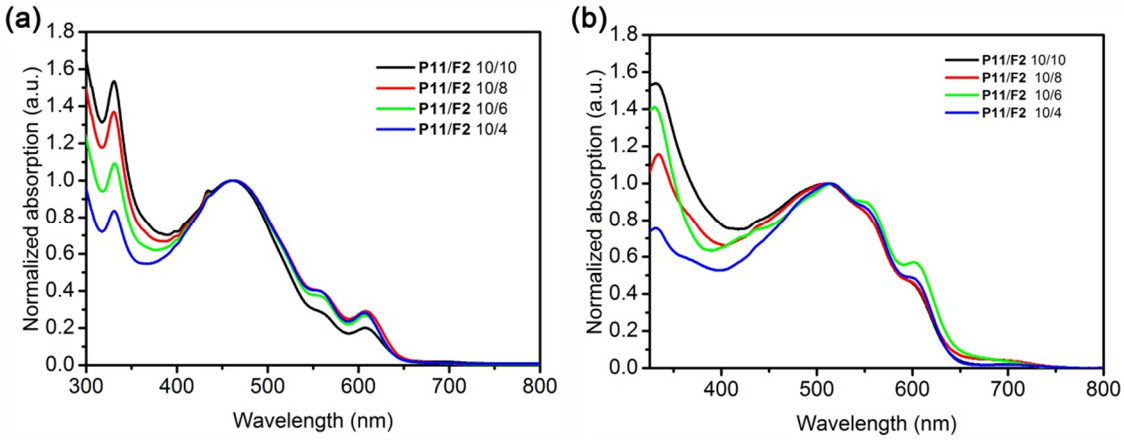


**Figure 4.11** UV-Vis spectra of **P11**/**F2** at different conditions (a) in solution, hexanes/CB (1/2 vol/vol); (b) spin-casted films from corresponding solutions, annealed at 150 ºC for 15 min.

### 4.4.2 TEM measurements

It is speculated that the presence of **F2** in **P11** solution could change the packing pattern due to the dynamic attachment of **F2** onto **P11** through the "three-point" hydrogen bonding interactions. Therefore, TEM investigations on **P11**/**F2** solutions with different weight ratios were conducted to direct visualize the morphology differences. The samples were prepared by drop casting the corresponding **P11**/**F2** solutions (10mg/mL for **P11**) onto a TEM copper grid atop a filter paper to fast remove the excessive solvent. The results are shown in Figure 4.12. Interestingly, different morphologies in solution were observed in the **P11**/**F2** blend solutions at different ratios,

which is probably due to the cooperative self-assembly between **P11** and **F2**, suggesting the tunable morphologies achieved by simply adjusting the contents of **F2** in the blend.

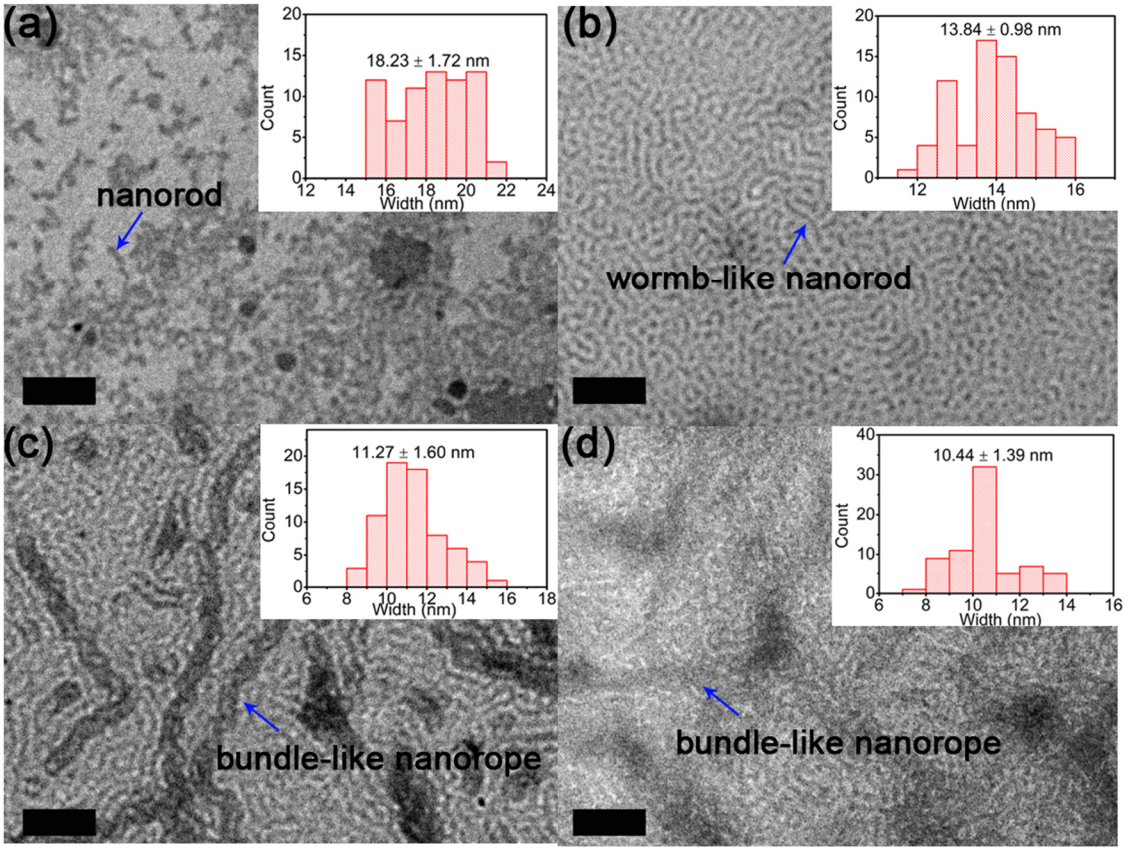


**Figure 4.12** TEM images of **P11**/**F2** solutions at different weight ratios in hexanes/CB (1/2 vol/vol); (a) 10/10; (b) 10/8; (a) 10/6; (b) 10/4. The concentration for **P11** is 10 mg/mL. The scale bar is 200 nm.

Specifically, when **F2** was incorporated into **P11** solution, controlled self-assembly of **P11** with **F2** was achieved as evidenced by the nanorods formation from the solutions with varied widths. Interestingly, the widths of the nanorods decreased with the contents of **F2** in the **P11**/**F2** solution, from 18.23 nm ± 1.73 nm for the 10/10 blend

solution to 13.84 ± 0.98 nm for 10/8 solution, and then decreased to 11.27 nm ± 1.60 nm to 10.44 ± 1.39 nm for the 10/6 and 10/4 solutions as shown in Figure 4.12(inset). It is worthy to note that the width of those **P11**/**F2** complexes in solutions are much bigger than that of **P11** solution alone, indicative of **F2** inclusion into those nanorods and possible unwinding of the hydrogen bonding block segments through the complexation with **F2**.

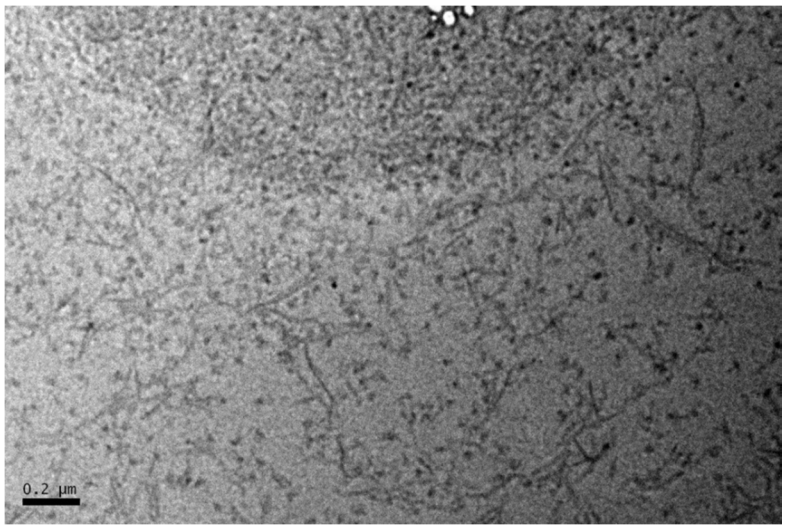


**Figure 4.13** TEM images of **P11**/**F2** solution at 10/4, in hexanes/CB (1/2 vol/vol), the concentration of **P11** in the solution mixture is 10 mg/mL. The scale bar is 200 nm.

Surprisingly, unexpected bigger aggregates for the **P11**/**F2** solutions at different ratios are also observed, especially when there are free hydrogen bonding sites on the polymer **P11**. As for the 10/8 solution (Figure 4.12b), regular womblike micelles with the length of 60 nm to 200 nm were observed, which has never been reported before for the all-conjugated polymers. The womblike micelles are longer than that of 10/10 solution, implying the interactions with free hydrogen bonding sites on **P11** may be responsible for

the difference. Less **F2** content in the 10/6 solution gives appreciable bundlelike nanoropes with ca 50 nm wide and several micrometers long (Figure 4.12c). Further decreasing **F2** concentration in the 10/4 solution presents more bundled nanoropes, ranging from 80 nm to 100 nm wide (Figure 4.12d). Besides the nanoropes, thinner micelles were also spotted in the 10/4 solution, suggesting that self-assembly of pure **P11** polymer competes with its **P11**/**F2** complex with less fullerenes **F2** present (Figure 4.13).

### 4.4.3 Possible P11/F2 nanostructure formation mechanism

Given that hexanes does not solvate the hydrogen bonding block but dissolves the P3HT block, solvent induced aggregation of the BCP **P11** would occur upon slow additions of hexanes into **P11** solution in chlorobenzene. As shown in Figure 4.14, I propose, with regard to **P11** solution alone, that hexanes will drive the hydrogen bonding block segment (in red color) to segregate from the disfavorable solvent and may intertwine with each other due to self-complementary hydrogen bonding interactions; whereas the P3HT block segment (the block in blue color) are solvated due to its less polar nature. As a result, the red blocks stay inside to form a sunflower-like unimer which then aggregates along its axis in a vertical way through hydrogen bonding interactions repeatedly to form the micelles.

The attachment of **F2** onto **P11** reduces the chance for self-complementary hydrogen bonding interactions between **P11** due to a stronger "three-point" hydrogen bonding interactions between **P11** and **F2**. Attachments of **F2** onto **P11** also increase the volume fraction of the red block and unfold the polymer chain to render the hydrogen bonding sites available for **F2**. When **F2** are attached, the red blocks with pendant

fullerenes prefer to orient perpendicular to each other in a fully stretched way where the blue blocks could pack tightly through the alkyl side chain vertically in an interdigitated way. Further stacking through π-π interactions gives the nanofibers as shown in Figure 4.14. Complete occupation with **F2** on **P11** (10/10) leaves no spot for the nanofibers to interact with each other through hydrogen bonding and results in short nanorods or nanodots. When there are some empty hydrogen bonding sites (10/8) on **P11**, **P11**/**F2** nanorods could interact with each other through weak hydrogen bonding but could not interplay with neighboring polymer chains due to limited interactions, however, it could bring those nanorods closer to present the womblike morphologies.

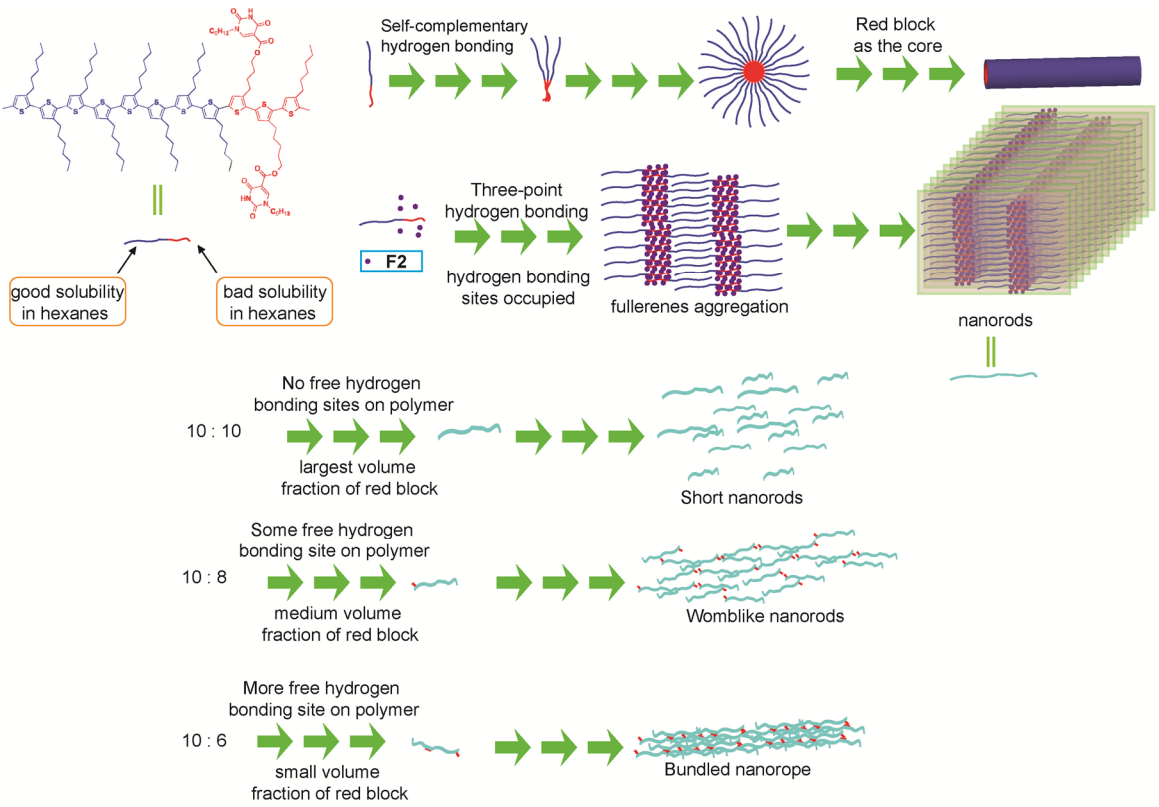


**Figure 4.14** Schematic illustration of **P11** micelle formation and nanostructures of **P11**/**F2** solution at different weight ratios.

With more free hydrogen bonding sites available on **P11**, **P11**/**F2** (10/6) nanorods could crosslink physically with each other in a more likelihood as shown in Figure 4.13c and Figure 4.14, in which two parallel nanorods twist with each other to form a doubled bundle, and the doubled bundle then increases again through hydrogen bonding which then elongates along the same direction to form the giant nanorope, which is supported by the width change from the nanorods to nanoropes. As for the 10/4 case, both **P11** nanofibers and **P11**/**F2** nanorods and nanoropes are coexisting since less **F2** could leave more free hydrogen bonding sites on **P11** where **P11** itself could segregate to form the micelle nanofibers but at the same time allow **P11**/**F2** to self-assemble in a similar manner with that of **P11**/**F2** at other ratios.

### 4.5 Solar cells fabrication from P11/F2 blends as active layers

To evaluate the efficacy of such "three-point" hydrogen bonding in modulating the final photovoltaic performance, BHJ solar cell devices were fabricated employing both **P11**/**F2** chlorobenzene solutions (conventional) and **P11/F2** hexanes/chlorobenzene (1/2 vol/vol) solutions (NF) as the active layers. Thermal annealing was employed to improve the cell performances. All solar cells adopted the structure of ITO/$MoO_3$ (10 nm)/active layer (ca. 100 nm)/Al (100 nm), which were constructed under identical conditions. The results were shown in Table 4.1 for the conventional and Table 4.2 for the **P11**/**F2** NF solar cells.

### 4.5.1 Solar cells employing P11/F2 well-dissolved solutions

It is worth noting that the 10/10 blend has the best photovoltaic performance, giving a PCE of 1.20 % ± 0.10% as shown in Table 4.1.

**Table 4.1** Device performance of conventional **P11** /**F2** at different weight ratios.[a]

| Condition | **P11**/**F2**[b] | *PCE* (%)[c] | $J_{SC}$ (mA/cm$^{-2}$)[c] | $V_{OC}$ (V)[c] | *FF*[c] |
|---|---|---|---|---|---|
| As-cast | 10 : 10 | 0.99 ± 0.05 | 4.68 ± 0.24 | 0.63 ± 0.00 | 0.33 ± 0.01 |
| | 10 : 8 | 0.81 ± 0.04 | 3.80 ± 0.20 | 0.64 ± 0.01 | 0.33 ± 0.01 |
| | 10 : 6 | 0.86 ± 0.10 | 3.90 ± 0.27 | 0.68 ± 0.02 | 0.32 ± 0.02 |
| | 10 : 4 | 0.46 ± 0.03 | 2.23 ± 0.09 | 0.68 ± 0.00 | 0.30 ± 0.01 |
| Optimized[d] | 10 : 10 | 1.20 ± 0.10 | 5.37 ± 0.32 | 0.65 ± 0.00 | 0.34 ± 0.01 |
| | 10 : 8 | 0.93 ± 0.06 | 4.14 ± 0.23 | 0.65 ± 0.01 | 0.35 ± 0.01 |
| | 10 : 6 | 0.91 ± 0.14 | 4.52 ± 0.39 | 0.65 ± 0.01 | 0.31 ± 0.02 |
| | 10 : 4 | 0.48 ± 0.02 | 2.75 ± 0.15 | 0.64 ± 0.01 | 0.28 ± 0.00 |

[a]Spin-cast at 400 rpm for 30s from chlorobenzene solution, with 2 vol% MeOH added.
[b]All ratios by weight. [c] An average of five cells. [d]Thermal annealing at 110 °C for 15 min.

The 10/8 and 10/6 blends give comparable results, with PCEs around 1%, indicating that slightly less fullerenes does not sacrifice the photovoltaic properties of the solar cells. This phenomenon implies that self-assembly of the **P11**/**F2** complex creates amenable morphology offsetting the fullerene loss in the blend. However, further reducing the **F2** content as in the 10/4 blend exhibits the worst PCE. As revealed by AFM, the 10/10 blend film presents the most homogenous nanofibers morphology via AFM (Figure 4.8a). Reducing the **F2** contents in the blends gives worse performance with less pronounced nanofibers morphology (Figure 4.8b-j).

I speculate that such nanofibers morphologies in the blend films may be good for solar cells. Indeed, the as-cast film of 10/6 had more pronounced nanofibers feature than that of 10/8 as shown in Figure 4.15, and the 10/6 blend happened to have a higher PCE of 0.86% ± 0.10% than that of 10/8 (0.81% ± 0.04%) as shown in Table 4.1. Less **F2** present in the blend in the 10/4 case would leave the self-assembly of **P11** in domination that the morphologies of 10/4 were reminiscent of that of **P11** itself alone.

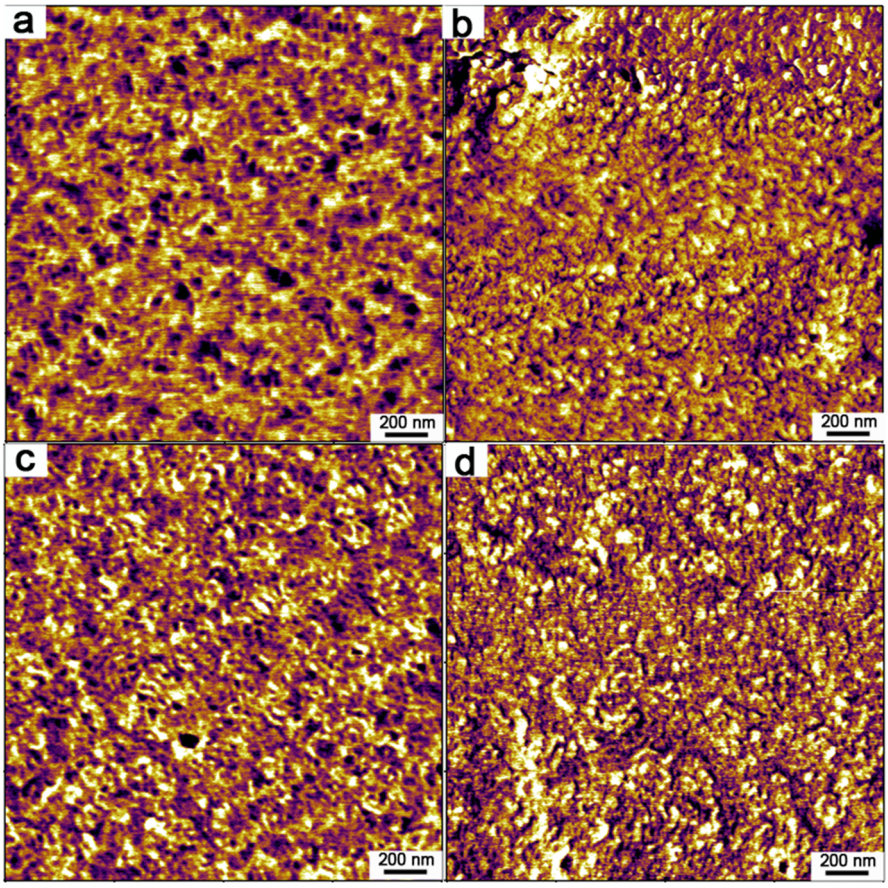


**Figure 4.15** AFM phase images (2 μm × 2 μm) of as-cast devices employing **P11** with **F2** at different weight ratios. (a) 10/10; (b) 10/8; (c) 10/6; (d) 10/4.

For the as-cast devices, it showed decreased power conversion efficiency (PCE) with less **F2** loadings of the **P11**/**F2** blends in general, from 0.99% ± 0.05% (10/10) to 0.46% ± 0.03% (10/4). Such photovoltaic performance difference seen by the short-circuit current ($J_{SC}$) dropped from 4.68 ± 0.24 mA/cm$^{-2}$ (10/10) to 2.23 ± 0.09 mA/cm$^{-2}$ (10/4), probably due to fewer **F2** involved in the charge separation and transport. Interestingly, the PCE of 10/6 blend was slightly higher than that of 10/8 blend, suggesting that self-assembly between **P11** and **F2** through complementary hydrogen bonding interactions could overcome the disadvantages of less **F2** loadings to achieve better performance. Besides, it is worth noting that the corresponding open-circuit voltage ($V_{OC}$) exhibited the opposite trend which increased from 0.63 V for the 10/10 blend to 0.68 V for the 10/6 and 10/4 blends, suggesting more amorphous nature of the **P11**/**F2** blends which could bring the HOMO level of **P11** further down.[24]

For the optimized devices, similar trend for the PCE drop was observed with decreasing **F2** concentration in the blends. However, the optimized ones exhibited higher PCEs than their as-cast devices. This slight improvement could be possibly due to the increased $J_{SC}$ that is associated with enhanced charge transport efficiency after thermal annealing. Interestingly, $V_{OCs}$ of all four optimized devices changed to ca. 0.65 V after thermal annealing, which are still higher than the optimized devices of **P8** or P3HT in our previous report.[2] This probably could be also explained by the fact that the amorphous nature of **P11** that possesses a deeper HOMO level.

### 4.5.2 Solar cells employing P11/F2 NF solutions

Further investigation of employing **P11**/**F2** NF solutions at different weight ratios to fabricate the corresponding solar cell devices were studied using those blends as active layers. The results are summarized in Table 4.2 and Figure 4.16. As shown in Table 4.2, such nanorods are beneficial to the solar cell performances as seen from the enhanced photovoltaic performances with higher PCE, $J_{SC}$ and $V_{OC}$ for the 10/8 to 10/4 cases, and thermal annealing at 150 °C gave improved PCE mainly due to increased $J_{SC}$. The $V_{OC}$ of the optimized devices showed slightly higher values (around 0.67 V) than that of their conventional BHJ ones, which probably due to the decreased crystallinity of those nanorods probably due to the inclusion of **F2**.

**Table 4.2** Device performance of **P11** /**F2** nanostructures as active layer.[a]

| Condition | **P11**/**F2**[b] | *PCE* (%)[c] | $J_{SC}$(mA/cm$^{-2}$)[c] | $V_{OC}$ (V)[c] | *FF*[c] |
|---|---|---|---|---|---|
| As-cast | 10 : 10 | 0.56 ± 0.06 | 2.78 ± 0.09 | 0.67 ± 0.00 | 0.29 ± 0.02 |
| | 10 : 8 | 1.20 ± 0.05 | 5.04 ± 0.18 | 0.67 ± 0.01 | 0.36 ± 0.02 |
| | 10 : 6 | 0.90 ± 0.07 | 3.65 ± 0.34 | 0.68 ± 0.01 | 0.36 ± 0.01 |
| | 10 : 4 | 0.54 ± 0.04 | 2.83 ± 0.16 | 0.67 ± 0.01 | 0.29 ± 0.01 |
| Optimized[d] | 10 : 10 | 0.27 ± 0.00 | 2.13 ± 0.05 | 0.59 ± 0.01 | 0.21 ± 0.00 |
| | 10 : 8 | 1.67 ± 0.13 | 6.28 ± 0.38 | 0.66 ± 0.01 | 0.40 ± 0.01 |
| | 10 : 6 | 1.30 ± 0.07 | 5.97 ± 0.34 | 0.68 ± 0.00 | 0.32 ± 0.01 |
| | 10 : 4 | 0.54 ± 0.04 | 2.83 ± 0.16 | 0.67 ± 0.01 | 0.29 ± 0.01 |

[a]Spin-cast at 400 rpm for 30s from chlorobenzene solution [b]measured by weight ratios. [c]an average of five cells. [d]thermal annealing at 150 °C for 15 min.

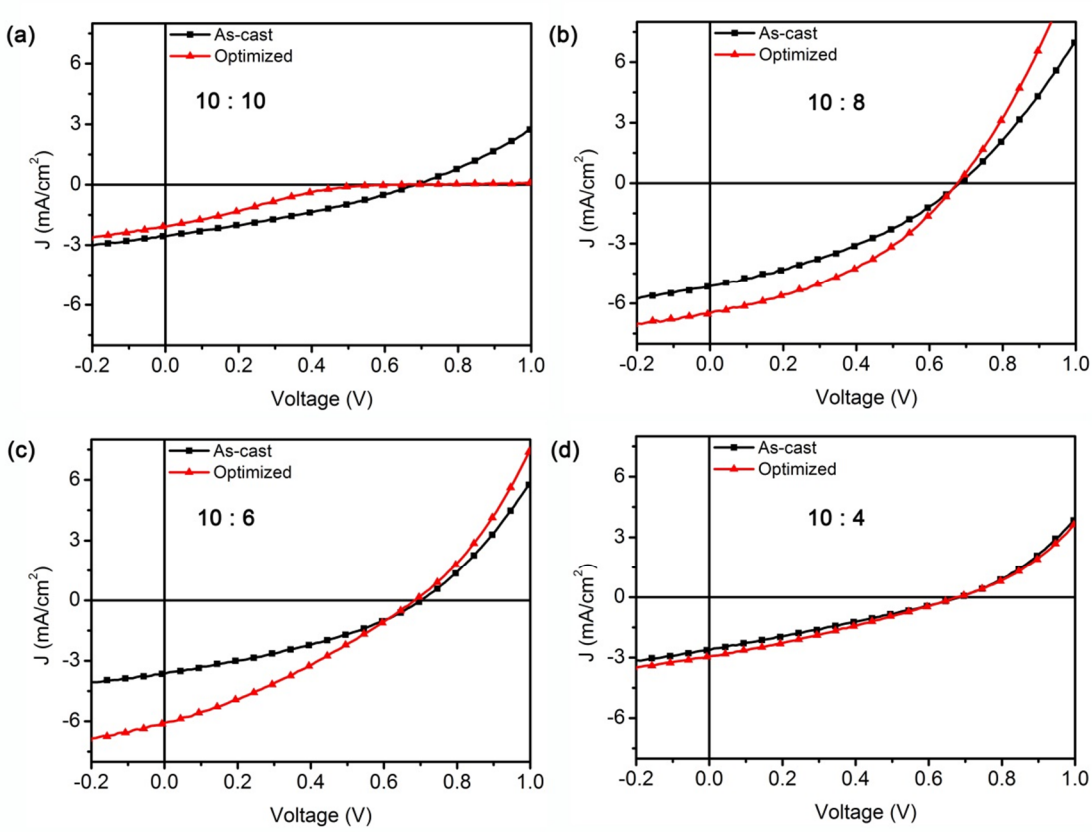


**Figure 4.16** I-V curves (under simulated AM1.5 G illumination) of **P11**/**F2** nanorods as active layer at various weight ratios. Thermal annealed at 150 ºC for 15 min.

Surprisingly, the 10/10 blend showed lower PCE than its conventional BHJ counterpart listed in Table 4.1, which even deteriorated upon thermal annealing as evidenced by a S-kink developed in their I-V curves (Figure 4.16 a). One possible reason could be that complete inclusion of **F2** caused imbalanced charge transport. The 10/8 and 10/6 blends showed the highest PCEs of 1.67% ± 0.13% and 1.30% ± 0.07%, which were about 30% more than their conventional BHJ solar cells. Currently, they are the best two performing solar cells in the **P11**/**F2** system herein. I suspected that the evenly formed

worm-like nanorods probably contributed to these highest PCEs. Indeed, the 10/8 to 10/4 blend were able to form those nanorods with different superstructures and these nanostructures showed improved photovoltaic performances. The wormlike nanorods in the 10/8 blend lack of obvious bigger aggregation formation might be the reason that it outperformed the 10/6 and 10/4 blends.

### 4.6 Conclusion

In summary, I successfully synthesized a polythiophene block copolymer functionalized with ca. 22% isoorotic acid moieties. The higher functional group concentration of the isoorotic acid moieties on the polymer has minimum impact on the optical, electronic and thermal properties. "Three-point" hydrogen bonding interactions between **P11** and **F2** worked in cooperation with self-assembly of **P11**/**F2** complex to achieve tunable morphologies as confirmed by UV-Vis spectroscopy, thin-film XRD, AFM and TEM. Such morphology tunability was simply achieved by changing **P11** and **F2** ratio in the blend. Correlation between morphologies and photovoltaic performances were established. Nanofibers morphologies in the conventional BHJ blends were good for the cell performances in the current **P11**/**F2** system. Such morphology tunability was also found in their solutions by slow adding hexanes into **P11**/**F2** solutions in chlorobenzene, which rendered the morphologies changing to nanorods with varied widths for the **P11**/**F2** complexes from the nanowires for pure **P11** solutions. The 10/8 to 10/4 blends showed wormlike nanowires which turned out to improve their solar cell performances, and the PCEs of 10/8 and 10/6 blends showed over 30% PCE increase than their

conventional BHJ solar cells. I postulated such PCE enhancement aroused from the wormlike nanowires morphologies which facilitated the exciton diffusion and charge separation.

### 4.7 Future work

By comparing the photovoltaic performances of **P8**/**F2** and **P11**/**F2** solar cells, I found that solar cells fabricated from **P11**/**F2** blends underperformed those from **P8**/**F2** blends, which in turn supported the conclusion in Chapter 3. A longer pure P3HT block in the BCP is essentially important in the current BCP/fullerene system to achieve high solar cells performances. Indeed, we found that the **P11**/**F2** solar cell devices outperformed the **P4**/**F1** cells, suggesting that **F2** is superior over **F1** as an electron acceptor. Moreover, by adding hexanes into the chlorobenzene solution of **P11**/**F2**, different nanostructures were obtained in a controlled way. Furthermore, solar cells fabricated from **P11**/**F2** nanostructures have shown better photovoltaic performances than their conventional BHJ ones employing **P11**/**F2** as active layers. The tunability of such nanostructures is simply achieved by controlling the amount of **F2** added in the solution. However, more work is needed to better understand the self-assembly of **P11**/**F2** blend in solution. Nonetheless, this fact enlightened me on the case of **P8**/**F2**. If I adopt similar methodology to prepare **P8**/**F2** nanostructures in solution by engineering the core-shell structure of **P8** where the pure P3HT block as the core while the hydrogen bonding block as the peripheral shell, could I obtain better solar cells than their conventional BHJ ones? Moreover, does the morphology tunability still exist in the **P8**/**F2** case? That's what I am going to discuss in the next chapter.

## 4.8 Experimental

### 4.8.1 Materials and general methods

All reagents and solvents were used as received from Sigma-Aldrich or Alfa Aesar unless otherwise noted. All the monomers were prepared in the reported way. THF was distilled from Na/benzophenone prior to use. Anhydrous chloroform and dichloromethane were obtained by distillation over $CaH_2$ and degassed through several freeze-pump-thaw cycles. 300.13 MHz $^{1}H$ and 75.48 MHz $^{13}C$ NMR spectra were recorded on a Bruker Avance III Solution 300 spectrometer. All solution $^{1}H$ and $^{13}C$ NMR spectra were referenced internally to solvent signals. Size exclusion chromatography (SEC) analyses were performed in chloroform with 0.5% (v/v) triethylamine (1 mL/min) using a Waters Breeze system equipped with a 2707 autosampler, a 1515 isocratic HPLC pump and a 2414 refractive index detector. Two styragel columns (Polymer Laboratories; 5 μm Mix-C), which were kept in a column heater at 35 °C, were used for separation. The columns were calibrated with polystyrene standards (Varian). Ultraviolet-Visible (UV-Vis) absorption spectra were recorded on a Shimadzu UV-2401 PC spectrometer over a wavelength range of 240-800 nm. Fluorescence emission spectra were obtained using a Varian Cary Eclipse Fluorimeter. Differential scanning calorimetry (DSC) measurements were performed on a Mettler Toledo DSC STAR$^{e}$ system with ca. 10 mg sample and at a scan rate of 10 °C / min. The results reported are from the second heating cycle. Cyclic Voltammetry was performed at 25 °C on a CH Instrument CHI604xD electrochemical analyzer using a glassy carbon working electrode, a platinum wire counter electrode and a Ag/AgCl reference electrode

calibrated using ferrocene redox couple (4.8 eV below vacuum). Atomic force microscopy (AFM) images were obtained on an Asylum MFP3D AFM instrument operated under tapping mode. Transmission electron microscopy (TEM) images were taken on a JEOL 2010 high resolution TEM operated under 200 kV. Thin film X-ray diffraction (XRD) patterns were recorded on a Rigaku SmartLab diffractometer.

### 4.8.2 Synthesis of BCPs P9-P11

BCPs **P9-P11** are obtained based on a similar strategy adopted for synthesizing **P5-P8** in Chapter 3. The difference lies in the conversion ratio of monomer **M1** and catalyst and monomer ratio. The $^{1}$H NMR spectra of **P9-P11** highly resemble their counterparts in P5-P8 in Chapter3 but with higher isoorotic acid moieties concentration.

**Block copolymer P9 Poly(3-hexylthiophene)-b-Poly(3-(6'-dimethyl-tert-butylsilyloxyl) hexylthiophene)**. Two three-necked round-bottomed flasks (250 mL and 50 mL) equipped with stopcock and septa were flamed dried under high vacuum and cooled to room temperature under $N_2$. Monomer **M1** (1.482 g, 3.972 mmol) and LiCl (168 mg, 3.972 mmol) was placed in the 250 mL flask under $N_2$, and then evacuated under high vacuum to remove any residual water and oxygen. After adding dry THF (40 mL) into the flask via a syringe, the solution was cooled to 0 °C. A 2 M solution of *i*-PrMgCl in THF (2 mL, 3.972 mmol) was added via syringe and the mixture was stirred at 0 °C for 30 min (solution 1). In the other 50 mL flask, 0.67 g (1.324 mmol) 3-(6'-dimethyl-tert-butylsilyloxyl) hexylthiophene was first reacted with 0.67 mL *i*-PrMgCl in the presence of 56.1mg LiCl (1.324 mmol) in 20 mL THF (solution 2) to yield **M2**. Solution 1 was heated up to 35 °C and Ni(dppp)$Cl_2$ catalyst (21.53 mg, 0.03972 mmol),

which was suspended in 5 mL dry THF, was added in one portion. The reaction mixture was stirred at 35 °C to polymerize for 12 min, an aliquot was withdrawn with a syringe and injected into a methanol solution to give **P1** for SEC analysis (RI, $CHCl_3$, 1 mL/min: **P9**: $M_n$ = 17396, $M_w$ = 19105, *PDI* = 1.10). Solution 2 containing **M2** was then transferred to solution **1** via a cannula. The resulting red solution was stirred at 35 °C for 40 min before 0.5 mL EtMgCl solution (2M in THF) was added. The polymer was isolated by precipitation into MeOH and successively washed by Soxhlet extraction using methanol, acetone, and chloroform. The polymer was recovered by precipitation of the chloroform solution into methanol and dried under high vacuum to give a black solid (0.86 g, 89%). $^1$H NMR (300.13 MHz, $CDCl_3$, δ): 0.041 (s), 0.070 (s), 0.89-0.94 (m), 1.25-1.71 (m), 2.81(t), 3.61 (t), 6.98 (s). SEC (RI, $CHCl_3$ 1 mL/min): $M_n$ = 28,741, $M_w$ = 34,493, *PDI* = 1.20;

**Block copolymer P10 Poly(3-hexylthiophene)-b-Poly(3-(6'-hydroxyl)hexylthiophene)**. In a 100 mL Schlenk flask was added 750 mg polymer **P9** and 100 mL THF under $N_2$. The solution became clear after stirring at 60 °C for ca. 30 min. Tetrabutylammonium fluoride (TBAF) solution (2 mL, 2M in THF) was then added dropwise via syringe. The reaction mixture was kept stirring at 60 °C for 8 h and concentrated under reduced pressure to ca. 5 mL. **P10** was recovered as a black solid by precipitation into a mixture of methanol and acetone (1/1, v/v) and dried under vacuum overnight (650 mg 88%). $^1$H NMR (300.13 MHz, $CDCl_3$, δ): 0.92 (t), 1.25-1.73 (m), 2.04 (s), 2.81 (t), 3.66 (t), 6.98 (s). SEC (RI, $CHCl_3$ 1 mL/min): $M_n$ = 25,548, $M_w$ = 30.204, *PDI* = 1.18.

**Block copolymer P11 Poly(3-hexylthiophene)-b-Poly(3-(6'-(1-hexylisoorotic acid amido))hexylthiophene)**. In a 25 mL three-neck flask equipped with a condenser and septa was added 246 mg (1.02 mmol) 1-N-hexylisoorotic acid and 2 mL thionyl chloride under nitrogen, and the solution was refluxed for 8 h to give the corresponding acid chloride. The excess $SOCl_2$ was removed in vacuo and the residue was dissolve in 10 mL of dry $CHCl_3$ and the solvent was removed under reduced pressure to get rid of the residual $SOCl_2$. In the other 250 mL Schlenk flask was added 200 mg **P10** and 30 mL $CHCl_3$ under nitrogen. The reaction mixture was kept stirring at 60 $^{\circ}$C for 20 min until all polymer dissolves and then triethylamine (0.3 mL) was added into the polymer solution. The acid chloride was dissolved in 15 mL $CHCl_3$ and transferred into the polymer solution via cannula. The reaction was kept at 60 $^{\circ}$C for another 8 h and concentrated under reduced pressure to ca. 5 mL. The crude polymer was isolated by precipitation into methanol and successively Soxhlet extracted using methanol, acetone, and chloroform. The chloroform solution was concentrated and precipitated into MeOH to give **P11** (200 mg, 78%). $^1$H NMR (300.13 MHz, $CDCl_3$, δ): 0.89 (t), 1.25-1.71 (m), 2.80 (t), 3.77 (t), 4.29 (t), 6.98 (s), 8.20 (s). SEC (RI, $CHCl_3$ 1 mL/min): $M_n$ = 30,600, $M_w$ = 37,900, *PDI* = 1.3.

### 4.8.3 Nanostructures preparation of P11/F2 in solution

In a dry vial was added 5 mg **P11** which was dissolved in 0.5 mL chlorobenzene. The solution was heated at 100 ºC for 1 h in a nitrogen glovebox and then stirred at room temperature for another 1 h. Hexanes (250 μL) were added in a slow way with agitation via a microsyringe. The solution continued to age with stirring at room temperature for

another 24 h before analysis. The color change of the solution indicated the formation of the micelles in solution. The **P11**/**F2** nanostructures at different ratios were prepared using the same recipe.

### 4.8.4 Solar cell fabrication and testing

The solar cell devices adopt a structure of ITO/$MoO_3$/active layer/Al. Thin films of active layers were spun-cast from blend solutions prepared by dissolving **P11** and **F2** at predetermined weight ratios in chlorobenzene and the concentration of **P11** was kept at 1 wt%. All solutions were stirred at 100 °C for 10 h in a nitrogen glove box (Innovative Technology, model PL-He-2GB, $O_2$ < 0.1 ppm, $H_2O$ < 0.1 ppm) before device fabrication. Solar cell devices were fabricated according to the following procedure: ITO-coated glass substrates (China Shenzhen Southern Glass Display. Ltd, 8 Ω/□) were cleaned by ultrasonication sequentially in detergent, DI water, acetone and isopropyl alcohol, each for 15 min. These ITO-coated glass substrates were further treated by UV-ozone (PSD Series, Novascan) for 45 min before being transferred to a nitrogen glove box (Innovative Technology, model PL-He-4GB-1800, $O_2$ < 0.1 ppm, $H_2O$ < 0.1 ppm) for $MoO_3$ deposition. $MoO_3$ (10 nm) was deposited using an Angstrom Engineering Åmod deposition system at a base vacuum level < $7 \times 10^{-8}$ Torr. The unfiltered **P11**/**F2** blend solution was used for spin-coating on top of the $MoO_3$ layer at 400 rpm for 30s. Al (100 nm) was thermally evaporated through patterned shadow masks as anodes. Current−voltage (I−V) characteristics were measured by a Keithley 2400 source-measuring unit under simulated AM1.5G irradiation (100 mW/cm$^{-2}$) generated by a Xe arc-lamp based Newport 67005 150-W solar simulator equipped with an AM1.5G filter.

The light intensity was calibrated by a Newport thermopile detector (model 818P-010-12) equipped with a Newport 1916-C Optical Power Meter.

## 4.9 References


(1) Li, F.; Yang, J.; Qin, Y. *J. Polym. Sci., Part A: Polym. Chem.* **2013**, 51, 3339.

(2) Li, F.; Yager, K. G.; Dawson, N. M.; Yang, J.; Malloy, K. J.; Qin, Y. *Macromolecules* **2013**, 46, 9021.

(3) Stefan, M. C.; Bhatt, M. P.; Sista, P.; Magurudeniya, H. D. *Polym. Chem.* **2012**, 3, 1693.

(4) Miyakoshi, R.; Yokoyama, A.; Yokozawa, T. *J. Am. Chem. Soc.* **2005**, 127, 17542.

(5) Yokoyama, A.; Miyakoshi, R.; Yokozawa, T. *Macromolecules* **2004**, 37, 1169.

(6) Iovu, M. C.; Sheina, E. E.; Gil, R. R.; McCullough, R. D. *Macromolecules* **2005**, 38, 8649.

(7) Loewe, R. S.; Ewbank, P. C.; Liu, J.; Zhai, L.; McCullough, R. D. *Macromolecules* **2001**, 34, 4324.

(8) Stefan, M. C.; Javier, A. E.; Osaka, I.; McCullough, R. D. *Macromolecules* **2009**, 42, 30.

(9) Li, F.; Dawson, N.; Yang, J.; Malloy, K.; Qin, Y. *Macromolecules* **2013**.

(10) Wu, P.-T.; Xin, H.; Kim, F. S.; Ren, G.; Jenekhe, S. A. *Macromolecules* **2009**, 42, 8817.

(11) Hou, J.; Chen, T. L.; Zhang, S.; Huo, L.; Sista, S.; Yang, Y. *Macromolecules* **2009**, 42, 9217.

(12) Colladet, K.; Fourier, S.; Cleij, T. J.; Lutsen, L.; Gelan, J.; Vanderzande, D.; Huong Nguyen, L.; Neugebauer, H.; Sariciftci, S.; Aguirre, A.; Janssen, G.; Goovaerts, E. *Macromolecules* **2006**, 40, 65.

(13) Kanai, K.; Miyazaki, T.; Suzuki, H.; Inaba, M.; Ouchi, Y.; Seki, K. *Phys. Chem. Chem. Phys.* **2010**, 12, 273.

(14) Chiu, M.-Y.; Jeng, U. S.; Su, M.-S.; Wei, K.-H. *Macromolecules* **2009**, 43, 428.

(15) Zhokhavets, U.; Erb, T.; Hoppe, H.; Gobsch, G.; Serdar Sariciftci, N. *Thin Solid Films* **2006**, 496, 679.

(16) Chen, J.-T.; Hsu, C.-S. *Polym. Chem.* **2011**, 2, 2707.

(17) Berson, S.; De Bettignies, R.; Bailly, S.; Guillerez, S. *Adv. Funct. Mater.* **2007**, 17, 1377.

(18) Jo, S. B.; Lee, W. H.; Qiu, L.; Cho, K. *J. Mater. Chem.* **2012**, 22, 4244.

(19) He, M.; Zhao, L.; Wang, J.; Han, W.; Yang, Y.; Qiu, F.; Lin, Z. *ACS Nano* **2010**, 4, 3241.

(20) Li, L.; Lu, G.; Yang, X. *J. Mater. Chem.* **2008**, 18, 1984.

(21) Kim, J.-H.; Park, J. H.; Lee, J. H.; Kim, J. S.; Sim, M.; Shim, C.; Cho, K. *J. Mater. Chem.* **2010**, 20, 7398.

(22) Ihn, K. J.; Moulton, J.; Smith, P. *J. Polym. Sci., Part B: Polym. Phys.* **1993**, 31, 735.

(23) Liu, J.; Arif, M.; Zou, J.; Khondaker, S. I.; Zhai, L. *Macromolecules* **2009**, 42, 9390.

(24) Tsoi, W. C.; Spencer, S. J.; Yang, L.; Ballantyne, A. M.; Nicholson, P. G.; Turnbull, A.; Shard, A. G.; Murphy, C. E.; Bradley, D. D. C.; Nelson, J.; Kim, J.-S. *Macromolecules* **2011**, 44, 2944.

# Chapter 5

# Nanofibers with Controllable Dimensions through Block Polythiophene Copolymer Self-Assembly and Hydrogen Bonding Interactions and Their Applications in Solar Cells

(This chapter is based on a manuscript in preparation)

## 5.1 Introduction

Over the past decade, nanofibers and nanowires self-assembled from conjugated polymers, e.g. poly(3-akylthiophene) (P3AT) in solution have received great deal of attention due to their unique properties in organic electronics.[1-5] Therefore, the preparations of such P3AT nanofibers have become the key consideration to access those desired optoelectronic properties. Generally, P3AT nanofibers (NFs) prepared in solution are mainly from two methods: (a) whisker method[6-10] in which a dilute solution of P3AT is heated in a marginal solvent, for example, toluene,[11,12] for complete dissolution before slowly cooling down of the heated solution for the nanofibers formation; (b) mixed-solvent method[13-15] where P3AT is completely dissolved in a good solvent first such as chlorobenzene then a "bad" solvent is added in a slow manner at room temperature to facilitate the nanofibers formation. The formation of P3AT nanofibers in solution was driven by P3AT crystallizations where the two untangled polymer chains stack through the side chain intercalations in a coplanar manner first, and then the formed one-dimensional aggregate packs through $\pi$-$\pi$ interactions perpendicular to the side chain

packing direction in an "edge-on" fashion to form the nanofibers.[9,16-19] Due to the increased crystallinity and charge mobilities of the P3AT NFs from the well packed polymer chains[18,20,21], solar cells fabricated from P3AT NFs exhibited higher power conversion efficiencies (PCEs) than their as-cast devices from the well-dissolved solutions due to its preorganzied morphologies. In the BHJ solar cells, e.g. the P3AT NFs/PCBM blends, PCBM could be added either after the preformed P3AT nanofibers[1,22-24] (preformed NFs) or in situ mixed with the P3AT together in solution to form the nanofibers[13,19,25,26] (in situ formed NFs). The order of PCBM addition in the P3AT nanofibers solution did not impact the solar cell device performance when careful optimizations were carried out. However, a weight ratio of 10/10 (wt/wt) or 10/8 (wt/wt) for P3AT NFs/PCBM is usually required to attain high PCEs, and less fullerene loadings fails to ensure its high photovoltaic properties and was less seen in literature. On the other hand, much attention has been paid to improving the PCEs and controlling the morphologies by tuning the synthetic parameters of the P3AT NF over the years, and the thermal stabilities of such P3AT NF/PCBM solar cells were less investigated.[27]

In Chapter 3, I described the synthesis of a polythiophene block copolymer selectively bearing 7% isoorotic acid moieties (**P8**) (Figure 5.1) and a 2, 6-diaminopyridine tethered fullerene (**F2**). Complementary hydrogen bonding interactions between the polymer and **F2** could form a "bottle-brush" type copolymer where the self-assembly modulated phase separation of the polymer/fullerene complexes offers thermally stable solar cells with ordered nanomorphologies.[28]

With an aim to pursue solar cells with higher PCEs by controlling the morphology of the active layers with those preformed nanofibers, I tentatively prepared the nanofibers of **P8** using a mixed-solvent method, and examined the **P8** nanofibers formation through mixing with PCBM or **F2** via UV-vis spectroscopy, X-ray diffraction (XRD) and transmission electron microscopy (TEM). Moreover, solar cells from **P8** NF/PCBM (**F2**) at a weight ratio of 10/4 as active layers both in the preformed and in situ formed situations were fabricated and tested. In addition, the thermal stabilities of the solar devices using **P8**/PCBM (**F2**) nanofibers were also investigated. As a control, I also fabricated and tested solar devices employing P3HT/PCBM nanofibers under the same conditions.

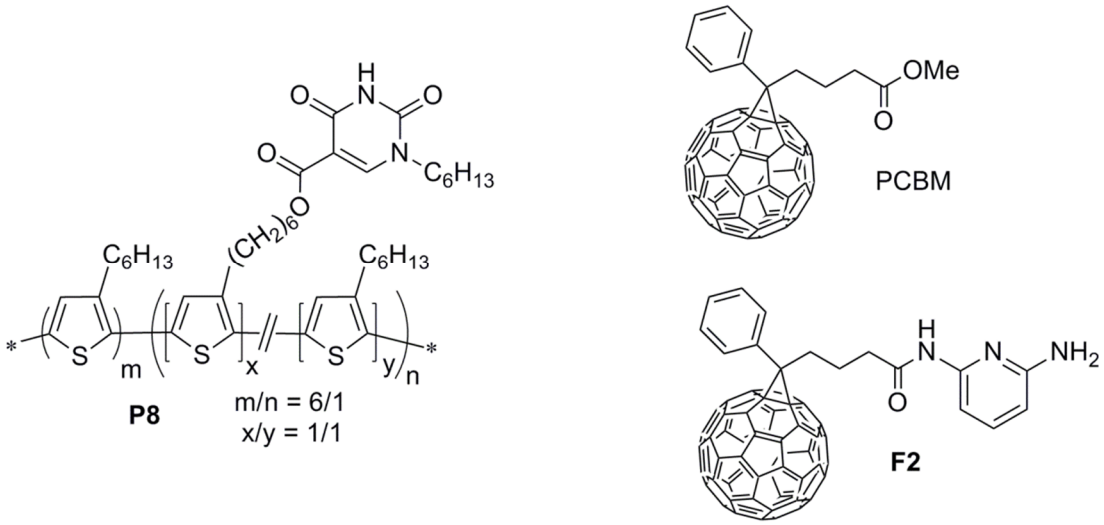


**Figure 5.1** Structures of **P8** and PCBM and **F1** studied herein.

## 5.2 P8/PCBM nanofibers and their applications in solar cells

### 5.2.1 Fluorescent titration experiments

The chemical structure of block copolymer **P8** was illustrated in Figure 5.1 and its synthesis and characterization were reported in chapter 3 where the hydrogen bonding moieties on **P8** is ca. 7% based on the $^{1}$H NMR calculation.[28]

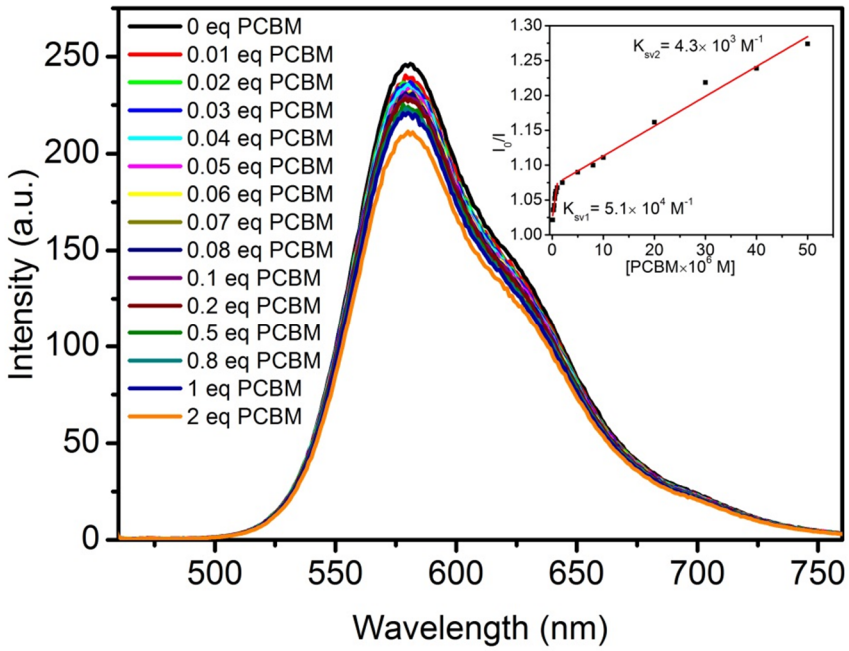


**Figure 5.2** Fluorescence quenching measurement on **P8** in chlorobenzene ($10^{-5}$ M) excited at 458 nm with gradual addition of PCBM ($1\times10^{-4}$ M for the first 0.07 eq, and $5\times10^{-4}$ M thereafter). The concentrations of polymers and equivalents of PCBM are calculated based on total number of repeating units in corresponding polymers. The inset is Stern-Volmer plot and linear fit for calculations of quenching constants.

The weak hydrogen bonding interactions between the ester group on PCBM and the imide group of the isoorotic acid moieties on **P8** was investigated in a similar manner by fluorescent titration experiment as shown in Figure 5.2 where a two-step transition was observed when a linear fit for its Stern-Volmer plot was applied.[28,29] The first step has a larger Stern-Volmer quenching constant ($K_{sv1}$) of $5.1 \times 10^4$ $M^{-1}$, and the latter has a $K_{sv2}$ of $4.3 \times 10^3$ $M^{-1}$ where the transition point occurs when 0.07eq of PCBM was added, indicating full complexation of all the hydrogen bonding sites on **P8** with PCBM. Compared with the complementary "three-point" hydrogen bonding interactions investigated in our previous work in Chapter 3, the interactions between **P8** and PCBM are relatively weaker due to its monotopic hydrogen bonding nature.

### 5.2.2 UV-Vis observations of P8/PCBM nanofibers

The formations of **P8** nanofibers started with dissolving **P8** in chlorobenzene (CB) completely first before sequential addition of acetone in a dropwise manner. The mixed-solvent mixture was then aged at room temperature with constant stirring for predetermined time. UV-vis spectroscopy was employed to monitor the growth of **P8** nanofibers in solution where the evolutions of the vibronic peaks at ca. 514 nm (0-2), 552 nm (0-1), and 603 (0-0) nm together with the redshift of the peak at ca. 458 nm are the indicators of nanofibers formation.[11,12] A volume ratio of 1/5 (vol/vol) of acetone/chlorobenzene (CB) was selected due to its enhanced vibronic patterns and maintained good solubility in solution (Figure 5.3). Further increasing acetone concentration in chlorobenzene caused precipitations of the polymer despite its more pronounced vibronic patterns under dilute conditions, which hindered its applications in

solar cells and therefore were not further investigated. The concentration of **P8** solution and **P8** in **P8**/PCBM blend solutions in chlorobenzene was set to be 10 mg·mL$^{-1}$ for direct solar devices fabrication purpose.

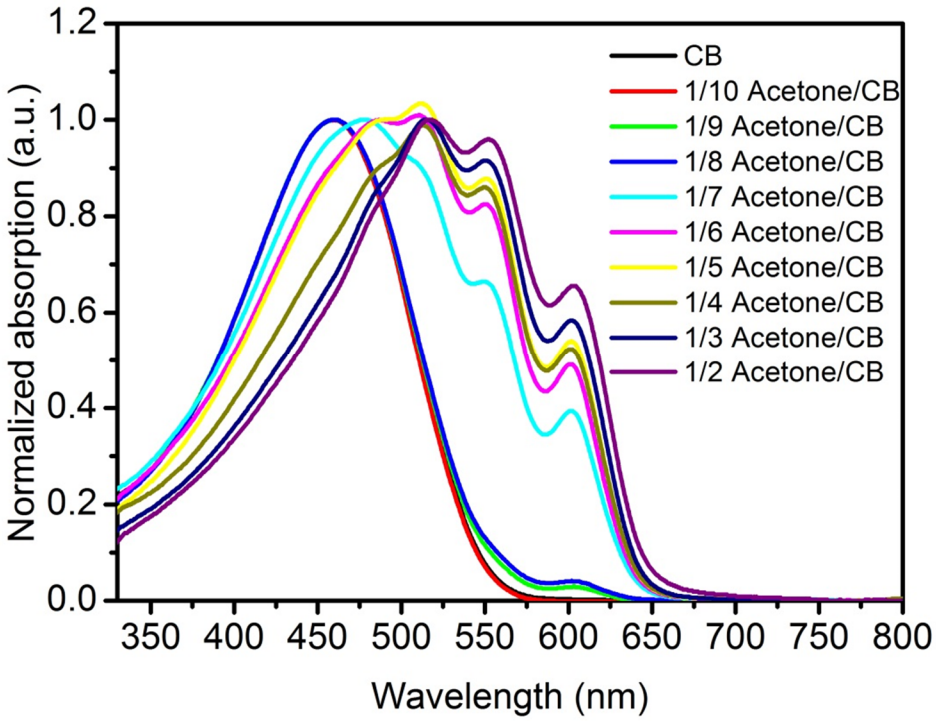


**Figure 5.3** UV-vis spectra of **P8** solution in chlorobenzene at different acetone concentrations (vol/vol). The concentration of **P8** in chlorobenzene is 0.025 mg·mL$^{-1}$ from dilution of 10 mg·mL$^{-1}$.

The time-dependent solution UV-vis spectra of **P8** and **P8**/PCBM (10/4 wt/wt) nanofibers in 1/5 (vol/vol) acetone/CB mixture are monitored and shown in Figure 5.4. Due to high optical density of the original solution, a sample was withdrawn at

predetermined time intervals and diluted with identical mixed solvents 400 times for absorption measurements.

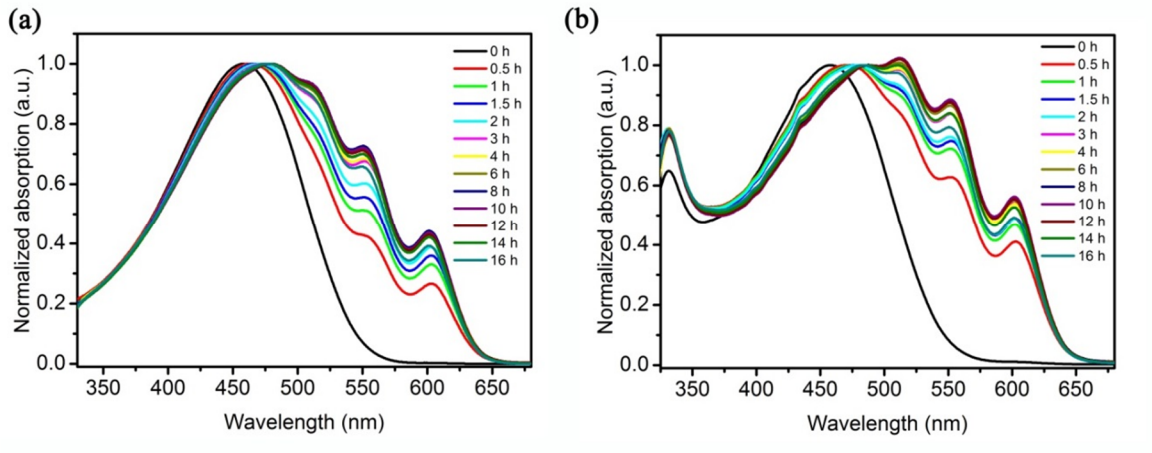


**Figure 5.4** UV-vis spectra of **P8** and **P8**/PCBM (10/4) solutions in acetone/CB (1/5, vol/vol) measured at different time. The concentration of **P8** in chlorobenzene is 0.025 mg· $mL^{-1}$ from the dilution of 10 mg· $mL^{-1}$.

As shown in Figure 5.4a, the peak at 458 nm corresponding to the π-π* transitions of the polythiophenes[14] shifts to 480 nm together with the appearance of new vibronic peaks at 552 nm and 603 nm, which indicates the **P8** nanofibers formation. In the absorption spectra, the vibronic peaks increase in relative intensity up to 12 h aging time, beyond which a slight decrease was observed. It is possible that frequent sampling led to slow evaporation of the more volatile acetone solvent, resulting in better solvation for **P8**. This change in solvents composition likely explains the unexpected more pronounced vibronic features in the 1/5 composition absorption profile in Figure 5.3 when compared with the 14 h aging trace in Figure 5.4a. Both conditions should supposedly lead to

similar **P8** nanostructures and absorption profiles but in the former case the solution was kept tightly closed throughout the entire duration of experiment and thus no acetone evaporation was possible. As a result, seemingly stronger aggregation behavior was observed. On the other hand, incorporation of PCBM with **P8** in situ in solution (**P8**/PCBM NF in situ formed) somehow facilitates the **P8**/PCBM NF formation as evidenced by the stronger intensities of those vibronic patterns of **P8** under the same time intervals as shown in Figure 5.4b. One possible reason accountable for this is that the occupation of those active hydrogen bonding sites by PCBM reduces the intrachain and interchian self-complementary hydrogen bonding interactions of **P8** and thus rendered the **P8**/PCBM complex in a more stretched way to self-assemble. Interesting, the maximum intensities of those vibronic peaks subside after aging for 12 h, which coincides with its preformed **P8** NF case.


**Figure 5.5** Photographs of **P8** solutions in acetone/CB (1/5, vol/vol) at different aging time. The concentration of **P8** in chlorobenzene is 0.025 mg· $mL^{-1}$ from the dilution of 10 mg· $mL^{-1}$.

In addition to UV-vis spectroscopy, monitoring the color change of **P8** solutions is another way to tell the nanofibers formation. Specifically, the formation of **P8** nanofibers was firstly seen by its gradual color change from orange to brownish red. Photographs of the dilute solutions of **P8** nanofibers taken at various time intervals were seen in Figure 5.5 where the color changed from brown to light purple over a period of 16 h.

### 5.2.3 TEM investigations of P8/PCBM and P3HT/PCBM nanofibers

TEM measurements of those nanofibers give us more information on their dimensions (Figure 5.6). Statistical measurements over 100 individual nanofibers provide the histograms of the width distributions of the nanofibers as indicated in Figure 5.6. **P8** NFs have a width of 15.92 ± 0.76 nm, and this value increases to 19.33 ± 0.86 nm and 19.57± 0.74 nm upon mixing with PCBM for the preformed NFs and in situ formed NFs (Figure 5.6 a-c), respectively. It seems that the order of PCBM addition does not influence much on the width of the final **P8**/PCBM compostite nanofibers, suggesting that the hydrogen bonding block may be placed at the periphery of the **P8** naofibers. The width increase of the nanofibers is probably due to the weak hydrogen bonding interactions between **P8** and PCBM that bring PCBM into close proximity to **P8** to form the composite P8/PCBM nanofibers.

As a proof of concept, I also prepared P3HT nanofibers incapable of hydrogen bonding interactions. P3HT nanofibers have an averaged width of 14.08 ± 0.73 nm using acetone/CB (1/12.5, vol/vol). The width of P3HT nanofibers did not change significantly

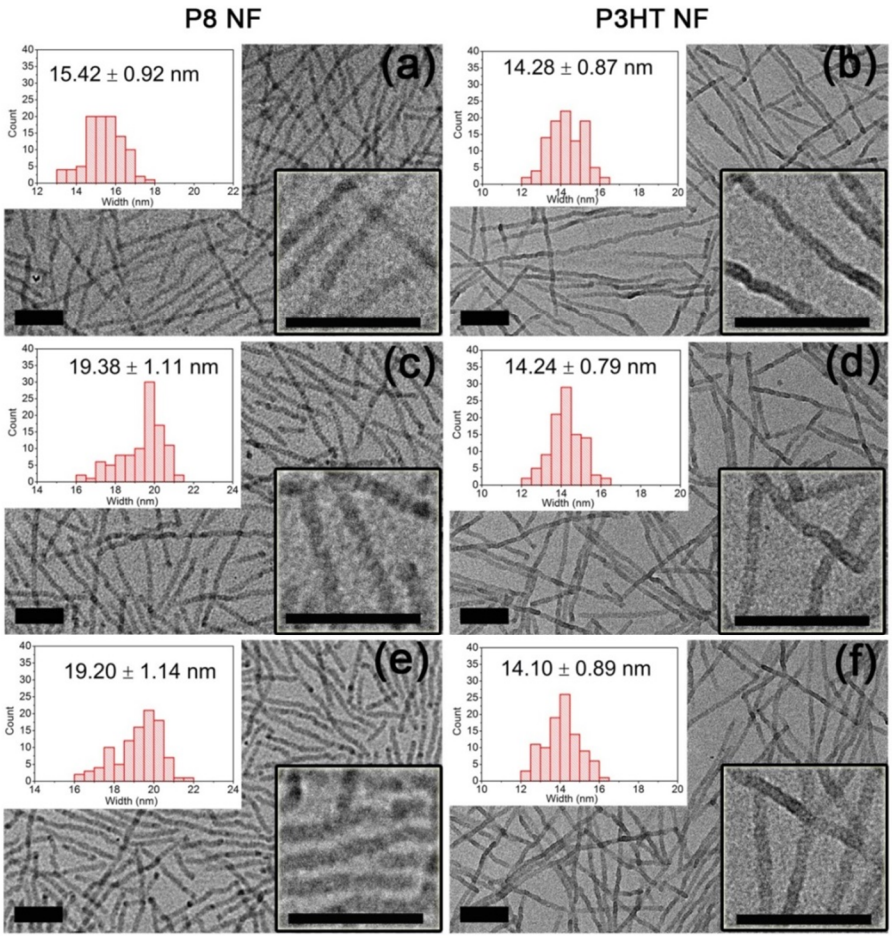


**Figure 5.6** TEM images of **P8** NF (a), **P8** NF/PCBM (10/4) preformed (c), and **P8**/PCBM (10/4) NF in situ formed (e); P3HT NF (b), P3HT NF/PCBM (10/4) preformed (d) and P3HT/PCBM (10/4) NF in situ formed (f). Inserts on the left top of each TEM micrograph are the histograms of width statistics of the nanofibers measured over 100 NFs, and on the right bottom are the images of magnified regions of the nanofibers under 20k magnifications. The concentration for **P8** solution is 10 mg· $mL^{-1}$, and 10 mg· $mL^{-1}$ for **P8**/PCBM (10/4) and P3HT and P3HT/PCBM (10/4) solutions based on the polymer weight. The scale bar is 200 nm.

upon incorporation of PCBM in P3HT solution (Figure 5.6 d), giving a width of 14.16 ± 0.42 nm and 14.06 ± 0.40 nm for the preformed P3HT NF/PCBM and in situ formed P3HT/PCBM NF complexes, respectively (Figure 5.6 e and 5.6 f). Such width differences between **P8** and P3HT nanofibers indicate that hydrogen bonding interactions between **P8** and PCBM do play a role upon blending with PCBM.

### 5.2.4 XRD investigations of P8/PCBM and P3HT/PCBM nanofibers

In order to further probe the influence of the hydrogen bonding moieties on the packing of **P8** during the nanofibers formation, X-ray diffraction (XRD) measurements were carried out on the thin films of **P8** nanofibers and their blends with PCBM (10/4) (Figure 5.7). As a control, P3HT nanofibers and their blends with PCBM (10/4) were also studied in parallel (Figure 5.8). All the films possess a strong (100) peak corresponding to a d-spacing of ca. 1.6 nm.

Thermal annealing enhances the crystallinity for all the films under different blending conditions as seen from more intense diffraction patterns in their thermal annealed films. It is noted, all the nanofibers blends have more pronounced (200) and (300) diffraction peaks than their BHJ films, indicating higher crystallinity and more ordered packing for the nanofibers (**P8** or P3HT NFs). Interestingly, **P8** nanofibers and their blends are less crystalline when in comparison with that of the P3HT nanofibers and their blends, probably due to the existence of such small portion of hydrogen bonding moieties on **P8**.

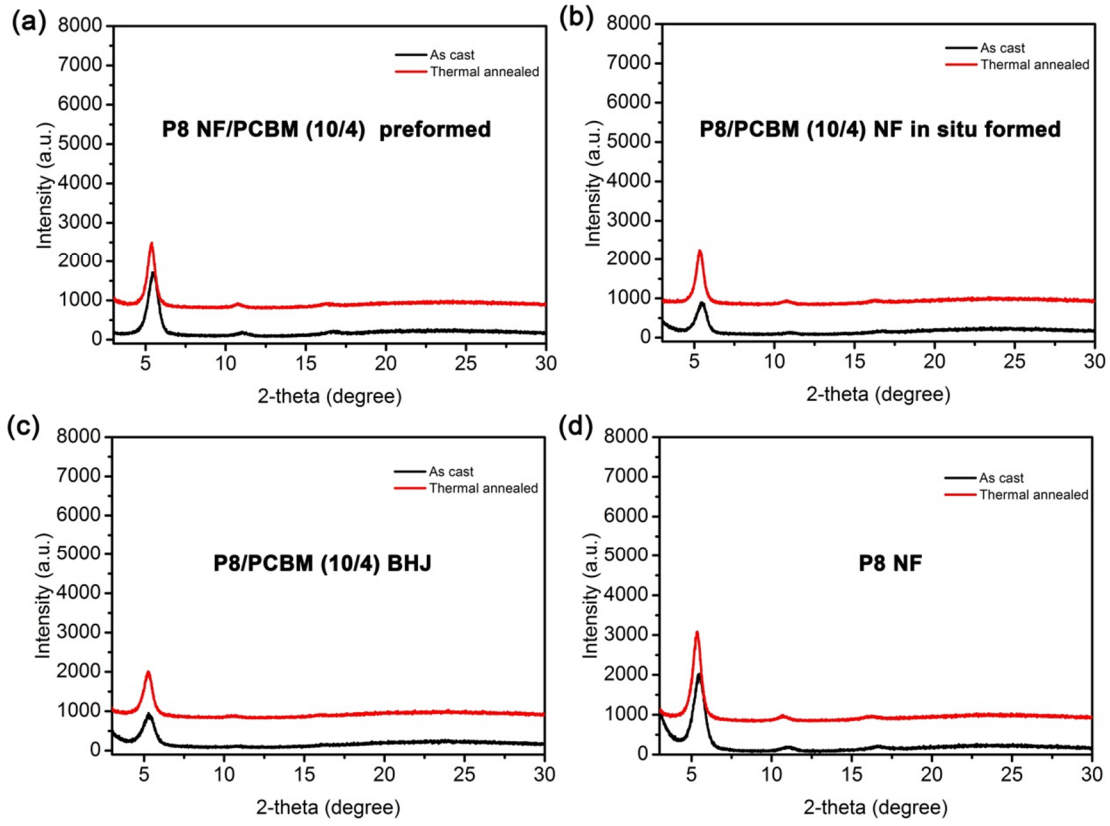


**Figure 5.7** Thin film XRD profiles of **P8** nanofibers and blends with PCBM (10/4) at different conditions.

Moreover, **P8** NFs alone present slightly higher crystallinity than that of their blends with PCBM, suggesting that attachment of fullerenes reduces the crystallinity of the blend films. However, such crystallinity variations are not seen in P3HT NFs and their nanofibers blends with PCBM, indicating that the connection between **P8** and PCBM through weaker interactions somehow interrupts the polymer packing. Moreover, less diffraction intensity was also observed in their BHJ blends when compared with that in their nanofibers blends.

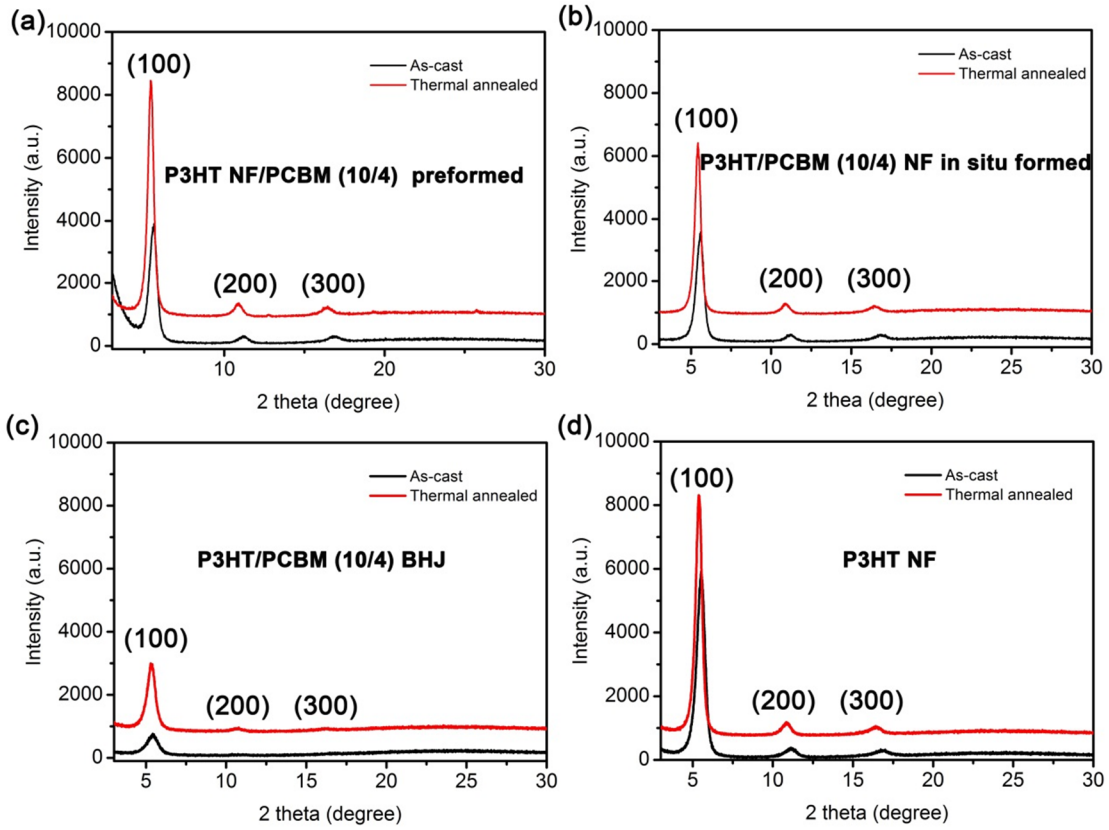


**Figure 5.8** Thin film XRD profiles of P3HT nanofibers and blends with PCBM (10/4) at different conditions.

### 5.2.5 Photovoltaic performances of solar cells employing nanofibers as active layers

#### 5.2.5.1 Photovoltaic evaluation of solar cells employing nanofibers as active layers

Those **P8**/PCBM NFs have a width of ca. 20 nm which is comparable to exciton diffusion length in polymer solar cells. Therefore, further investigations on photovoltaic performance employing those **P8**/PCBM (10/4) nanofibers were conducted. As a control, **P8**/PCBM (10/4) and P3HT/PCBM (10/4) bulk heterojunction (BHJ) solar cells were

also fabricated under identical conditions to test the utilities of such nanofibers in improving PCEs (Table 5.1).

**Table 5.1** Best cell performance of polymer/PCBM (10/4) under different condition.[a]

| | Conditions[b] | *PCE* (%)[c] | $J_{SC}$ (mA/cm$^{-2}$)[c] | $V_{OC}$ (V)[c] | *FF*[c] |
|---|---|---|---|---|---|
| **P8**/PCBM | preformed | 4.17 ± 0.15 | 11.23 ± 0.53 | 0.62 ± 0.00 | 0.60 ± 0.01 |
| | in-situ formed | 3.52 ± 0.20 | 11.62 ± 0.51 | 0.61 ± 0.01 | 0.50 ± 0.01 |
| | BHJ | 3.00 ± 0.08 | 8.82 ± 0.28 | 0.65 ± 0.01 | 0.52 ± 0.00 |
| P3HT/PCBM | preformed | 3.32 ± 0.21 | 9.93 ± 0.53 | 0.57 ± 0.01 | 0.59 ± 0.01 |
| | in-situ formed | 3.11 ± 0.21 | 10.63 ± 0.52 | 0.52 ± 0.01 | 0.56 ± 0.01 |
| | BHJ | 2.85 ± 0.07 | 9.20 ± 0.39 | 0.59 ± 0.01 | 0.52 ± 0.01 |

[a]spin-cast at 400 rpm for 30s, [b] thermal annealing at 150 °C for 15 min, [c]an average of five cells.

In general, **P8**/PCBM NF solar devices outperformed the P3HT/PCBM NF solar cells under the same conditions where the optimized devices were obtained by subjecting to thermal annealing at 150 °C for 15 min. The two best-performing devices are fabricated from the **P8** NF/PCBM preformed and **P8**/PCBM NF in situ formed blends, giving PCEs of 4.17 % ± 0.15 % and 3.52 % ± 0.20 %, respectively. Their top PCEs mainly result from high $J_{SC}$s which are probably due to the enhanced charge separation efficiency within the **P8**/PCBM composite nanofibers. To proof this point, we also made the devices employing the BHJ blends of **P8**/PCBM and P3HT/PCBM at the same weight

ratios. Indeed, both devices showed lower $J_{SC}$s, only with a value of 8.82 ± 0.28 mA/cm$^{-2}$ and 9.20 ± 0.39 mA/cm$^{-2}$, respectively. This probably supports our claim that active layers using those nanofibers are better for BHJ solar cells over their BHJ counterparts.

Notably, **P8**/PCBM blends have higher $V_{OC}$s than that of P3HT/PCBM blends, and the BHJ blends also possess higher $V_{OC}$s than that of their corresponding nanofibers blends, which could be explained from the perspective of crystallinities of the blends. As suggested by XRD analyses, **P8**/PCBM nanofibers blends are less crystalline than that of P3HT/PCBM nanofibers blends, and their BHJ blends show less crystallinity compared with their nanofibers blends, too. In fact, solar devices fabricated from the P3HT/PCBM blends with less crystallinity are reported to increase the $V_{OC}$ of the solar cells due to its low-lying HOMO levels.[30] Another interesting phenomenon that we observed is that both devices employing the preformed NF blends have a higher fill factor (FF) than that of that from in-situ formed NF, indicating charge extractions and transport from the preformed NF blends are probably easier, possibly due to the fact that preformed nanofibers have more undisturbed molecular packing during the nanofibers formations.

It is surprising to find out that in our **P8** nanofibers system, fewer PCBM loadings in the blends (10/4, wt/wt) are still capable of achieving high efficiencies, indicating that high fullerene loadings are not necessarily required in the polymer/fullerene blends to guarantee the cell performances, and it could be overcome by proper polymer and fullerenes molecular arrangements. Specifically, in our **P8**/PCBM NF system, formation of **P8** nanofibers could enhance the charge generation efficiencies,

and it is also true in the P3HT/PCBM NF system. However, fullerenes in the close proximity of **P8** due to weak hydrogen bonding interactions between them could facilitate the charge separation because of facilitated exciton diffusions. As a matter of fact, the PCEs of **P8**/PCBM NF solar devices in this study are much better than the records we reported in our previous work where **P8**/**F2** (PCBM) devices are less efficient but thermally stable due to the hydrogen bonding interactions.[28]

#### 5.2.5.2 Thermal stability evaluation of solar cells empolying P8/PCBM and P3HT/PCBM nanofibers as active layers

To evaluate the thermal stability of such nanofibers devices, we subjected all the solar cells fabricated from **P8**/PCBM blends by annealing all the devices at 110 ºC under nitrogen for various time. We envisioned that the weak hydrogen bonding interactions between **P8** and PCBM could slow down the macrophase separations of the **P8**/PCBM blends. As a control, solar devices made from P3HT/PCBM NFs and their conventional BHJ blends were also tested due to their incapability of hydrogen bonding interactions. The results are summarized in Figure 5.9 and Figure 5.10.

As shown in Figure 5.9a, devices fabricated from **P8**/PCBM blends exhibited the highest thermal stabilities, with only ca. 20% of their initial PCEs loss. Whereas P3HT/PCBM devices presented worse PCEs against aging tests in which the worst one lost about 50% of its original power.

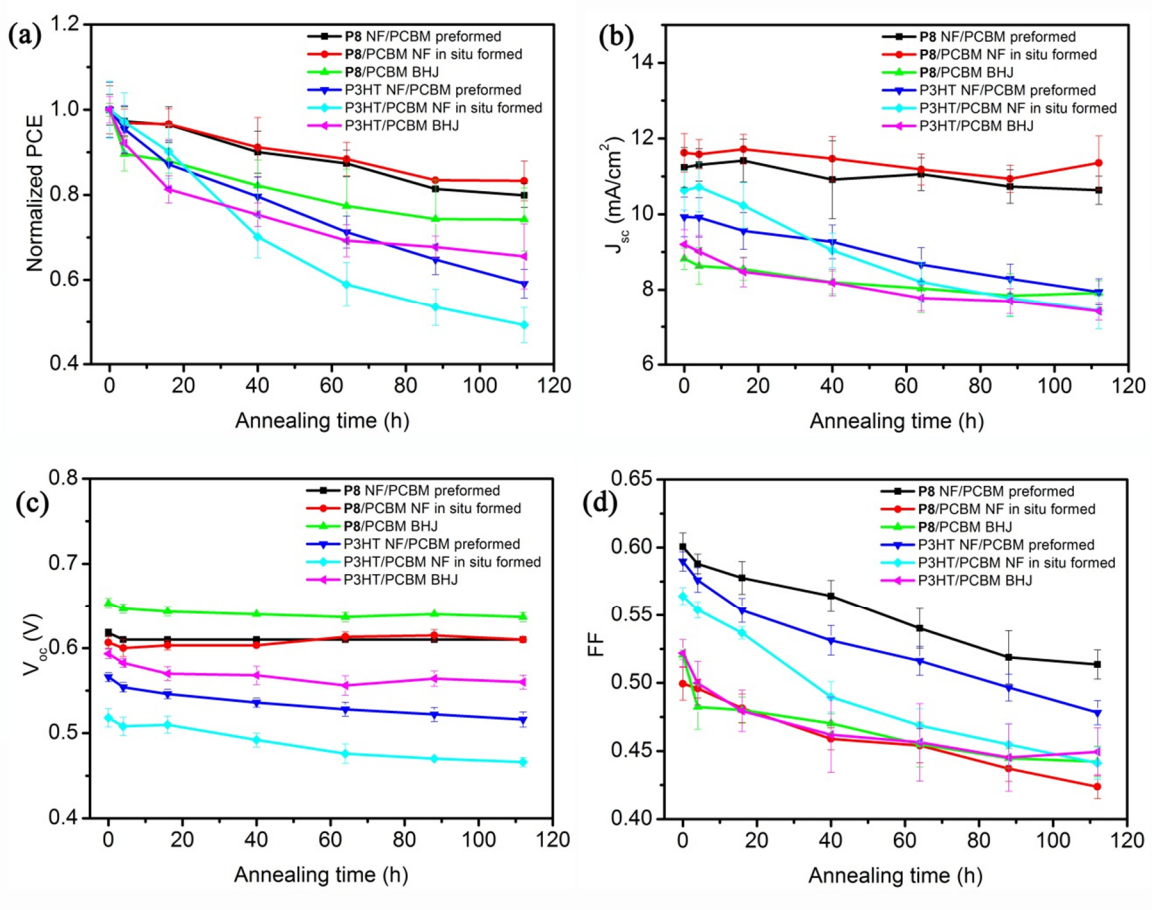


**Figure 5.9** Thermal stability tests of devices employing **P8**/PCBM (10/4) NFs at different blending conditions and P3HT/PCBM NFs standard devices. Corresponding BHJ devices using the same weight ratios were also tested. Devices were annealed at 110 ºC under nitrogen for various times: (a) normalized *PCE* against annealing time; (b) $J_{SC}$ against annealing time. (c) $V_{OC}$ against annealing time; (d) FF against annealing time.

The major cause for the thermal stability differences arouse from the $J_{SC}$ drops (Figure 5.9b) and FF decrease (Figure 5.9d). Interestingly, extended aging time reduced the $J_{SC}$s and $V_{OC}$s of P3HT/PCBM devices but had minimum impact on those of

**P8**/PCBM devices (Figure 5.9b and Figure 5.9c). Although all the devices showed reduced FF, it is noticed that **P8**/PCBM devices dropped in a slower way when compared with that of P3HT/PCBM cells. All I-V curves of the devices under aging tests are shown in Figure 5.10.

We reasoned that the weak hydrogen bonding interactions between **P8** and PCBM are able to preserve the morphologies of the blends and thus slow down the PCBM crystallization from the polymer matrix in a slower manner. It is noted, in the **P8**/PCBM systems, **P8** NF/PCBM preformed blends are slightly less thermal stable than that of the **P8**/PCBM NF in situ blends, possibly due to the better intermixing of **P8** and PCBM during the nanofibers formation in the latter case. However, in the P3HT/PCBM system, its BHJ devices are the most thermal stable ones and the P3HT/PCBM NF in situ formed blends shows the least thermal stability. We speculate that one possible reason responsible for the varied thermal stabilities is that P3HT and PCBM are better intermixed in their BHJ blend on the nanoscale, while in the P3HT/PCBM NF cases, the lack of specific interactions between P3HT and PCBM rendered PCBM crystallization easier especially when P3HT are preferably preorganized into nanofibers first before mixing with PCBM.

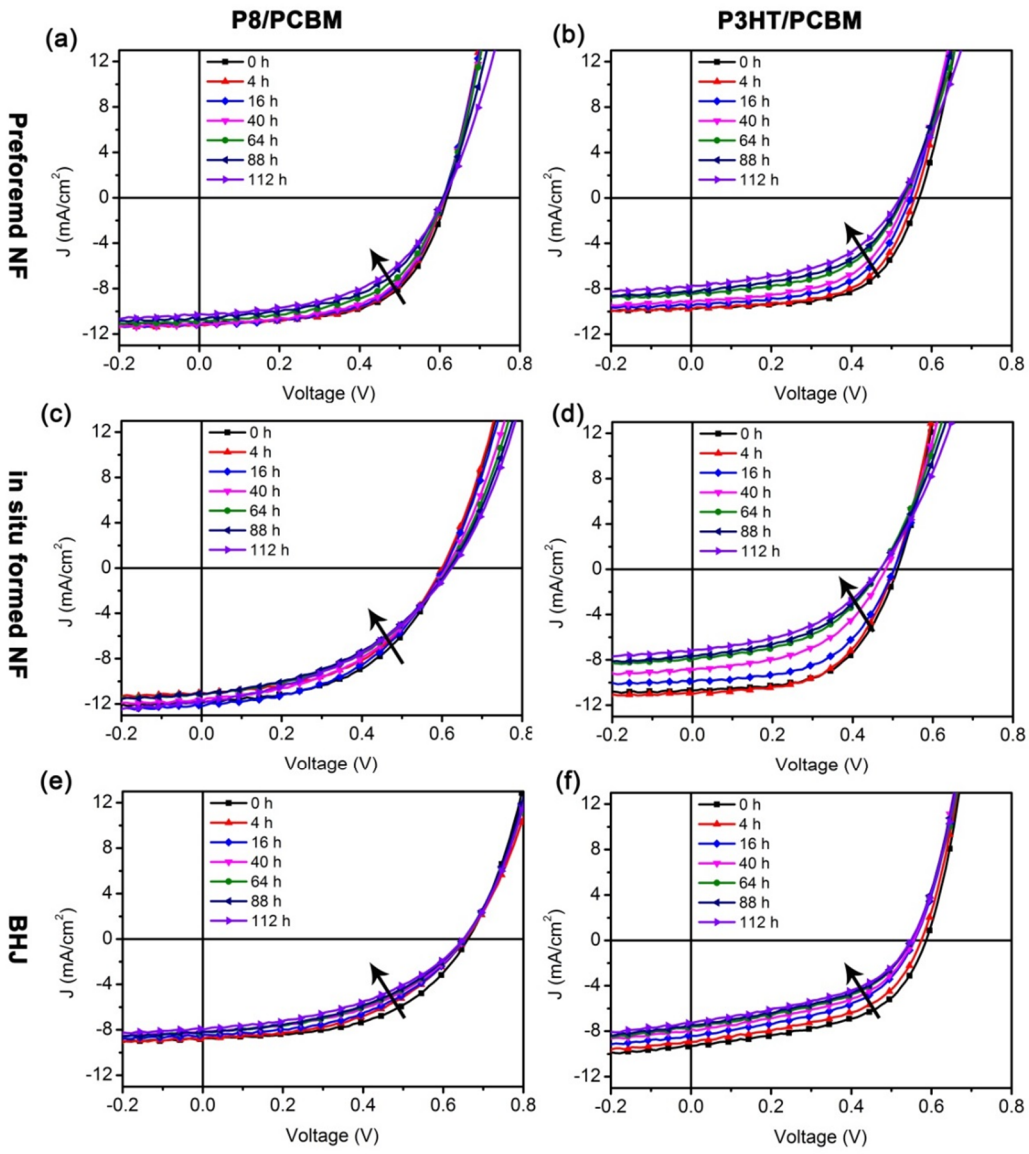


**Figure 5.10** I-V curves (under simulated AM1.5 G irradiation) of different devices employing **P8**/PCBM (10/4, wt/wt) or P3HT (10/4, wt/wt) at different blending conditions measured after annealing at 110 °C for various times: (a) **P8** NF/PCBM preformed, (b) P3HT NF/PCBM preformed; (c) **P8**/PCBM NF in situ formed, (d) P3HT/PCBM NF in situ formed; (e) **P8**/PCBM BHJ, (f) P3HT/PCBM.

### 5.2.6 Morphological investigations of the active layers

#### 5.2.6.1 Optical microscopy analysis

To rationalize the photovoltaic performance and stabilities differences, optical microscopy was firstly used to understand the device thermal stabilities and the results are shown in Figure 5.11. By observing the evolution of the PCBM crystallizations on the micron-size scale with aging time, I could roughly evaluate the degree of the macrophase separations in the polymer/PCBM blends.

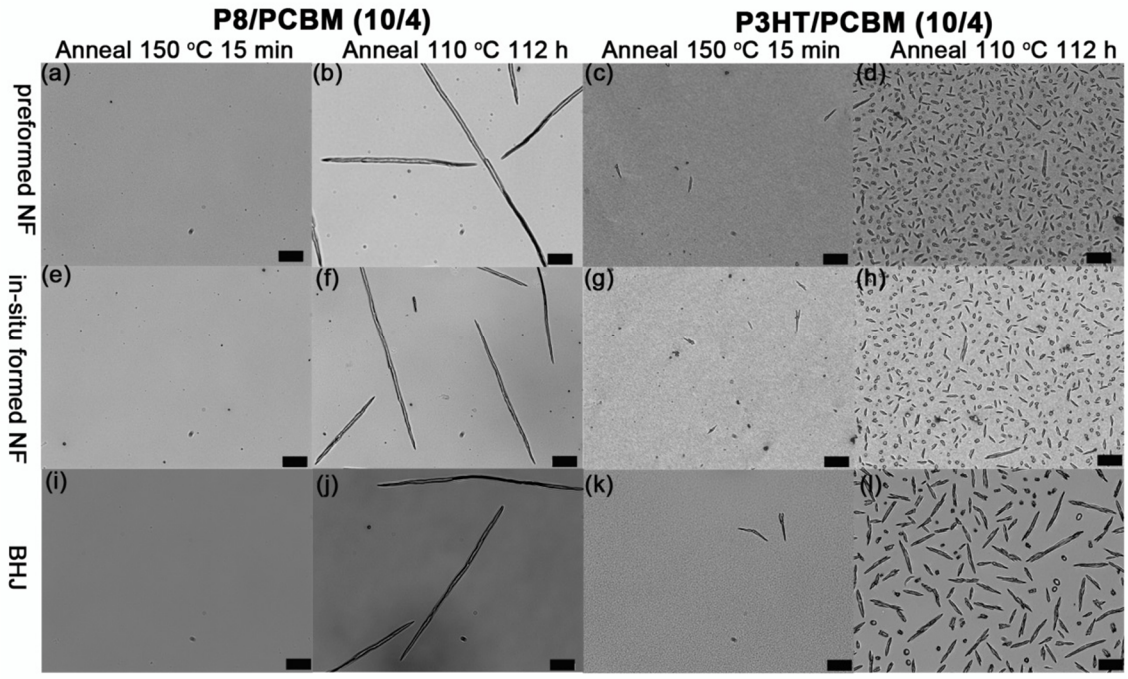


**Figure 5.11** Optical micrographs of devices empolying **P8**/PCBM (10/4) (left two columns) and P3HT/PCBM (10/4) (right two columns). The scale bar is 20 μm.

As shown in Figure 5.11, all the optimized devices exhibit visible PCBM crystals (c, g, k) from P3HT/PCBM blends while no apparent PCBM crystals are spotted in **P8**/PCBM blends (a, e, i), indicating that the weak hydrogen bonding interactions between **P8** and PCBM are probably responsible for such thermal stabilities differences. The sizes of the PCBM crystals are on the order of ca. 15 to 30 micrometers. Moreover, such PCBM crystallizations become more pronounced for the P3HT/PCBM devices after aging tests as shown from denser and shorter PCBM crystals (Figure 5.11, d, h, l); whereas the **P8**/PCBM cells presented less but much longer needle-like crystals around 200 micrometers long (Figure 5.11, b, f , j). We speculated that the longer needle-like PCBM crystals were slowly formed during the aging process and thus slower macrophase separation between **P8** and PCBM could be ascribed to their improved device thermal stabilities. As a proof of our hypothesis, we also observed longer needle-like PCBM crystals in the P3HT/PCBM BHJ devices than that of their NF solar cells, which was consistent with the trend in their device thermal stabilities as shown in Figure 5.10 and Figure 5.11.

#### 5.2.6.2 Atomic force microscopy analysis

To further gain insight on the PCEs and thermal stabilities for the **P8**/PCBM and P3HT/PCBM devices, atomic force microscopy (AFM) was employed to probe the morphological changes of the active layers of those devices upon different processing conditions. Their phase and corresponding height images were shown in Figure 5.12 and Figure 5.13.

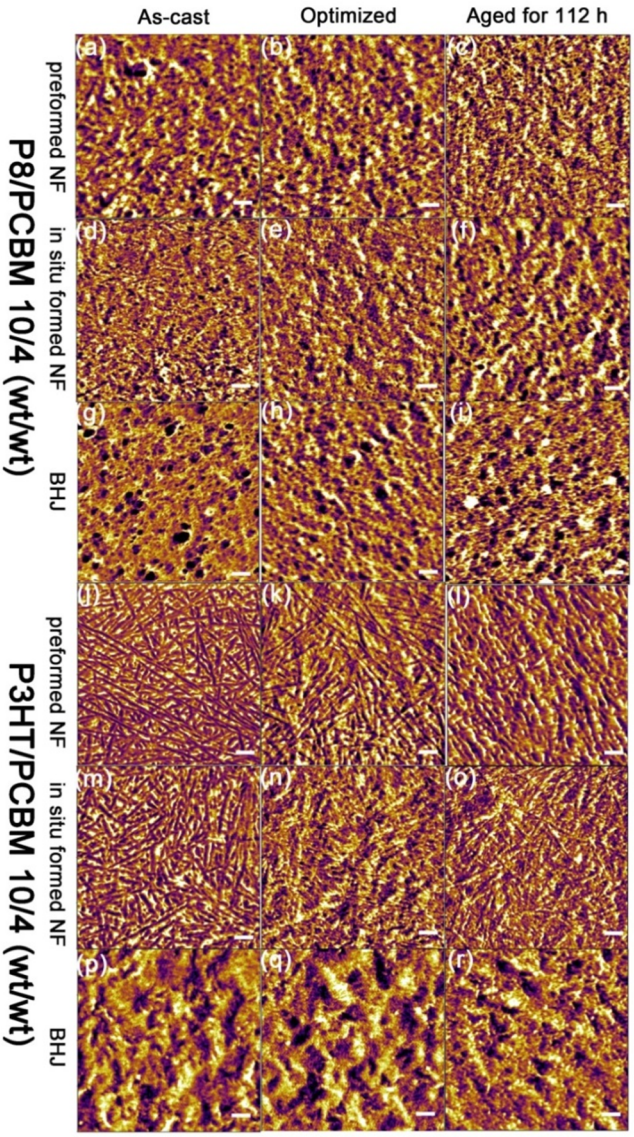


**Figure 5.12** Atomic force microscopy (AFM) phase images (2 μm × 2 μm) of devices employing **P8**/PCBM blends (top three rows) and P3HT/PCBM blends (bottom three rows) as active layers (left column: as-cast; middle column: annealed at 150 °C for 15 min; right column aged at 110 °C for 112 h), the weight ratio for the blends is 10/4. The scale bar is 200 nm.

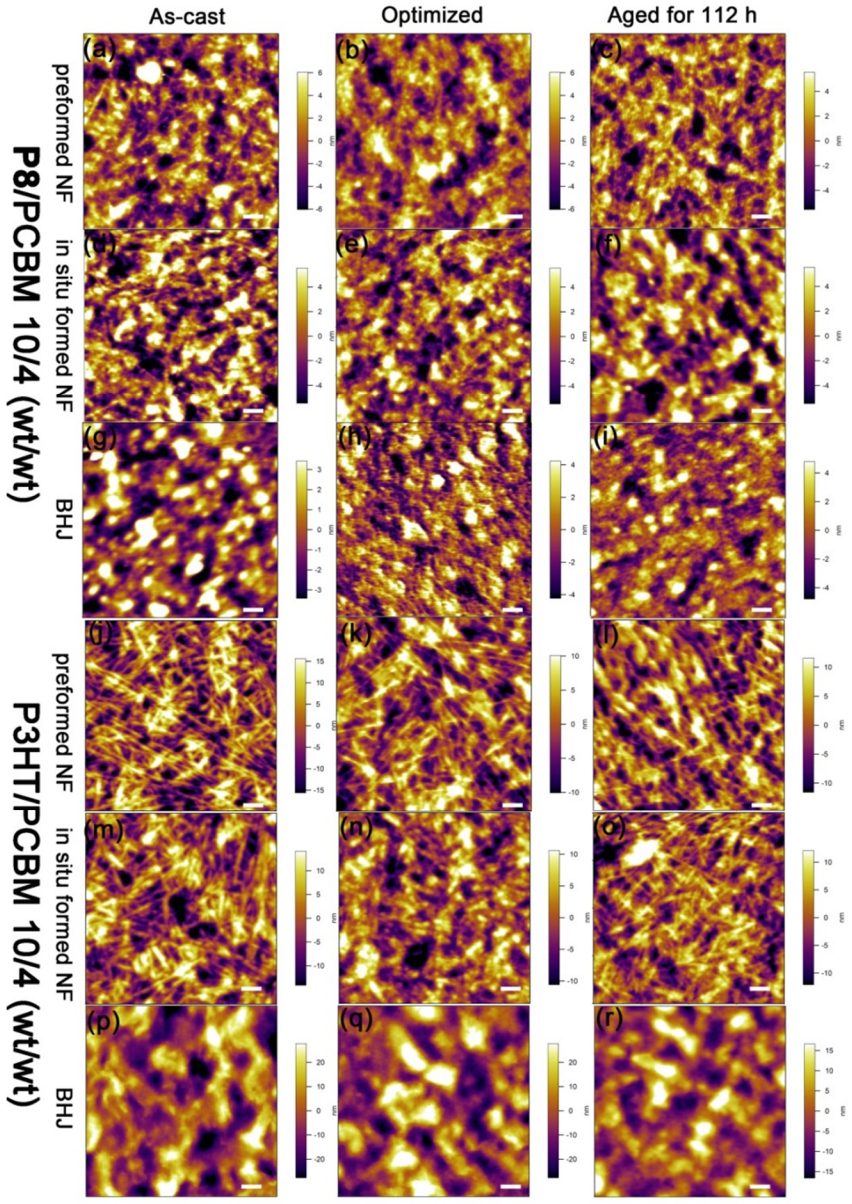


**Figure 5.13** AFM height images (2 μm × 2 μm) of devices employing **P8**/PCBM blends (top three rows) and P3HT/PCBM blends (bottom three rows) as active layers (left column: as-cast; middle column: annealed at 150 °C for 15 min; right column aged at 110 °C for 112 h), the weight ratio for the blends is 10/4. The scale bar is 200 nm.

As indicated in Figure 5.12, **P8**/PCBM NF as-cast devices exhibited less pronounced nanofibers features (a and d) than that of the P3HT/PCBM nanofibers solar cells (j and m). This was probably due to the fact that the attached PCBM onto **P8** through hydrogen bonding interactions prevented further aggregation between the **P8**/PCBM nanofibers during the solvent drying process at the stage of spin coating the active layers. Another possible explanation is that **P8** NFs are capable of self-complementary hydrogen bonding interaction that may promote the aggregation between the individual **P8** nanofibers, which makes it hard to visualize directly in the thin film state. Thermal annealing somehow eliminated the nanofibers features in P3HT/PCBM nanofibers (k and n) and the domains became more interconnected (Figure 5.13), which probably accounted for the enhanced PCEs. Prolonged annealing caused bigger domain sizes (l and o) and the nanofibers features became even less obvious. As for the **P8**/PCBM NFs blends, the preformed NFs film showed better nanofibers features (a) than that of its in-situ formed films (d), suggesting a better molecular arrangement of the polymer and fullerenes probably due to its more preorganized nature before adding PCBM. Such molecular arrangement did not alter significantly upon thermal annealing, but more fullerene nanocrystals were spotted in its preformed **P8**/PCBM NFs (b) than its in situ formed case (e). Such nanocrystals of PCBM may better connect the electron transport pathway that enhances the charge transport efficiencies as seen higher PCE in the preformed **P8**/PCBM case. The domain sizes of **P8**/PCBM NFs are finer than that of P3HT/PCBM nanofibers (Figure 5.13), probably due to the better self-assembled morphologies from **P8**/PCBM complexes. Such self-assembly behavior better preserved

the morphologies of **P8**/PCBM NFs (e and f) upon prolonged thermal annealing, which gave possible explanation to the enhanced thermal stabilities of **P8**/PCBM NFs devices.

It is noted that in the in situ formed **P8**/PCBM device, smaller PCBM nanocrystals were observed (f) than that of its preformed nanofiber device (e) after the aging test (Figure 12 and 13). Such nanocrystals in the thin film device from the in situ NFs resembles those in its optimized preformed NFs case (b), indicating possibly certain correlation with its high photovoltaic performance and thermal stability with those small nanocrystals. For the BHJ devices, both P3HT/PCBM (g to i) and **P8**/PCBM devices (p to r) showed coarser films with big PCBM nanocrystals randomly distributed within the films. Thermal annealing promoted the reorganization of the polymers and fullerenes in the blends and created bigger domains but more interconnected. Further annealing the BHJ devices led to even bigger domains and thus deteriorated the cell performances. It is noted in the P3HT/PCBM BHJ thin films, coarser surfaced were observed than those of **P8**/PCBM films (Figure 13, m to r), implying that the cooperative self-assembly between BCP **P8** and PCBM could lead to smoother morphologies that are better for solar cells.

#### 5.2.6.3 Grazing-incidence X-ray scattering studies

In order to gain a deeper insight into the effectiveness of our composite NF strategy on morphology controllability, we performed both grazing-incidence wide-angle X-ray scattering (GIWAXS) and grazing-incidence small-angle X-ray scattering (GISAXS) measurements on thin films of polymer NFs, polymer/PCBM composite NFs

and polymer/PCBM BHJ blends. The results are summarized in Figures 5.14 and 5.15, Table 5.2 and Figures 5.16 and 5.17.

GIWAXS enables probing of the molecular-scale packing of the components, and is particularly sensitive to the efficient organization of P3HT (or **P8**) in two orthogonal directions: the π–π stacking of the aromatic thiophene rings, and the lamellar stacking that results from the disordered alkane side-chains.

We note that the third orthogonal direction (along the polymer backbone) does not give rise to a well-defined GIWAXS peak. The intensity along the scattering rings can also be used to quantify the orientation distribution of the material, and thus the fractions of materials oriented in different directions.[31,32] We observed strong scattering peaks for all of the processing conditions, indicating good ordering (crystallization) of the P3HT (or **P8**) phase. However there are notable differences between the different materials and processing conditions. Thin films containing P3HT NFs generally gave stronger and more defined higher order scattering peaks than those containing **P8** NFs under comparable conditions as shown in Figures 5.14 and 5.16, indicating higher crystallinity in the P3HT NFs. This is consistent with the higher $V_{OC}$ observed in OPV devices employing **P8** NFs due to the less crystalline nature.

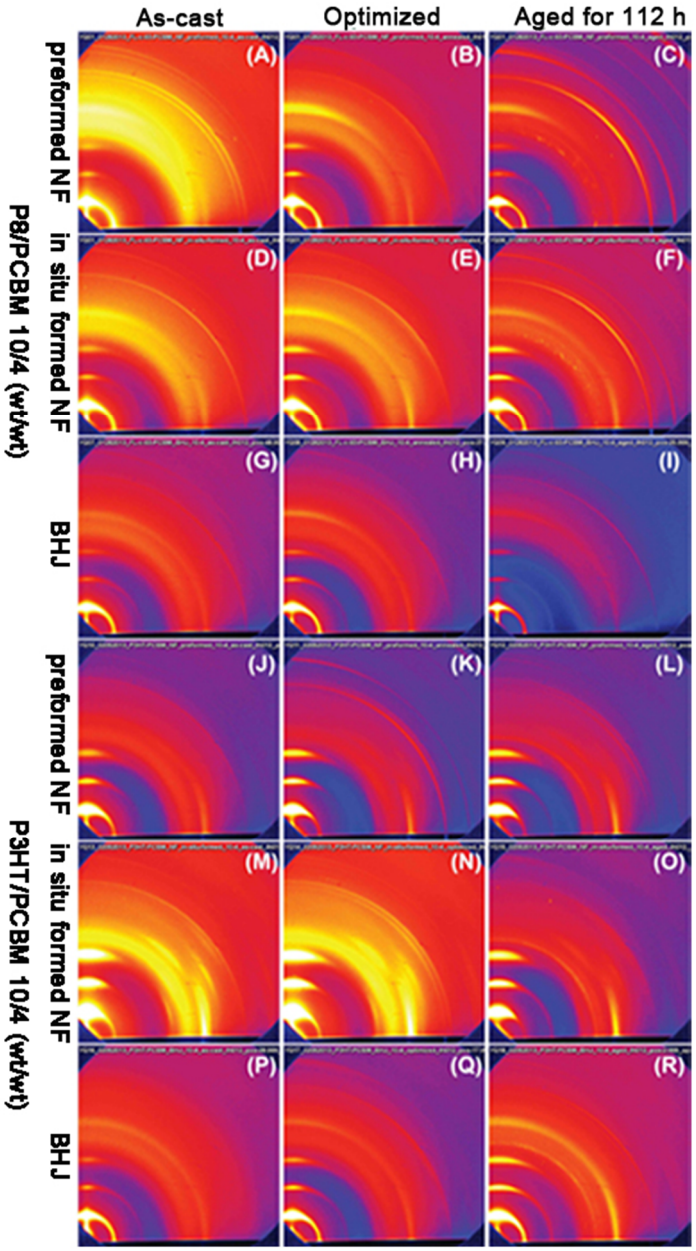


**Figure 5.14** Grazing-incidence wide-angle X-ray scattering (GIWAXS) profiles of as-cast (left column), optimized (150 °C, 15 min, middle column) and aged (110 °C, 112 h, right column) devices employing pre-formed **P8**/PCBM composite NFs (a to c), in-situ formed **P8**/PCBM composite NFs (d to f), **P8**/PCBM BHJ blends (g to i), pre-formed P3HT NF/PCBM (j to l), in-situ formed P3HT/PCBM NFs (m to o) and P3HT/PCBM BHJ blends (p to r). Polymer/fullerene weight ratio is 10/4 in all devices. The presented images are for a grazing-incident angle of 0.12° (other angles measured gave similar results).

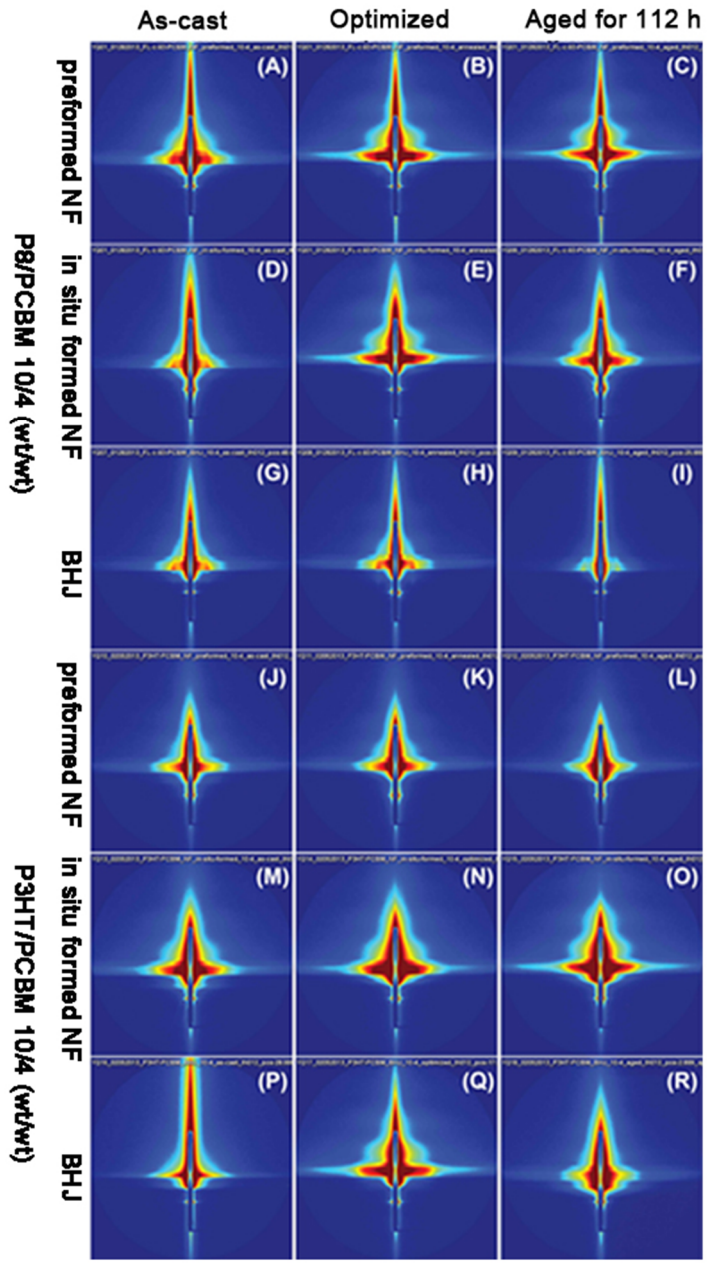


**Figure 5.15** Grazing-incidence small-angle X-ray scattering (GISAXS) profiles of as-cast (left column), optimized (150 °C, 15 min, middle column) and aged (110 °C, 112 h, right column) devices employing pre-formed **P8**/PCBM composite NFs (a to c), in-situ formed **P8**/PCBM composite NFs (d to f), **P8**/PCBM BHJ blends (g to i), pre-formed P3HT NF/PCBM (j to l), in-situ formed P3HT/PCBM NFs (m to o) and P3HT/PCBM BHJ blends (p to r). Polymer/fullerene weight ratio is 10/4 in all devices. The presented images are for a grazing-incident angle of 0.12° (other angles measured gave similar results).

**Table 5.2** Summary of grazing incidence X-ray scattering results.[a]

| Conditions | | GIWAXS (As Cast/Optimized/Aged)[b] | | | GISAXS(As Cast/Optimized/ aged)[c] | |
|---|---|---|---|---|---|---|
| | | Face-On (%) | Edge-On (%) | Isotropic (%) | d−spacing (nm) | Grain Size (nm) |
| **P8**/PCBM | **P8** only NFs | 8 / 5 / 4 | 67 / 81 / 68 | 25 / 14 / 27 | – | – |
| | Pre-formed NFs | 11 / 15 / 11 | 27 / 39 / 36 | 63 / 46 / 52 | 33 / 34 / – | 243 / 190 / – |
| | In-situ formed NFs | 3 / 2 / 2 | 51 / 58 / 68 | 47 / 41 / 30 | 35 / 35 / 34 | 199 / 179 / 209 |
| | BHJ | 7 / 2 / 4 | 48 / 44 / 41 | 45 / 54 / 55 | 35 / 35 / 35 | 196 / 194 /201 |
| P3HT/PCBM | P3HT only NFs | 2 / 3 / 1 | 97 / 92 / 98 | 2 / 5 / 1 | – | – |
| | Pre-formed NFs | 5 / 3 / 3 | 75 / 90 / 94 | 19 / 7 / 3 | – | – |
| | In-situ formed NFs | 2 / 2 / 1 | 93 / 94 / 96 | 5 / 4 / 2 | – | – |
| | BHJ | 6 / 3 / 6 | 44 / 56 / 70 | 50 / 41 / 24 | – | – |

[a] Thin films were deposited using identical conditions as that applied in OPV device fabrication. Optimized: 150 ºC, 15 min; aged: 110 ºC, 112h. [b] Grazing-incidence wide-angle X-ray scattering. Percentages of different polymer orientations are estimated by integration the intensity along the scattering rings. [c] Grazing-incidence small-angle X-ray scattering. "–" indicates not observed.

The P3HT/PCBM samples all exhibit the 'edge-on' orientation typically observed for these materials, wherein the side-chains interact with the substrate interface, giving rise to the out-of-plane lamellar peaks, and corresponding in-plane π–π peak. This should be contrasted with the 'face-on' orientation, which has the aromatic rings are instead stacked along the film normal, and which is expected to give rise to higher out-of-plane hole mobility and thus more suitable for OPV operations. Whereas the P3HT/PCBM samples all exhibit predominantly edge-on orientation (with <7% face-on orientation), as

summarized in Table 5.2, the **P8**/PCBM materials instead break this deleterious orientational effect. For instance, the P3HT/PCBM pre-formed NFs, after aging, exhibited 94% edge-on orientation. By comparison, the corresponding pre-formed **P8**/PCBM composite NFs exhibited only 36% edge-on orientation (and 11% face-on plus 52% of a uniformly-distributed (isotropic) material). This reorientation of material can be seen as a bimodal distribution of scattering intensity along the **P8** lamellar scattering peaks. It is possible that the P3HT/PCBM NFs are efficiently oriented by the substrate-wetting preference of the P3HT alkyl side-chains. The strong interactions between **P8** and PCBM modify this substrate interaction, and allow the composite NFs to achieve greater orientational freedom about their long axis. This modified orientation distribution is likely to contribute to higher hole mobility (c.f. improved $J_{SC}$), and thus improved solar cell performance.

Unsurprisingly, annealing improves order for all the materials studied, with higher-order peaks becoming better defined. Interestingly, however, there is some suggestion that the **P8**/PCBM composite NFs cause the PCBM phase to crystallize, as evidenced by the appearance of textured scattering rings at the distance corresponding to PCBM packing. This was only observed for aged samples of **P8**/PCBM composite NFs, indicating that NFs of this material cause some structuring of surrounding material (even while preventing larger-scale phase-separation). The aged materials (annealing for 112 h) exhibit some reorientation of the material. Notably, this reorientation was less pronounced for **P8** than for P3HT composites, again suggesting that the strong interactions between **P8** and PCBM stabilize the morphology.

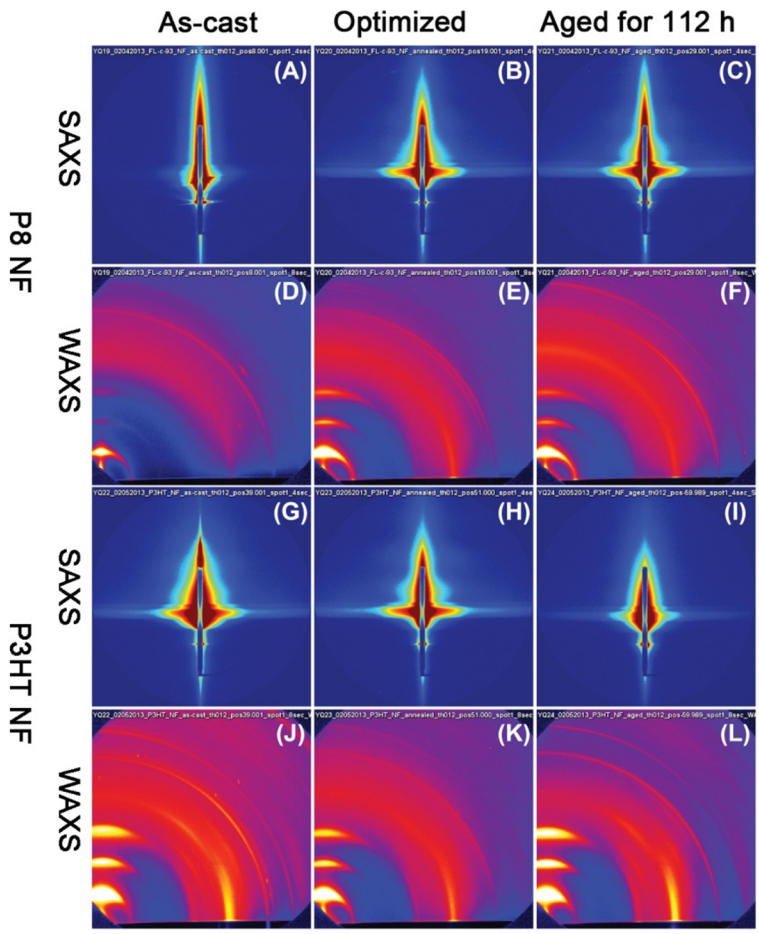


**Figure 5.16** Grazing-incidence small-angle X-ray scattering (GISAXS) profiles (A-C and G-I) and grazing-incidence wide-angle X-ray scattering (GIWAXS) profiles (D-F and J-L) of as cast (left column), optimized (150 °C, 15 min, middle column) and aged (110 °C, 112h, right column) thin films spun cast from solutions of **P8** nanofibers (A-F) and P3HT nanofibers (G-L).

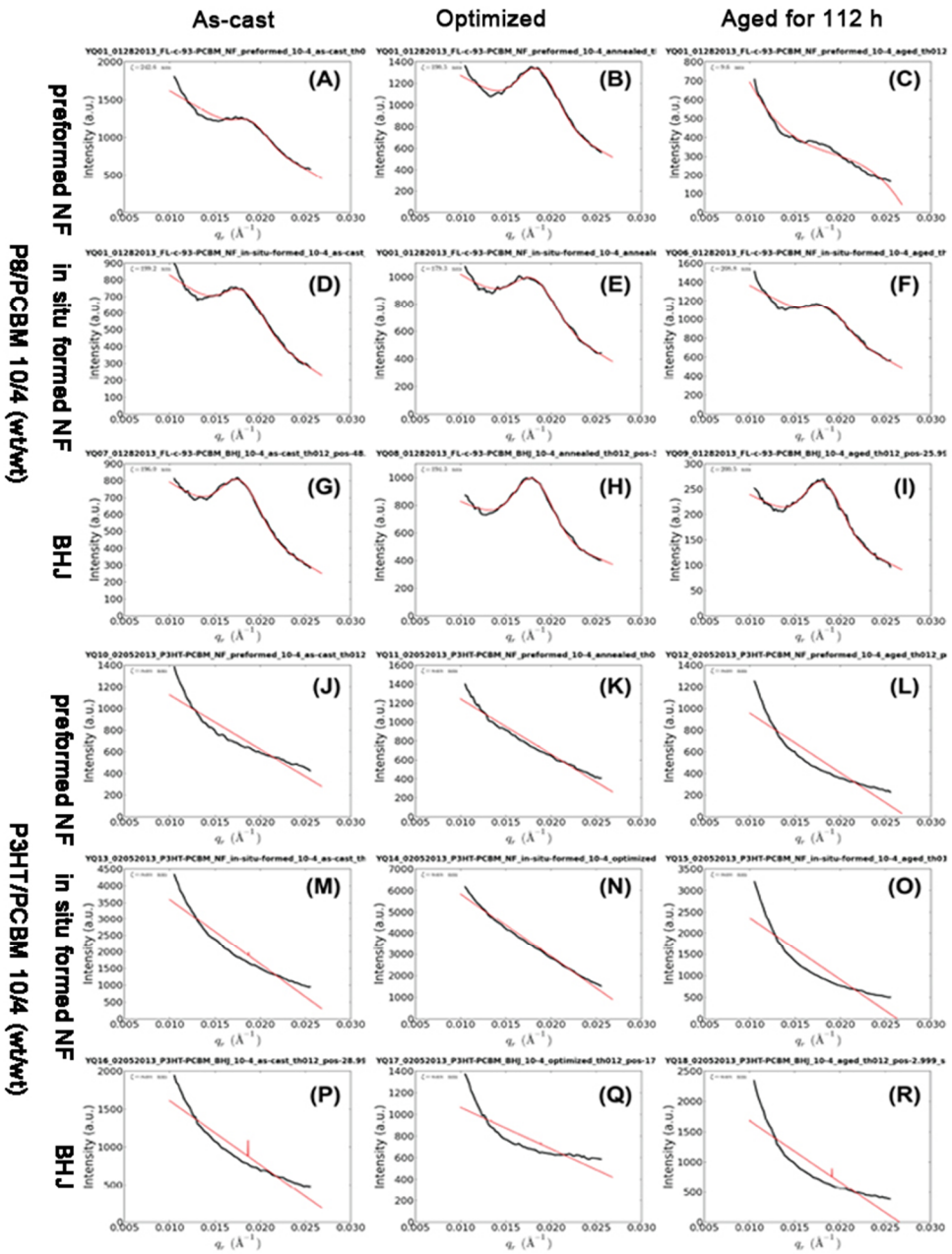


**Figure 5.17** Grazing-incidence small-angle X-ray scattering (GISAXS) line-cut profiles of as-cast (left column), optimized (150 °C, 15 min, middle column) and aged (110 °C, 112 h, right column) devices employing pre-formed **P8**/PCBM composite NFs (a to c), in-situ formed **P8**/PCBM composite NFs (d to f), **P8**/PCBM BHJ blends (g to i), pre-formed P3HT NF/PCBM (j to l), in-situ formed P3HT/PCBM NFs (m to o) and P3HT/PCBM BHJ blends (p to r). Polymer/fullerene weight ratio is 10/4 in all devices.

The GISAXS data probes nanoscale order and confirms the AFM observations previously described. The NF samples exhibit a broad undulation of scattering intensity along the vertical direction (Figures 5.15 and 5.16), whose spacing (0.035 $Å^{-1}$) is consistent with the form-factor for the cylindrical cross-section of the NFs (ca. 18 nm diameter). In the **P8**/PCBM composite NFs as well as BHJ thin films, a distinct in-plane GISAXS peak is observed, which suggests a well-defined nanoscale ordering of the two heterojunction materials. In particular, a well-defined spacing of 33-35 nm with a corresponding grain-size of ca. 200 nm (measured from the peak width) exists in all the **P8** samples (Figure 5.17), and appears to be robust with respect to annealing. On the other hand, no such ordering could be observed in all thin films containing P3HT and those of **P8** NF alone. These results suggest that the strong interactions between **P8** and PCBM can indeed lead to the formation of a well-defined and highly stable nanoscale morphology.

### 5.2.7 Conclusion

In conclusion, we have prepared nanofibers in acetone/CB (1/5, vol/vol) from a block polythiophene copolymer carrying ca. 7% isoorotic acid moieties (**P8**) which is capable of forming monotopic hydrogen bonding interactions with PCBM. The formations of **P8**/PCBM nanofibers is both investigated in preformed and in situ formed fashions where presence of PCBM could increase the width of the nanofibers from 16 nm to ca. 20 nm. Devices using **P8**/PCBM (10/4, by weight) presented a PCE of 4.17% which is high-performing regarding the low percentage of PCBM in the blends. Further thermal stability explorations through aging tests indicated that such **P8**/PCBM (10/4)

nanofibers are thermally robust as rationalized via optical microscopy and AFM analysis. The blend morphology from **P8**/PCBM (10/4) adopts more "face-on" orientation and nanostructured, as evidenced by the GIWAXS and GISAXS analyses.

### 5.3 P8/F2 nanofibers (10/4) and their applications in solar cells

In the previous section, I first investigated the **P8**/PCBM (10/4) nanofibers and studied their applications in polymer solar cells. The interactions between **P8** and PCBM are weak due to the monotopic hydrogen bonding nature. However, this weak hydrogen bonding interactions enabled high-performing solar cells fabricated from **P8**/PCBM (10/4) NF blends and in the meantime the **P8**/PCBM (10/4) solar devices exhibited superior thermal stabilities. We speculated the self-assembly between **P8** and PCBM accounted for such photovoltaic properties. Stimulated by such findings, I then started the **P8**/**F2** (10/4 w/w) nanofibers explorations where the three-point complementary hydrogen bonding interactions exist between **P8** and **F2**. I expect the "three-point" hydrogen bonding interactions will have different photovoltaic behaviors due to the stronger nature of the "three-point" interactions.

#### 5.3.1 UV-vis measurements of P8/F2 (10/4) nanofibers

A facile way to monitor the nanofibers formation in solution is UV-vis spectroscopy where the rise of the vibronic peaks at low energy region (ca. 515 nm, 550 nm, and 603 nm) indicates the existence of the nanofibers species. As seen in Figure 5.18a, similar to what I observed in the **P8**/PCBM (10/4) NFs, I carried out the UV-vis

measurements of **P8**/**F2** (10/4) solutions as preliminary means to assess the formation of the nanofibers in the presence of **F2**.

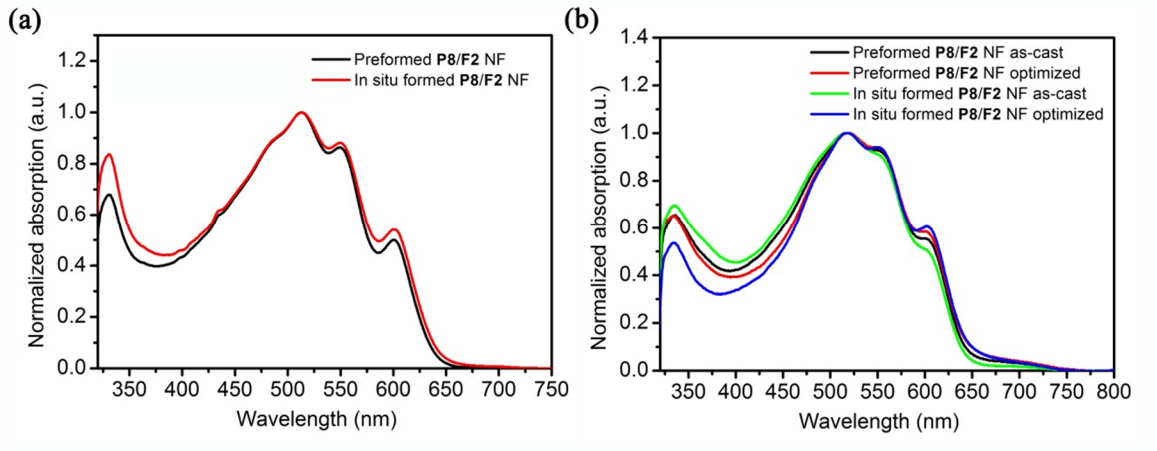


**Figure 5.18** UV-vis spectra of **P8**/**F2** (10/4) solutions in acetone/CB (1/5, vol/vol) after aging for 12 h (a) and thin-films spincoated at 400 rpm for 30 s (b).

The UV-vis spectra of the preformed **P8/F2** (10/4) NFs solution highly resemble its in situ formed counterpart both in solution and in thin films, regardless of the processing conditions applied. This indicates that **F2** had minimum impact on the packing of **P8** during the nanofibers formation process. Moreover, the vibronic absorption peak around 600 nm is slight enhanced in both solution and thermal annealed films, suggesting somehow a more packed stacking of **P8** polymer chains in the in-situ formed case.

### 5.3.2 TEM investigations of P8/F2 (10/4) nanofibers in solution

The direct visualization of nanofibers was realized via TEM measurements. Similar to previous operations on the P8/PCBM, the aged solutions of **P8**/F2 blends were measured by drop casting the solutions onto a TEM grid atop a filter paper.

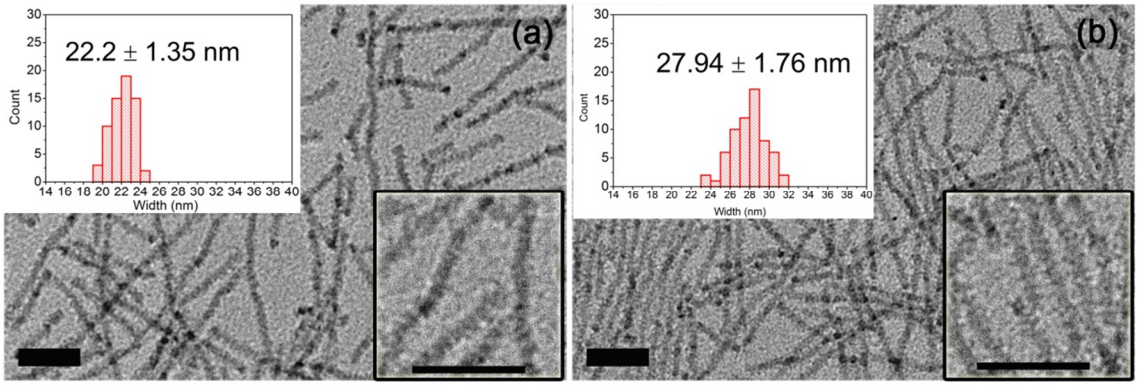


**Figure 5.19** TEM images of **P8** NF /**F2** (10/4) preformed (a), and **P8**/**F2** (10/4) NF in situ formed (b). Inserts on the left top of each TEM micrograph are the histograms of width statistics of the nanofibers, and on the right bottom are the images of magnified regions of the nanofibers under 15 k magnifications. The concentration for **P8**/**F2** (10/4) solution is 10 mg· $mL^{-1}$ based on the polymer weight. The scale bar is 200 nm.

As shown in Figure 5.19, the preformed naofibers have an average width of 22.2 ± 1.35 nm (a), and the in-situ formed nanofibers are wider than that of the preformed ones, giving a width of 27.94 ± 1.76 nm. The nanofibers grown from **P8**/**F2** are thicker than that of **P8**/PCBM NFs, indicating more **F2** were attached to the periphery of the polymer **P8** nanofibers. One possible reason is that the stronger interactions between **P8** and **F2** enables more **F2** attachment, and thus increase the width of the **P8** nanofibers. It is noted that the in-situ formed nanofibers are thicker than that of the preformed **P8**/**F2**

nanofibers. Such width differences could be explained by the fact that in the in-situ formed **P8**/**F2** nanofibers case, better intermixing between **P8** and **F2** enabled possible inclusion of the fullerenes during the nanofibers formation or **F2** have a better chance to approach the polymer's active hydrogen bonding sites.

### 5.3.3 Solar cells employing P8/F2 (10/4) nanofibers as active layers

To further explore the "three-point" hydrogen bonding interactions in modulating the morphologies of the active layers and solar cell performances from the nanofibers complexes, we fabricated the solar cells employing **P8/F2** (10/4) nanofibers as active layers where all the hydrogen bonding sites are fully occupied by **F2**. The results are shown in Table 5.3

**Table 5.3** Solar devices of **P8** /**F2** (10/4) NFs grown in acetone/CB (1/5 vol/vol) mixture[a]

| Conditions | | *PCE* (%)[c] | $J_{SC}$ (mA/cm$^{-2}$)[c] | $V_{OC}$ (V)[c] | *FF*[c] |
|---|---|---|---|---|---|
| as-cast | preformed | 0.78 ± 0.11 | 3.36 ± 0.44 | 0.50 ± 0.01 | 0.46 ± 0.01 |
| | in situ formed | 0.63 ± 0.08 | 2.90 ± 0.32 | 0.47 ± 0.02 | 0.46 ± 0.02 |
| annealed[b] | preformed | 2.34 ± 0.19 | 8.71 ± 0.70 | 0.55 ± 0.01 | 0.49 ± 0.01 |
| | in situ formed | 2.27 ± 0.14 | 8.85 ± 0.62 | 0.53 ± 0.01 | 0.48 ± 0.01 |

[a] spin-cast at 400 rpm for 30s, [b] thermal annealing at 150 °C for 15 min, [c]an average of five cells.

As listed in Table 5.3, the as-cast devices fabricated from **P8**/**F2** nanofibers give PCEs less than 1%, which was mainly limited by the low $J_{SC}$s and $V_{OC}$s. Cells made from

**P8**/**F2** preformed nanofibers showed largely similar PCEs as its in situ formed counterparts, indicating the presence of **F2** did not affect the **P8** nanofibers packing significantly. Thermal annealing boosts the cells performances by three- to four-fold due to the increased $V_{OC}$ and $J_{SC}$, indicating that more amenable charge separation and transport pathways were created. These devices yield PCEs over 2%, which outperformed its conventional BHJ cells using the same weight ratio as I described in Chapter 3. The increase could also be attributed to the enhanced $J_{SC}$, suggesting that the nanofibers morphology could facilitate the charge generation process. Therefore, we could conclude that by rational design on the aggregation form of polymer and fullerenes, better solar cells with high efficiencies could be achieved. Moreover, high fullerene loadings are not necessarily required to attain high photovoltaic performances, which is more cost-effective for mass production.

Furthermore, to test the efficacy of the complementary hydrogen bonding interactions between the polymer **P8** and fullerenes **F2** in mediating the thermal stabilities of the solar cells, I subjected the **P8**/**F2** (10/4) nanofibers solar devices to prolonged thermal annealing at 110 ºC up to 112 h, a similar strategy adopted for **P8**/PCBM (10/4) nanofibers devices. The results are shown in Figure 5.20 and Figure 5.21. Unexpectedly, both **P8**/**F2** preformed and in-situ formed nanofibers devices are not thermally stable against aging test. About 50% of the initial power was lost for the **P8**/**F2** nanofibers devices, mainly due to the decreased $J_{SC}$ and FF. The in-situ formed **P8**/**F2** nanofibers devices exhibited slightly enhanced thermal stability over the preformed counterparts, which is consistent with the **P8**/PCBM nanofibers' case. Such trend

indicates a better **P8**/**F2** intermixing occurs in the in-situ formed nanofibers case. The thermals stabilities of **P8**/**F2** nanofibers devices are similar to its conventional BHJ counterpart as reported Chapter 3, indicative of thermally instable morphology of **P8**/**F2** blend.

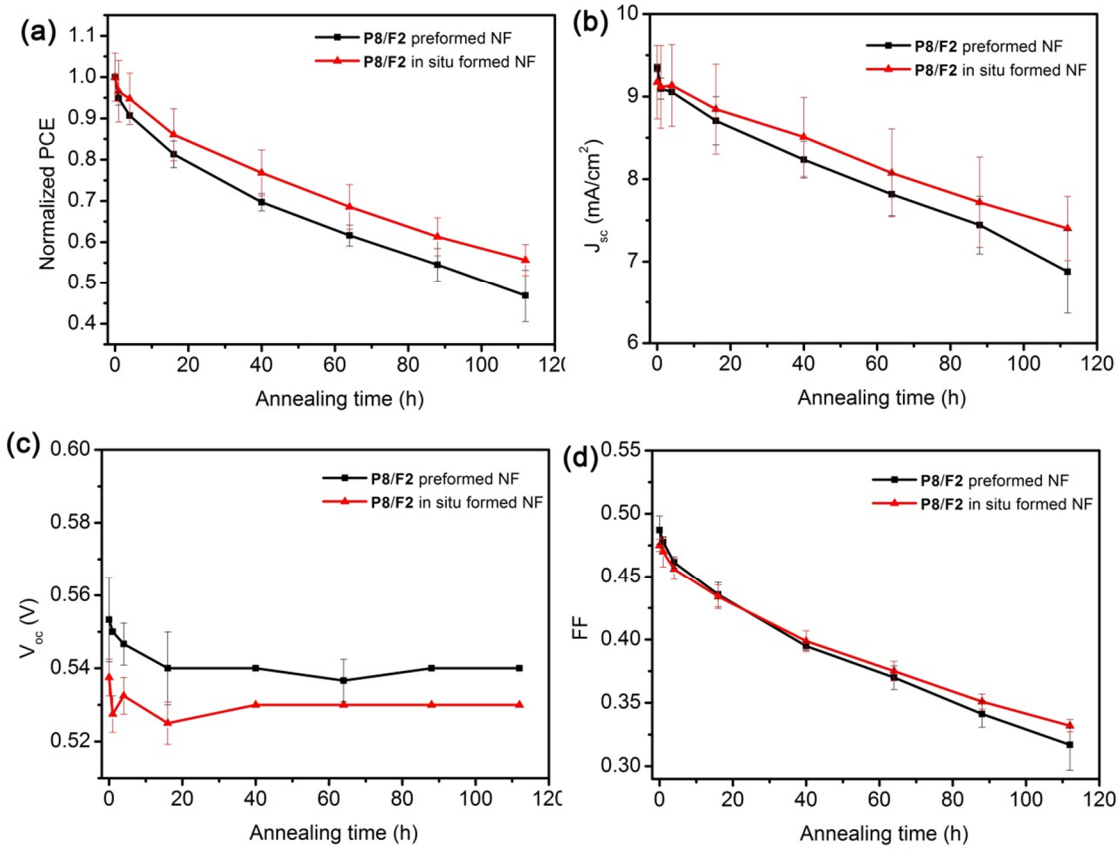


**Figure 5.20** Thermal stability tests of devices employing **P8**/**F2** (10/4) NFs at different blending conditions. Devices were annealed at 110 ºC under nitrogen for various times: (a) normalized *PCE* against annealing time; (b) $J_{SC}$ against annealing time. (c) $V_{OC}$ against annealing time; (d) FF against annealing time.

One possible reason to explain the photovoltaic and thermal stabilities differences lies in the interactions strength between the polymer **P8** and fullerenes. As for the 10/4 case, all the hydrogen bonding sites are fully complexed with fullerenes in. In the **P8**/**F2** (10/4) situation, the interactions between **P8** and **F2** are stronger than that of **P8**/PCBM due to the complementary hydrogen bonding interactions. Thermal annealing could not break the interactions between **P8** and **F2**, whereas in the **P8**/PCBM case, the interactions between **P8** and PCBM are weaker, the polymer **P8** and PCBM have a better change to reorganize upon thermal annealing. As a result, more interconnected charge transport pathways were created, which accounted for the higher photovoltaic performances of the **P8**/PCBM (10/4) devices.

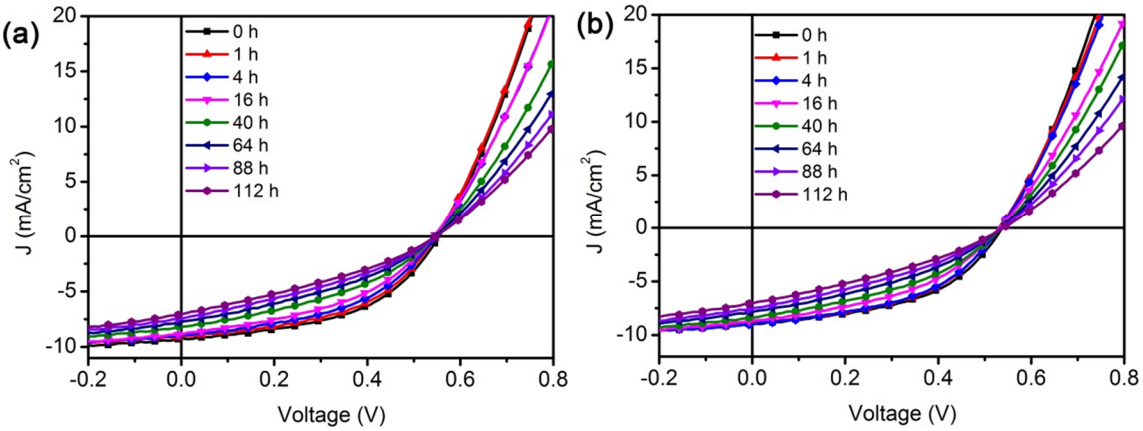


**Figure 5.21** I-V curves (under simulated AM1.5 G irradiation) of different devices employing **P8**/**F2** (10/4, wt/wt) measured after annealing at 110 °C for various times: (a) **P8** NF/**F2** preformed, (b) **P8**/**F2** NF in situ formed.

### 5.3.4 AFM analysis on the active layers of P8/F2 (10/4) NF devices

AFM was carried out on the active layers directly from the **P8**/**F2** (10/4) NF devices under different processing conditions to better understand the device photovoltaic properties. The results are shown in Figure 5.22 and Figure 5.23.

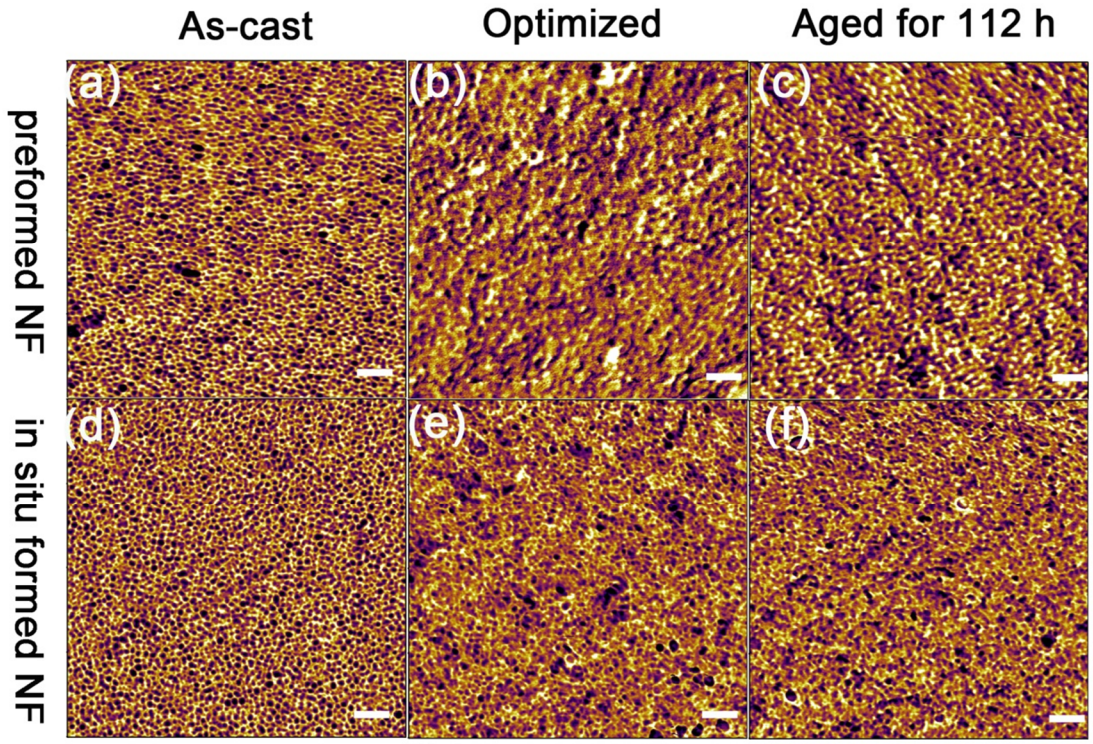


**Figure 5.22** Atomic force microscopy (AFM) phase images (2 μm × 2 μm) of devices employing **P8**/**F2** (10/4) NF blends as active layers first row: preformed, second row: in-situ formed (left column: as-cast; middle column: annealed at 150 °C for 15 min; right column aged at 110 °C for 112 h). The scale bar is 200 nm.

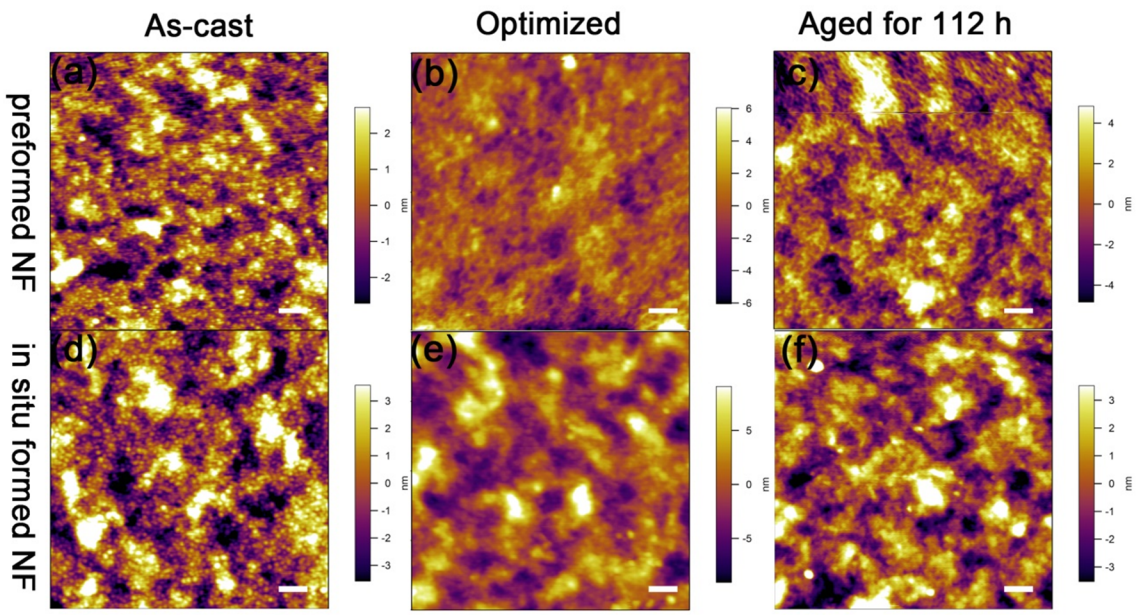


**Figure 5.23** Atomic force microscopy (AFM) height images (2 μm × 2 μm) of devices employing **P8**/**F2** (10/4) NF blends as active layers first row: preformed, second row: in-situ formed (left column: as-cast; middle column: annealed at 150 °C for 15 min; right column aged at 110 °C for 112 h). The scale bar is 200 nm.

Surprisingly, unlike the **P8**/PCBM (10.4) NF thin films, the **P8**/**F2** (10/4) NF thin films did not show nanofibers features as shown in Figure 5.22. The as-cast **P8**/**F2** (10/4) NF devices from both preformed and in-situ formed NF showed similar morphologies (a and d) where the nano-sized **F2** nanocrystals were embedded in the **P8** polymer matrix of dots or cylinders. This type of morphology is reminiscent of the **P8**/**F2** (10/8) BHJ device reported in Chapter 3. Thermal annealing destroyed such ordered, mainly due to the fact that the **F2** nanocrystals were more concentrated on top of the film surface. The enhanced PCEs for **P8**/**F2** (10/4) devices could be ascribed to the more connected electron transport

pathway since the **F2** nanocrystals aggregate into bigger domains that were less pronounced (Figure 5.22 b and d). Besides, the film surface became rougher (Figure 5.23 b and d), which may make the polymer nanodomains more interconnected. Prolonged annealing at 110 ºC for 112 h caused even bigger domains (Figure 5.23 c and f)

### 5.4 P8/F2 (10/8) nanofibers and their applications in solar cells

To further explore the influence of **F2** loadings on the width of the nanofibers and the resulting solar cells performances from **P8**/**F2** nanofibers blends, I deliberately increased the **F2** contents in the **P8**/**F2** 10/8 NF blends and studied their properties accordingly. With more fullerenes in the **P8**/**F2** blend, there is a bigger chance for **F2** to interact with **P8**. I anticipate that the more **F2** loadings in the **P8**/**F2** NF blends would have an impact on the **P8**/**F2** nanofibers and provide better photovoltaic performances, which is what I observed in the **P8**/**F2** BHJ solar cells in Chapter 3.

#### 5.4.1 UV-vis measurements of P8/F2 (10/8) nanofibers

As shown in Figure 5.13 a, both the **P8**/**F2** (10/8) NFs exhibited similar absorption patterns that is reminiscent of the spectra of **P8**/**F2** (10/4) NFs in solution, suggesting that more **F2** has little influence on the aggregation of **P8** nanofibers in solution. The vibronic patterns of the UV-vis spectra of the preformed **P8**/**F2** (10/8) NFs are similar to those of its in-situ formed version, indicating that the order of adding **F2** does not influence much on the formation of **P8**/**F2** nanofibers in solution. However, in their thin film UV-vis spectra, less pronounced vibronic features were seen in the 10/8 NF blends (Figure 5.24 b) than those of the 10/4 NF blend (Figure 5.22 b), implying that

more **F2** does impact the packing of the **P8**/**F2** blends in the solid state. It is worthy to note, the fullerene peak at ca 335 becomes broadened upon thermal annealing for the **P8**/**F2** NF thin films both in the preformed and in-situ formed NFs, the reason for which is currently unknown.

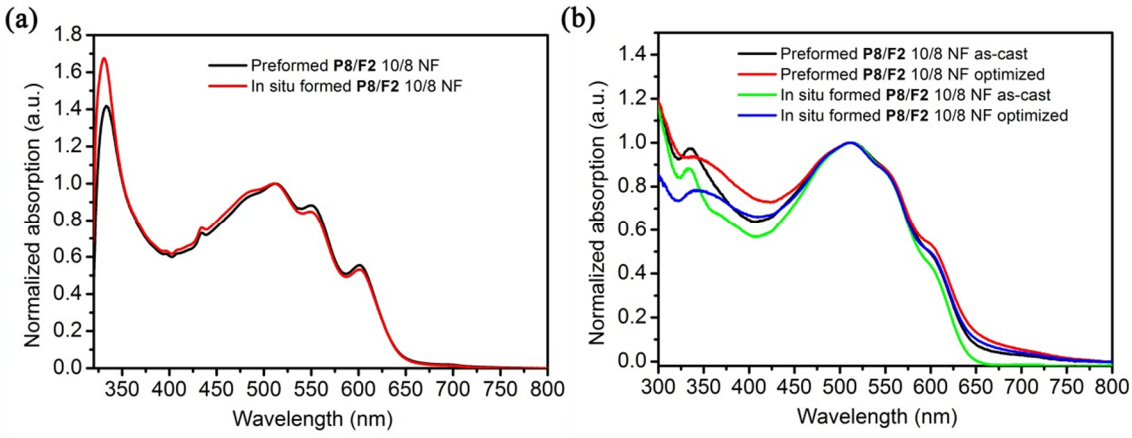


**Figure 5.24** UV-vis spectra of **P8**/**F2** (10/8 solutions in acetone/CB (1/5, vol/vol) after aging for 12 h (a), and corresponding thin-films annealed at 150 ºC for 15 min (b).

### 5.4.2 TEM investigations of P8/F2 (10/8) nanofibers in solution

TEM measurements on the **P8/F2** (10/8) nanofibers in solution provide more direct dimensional information on the nanofibers as shown in Figure 5.25. Due to more fullerenes present in the **P8**/**F2** blend solution, the widths of **P8**/**F2** (10/8) NFs are thicker than that of its 10/4 blends. The in-situ formed NFs are wider than its preformed counterparts, giving an average width of 27.58 nm and 30.60 nm, respectively. This trend is consistent with the observations in the **P8/F2** (10/4) NF cases. Such width increase of the nanofibers implies that by controlling the fullerenes contents in the **P8/F2** blend, the

width of the nanofibers could be tuned accordingly. It is postulated that the self-complementary hydrogen bonding interactions between **F2 and** coaggregation of **F2** may account for the further width increase of the composite nanofibers.

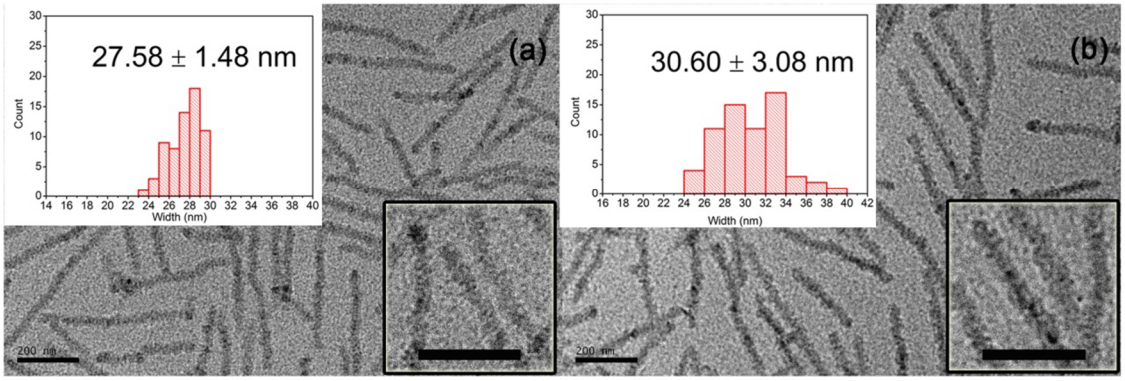


**Figure 5.25** TEM images of **P8** NF /**F2** (10/8) preformed (a), and **P8**/**F2** (10/8) NF in situ formed (b). Inserts on the left top of each TEM micrograph are the histograms of width statistics of the nanofibers, and on the right bottom are the images of magnified regions of the nanofibers under 15 k magnifications. The concentration for **P8**/**F2** (10/4) solution is 10 mg· $mL^{-1}$ based on the polymer weight. The scale bar is 200 nm.

### 5.4.3 Solar cells employing P8/F2 (10/8) nanofibers as active layers

To further examine the influence of more fullerenes on the photovoltaic performances, solar cells were made and tested using **P8/F2** (10/8) as active layers. The results are shown in Table 5.4 and Figure 5.26. Increasing the fullerenes contents in the **P8/F2** (10/8) blends indeed showed better PCEs than the **P8/F2** (10/4) cells for the as-cast devices, and the best efficiencies come from the preformed NF blend, with a PCE of 1.37% ± 0.05%. The low PCE was caused by the low $J_{SC}$, $V_{OC}$, and FF. implying an

unfavorable morphology for exciton diffusions and separations. Thermally annealing at 150 ºC for 15 min is an effective way to improve the device performances and in the **P8/F2** (10/8) NF cells, all the efficiencies are increased by one-fold, with PCEs over 2%. Such photovoltaic performance increase results mainly from the short-circuit current density $J_{SC}$. This suggests that thermal annealing promotes the polymer and fullerenes rearrangements for better charge separation and transport. Interestingly, **P8**/**F2** (10/8) blend did not show improved efficiencies significant compared with its 10/4 cases.

**Table 5.4** Solar cells of **P8** /**F2** (10/8) NFs grown in acetone/CB (1/5 vol/vol) mixture[a]

| Conditions | | *PCE* (%)[c] | $J_{SC}$ (mA/cm$^{-2}$)[c] | $V_{OC}$ (V)[c] | *FF*[c] |
|---|---|---|---|---|---|
| As-cast | preformed | 1.37 ± 0.05 | 5.59 ± 0.33 | 0.52 ± 0.01 | 0.47 ± 0.02 |
| | in situ formed | 1.03 ± 0.07 | 4.50 ± 0.24 | 0.52 ± 0.01 | 0.45 ± 0.02 |
| annealed[b] | preformed | 2.82 ± 0.17 | 9.39 ± 0.57 | 0.57 ± 0.01 | 0.53 ± 0.01 |
| | in situ formed | 2.25 ± 0.14 | 7.65 ± 0.55 | 0.56 ± 0.01 | 0.52 ± 0.01 |

[a] spin-cast at 400 rpm for 30s, [b] thermal annealing at 150 °C for 15 min, [c] an average of five cells.

It is noted, there is an S-kink in the in-situ formed NF 10/8 as-cast device (Figure 5.26 b), indicating unbalanced charge transport during the charge generation. This phenomenon implies that more fullerenes attachment onto the **P8** nanofibers may impede the charge generations in the as-cast device. However, thermal annealing eliminated such S-kink and thus makes the **P8**/**F2** domains more favorable in charge transport as

exhibited by the enhanced PCE. For the thermally optimized devices, larger $V_{OC}$s (ca. 0.56 V) and $J_{SC}$s are obtained for both preformed NF and in situ formed NF devices. This trend is in line with what I observed in the **P8/F2** 10/4 NF devices. Similar to the other NF devices in the current study, the preformed NF **P8/F2** 10/8 device outperformed its in situ formed version. The reason accountable for such difference is possibly due to less disturbed **P8** NF formation in the preformed case and thus less **F2** intercalation during the mixing process in solution for the **P8**/**F2** blends. However, further work on the thermal stability test on the **P8**/**F2** NF devices are needed to better understand such system.

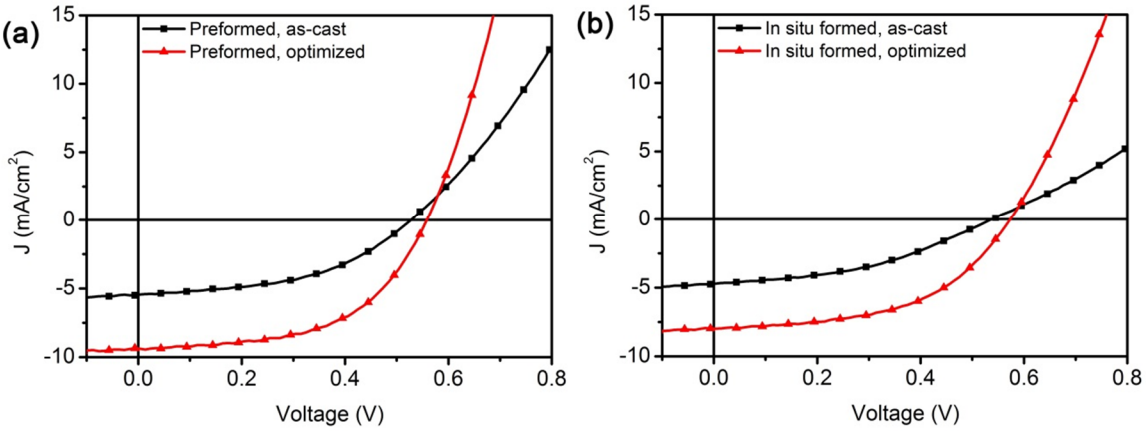


**Figure 5.26** I-V curves (under simulated AM1.5 G irradiation) of devices employing **P8**/**F2** (10/8, wt/wt) under different processing conditions: (a) preformed NF, (b) in situ formed NF.

### 5.4.4 Conclusion

By increasing the **F2** content in the **P8**/**F2** blend, nanofibers from the **P8**/**F2** (10/8) blend were still achieved. The widths of the nanofibers are bigger than those of its

10/4 blend, suggesting that more fullerenes could increase the width of the nanofibers. Such phenomenon indicates a controllable nature of the **P8**/**F2** blend nanofibers simply by tuning the contents of **F2** in the blends. Moreover, by incorporating such **P8**/**F2** (10/8) nanofibers into solar cell devices, the optimized cells showed similar PCEs compared with its 10/4 devices, indicating that fullerene contents in the **P8**/**F2** NF devices does not play a determining role in the solar devices. This is different from what is observed in their BHJ devices. One possible reason lies in how the fullerenes are orientated towards the **P8** nanofibers. More fullerenes are not necessary in the **P8**/**F2** NF system for high performing solar cells.

### 5.5 Possible formation mechanism of P8 nanofibers

Based on the experiments carried out on the **P8** nanofibers, I propose a possible formation mechanism of the **P8** nanofibers in acetone/CB mixed-solvents as shown in Figure 5.27.

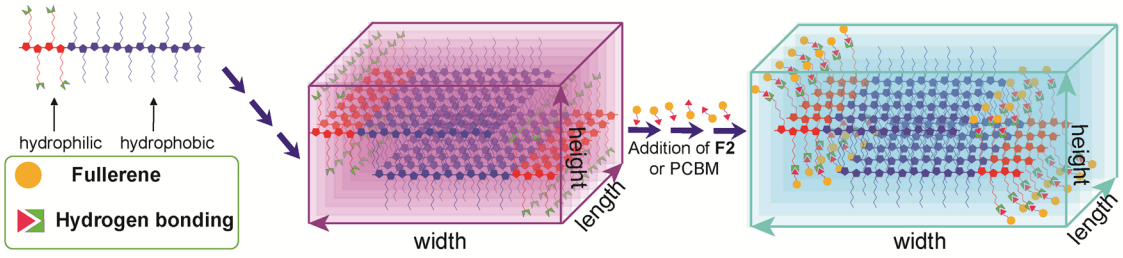


**Figure 5.27** Schematic illustration of the formation mechanism of **P8** nanofibers and its complex with fullerenes to form the **P8**/fullerenes complex nanofibers. The length of the nanofibers is reduced in the graph for clearance purpose.

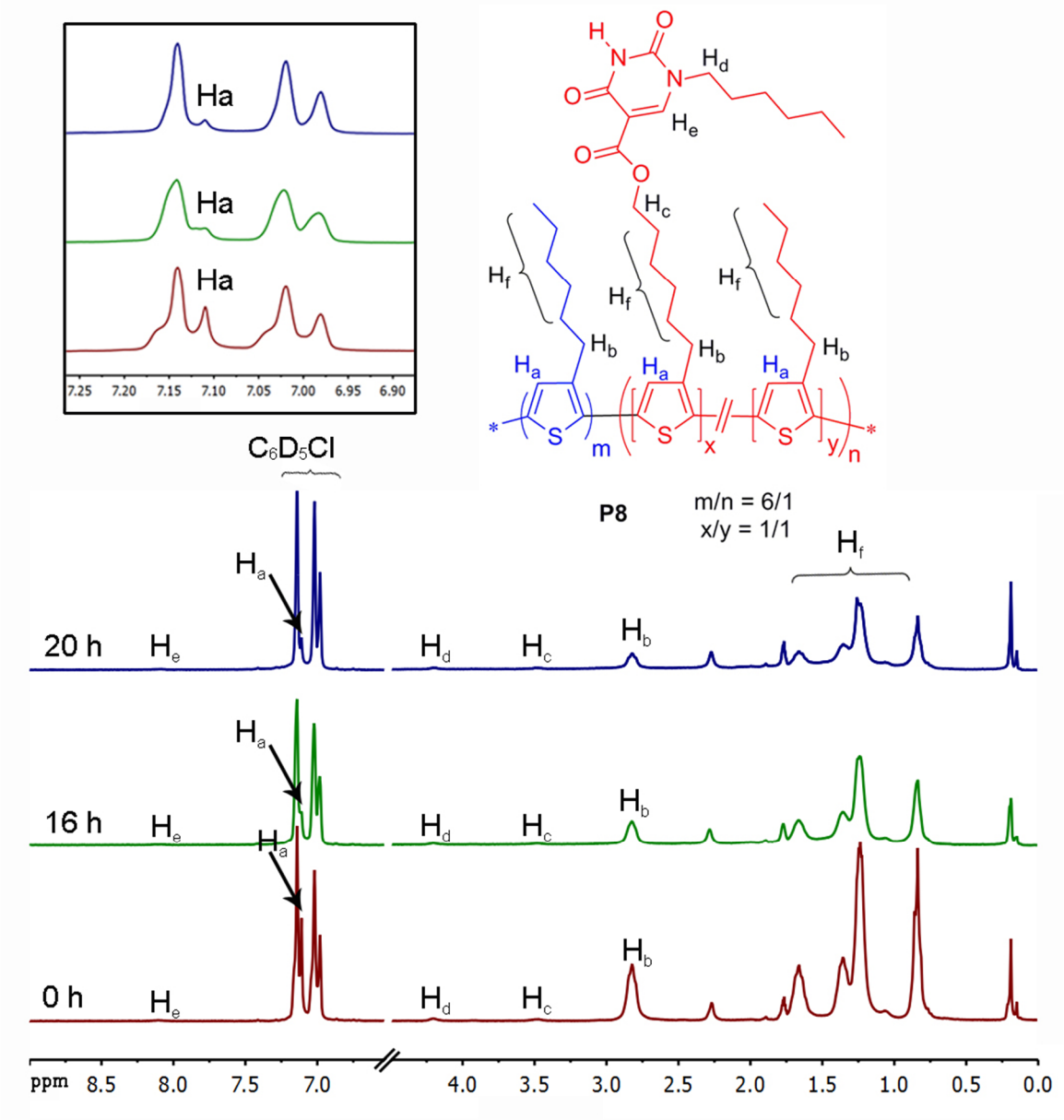


**Figure 5.28** Stacked $^{1}$H NMR spectra of **P8** in deuterated d5-chlorobenzene/ d6-acetone mixed-solvent (1/5, vol/vol) with different aging time. The inset on the top left is the zoomed-in aromatic regions and the inset on the top right is the chemical structure of **P8** and its major characteristic protons assignments. The peak at 2.25 ppm is assigned to water trace from the deuterated solvents as confirmed by control experiments.

Since acetone is a good solvent for the hydrogen bonding block segment (in red color) but a bad solvent for the pure P3HT block(in blue color). When acetone is added in to the chlorobenzene solution of **P8**, as a result, due to "the like dissolves like" principle, the pure P3HT block segment would be segregated to form the core of the nanofibers where the hydrogen bonding block protrudes outside as the periphery of the nanofibers. In light of the fact that the pure P3HT block is much longer than the hydrogen bonding block, the P3HT block will pack in an interdigitated way through the side chains intercalations which then aggregates in a face to face fashion along the axis perpendicular to the polymer side chain. Given the hypothesis that the hydrogen bonding block are placed at the exterior of the **P8** nanofibers, addition of the fullerenes (**F2** or PCBM) will be attached to the **P8** nanofibers backbone due to the hydrogen bonding interactions and thus give a **P8**/fullerene composite nanofibers with increased width.

Indeed, $^{1}$H NMR spectra of **P8** solution in deuterated d5-cholorbenzene/d6-acetone (1/5, vol/vol) aged for different time supports our postulation on the formation mechanism of **P8** nanofibers. As shown in Figure 5.28, when **P8** began to form nanofibers, the pure P3HT block partially went unsolvated due to the solvent segregation. Consequently, the protons from the pure P3HT block, namely, partial protons $H_a$ from the thiophene ring and the protons from the hexyl chains $H_b$ and $H_f$ were partially shielded. As a result, the intensities and integrations of Ha, $H_b$ and $H_f$ decreased with aging time (16 h). Even lower peak intensities and integrations of the protons were observed for the **P8** solution aged for 20 h. On the other hand, the intensities and integrations of protons from the hydrogen bonding block remained largely intact as seen from protons $H_c$, $H_d$ and

$H_e$. A slower spin relaxation time from the aggregated P3HT block than that from the well-dissolved hydrogen bonding block may explain this phenomenon. Such observations agree well with our TEM measurements on the **P8** nanofibers before and after adding the fullerenes. It is also in line with our findings on the results for the **P8**/**F2** composite NFs for preformed and in-situ formed fashion due to minimum difference in their NF width and photovoltaic performances of their devices.

### 5.6 Conclusion

By exploring the formation of **P8**/**F2** nanofibers and their utility in polymer solar cells, we found that the width of the nanofibers is tunable depending on the fullerene loadings in the blends. Moreover, the solar cells fabricated from **P8**/**F2** (10/4) showed worse photovoltaic performance than the **P8**/PCBM (10/4) devices. However, the devices fabricated from **P8**/fullerenes composite nanofibers have exhibited superior photovoltaic response than their conventional BHJ solar cells. Therefore, our method suggests that by rational design of the form of polymer aggregation, i.e. nanofibers, could enhance the power conversion efficiencies of the solar cells where low fullerene loadings could also achieve high PCEs. This is important giving the current expensive nature of PCBM. In the meantime, by tethering hydrogen bonding moieties on the polymer, weak interactions between the polymer and fullerenes through the hydrogen bonding interactions could build in conjugated polymer/fullerene composite nanofibers with domain sizes amenable to exciton diffusion and charge separation, which leads to thermally stable high-efficient solar cells. I believe this strategy that we developed could guide the polymer designs with controlled morphologies toward better polymer solar cells.

### 5.7 P8/F2 nanofibers grown from MeOH/chlorobenzene mixtures

During my exploration for the conditions to prepare the **P8/F2** nanofibers, I also found **P8/F2** could form nanofibers in MeOH/cholorobenzene mixed-solvent system. MeOH is also another polar solvent just like acetone, but it is protic whereas acetone is aprotic. In the acetone/CB system, I found good nanofibers could be induced with controllable widths from the **P8/F2** blend solution. Therefore, I speculate the self-assembly of **P8/F2** in MeOH/CB system will be different since MeOH will compete with **F2** for the hydrogen bonding sites on **P8** and thus the photovoltaic properties may be different and worth investigating. This part of data presented herein is preliminary and needs further work to compete the whole project.

#### 5.7.1 UV-Vis investigation of P8/F2 nanofibers

Based on the experience that I gained on the **P8**/**F2** nanofibers grown from acetone/CB mixtures, I adopted a similar strategy to prepare the **P8**/**F2** nanofibers both in preformed and in situ formed fashions. The volume ratio between methanol and cholrobenzene is set to be 1 to 5 by volume. The UV-vis absorption spectra of **P8**/**F2** nanofibers are summarized in Figure 5.29. Again, the appearance of the vibronic peaks (ca. 514 nm, 552 nm and 603 nm) at the lower energy region indicates the formation of nanofibers. Interestingly, the **P8**/**F2** 10/8 solutions showed higher vibronic peaks than those of its **P8**/**F2** 10/4 solutions as shown in Figure 5.29a where the peak intensity at ca. 514 nm is more pronounced. The peak at ca.330 nm is from the fullerenes absorption and its intensity is associated with its concentration in the **P8**/**F2** blend.

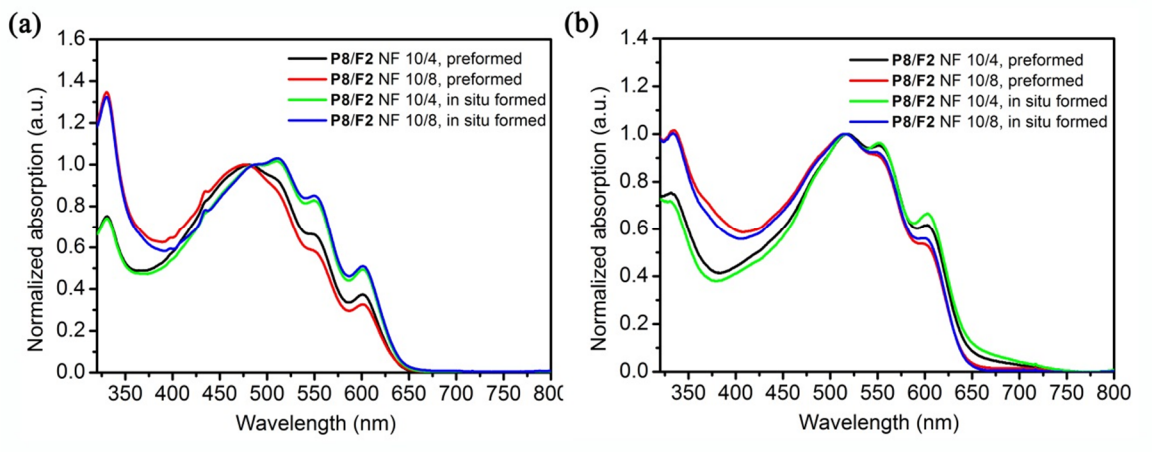


**Figure 5.29** UV-vis spectra of **P8**/**F2** (10/8 solutions in MeOH/CB (1/5, vol/vol) after aging for 12 h (a), and corresponding thin-films annealed at 150 ºC for 15 min (b).

The higher vibronic intensities in the 10/8 blends in solution could be explained by the fact by more **F2** would reduce the chance for the self-complementary hydrogen bonding interactions in solution between **P8** polymer chains due to the stronger complementary hydrogen bonding interactions between **P8** and **F2**. As a result, the packing of **P8** to form nanofibers will be more accessible. However, in their thin films, slightly enhanced vibronic patterns were observed in the 10/4 blend, indicating that more fullerenes would disrupt the packing of the polymer **P8** in the thin films, which agreed well with what I observed in their NFs in acetone/CB cases. One reason accountable for the difference is that fullerenes attached onto **P8** will make the side chains more crowded and thus less efficient for the **P8** chains to pack into nanofibers.

### 5.7.2 TEM investigations of P8/F2 nanofibers in solution

To better gain insight on the dimensional information on the nanofibers, one facile way to evaluate the **P8/F2** NFs is the TEM visualizations. The results for all the nanofibers formed in solutions at different conditions are shown in Figure 5.30. Similar to the nanofibers formed in acetone/CB mixtures, the **P8/F2** nanofibers could be formed from both preformed and in situ formed fashions.

The **P8** NF alone shows a width of ca. 17.13 nm and it increased to 21.79 nm upon the addition of **F2** at the weight ratio of 10/8. Further increasing the content of **F2** in the **P8/F2** yields thicker nanofibers, giving an averaging width of 28.52 nm and 31.53 nm for the preformed and in situ formed 10/8 NFs. It is noted, in the preformed 10/4 **P8/F2** NFs, the width of the nanofibers did not change much upon the addition of **F2**, which is slightly different with what I observed with other **P8/F2** cases. One possible reason is that, in the preformed **P8/F2** 10/4 NF case, all the hydrogen bonding sites on **P8** NFs are placed on the periphery of the nanofibers where the large amount of methanol present in the solution could solvate the hydrogen bonding sites against **F2** attachments since methanol itself are capable of a "two-point" D-A hydrogen bonding interactions. Due to the limited amount of **F2** in the **P8**/**F2** 10/4 blend, **F2** might fail to compete against methanol giving its large excess in the solution. Further increasing the amount of **F2** in the **P8**/**F2** blend could solve this problem as seen from the width increase both in the preformed and in situ formed 10/8 NF cases. This is consistent with trend for the width of **P8/F2** NFs formed in acetone/CB. However, in the in situ formed 10/4 blend, since **P8** and **F2** are in closed proximity in solution, it is speculated that the stronger "three-point"

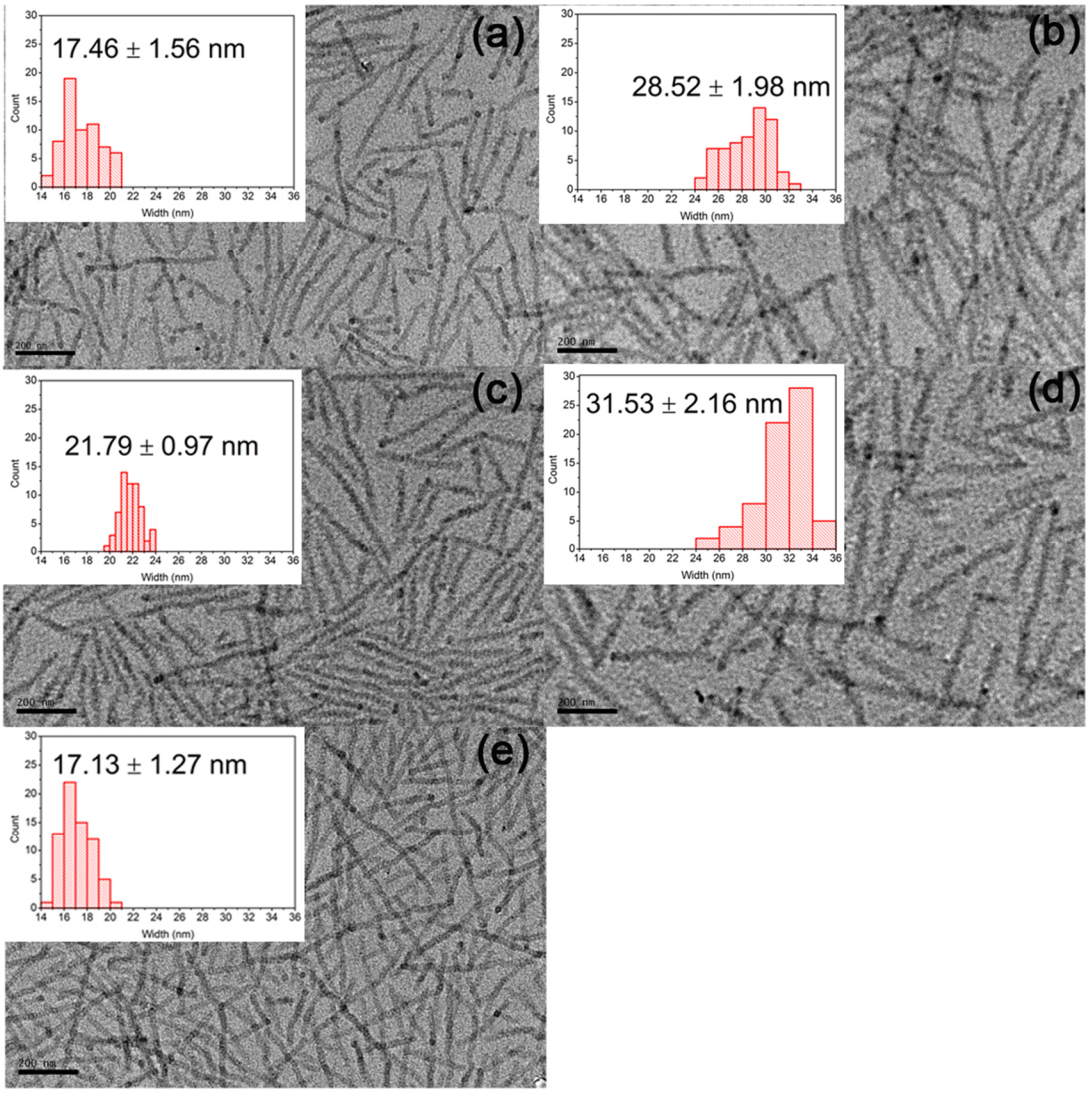


**Figure 5.30** TEM images of **P8/F2** nanofibers at conditions. (a) **P8/F2** 10/4 preformed NF, (b) **P8/F2** 10/8 preformed NF, (c) **P8/F2** 10/4 in situ formed NF, (d) **P8/F2** 10/8 in situ formed NF, (e) **P8** NF. Inserts on the left top of each TEM micrograph are the histograms of width statistics of the nanofibers. The concentration for **P8**/**F2** (10/4) solution is 10 mg· $mL^{-1}$ based on the polymer weight. The scale bar is 200 nm.

complementary hydrogen bonding interactions would enable the attachment of **F2** onto **P8**. When methanol is added in the **P8**/**F2** solution in cholorobenzene, it could not solvate the hydrogen bonding sites on **P8** as effectively as it does in the preformed case. These findings are interesting considering methanol itself could form self-complementary hydrogen bonding interactions. However, the results presented in this part are preliminary and further investigations are needed to better understand the formations of the **P8**/**F2** nanofibers in MeOH/CB mixtures.

### 5.7.3 Solar cells employing P8/F2 nanofibers as active layers

Likewise, the ultimate goal of the current research is to evaluate the **P8**/**F2** nanofibers in the application of polymer solar cells. By fabricating solar cells employing **P8**/**F2** as active layers, the influence of solvent used on the growth of nanofibers on the final photovoltaic performances of the solar cells could be better understood. The results are summarized in Table 5.5 and Figure 5.31.

Unexpectedly, the as-cast solar cells fabricated either from the preformed or in situ formed nanofibers at all weight ratios (10/4 and 10/4, **P8**/**F2**) do not exhibit good PCEs, with a best PCE of 0.28% ± 0.04% from the preformed **P8**/**F2** 10/8 blend. The low efficiencies were seen from its low $J_{SC}$s, $V_{OC}$s and FFs. Interestingly, higher **F2** loadings in the blends provided higher $J_{SC}$s and $V_{OC}$s but at the cost of reducing the FFs. Thermal annealing significantly improved the PCEs, mainly due to the enhancement from all parameters. Generally, the 10/4 blend gave the best PCEs of 1.11% ± 0.18% from the in situ formed NF devices, while the 10/8 blend yielded slight better performances, with

best PCEs of 1.91% ± 0.16% from the preformed NF devices. However, in contrast to the devices made from **P8**/**F2** NFs (grown in acetone/CB mixtures), the cells herein underperformed somehow.

**Table 5.5** Solar cell devices of **P8** /**F2** NFs grown in MeOH/CB (1/5 vol/vol) mixture[a]

| Conditions[c] | | *PCE* (%)[d] | $J_{SC}$ (mA/cm$^{-2}$)[d] | $V_{OC}$ (V)[d] | *FF*[d] |
|---|---|---|---|---|---|
| as-cast | 10/4 (Pre) | 0.12 ± 0.02 | 1.00 ± 0.08 | 0.29 ± 0.02 | 0.41 ± 0.02 |
| | 10/8 (Pre) | 0.28 ± 0.04 | 3.05 ± 0.23 | 0.35 ± 0.01 | 0.26 ± 0.02 |
| | 10/4 (In situ) | 0.11 ± 0.01 | 0.97 ± 0.10 | 0.29 ± 0.01 | 0.41 ± 0.02 |
| | 10/8 (In situ) | 0.20 ± 0.03 | 2.42 ± 0.14 | 0.32 ± 0.00 | 0.26 ± 0.03 |
| annealed[b] | 10/4 (Pre) | 0.76 ± 0.22 | 4.70 ± 0.35 | 0.44 ± 0.11 | 0.36 ± 0.04 |
| | 10/8 (Pre) | 1.91 ± 0.16 | 10.37 ± 0.77 | 0.51 ± 0.00 | 0.36 ± 0.01 |
| | 10/4 (In situ) | 1.11 ± 0.18 | 6.54 ± 0.82 | 0.47 ± 0.01 | 0.36 ± 0.03 |
| | 10/8 (In situ) | 1.72 ± 0.19 | 10.19 ± 0.67 | 0.49 ± 0.00 | 0.34 ± 0.02 |

[a] spin-cast at 400 rpm for 30s, [b] thermal annealing at 150 °C for 15 min, [c] different weight ratios (Pre: preformed NF, In situ: in situ formed NF) [d]an average of five cells.

As seen in Figure 5.31, severe charge recombination exists in all **P8**/**F2** NF devices, as indicated by the presence of an S-kink in their I-V curves. The S-kink is more severe in the 10/8 NF devices and more obvious in their as-cast devices (b and d). This phenomenon implies an unbalanced charge transport inside the solar devices which was possibly due to more **F2** attachment onto the **P8** nanofibers. Such S-kink is less pronounced in their thermally optimized devices. It is postulated that thermal annealing

may redistribute the orientations of **P8** and **F2** and thus promotes the crystallization of fullerenes **F2** and the reorganizations of polymer **P8**, which may create better balanced charge transport pathways. It is unclear for the reasons of the bad solar cells performances in the **P8**/**F2** NF grown from MeOH/CB mixtures. More studies are needed to better understand the PV performance differences of the solar cell devices.

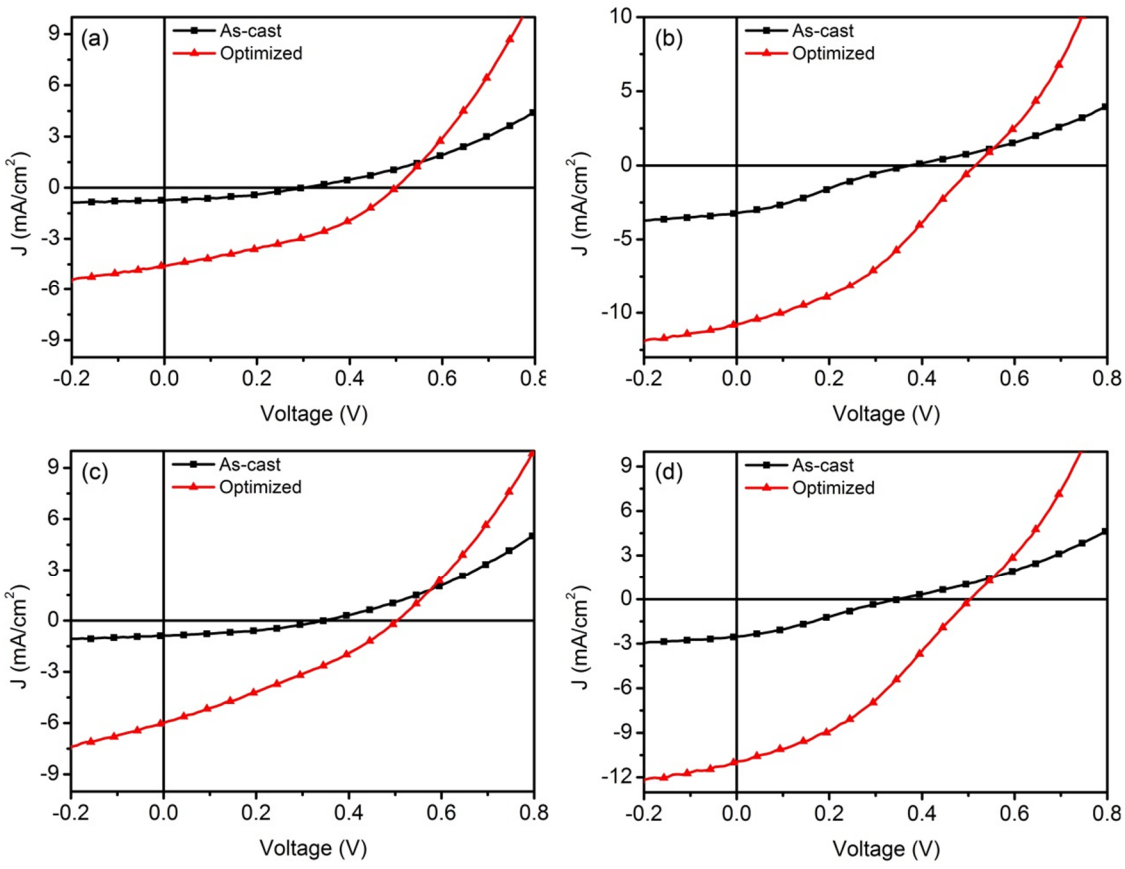


**Figure 5.31** I-V curves (under simulated AM1.5 G irradiation) of devices employing **P8**/**F2** NF under different processing conditions: (a) preformed NF 10/4, (b) preformed NF 10/8, (c) in situ formed NF 10/4, (d) in situ formed NF 10/8.

### 5.7.4 Conclusion

**P8**/**F2** blend is able to form nanofibers in MeOH/CB (1/5, v/v) mixtures as initially investigated via UV-vis spectroscopy. The dimensions of the **P8**/**F2** NFs are similar to those grown from acetone/CB mixtures as revealed by TEM analysis. The width of the P8/**F2** NFs is tunable depending on the concentration of **F2** in the **P8**/**F2** blend. Further explorations of the **P8**/**F2** NFs grown from MeOH/CB mixtures in the field of polymer solar cells as active layers did not show comparable results compared with results that obtained from the NFs grown in acetone/CB. Nonetheless, the results present in this section are preliminary and more systematical work is desired to finish this part of the project. Moreover, the reasons accountable for the inferior photovoltaic performances of the devices fabricated from the **P8**/**F2** NFs grown from MeOH/CB mixtures are currently unknown. In view that the differences between acetone and methanol as solvent additives are marginal, more experiments are needed to better reveal the charge transport pathways of solar cells in such polymer/fullerene nanofibers system. Nevertheless, my initial effort to prepare the polymer/fullerene nanocomposite through noncovalent interactions was successful aiming at obtaining high-efficient stable solar cells with tunable morphologies. Moreover, such morphology tunability could be realized simply by controlling the ratios of polymer and fullerenes in the blend.

## 5.8 Future work

In light of the success on controlling the morphologies of the active layers of the solar cells through the self-assembly of block copolymers and hydrogen bonding interactions, solar devices with high PCEs and enhanced thermal stabilities could be

fabricated. By modulating the relative orientation of the polymers and fullerenes and their aggregation pattern, i.e. composite nanofibers, we could probably reduce the fullerene loadings while still achieving high device performances. In the current **P8**/PCBM NF system, a weight ratio of 10/4 for the composite blend is still capable of obtaining high performing solar cells. However, by simply substituting PCBM with **F2** and in the **P8**/**F2** NF system, the resulting solar cells employing **P8**/**F2** NFs as active layers are less efficient and less stable than the **P8**/PCBM NF system. More work is still needed to better understand exact the reasons for this difference. It is proposed that probably the weaker interaction between PCBM and **P8** enables the reorganizations of the polymers and fullerenes easier to build the interconnected charge transport pathway. The current work brings forth a showcase that by engineering the structures of polymers and fullerenes and their self-assembly properties, high-efficient stable solar cells with enhanced thermal stabilities are accessible in a facile way. Since P3HT is a well-studied polymer and its maximum efficiency is around 5%, I believe the exhibited methodology could be applied in other high-performing polymers system to improve their thermal stabilities. However, more work is still required through collaborations to better understand the charge separation and transport process and thus provide guidelines for better solar cells designs.

## 5.9 Experimental

### 5.9.1 Materials and general methods

**P8** and **F2** were prepared according to the method as described in Chapter 3. Ultraviolet-Visible (UV-Vis) absorption spectra were recorded on a Shimadzu UV-2401 PC spectrometer over a wavelength range of 240-800 nm. Fluorescence emission spectra were obtained from a Varian Cary Eclipse Fluorometer. Transmission electron microscopy (TEM) images were taken on a JEOL 2010 high resolution TEM operated under 200 kV. Thin film X-ray diffraction (XRD) patterns were recorded on a Rigaku SmartLab diffractometer.

### 5.9.2 Genearl method for nanofibers preparation

In a dry vial was added 5 mg polymer (**P8** or P3HT) which was dissolved in 0.5 mL chlorobenzene. The solution was heated at 100 ºC for 1 h in a nitrogen glovebox and then stirred at room temperature (r.t) for another 1 h. Acetone (or methanol) with calculated volume was then added in a slow way with agitation via a microsyringe. The solution continued to age with stirring at room temperature for extended aging before analysis. The color change of the solution indicated the formation of the nanofibers in solution. The **P8**/PCBM nanofibers were prepared in two ways: (a) **P8** NF/PCBM preformed was synthesized by forming the **P8** nanofibers first and then transferring the P8 NF solution to another vial containing PCBM powder. Continuous stirring at r.t. for another 12 h before further analysis; (b) **P8**/PCBM NF in situ formed NF was prepared by dissolving **P8** with PCBM at 100 ºC for 1h to ensure complete dissolution of the

blend. The solution was then placed at .r.t with stirring. 100 μL of acetone or methanol was added into added in a slow way with agitation via a microsyringe at r.t. Continuous stirring at r.t. for another 12 h before further analysis. P3HT/PCBM nanofibers solutions were prepared in a similar way as described above.

### 5.9.3 Solar cell fabrication and testing

A structure of ITO/$MoO_3$/active layer/Al was adopted for the solar cell devices studied herein. Thin films of active layers were spun-cast from blend solutions prepared from the polymer/PCBM NF and their BHJ solutions. Solar cell devices were fabricated according to the following procedure: ITO-coated glass substrates (China Shenzhen Southern Glass Display. Ltd, 8 Ω/□) were cleaned by ultrasonication sequentially in detergent, DI water, acetone and isopropyl alcohol, each for 15 min. These ITO-coated glass substrates were further treated by UV-ozone (PSD Series, Novascan) for 45 min before being transferred to a nitrogen glove box (Innovative Technology, model PL-He-4GB-1800, $O_2$ < 0.1 ppm, $H_2O$ < 0.1 ppm) for $MoO_3$ deposition. $MoO_3$ (10 nm) was deposited using an Angstrom Engineering Åmod deposition system at a base vacuum level < $7 \times 10^{-8}$ Torr. The unfiltered **P8** (P3HT)/fullerenes NF blend solution was used for spin-coating on top of the $MoO_3$ layer at 400 rpm for 30s. Al (100 nm) was thermally evaporated through patterned shadow masks as anodes. Current−voltage (I−V) characteristics were measured by a Keithley 2400 source-measuring unit under simulated AM1.5G irradiation (100 mW/cm$^{-2}$) generated by a Xe arc-lamp based Newport 67005 150-W solar simulator equipped with an AM1.5G filter. The light intensity was calibrated

by a Newport thermopile detector (model 818P-010-12) equipped with a Newport 1916-C Optical Power Meter.

## 5.9 References


(1) Berson, S.; De Bettignies, R.; Bailly, S.; Guillerez, S. *Adv. Funct. Mater.* **2007**, 17, 1377.

(2) Jo, S. B.; Lee, W. H.; Qiu, L.; Cho, K. *J. Mater. Chem.* **2012**, 22, 4244.

(3) Bedford, N. M.; Dickerson, M. B.; Drummy, L. F.; Koerner, H.; Singh, K. M.; Vasudev, M. C.; Durstock, M. F.; Naik, R. R.; Steckl, A. J. *Adv. Energy Mater.* **2012**, 2, 1136.

(4) Byun, M.; Laskowski, R. L.; He, M.; Qiu, F.; Jeffries-El, M.; Lin, Z. *Soft Matter* **2009**, 5, 1583.

(5) Yang, X.; Loos, J.; Veenstra, S. C.; Verhees, W. J. H.; Wienk, M. M.; Kroon, J. M.; Michels, M. A. J.; Janssen, R. A. J. *Nano Lett.* **2005**, 5, 579.

(6) Ihn, K. J.; Moulton, J.; Smith, P. *J. Polym. Sci., Part B: Polym. Phys.* **1993**, 31, 735.

(7) Samitsu, S.; Shimomura, T.; Heike, S.; Hashizume, T.; Ito, K. *Macromolecules* **2008**, 41, 8000.

(8) Samitsu, S.; Shimomura, T.; Heike, S.; Hashizume, T.; Ito, K. *Macromolecules* **2010**, 43, 7891.

(9) Liu, J.; Arif, M.; Zou, J.; Khondaker, S. I.; Zhai, L. *Macromolecules* **2009**, 42, 9390.

(10) Oosterbaan, W. D.; Vrindts, V.; Berson, S.; Guillerez, S.; Douheret, O.; Ruttens, B.; D'Haen, J.; Adriaensens, P.; Manca, J.; Lutsen, L.; Vanderzande, D. *J. Mater. Chem.* **2009**, 19, 5424.

(11) Niles, E. T.; Roehling, J. D.; Yamagata, H.; Wise, A. J.; Spano, F. C.; Moulé, A. J.; Grey, J. K. *J. Phys. Chem. Lett.* **2012**, 3, 259.

(12) Roehling, J. D.; Arslan, I.; Moule, A. J. *J. Mater. Chem.* **2012**, 22, 2498.

(13) Sun, S.; Salim, T.; Wong, L. H.; Foo, Y. L.; Boey, F.; Lam, Y. M. *J. Mater. Chem.* **2011**, 21, 377.

(14) Li, L.; Lu, G.; Yang, X. *J. Mater. Chem.* **2008**, 18, 1984.

(15) He, M.; Zhao, L.; Wang, J.; Han, W.; Yang, Y.; Qiu, F.; Lin, Z. *ACS Nano* **2010**, 4, 3241.

(16) Li, L.; Tang, H.; Wu, H.; Lu, G.; Yang, X. *Org. Electron.* **2009**, 10, 1334.

(17) Park, Y. D.; Lee, S. G.; Lee, H. S.; Kwak, D.; Lee, D. H.; Cho, K. *J. Mater. Chem.* **2011**, 21, 2338.

(18) Xu, W.; Li, L.; Tang, H.; Li, H.; Zhao, X.; Yang, X. *J. Phys. Chem.B* **2011**, 115, 6412.

(19) Kim, J.-H.; Park, J. H.; Lee, J. H.; Kim, J. S.; Sim, M.; Shim, C.; Cho, K. *J. Mater. Chem.* **2010**, 20, 7398.

(20) Liu, W.; Liu, R.; Wang, W.; Li, W.; Liu, W.; Zheng, K.; Ma, L.; Tian, Y.; Bo, Z.; Huang, Y. *J. Phys. Chem. C* **2009**, 113, 11385.

(21) Seidler, N.; Lazzerini, G. M.; Li Destri, G.; Marletta, G.; Cacialli, F. *J. Mater.Chem.C* **2013**, 1, 7748.

(22) Moerman, D.; Lazzaroni, R.; Douhéret, O. *Appl. Phys. Lett.* **2011**, 99, 093303.

(23) Xin, H.; Kim, F. S.; Jenekhe, S. A. *J. Am. Chem. Soc.* **2008**, 130, 5424.

(24) Bertho, S.; Oosterbaan, W. D.; Vrindts, V.; D'Haen, J.; Cleij, T. J.; Lutsen, L.; Manca, J.; Vanderzande, D. *Org. Electron.* **2009**, 10, 1248.

(25) Xin, H.; Ren, G.; Kim, F. S.; Jenekhe, S. A. *Chem. Mater.* **2008**, 20, 6199.

(26) Xin, H.; Reid, O. G.; Ren, G.; Kim, F. S.; Ginger, D. S.; Jenekhe, S. A. *ACS Nano* **2010**, 4, 1861.

(27) Li, L.; Jacobs, D. L.; Che, Y.; Huang, H.; Bunes, B. R.; Yang, X.; Zang, L. *Org. Electron.* **2013**, 14, 1383.

(28) Li, F.; Yager, K. G.; Dawson, N. M.; Yang, J.; Malloy, K. J.; Qin, Y. *Macromolecules* **2013**, 46, 9021.

(29) Li, F.; Yang, J.; Qin, Y. *J. Polym. Sci., Part A: Polym. Chem.* **2013**, 51, 3339.

(30) Tsoi, W. C.; Spencer, S. J.; Yang, L.; Ballantyne, A. M.; Nicholson, P. G.; Turnbull, A.; Shard, A. G.; Murphy, C. E.; Bradley, D. D. C.; Nelson, J.; Kim, J.-S. *Macromolecules* **2011**, 44, 2944.

(31) Johnston, D. E.; Yager, K. G.; Hlaing, H.; Lu, X.; Ocko, B. M.; Black, C. T. *ACS Nano* **2014**, 8, 243.

(32) Allen, J. E.; Ray, B.; Khan, M. R.; Yager, K. G.; Alam, M. A.; Black, C. T. *Appl. Phys. Lett.* **2012**, 101, 063105.